UNIVERSITY OF SOUTHAMPTON

FACULTY OF PHYSICAL SCIENCES AND ENGINEERING

Physics and Astronomy

Inorganic nanoparticle-oligonucleotide conjugates for bio-sensing and therapeutics

by

Patrick dos Santos Vilela

Thesis for the degree of Doctor of Philosophy

August 2017

UNIVERSITY OF SOUTHAMPTON

ABSTRACT

FACULTY OF PHYSICAL SCIENCES AND ENGINEERING

Physics and Astronomy

Thesis for the degree of Doctor of Philosophy

Inorganic nanoparticle-oligonucleotide conjugates for bio-sensing and therapeutics

By

Patrick dos Santos Vilela

In recent years, advances in conjugation techniques have allowed for the development of a vast range of hybrid materials nanomaterials with biomolecules. The use of hybrid nanomaterials has improved the imaging, treatment and diagnostics of specific biological processes. In this project, the main aim was to explore the uses of nanoparticle-oligonucleotide conjugates for biomedical applications.

Gold nanoparticle-DNA probes for the intracellular detection of Vimentin mRNA were synthesized. These probes showed great target specificity and biocompatibility. Additionally, by means of light sheet microscopy, the three-dimensional visualization of Vimentin mRNA expression in tissue was performed in order to allow a deeper understanding of spatial and temporal expression events in wounded tissue.

Furthermore, gold nanoparticles were also conjugated with siRNA sequences for the knockdown of SMAD3 gene in order to reduce the overproduction of TGF-β. This hybrid material showed efficient delivery of siRNA duplexes into both human and mice cells, with minimal toxicity. Upon applying the gold nanoparticle-siRNA silencing probes in *in vivo* murine models, preliminary results *via* photography and histological analysis pointed to a reduction of scar tissue formation.

Finally, the conjugation of lanthanide upconversion nanoparticles and oligonucleotide sequences was performed for the successful development of a FRET type of sensor. This sensor was aimed for the detection of mRNA biomarkers of prostate cancer and Alzheimer's disease. Using graphene oxide as an electron acceptor, the nanoparticle-DNA conjugates specifically detected the presence of the target mRNA biomarker in low concentrations, both in blood plasma and cell lysate solutions.

Table of Contents

Table of Tables

Table of Figures

Table of Equations

List of Accompanying Materials

Academic Thesis: Declaration of Authorship

I, **Patrick dos Santos Vilela,**

declare that this thesis and the work presented in it are my own and has been generated by me as the result of my own original research.

Inorganic nanoparticle-oligonucleotide conjugates for biosensing and therapeutics

I confirm that:

1. This work was done wholly or mainly while in candidature for a research degree at this University;
2. Where any part of this thesis has previously been submitted for a degree or any other qualification at this University or any other institution, this has been clearly stated;
3. Where I have consulted the published work of others, this is always clearly attributed;
4. Where I have quoted from the work of others, the source is always given. With the exception of such quotations, this thesis is entirely my own work;
5. I have acknowledged all main sources of help;
6. Where the thesis is based on work done by myself jointly with others, I have made clear exactly what was done by others and what I have contributed myself;
7. Parts of this work have been published as:

Articles in academic Press:

1. Alonso-Cristobal, P.; **Vilela, P.**; El-Sagheer, A.; Lopez-Cabarcos, E.; Brown, T.; Muskens, O. L.; Rubio-Retama, J.; Kanaras, A. G.; Highly Sensitive DNA Sensor Based on Upconversion Nanoparticles and Graphene Oxide, *ACS Appl. Mater. Interfaces*, 2015, 7 (23), pp 12422–12429

2. **Vilela, P.;** El-Sagheer, Millar, T. M.; Brown, T.; Muskens, O. L.; Kanaras, A. G.; Graphene Oxide-Upconversion Nanoparticle Based Optical Sensors for

Targeted Detection of mRNA Biomarkers Present in Alzheimer's Disease and Prostate Cancer, *ACS Sens.,* 2017, 2 (1), pp 52–56

3. **Vilela, P.;** Heuer-Jungemann, A.; El-Sagheer, A.; Brown, T.; Muskens, O. L.; Smyth, N. R.; Kanaras, A. G.; Sensing of Vimentin mRNA in 2D and 3D models of wounded skin using DNA-coated gold nanoparticles, *Small*, 2018, doi:10.1002/smll.201703489

Abstracts, Posters or Presentations at Conferences:

1. HINT BCN Scientific Workshop (June 2015, Barcelona, Spain
2. COST Action TD1004–European Meeting (September 2015, Belgrade, Serbia)
3. SET for Britain Event (March 2016, London, UK)
4. E-MRS Spring Meeting (May 2016, Lyon, France)

Signed: .....Patrick dos Santos Vilela.....

Date: .....

Acknowledgements

Firstly, I would like to thank my main supervisor Dr. Antonios Kanaras for providing me with the tools, advice and help to carry out such an interesting research project and allow me to present my work in a variety of scientific settings. I would also like to thank my second supervisor Dr. Neil Smyth for all his advice and support with the biological part of the project, since without him I would have been lost so many times along the journey. I go out of this PhD with a set of different scientific skills thanks to both their contributions.

Thank you to all the staff of Biomedical Imaging Unit (Dr. Anton Page, Dr. David Johnston, Dr. Elizabeth Angus, Mrs. Patricia Goggin, Mr. James Thompson) for all their support with microscopy. A special thanks to Dr. Suzanne Brooks for all her help with the Light Sheet. Many thanks to all the Histochemistry Research Unit staff (Dr. Susan Wilson, Mr. John Ward, Mrs. Jenny Norma, and Mrs. Jamila McRobb) for their support in the histology part of my project. Everyone in both units had all the patience in the world to answer my questions and to help me in my project, giving nothing but a smile in return.

A special thanks to Prof. Tom Fleming and his group (Dr. Bhav Sheth, Joanna Gould, Laura Caetano, Reyna Penailillo and Diego Pedraza) for warmly receiving me in their group in the General Hospital. Without their output in some crucial details, I would not have achieved half of what I did experimentally. A heartfelt thank you to Pooja Khurana for being a great friend during those long cell work days.

A big thank you to all the people of my research group in Physics/Chemistry (permanent and visiting): Dr. Rute Fernandes, Dr. Amelie Heuer-Jungemann, Dr. Davide Giust, Dr. Pascal Harimech, Dr. Paulino Alonso-Cristobal, Johanna Midelet, Marilena Kyriazi, Angela DeFazio, Peter Shaw, Elena Urena, Alex Greenwood and Silvia Quaresma for all the support, help and good moments we spent together. Every bit helped in one way or another.

I would also like to thank the support and love of all my friends and family. A special thanks (and 75 msk) to Catarina and Ralfe for being such “WOW”nderful friends during writing. An enormous thank you to my parents, godmother and my borrowed family (my future-to-be in-laws) for all their support and love. Finally, my deepest and sincerest thanks to the most important people in my life: my hardworking exemplary brother (Ruben), from whom I got inspiration to keep on going forward just by being the extraordinary human being that he is; and my “mori” (Inês), for she has been my light in the darkest moments, my support when I could not continue and the reason why I now think that true happiness is possible when you have the right person on your side.

Definitions and Abbreviations

16HBE – Human Bronchial Epithelial Cells

2D – Two-dimensional

3D – Three-dimensional

A – Adenine

Aβ – Beta-Amyloid

AD – Alzheimer's Disease

Ag – Silver

APTMS – (3-Aminopropyl)trimethoxysilane

ATP – Adenosine Triphosphate

Au – Gold

AuCl – Gold Chloride

AuNP – Gold Nanoparticle

BACE-1 – Beta-Secretase 1

BLAST – Basic Local Alignment Search Tool

BNA – Bridged Nucleic Acid

BRAF – B-Raf gene

BRCA1 – Breast Cancer 1 gene

BSA – Bovine Serum Albumin

BSPP – Bis(p-sulfonatophenyl)phenylphosphine

C – Cytosine

Ca – Calcium

CO_2 – Carbon Dioxide

COOH – Carboxylic Acid

CR – Cross Relaxation

CTAB – Cetyl Trimethylammonium Bromide

CTGF – Connective Tissue Growth Factor

Cu – Copper

Cy3 – Cyanine 3 dye

Cy5 – Cyanine 5 dye

DAPI – (4',6-diamidino-2-phenylindole)

DCM – Dichloromethane

DMEM – Dulbecco's Modified Eagle's Medium

DMF – Dimethylformamide

DMSO – Dimethyl Sulfoxide

DNA – Deoxyribonucleic Acid

dsDNA – Double Stranded Deoxyribonucleic Acid

dsRNA – Double Stranded Ribonucleic Acid

DTT – Dithiothreitol

E1 – First Energy Level

E2 – Second Energy Level

EDC – 1-Ethyl-3-(3-dimethylaminopropyl)carbodiimide

EDTA – Ethylenediaminetetraacetic acid

EDX – Energy-dispersive X-ray Spectroscopy

EGF – Epidermal Growth Factor

EGFP – Enhanced Green Fluorescence Protein

EMT – Epithelial-Mesenchymal Transition

Er – Erbium

ESA – Excited-Stated Absorption

ETU – Energy Transfer Upconversion

FAM – Fluorescein Amidite

FBS – Foetal Bovine Serum

FGF – Fibroblast Growth Factor

FISH – Fluorescent *In Situ* Hybridization

FRET – Förster Resonance Energy Transfer

FTIR – Fourier Transform Infrared Spectroscopy

G – Guanine

Gd_2O_3 – Gadolinium (III) Oxide

GM3 – Monosialodihexosylganglioside

GO – Graphene Oxide

GSH – Gluthathione

H_2SO_4 – Sulfuric Acid

HBSS – Hanks' Balanced Salt Solution

HEPES – 4-(2-Hydroxyethyl)piperazine-1-ethanesulfonic acid

HER2 – Human Epidermal Growth Factor Receptor 2

Hg – Mercury

HIV – Human Immunodeficiency Virus

Ho – Holmium

I_2 – Iodine

IGEPAL Co-520 – Polyoxyethylene (5) nonylphenylether

IL-1/IL-β – Interleukin Beta

IR – Infrafred

KI – Potassium Iodide

$KMnO_4$ – Potassium Permanganate

KOH – Potassium Hydroxide

LaF_3 – Lanthanum Fluoride

$LiYF_4$ – Yttrium Lithium Fluoride

LNA – Locked Nucleic Acid

LSPR – Localized Surface Plasmon Resonance

MEF – Mouse Embryonic Fibroblast

MEM – Minimum Essential Media

Mg – Magnesium

MRC-5 – Human Lung Fibroblasts

mRNA – Messenger Ribonucleic Acid

MTT – (3-(4,5-Dimethylthiazol-2-yl)-2,5-Diphenyltetrazolium Bromide

$NaGdF_4$ – Gadolinium Sodium Fluoride

$NaLnF_4$ – Lanthanide Sodium Fluoride

$NaPO_4$ – Sodium Phosphate

$NaYF_4$ – Yttrium Sodium Fluoride

NCBI – National Center for Biotechnology Information

Nd – Neodymium

NH_2 – Amide

Sulfo-NHS – (N-hydroxysulfosuccinimide)

NIR – Near Infrared

O – Oxygen

OA – Oleic Acid

O.D. – Optical Density

P13K – Phosphoinositide 3-kinase

PA – Photon Avalanche

PAA - Polyacrylic Acid

PAGE – Polyacrylamide Gel

Pb – Lead

PBS – Phosphate Buffered Saline

PCA3 – Prostate Cancer Antigen 3

PCR – Polymerase Chain Reaction

PDGF – Platelet-derived Growth Factor

PEG – Polyethylene Glycol

PEI – Polyethylenimine

PIPES – 1,4-Piperazinediethanesulfonic acid

PL – Photoluminescence

PNA – Peptide Nucleic Acid

PVDF – Polyvinylidene Difluoride

PVP – Polyvinylpyrrolidone

qPCR – Quantitative Polymerase Chain Reaction

Ras – Rat Sarcoma Protein Family

RhoA – Ras Homolog gene family member A

RhodB – Rhodamine B (Tetraethylrhodamine)

RISC – RNA-induced Silencing Complex

RNA – Ribonucleic Acid

RNAi – RNA interference

rpm – Rotations per minute

R-SMAD – Receptor-regulated SMAD

RT – Room Temperature

RT-qPCR – Real Time Quantitative Polymerase Chain Reaction

SDS – Sodium Dodecyl Sulfate

SERS – Surface-enhanced Raman Spectroscopy

Si – Silica

siRNA – Small Interfering RNA

SMAD – SMA Mothers Against Decapentaplegic protein

ssDNA – Single-stranded DNA

T – Thymine

TAMRA – (5-Carboxytetramethylrhodamine)

TBE – Tris/Borate/EDTA

TEOS – Tetraethyl Orthosilicate

TGF-β – Transforming Growth Factor Beta

THF – Tetrahydrofuran

Tm – Melting Temperature

TNF-α – Tumor Necrosis Factor Alpha

TOAB – Tetraoctylammonium Bromide

TOPO – Trioctylphosphine Oxide

TRITC – Tetramethylrhodamine

U – Uracil

UC – Upconversion

UCNP – Upconversion Nanoparticle

UV – Ultraviolet

v/v – Volume Percent Concentration

VEGF – Vascular Endothelial Growth Factor

Vis – Visible

Yb – Ytterbium

YF_3 – Yttrium Fluoride

ζ – Zeta

Chapter 1: Introduction

The line that separates the areas of nanotechnology and biology has gotten blurrier and in the last decades the use of the previous to solve problems of the latter has been increasing exponentially. Inter-disciplinarity has been a novel way to understand and solve biological problems, mechanisms and applications and shine a light on them under a new lens. [1] Moreover, the growing application of nanomaterials has led to the creation and uplifting of novel areas of research such as nano-electronics, nano-photonics, nanotechnology and nanobiotechnology. [2–6] The latter has been on the rise for the past three decades, with the use of inorganic nanoparticles and their unique physical and chemical properties for biomedical applications being an area of increasing impact and interest. [7–11]

The conjugation of biomolecules to inorganic nanomaterials is an example of a nanotechnology solution for some biological problems and hurdles. [12, 13] For example, the specific intracellular and systemic delivery of biomolecules such as peptides, biopolymers and nucleic acids is sometimes expensive and/or inefficient. [14–16] However, this has been improved by using nanomaterials as a delivery vehicles capable of specifically targeted and triggered delivery. [17, 18] At the same time, the combination of specific properties from both biomolecules and nanomaterials have been explored to allow the development of novel hybrid nanomaterials. [19–21] The nanomaterials have found applications in different areas such as material sciences, electronics, optics, chemistry, environmental science, etc. More specifically in biology, these combinatory nanomaterials have a range of different applications such as drug delivery [17], bioimaging [22], biosensing [23] and gene engineering [24], amongst others. Hence, the relevance of bionanomaterials is patently clear not only as tools for the advancement of specific areas (e.g. material science, biology, chemistry) but also as core research topics in interdisciplinary research on its own. This work focus on the investigation of two different types of inorganic nanoparticles for three different types of bio-applications, with the ultimate goal of achieving a better overall understanding and manipulations of the scarring process and improving the detection of biomarkers for specific diseases.

In Chapter 4, the conjugation of gold nanoparticles with DNA sequences for imaging of scarring pathways is demonstrated. The combination of fluoro-tagged oligonucleotide and inorganic nanoparticles of specific optical properties allows the visualization of mRNA expression in both *in vitro* and *ex vivo* models of the skin for a more complete imaging of the cell migration process and, consequently, of wound healing. Taking advantage of a recent microscopic technique – light sheet microscopy – the visualisation of the mRNA expression was done in three dimensions over a short period of time, allowing a deeper understanding of both the spatial and the temporal expression events in a complex tissue environment.

Chapter 5 illustrates a pilot study where the application of RNA-gold nanoparticles conjugates as an engineering tool for gene knockdown purposes is investigated. The hybrid material shows potential as an efficient intracellular delivery of siRNA duplexes for the manipulation of one of the main wound healing pathways (TGF-β) in order to reduce scarring and consequently improve the healing of tissue. The oligo-nanoparticle conjugates were applied to *in vitro* and *in vivo* models, with different types of studies done to investigate the toxicity, cellular effect and histological impact of the application of these hybrid nanomaterials in different skin representative environments. Ultimately, this pilot study pointed to preliminary evidence on the potential of AuNP-siRNA complexes as silencing treatment tools of scarring tissue.

Chapter 6 discusses the conjugation of another type of inorganic nanoparticles – lanthanide upconversion nanoparticles – with oligonucleotides for biosensing. By combining the fluorescence properties of these particles with the specificity of oligonucleotides it is possible to create a sensor to detect specific biomarkers for diseases such as Alzheimer's disease or prostate cancer. Using graphene oxide as a quenching platform, the nanoparticle-oligonucleotide conjugates have the ability to specifically detect the presence of the targets of interest in low concentrations, both in tube conditions and in complex biological media such as blood plasma and cell lysate.

References

1. Van Noorden, R. (2015). Interdisciplinary research by the numbers. *Nature*, *525*(7569), 306–307. doi:10.1038/525306a

2. Haselman, M., & Hauck, S. (2010). The future of integrated circuits: A survey of nanoelectronics. *Proceedings of the IEEE*, *98*(1), 11–38. doi:10.1109/JPROC.2009.2032356

3. Duan, X., Fu, T. M., Liu, J., & Lieber, C. M. (2013). Nanoelectronics-biology frontier: From nanoscopic probes for action potential recording in live cells to three-dimensional cyborg tissues. *Nano Today*, *8*(4), 351–373. doi:10.1016/j.nantod.2013.05.001

4. Kirchain, R., & Kimerling, L. (2007). A roadmap for nanophotonics. *Nature Photonics*, *1*(6), 303–305. doi:10.1038/nphoton.2007.84

5. John F. Mongillo. (2007). Nanotechnology 101. *Nanotechnology 101*, 63.

6. Maine, E., Thomas, V. J., Bliemel, M., Murira, A., & Utterback, J. (2014). The emergence of the nanobiotechnology industry. *Nature nanotechnology*, *9*(1), 2–5. doi:10.1038/nnano.2013.288

7. Koopmans, R. J., & Aggeli, A. (2010). Nanobiotechnology—quo vadis? *Current Opinion in Microbiology*, *13*(3), 327–334. doi:10.1016/j.mib.2010.01.012

8. Whitesides, G. M. (2003). The “right” size in nanobiotechnology. *Nature Biotechnology*, *21*(10), 1161–1165. doi:10.1038/nbt872

9. Kohli, P., & Martin, C. R. (2005). Smart nanotubes for biotechnology. *Current pharmaceutical biotechnology*, *6*(1), 35–47. doi:10.1081/E-ENN

10. Elaissari, A. (2007). *Colloidal Nanoparticles in Biotechnology*. *Colloidal Nanoparticles in Biotechnology*. doi:10.1002/9780470258552

11. Hütten, A., Sudfeld, D., Ennen, I., Reiss, G., Hachmann, W., Heinzmann, U.,

Wojczykowski, K., Jutzi, P., Saikaly, W., Thomas, G. (2004). New magnetic nanoparticles for biotechnology. *Journal of Biotechnology*, *112*(1–2), 47–63. doi:10.1016/j.jbiotec.2004.04.019

12. Sperling, R. a, & Parak, W. J. (2010). Surface modification, functionalization and bioconjugation of colloidal inorganic nanoparticles. *Philosophical transactions. Series A, Mathematical, physical, and engineering sciences*, *368*(1915), 1333–1383. doi:10.1098/rsta.2009.0273

13. Montenegro, J.-M., Grazu, V., Sukhanova, A., Agarwal, S., de la Fuente, J. M., Nabiev, I., Greiner, A., Parak, W. J. (2013). Controlled antibody/(bio-) conjugation of inorganic nanoparticles for targeted delivery. *Advanced Drug Delivery Reviews*, *65*(5), 677–688. doi:10.1016/j.addr.2012.12.003

14. Langer, R. (1998). Drug delivery and targeting. *Nature*. doi:10.1517/14728222.2.1.145

15. Weill, C. O., Biri, S., Adib, A., & Erbacher, P. (2008). A practical approach for intracellular protein delivery. *Cytotechnology*, *56*(1), 41–48. doi:10.1007/s10616-007-9102-3

16. Torchilin, V. P. (2006). Recent approaches to intracellular delivery of drugs and dna and organelle targeting. *Annual Review of Biomedical Engineering*, *8*(1), 343–375. doi:10.1146/annurev.bioeng.8.061505.095735

17. Farokhzad, O. C., & Langer, R. (2009). Impact of nanotechnology on drug delivery. *ACS Nano*, *3*(1), 16–20. doi:10.1021/nn900002m

18. Barua, S., & Mitragotri, S. (2014). Challenges associated with penetration of nanoparticles across cell and tissue barriers: A review of current status and future prospects. *Nano Today*, *9*(2), 223–243. doi:10.1016/j.nantod.2014.04.008

19. Yata, T., Lee, K.-Y., Dharakul, T., Songsivilai, S., Bismarck, A., Mintz, P. J., & Hajitou, A. (2014). Hybrid Nanomaterial Complexes for Advanced Phage-guided Gene Delivery. *Molecular therapy. Nucleic acids*, *3*(August), e185.

doi:10.1038/mtna.2014.37

20. Huang, X., Tan, C., Yin, Z., & Zhang, H. (2014). 25th Anniversary Article: Hybrid Nanostructures Based on Two-Dimensional Nanomaterials. *Advanced Materials*, *26*(14), 2185–2204. doi:10.1002/adma.201304964

21. Katz, E., & Willner, I. (2004). Integrated nanoparticle-biomolecule hybrid systems: Synthesis, properties, and applications. *Angewandte Chemie - International Edition*, *43*(45), 6042–6108. doi:10.1002/anie.200400651

22. Yao, J., Yang, M., & Duan, Y. (2014). Chemistry, biology, and medicine of fluorescent nanomaterials and related systems: New insights into biosensing, bioimaging, genomics, diagnostics, and therapy. *Chemical Reviews*. doi:10.1021/cr200359p

23. Zhong, W. (2009). Nanomaterials in fluorescence-based biosensing. *Analytical and Bioanalytical Chemistry*. doi:10.1007/s00216-009-2643-x

24. Jin, L., Zeng, X., Liu, M., Deng, Y., & He, N. (2014). Current progress in gene delivery technology based on chemical methods and nano-carriers. *Theranostics*. doi:10.7150/t

Chapter 2: Theoretical Background

Nanotechnology, a term coined in 1959 by Prof. Richard Feynman [1], refers to the study and application of technologies and phenomena in the nanoscale (10^{-9} m) [2]. This ever growing field of research has a high applicability to several subjects, ranging from nano-optics [3], nano-fabrication [4] and nano-electronics [5] to nano-chemistry [6] and nano-biology [7, 8].

The work described in this thesis is based on the interdisciplinary research within the remits of nanotechnology, chemistry and biology. Therefore, this work is an example of how nanotechnology can be applied to other disciplines.

The combination of different building blocks used in this work, such as nanoparticles, oligonucleotides and graphene oxide, was done for biomedical applications. In Chapter 4, imaging of mRNA in cells and tissue is achieved using gold nanoparticles-oligonucleotide conjugates. In Chapter 5 the manipulation of the wound healing process in damaged tissue is demonstrated using gold nanoparticles-oligonucleotide conjugates. Finally, in Chapter 6 the development and application of an upconversion nanoparticle-graphene oxide sensor is for the detection of mRNA biomarkers of Alzheimer's disease and prostate cancer in complex biological environments (e.g. blood) is demonstrated.

2.1. Nano-blocks: thinking big by focusing on the small

In the past decades, the study and developmetn of nanoscale building blocks has become an integral part of many fields [9]. At the nanoscale, inert materials such as gold acquire new properties that can be explored and used in different ways than the bulk form. [2] Synthesis of nanomaterials can be done employing a range of different techniques, ranging from lithography and etching of bulk materials [10–12] to careful synthesis and controlled growth of nanoscale particles [13, 14] (i.e. nanoparticles). As made nanomaterials can be of different chemical composition: organic (e.g. lipids [15], protein [16], etc.) or inorganic (e.g. metal [17], silica [18], etc.) and each individual type of nanomaterial can benefit different areas of

research. For example, pharmaceutical sciences have improved areas such as cosmetics and drug delivery by taking advantage of nanoparticles as delivery agents for different drugs and active compounds [19–21]. Biomedical sciences in specific have seen an increase in nanomaterial research into new delivery agents, imaging tools [22, 23], sensors [24–26] and as part of treatment plans [27–30]. Further examples of nanomaterials applied in biomedical areas include gold nanoparticles (section 2.1.1.), lanthanide nanoparticles (section 2.1.2.), graphene oxide (section 2.1.3.) and oligonucleotides (section 2.1.4.).

2.1.1 Gold Nanoparticles

Colloidal gold is one of the oldest forms of nanotechnology known. Its first use was reported in glass staining by ancient civilizations [31, 32]. Unlike the yellow and mostly unreactive bulk form, gold nanoparticles (AuNPs) can interact with light by absorbance and scattering to create red and blue colours [33, 34]. However, the first reported study on the synthesis and properties of gold nanoparticles was only published in the 19th century by Faraday [35]. Further refinements of the synthesis were reported by Turkevich [36] and later by Frens [37, 38].

The synthesis of colloidal gold is based on the reduction of gold salts in the presence of a capping agent [39]. The most vastly studied and commonly used method for the synthesis of gold nanoparticles is the citrate reduction method (also known as the Turkevich-Frens method). [36, 40–42] This process consists of reducing an aqueous solution of tetrachloroauric acid (or sodium tetrachloroaurate) using an aqueous solution of trisodium citrate at boiling temperature. The size of the resulting colloids can be fine-tuned by adjusting the molar ratio of the gold precursor to citrate [38]. The underlying reaction consists of a series of chemical mechanisms (Figure 2.1.).

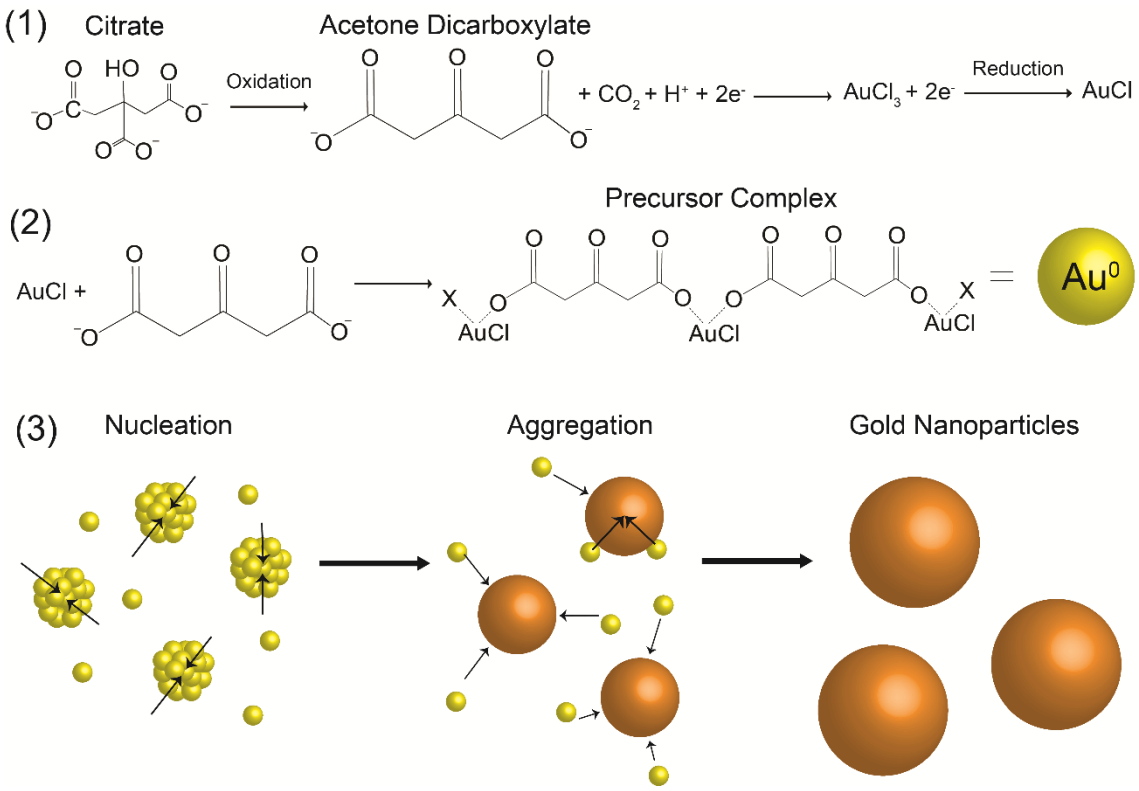

Figure 2.1 Synthesis of gold nanoparticles by the Turkevich-Frens method. The synthesis of gold nanoparticles can be divided into three steps: 1) oxidation of citrate molecules, followed by the reduction of gold (III) chloride into gold (I) chloride; 2) formation of a complex between the acetone dicarboxylate and the gold (I) chloride molecules designated as Au0 (X = continuation of the citrate-AuCl complex); 3) The precursor complex starts the accumulation of the Au0 precursor complex around nucleation points, which leads to progressive aggregation around the bigger particles until complete depletion of the Au0 precursor. This results in the formation of fully synthesised gold nanospheres.

In the first step of this reaction, citrate is oxidised into acetone dicarboxylate and, simultaneously, the gold (III) precursor is reduced to form gold (I) chloride (Figure 2.1.). The two compounds form stable complexes and start the nucleation process, forming gold nuclei (Au^0) from the disproportionation of gold chloride. Finally, the nanoparticles are formed due to the aggregation of gold atoms around these nucleation points, which in turn grow in size. As a result, nanoparticle dispersity depends on the rate of coagulation [43]. Xia and co-workers (2010) demonstrated that a rapid coagulation could be promoted by a rapid formation of acetone

dicarboxylate, resulting in a more uniform particle size [44, 45]. However, as discussed by Libert *et al*. (2003), decomposition of acetone dicarboxylate to acetone is favoured at high temperature and high pH [46]. This can lead to uncontrolled reduction of gold (III) by acetone [47], which in turn can result in further nucleation events. The occurrence of nucleation events at different time-points causes an increasingly broad size distribution of the resulting nanoparticles.

At the same time, citrate has a three-part role in the synthesis of colloidal gold. Peng and co-workers (2007) [42] reported that citrate works as: (1) a reducing agent that induces the formation of Au^{+} from Au^{3+}; (2) a capping agent that prevents further aggregation between formed nanoparticles; and (3) a pH regulator during the reaction, influencing the overall kinetics. However, the binding between carboxylic groups (from citrate) and the gold surface of nanoparticles is considerably weak. Any alteration of the pH or the overall net charge of the nanoparticles (for example, by adding sodium chloride) can lead to an irreversible aggregation [48–51]. To stabilize these nanoparticles, the use of stronger capping agents has been investigated. For example, synthetic protocols have been developed for the use of organic capping agents, such as tetraoctylammonium bromide – TOAB [52, 53] – or poly(vinyl pyrrolidone) – PVP [54–56], which control more precisely the size of the nanoparticles and increase the inter-particle stability.

However, these syntheses occur exclusively in organic solvents and the use of the resulting nanoparticles for biomedical applications requires a further step of functionalization in order to bring the particles to an aqueous media [57, 58]. Other synthesis performed exclusively in aqueous media tend to alter the reducing agent and keep citrate as the capping agent [59]. Many protocols have instead opted for exchanging the capping agents after the nanoparticles are already synthesised. The most commonly used is bis(p-sulfonatophenyl)phenylphospine (BSPP) [60, 61], since it increases the overall stability of gold nanoparticles *via* electrostatic interactions and enables the reversible aggregation of particles using salt. [62] At the same time, BSPP is not covalently bound to the surface of the gold nanoparticles. This allows further functionalization using molecules with a thiol functional group by taking advantage of sulphur-gold chemistry. [63]

Sulphur-gold chemistry has been strongly researched for the synthesis and functionalization of gold nanoparticles. The high affinity of gold surfaces for thiol functional groups facilitates ligand exchange reactions with more labile capping agents (e.g. BSPP). [64] In turn, the strength of the resulting gold-sulphur bond has been described as similar to that of gold-gold bonds. [65, 66] Additionally, thiolated capping agents can further infer functionality to the nanoparticles. [67] For example, thiol functionalized polyethylene glycols (PEGs) are commonly used in biomedical applications as unreactive delivery ligands.[68] Gold nanoparticles functionalized with thiolated proteins can be applied in cellular and organelle targeting [69], while gold nanoparticles covered with thiolated lipids have been used for the study of cellular membranes [70]. Finally, thiolated oligonucleotides have been described in a range of different applications from intracellular sensing [71, 72] and silencing [73–75] to programmable self-assembly [76–78].

In addition to their uses in biomedical sciences, gold nanoparticles also have a set of interesting optical properties due to their unique interactions with light. [31, 34] Metal nanoparticles in general can show optical responses across the visible, ultra-violet and infrared spectra. These responses derive from the oscillation of free electrons of the conduction band caused by interactions with an electromagnetic field, which can be observed in gold, silver and copper. [79, 80] Upon interaction with electromagnetic radiation, these free electrons are displaced relative to the nanoparticle core, thus creating a dipole. In turn, the displaced electrons are also attracted to the core *via* Coulomb interactions, resulting in a coherent oscillation of the electrons that surround the nanoparticles (Figure 2.2). This oscillation is commonly referred to as surface plasmon resonance (SPR).

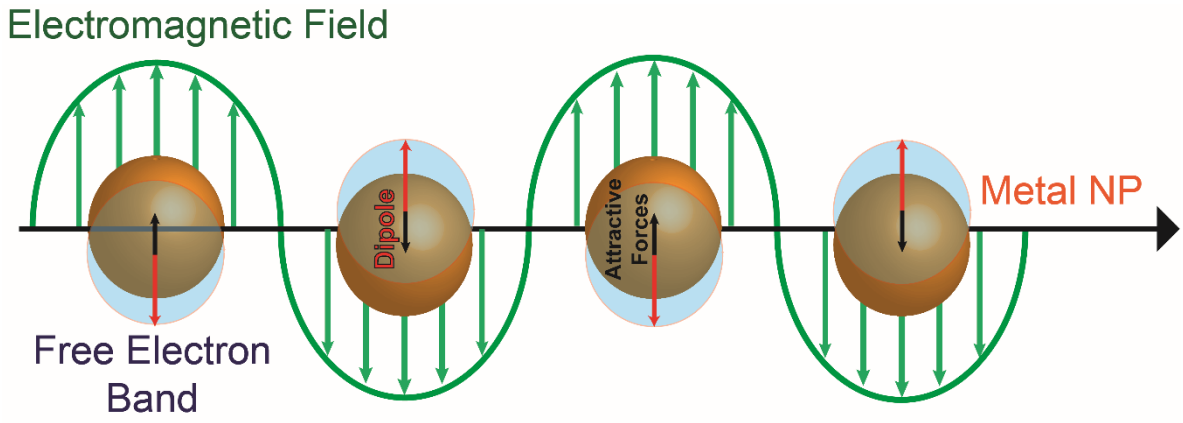

Figure 2.2 Schematic illustration of surface plasmon resonance on metal nanoparticles. The presence of an electromagnetic field (green) displaces the free electron of the conduction band (blue) relative to the nanoparticle core (golden). This creates a dipole (red) with the opposite direction of the electromagnetic field. Attraction forces (black) bring the electron band closer to the metal core, creating a surface plasmon resonance. Adapted from ref. [81]

Initially described by Mie *et al.* (1908) [82], the SPR can be affected by several factors, such as the size of the nanoparticles [81, 83]. This results in the possibility of controlling both the nature of the material and the size of the nanoparticles in order to control how the resulting nanomaterial will interact with light. This fine tuning of the optical properties of gold has been used mainly in the development of sensors [80], from on-field sensors that can detect the presence of specific proteins by changing from red to blue colour [84], to more sensitive sensors that can distinguish between different conformations of the same protein [85].

Finally, in combination with their optical properties and versatile chemistry, gold nanoparticles have been shown to be a relatively non-toxic metal type of nanoparticle. [86, 87] The toxicity of gold nanoparticles depends mostly on their size [88], coating agent [86] and overall net charge [89]. Sub-10 nm AuNPs have been shown to cause oxidative stress due to their ability to enter cellular organelles such as mitochondria and nucleus. [90] AuNPs coated with highly toxic cationic surfactants such as cetyl trimethylammonium bromide (CTAB) also demonstrate highly toxic effects on cells due to their ability to destabilize the phospholipid

membrane and to interrupt the ATPsynthase pathway from the resulting CTA+ cation by-products. [91–93] In contrast, anionic AuNPs above 12 nm have repeatedly been reported as non-toxic in a variety of different cell lines and models. [94–100] Consequently, biologically oriented applications of AuNPs have focused on the use of variations of AuNPs resulting from the Turkevich-Frens method.

2.1.2 Upconversion nanoparticles

The use of light sensitive nanoparticles in biomedical applications has seen a strong increase in the last decades. Several therapies have been developed based on light-activation for specific treatments, namely the release of targeted drugs in specific body locations (e.g. photodynamic therapy for destruction of tumours [101–103]) or heat treatment by non-radiative conversion of absorbed photon energy into heat (e.g. photothermal therapy for the disruption of cell structures and metabolic pathways [104–106]).

Additionally, molecular imaging using photoluminescence (PL) spectroscopy has become a well-studied method applied in medical diagnostics, DNA sequencing, cell imaging and bioassays. [107] PL spectroscopy can be used to study a wide range of biological specimens, from bacteria [108], viruses [109], cells [110] and animal models [111, 112]. PL imaging relies on exogenous contrast agents such as organic dyes [113], organo-silica materials [114], fluorescent proteins [115], metal complexes [116] and metal or semiconductor nanoparticles [116]. Most of these contrast agents rely on Stokes-shifted emission using excitation at more energetic wavelengths (such as ultra-violet or blue-green visible ranges) to emit at higher and less energetic wavelengths. [117, 118] However, this type of fluorescence mechanism has some drawbacks. These agents show low signal-to-background ratio due to unwanted scattering effects and auto-fluorescence of biological samples (e.g. tissue) when exposed to short wavelength light. [119] Additionally, ultra-violet (UV) and visible light have a short penetration depth in and out of tissue, making it harder for excitation and emission light to arrive at its target. [120] Finally, long

exposure to high energy light can lead to DNA damage and cellular death, increasing the overall toxicity of the treatment. [121–123]

Biological tissues have an optical transparency window in the near-infrared (NIR) range, from 700 to 1100 nm, where the interference with light from cells or tissue is minimal. [124] Consequently, research has focused on exploring this window using NIR excitation/emission mechanisms. This type of imaging not only allows for deeper penetration of the excitation light and reduced photo-damage but also offers lower background noise consequent of auto fluorescence or light scattering. [115, 124] Based on this, two types of PL imaging agents with NIR excitation have emerged: Stokes and anti-Stokes based agents.

Stokes shifted agents rely on the normal fluorescence mechanism to be excited at NIR and emit in the far-NIR or IR regions [125]. These take full advantage of the "biological window" but require upgraded and specialised microscopy and imaging techniques in order to detect in the IR spectral region. [126] Furthermore, at around 1300-1500 nm biomolecules start interacting with light, directing energy to vibrational and rotational movements of molecules. [127]

In contrast, agents based on anti-Stokes shifts take advantage of a mechanism where multiple photons of lower energy are absorbed sequentially and excite electrons with long lifetime and present in highly hierarchical energy levels. This converts two or more low-energy photons into shorter wavelength emissions making it possible to absorb in NIR and emit at the UV or visible regions. This process is usually referred to as upconversion (UC). [128]

As an example of the anti-Stoke type of PL imaging agents, lanthanide-doped upconversion nanoparticles (UCNPs) have been increasingly investigated as bioimaging tools. [129, 130] UCNPs are guest-host systems where trivalent lanthanide guest ions are dispersed in an appropriate host lattice. The dopants of lanthanide elements are optically active, which emit light when excited and have overlapping energy levels of excitation. This allows the transfer of photonic energy between ions of different dopant lanthanide elements (Figure 2.3.).

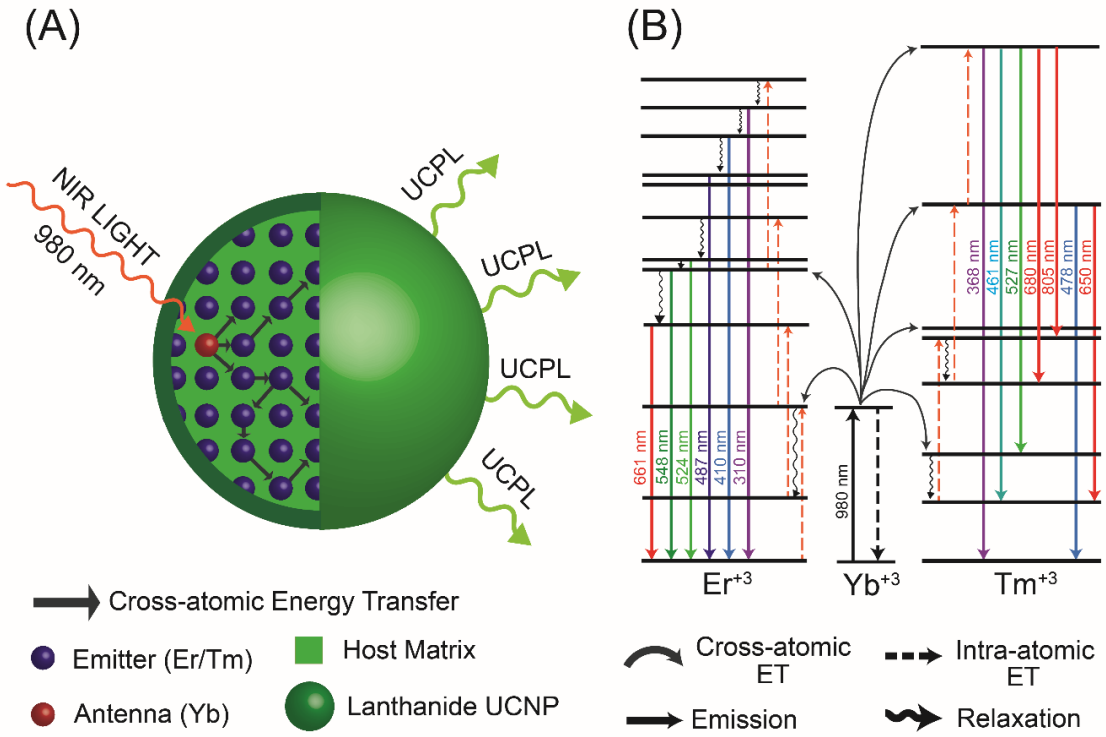

Figure 2.3. Working principle of lanthanide upconversion nanoparticles. The host lattice holds both the antenna (red) and the emitter (blue) lanthanide ions (A). The antenna absorbs near infrared light and the resulting energy is transferred to nearby emitter atoms. In turn, these atoms emit visible light in different wavelengths *via* cross-atomic energy transfer due to overlapping energy ladders of all the lanthanide elements (B). Adapted from ref. [130] and [131].

Generally, the UC PL arises from the 4f−4f orbital electronic transitions within a single lanthanide ion. The shielding of 4f electrons by the outer complete 5s and 5p shells results in sharp emissions, which exhibit high resistance to photo-bleaching and photochemical degradation. Furthermore, UC PL can be calculated with the following equation (equation 2.1.) [132, 133]:

$$I_{UCPL} = KP^n$$

Equation 2.1. Photoluminescence intensity of upconversion events. Where I_{UCPL} is the photoluminescence intensity of upconversion events, P is the power of pump laser, K is the coefficient related to the material used and n is the number of excitation photons required to produce the upconversion photoluminescence.

It is possible to infer from this equation that the intensity of the fluorescence emitted through UC PL is directly determined by the number of excitation photons that the material is exposed to. Therefore, the efficiency of a UC PL mechanism (also known as upconversion quantum yield) is strongly dependent on the excitation density. UC quantum yield is defined as the ratio of the number of emitted upconverted photons to the number of absorbed NIR photons. Thus, the UC quantum yield can be affected by the mechanism of UC PL of choice. [134, 135] Currently, there are two main mechanisms reported in recent literature.

Excited-state absorption (ESA) (Figure 2.4.a) is one of the most simple and explored mechanisms of UC. ESA derives from a successive absorption of two photons by a single electron of a specific ion. The electron is sequentially excited from a lower level of energy (ground state) to an intermediate level (E1) and afterwards from E1 to a higher energetic level (E2). Consequently, upconverted emission will occur from the E2 level. To achieve highly efficient ESA, a ladder-like arrangement of the energy states of a material is necessary. [136] Only a few lanthanide ions such as erbium (Er^{3+}), holmium (Ho^{3+}), thulium (Tm^{3+}) and neodymium (Nd^{3+}) have such energy level structures. The resulting nanoparticles usually rely only on the use of one lanthanide dopant. Therefore, the efficiency of the ESA mechanisms relies on the concentration of the single dopant on the lattice matrix. [137, 138]

Energy transfer Upconversion (ETU) mechanism (Figure 2.4.b)[139–141] involves two neighbouring ions , contrasting with ESA which uses a single lanthanide ion. In an ETU process, an ion known as the antenna (or sensitizer) is first excited from the ground state to its E1 level by absorbing a pump photon. It then transfers its harvested energy to the E1 level of the second ion, known as the emitter (or activator). This excites the second ion's electron to its upper emitting state E2, which upon relaxation releases energy in the form of a specific wavelength emission. The upconversion efficiency of an ETU process is sensitive to the average distance between the neighbouring antenna-emitter, which is determined by the concentrations of the two types of dopants. The ETU process is the most researched UC mechanism since it is considered to be the most efficient one for theranostics. To date, UCNPs utilize ion pairs (antenna/emitter) of Yb^{3+}/Tm^{3+} [142], Yb^{3+}/Er^{3+} [143], and Yb^{3+}/Ho^{3+} [144] for enhanced excitation at approximately 975 nm, which falls in the biological window. This is due to the fact that ytterbium (Yb^{3+}) works perfectly as an antenna, mostly as a consequence of its sufficiently large absorption cross-section in the NIR region at approximately 975 nm.[129, 145, 146] Moreover, its optimized concentration can be kept high (20−100% for fluoride matrices) without the loss of energy by other mechanisms (e.g. scattering). This results from the fact that Yb^{3+} has an only two energy level structures (see Figure 2.3.). Efficient ETU can also be observed in single lanthanide doped systems utilizing the lanthanide ion itself as the antenna, for example, in Er^{3+}-doped $LiYF_4$ nanoparticles that are excited at 1490 nm [147], or in Ho^{3+}-doped $NaGdF_4$ nanoparticles that excite at 1200 nm. [148] The versatility of this mechanism, in combination with the fact that it allows other mechanisms to simultaneously take place, is the main reason why it has been one of the most commonly used in recently reported UCNPs.

However, nanoparticles based only on the ESA or ETU mechanisms can still have energy loss if the interacting lanthanide ions are too sparsely localized in the host matrix or if the energy gaps are not perfectly matching. In order to increase the efficiency of the UC PL processes, two complementary mechanisms have been explored in the development of modern UCNPs: cross relaxation (CR) and photon avalanche (PA).

CR (Figure 2.4.c) appears as a minor energy transfer process that can happen as a secondary upconversion mechanism. [128, 131] It results from ion−ion interaction in which the first ion transfers part of its excited energy to the second ion, similarly to the ETU mechanism. In fact, part of the energy lost in ETU can still be transferred between ions via CR. The interacting ions can be either the same or different, and the absorbing ion can also be in its excited state in some cases. The efficiency of the CR process is in close relation with the dopant concentration and usually is utilized as a complementary mechanism to existing ones (such as ETU or PA) in order to increase upconversion efficiency.

PA (Figure 2.4.d) is a more complex combinatory looping process that involves processes of ESA for excitation and efficient CR to continue the feedback loop. [128, 131, 149] Briefly, the first excitation level (E1) of one ion is initially populated through non-resonant weak ground state absorption. The resulting relaxation does not directly induce an emission from the aforementioned ion. However, by taking advantage of an optimal matrix, the energy of the excited but non-emitting electrons can be transferred to a second ion through non-radiate energy transfer. This in turn excites the second ion's electrons that are already in upper energy level (e.g. E1) further exciting it to a higher level of energy (e.g. E2). When electrons relax from E2 they can either disperse energy in the form of observable radiation (i.e. emitted light) or transfer it back to ion 2. This ion-ion interchange of energy creates an energy loop that increases the chance of emission from electrons in high energy levels. Consequently, in optimal conditions, PA can facilitate the emission of light from a low-power excitation source and maximise the energy-to-emission turnover ratio. Therefore, the efficiency of a PA mechanism is highly dependent of two different aspects: the distance between different dopant ions (similar to ETU) and the constituent material of the host matrix.

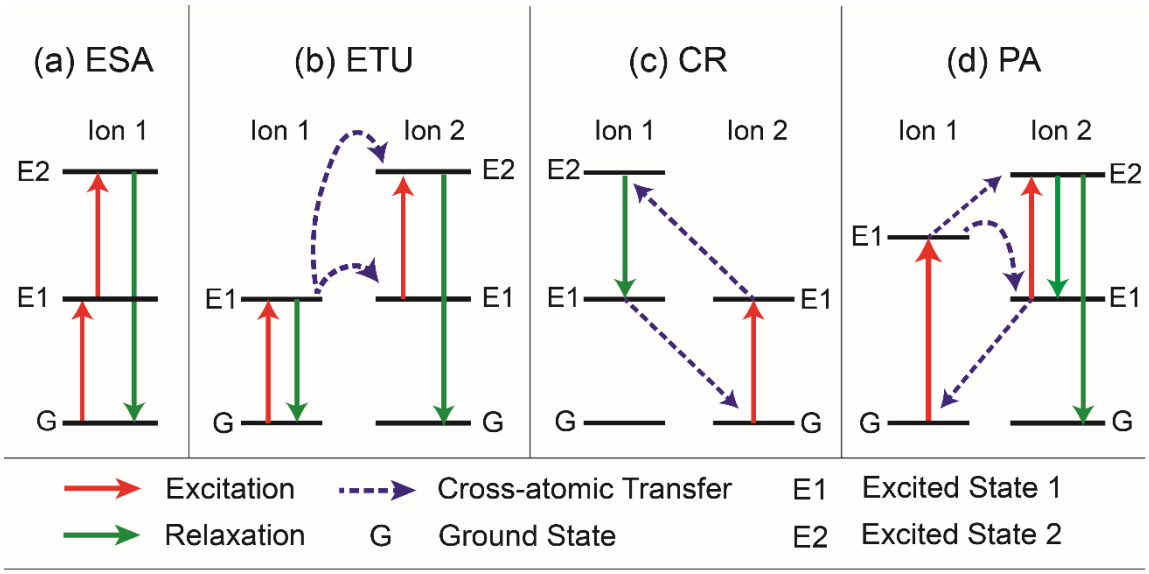

Figure 2.4 Principal UC processes for lanthanide-doped UCNPs.(a) Excited-state absorption (ESA), (b) energy transfer upconversion (ETU), (c) cross relaxation (CR) and (d) photon avalanche (PA).

An ideal host material should be transparent in the spectral range of interest, have high optical damage threshold and be chemically stable. However, the ultimate difference in the host matrix is both the shape that it adopts and its capacity of transferring energy without interference [131, 150]. Examples of host matrices range from LaF_3 nanoplates [151] and Gd_2O_3 nanodisks [152], to $NaLnF_4$ nano-hexahedrons [153] and YF_3 spheres [154]. Nonetheless, the most common matrix used for biological applications is $NaYF_4$ nano-hexagons. Groups such as Haase and co-workers (2004) [155], Zhang and co-workers (2008) [156] and Liu and co-workers (2008) [129] pioneered the use of $NaYF_4$ based UCNPs due to its straightforward synthesis, versatility in both size and colour tuning and its excellent chemical stability. $NaYF_4$ is one of the host matrices with less absorption in the NIR range (~ 980nm) and the highest throughput of energy *via* phonon effects. Thus, it maximises the energy that is redirected to the upconversion mechanisms. [129, 131] Therefore, by combining this type of matrix with Yb^{3+} as the antenna, which optimally absorbs in the NIR (~ 980 nm), and emitters such as Tm^{3+}, Er^{3+} and Ho^{3+}, which

have overlapping energy levels with Yb^{3+}, it is possible to understand why $NaYF_4$:Yb,X (X= Tm, Er, Ho) UCNPs are one of the most used and well-studied types of upconversion nanoparticles.

A multitude of methods have been investigated in order to achieve high-quality synthesis of lanthanide-doped UCNPs in $NaYF_4$ matrices. The three most reported strategies are Ostwald-ripening [157], solvothermal synthesis [158] and thermolysis [129, 142].

Ostwald-ripening consists of a process where amorphous particles, which are energetically less stable, are sacrificed in favour of particles with smaller surface-to-volume ratios. [159] The smaller particles dissolve and in turn are used as a re-deposition material to gradually increase the size of the more stable particles. The kinetics of this method is dependent on the overall energy of the system, making it easy to control the size distribution through factors such as temperature and reaction time. This synthesis characteristically avoids the use of ligands and capping agents, thus leading to the synthesis of bare particles that have increased UC PL efficiency. However, the resulting crystals are usually bigger than the ones obtained by other methods (50 – 200 nm) and are only soluble in organic solvents. Since the resulting UCNPs from Ostwald-ripening strategies are highly stable once they are formed, the incorporation of hydrophilic ligands is extremely difficult. Consequently, Ostwald-ripening syntheses are rarely used for bio-applications, being more frequently utilized in the development of inorganic-based sensors and photo-chemical applications. [160–162]

Solvothermal methods typically involve reactions that occur in a sealed environments under high pressure and temperature (e.g. autoclaves). The reaction happens above the critical temperature and/or pressure point of the solvent to increase the solubility and reactivity of the inorganic reagents. This leads to a higher control of the factors that influence the kinetics of the reaction and, consequently, can result in the synthesis of highly crystalline phases at lower temperatures. Moreover, the fact that synthesis happens at lower temperatures allows the use of a bigger variety of surfactants and precursors. Hydrophylic surfactants like ethylene cetyltrimethylammonium bromide (CTAB) [163] and polyethylenimine (PEI) [164]

have been incorporated on the synthesis of lanthanide UCNPs. However, this type of method has some drawbacks. First of all, the involved solvents and surfactants need to be of similar solubility and/or polarity in order to avoid dissonant critical points. Additionally, reagents need to be robust in order to withstand high pressure environments (thus excluding a wide variety of biological molecules). Furthermore, reactions happen in sealed vessels, which block any observations that one might want to conduct during the synthesis. Finally, monodispersity is usually sacrificed in order to obtain more crystalline structures. Therefore, solvothermal syntheses are reserved for research were crystallinity is the most important characteristic, such as the formation of different shapes (e.g. nanorods, nanotubes, nanodisks, etc). [165, 166]

Thermolysis is one of the most commonly used strategies for the synthesis of lanthanide UCNPs. This type of method generally employs organometallic compounds (i.e. precursors), which decompose at high temperatures in the presence of a surfactant. These surfactants typically contain functional capping groups (e.g. COOH) that coordinate with the metallic elements. The most commonly used ones are oleic acid [143], oleylamine [167] and trioctylphosphine oxide (TOPO) [168]. The presence of long hydrocarbon chains in these surfactants is also important, since it prevents nanoparticle aggregation. Thermolysis usually relies on the fast increase of temperature in order to decompose the metallic precursors and, consequently, create a burst of nucleation points. These points are then covered by the surfactant, creating restrict growing sites. This leads to the synthesis of monodisperse and homogenously distributed lanthanide UCNPs. Although this strategy results in less efficient UC PL processes, the use of capping agents permits the use of ligand exchange chemistry. In turn, it is possible to incorporate ligands that are hydrophilic, not only allowing the dispersion of UCNPs in aqueous media, but also the incorporation of biomolecules onto the UCNPs surface. The re-dispersion of lanthanide UCNPs in aqueous solvents can be achieved by exchanging oleic acid with a range of different hydrophilic capping agents such as poly(ethyleneglycol) (PEG) [169], mercaptopropionic acid (MPA) [170] or polyacrylic acid (PAA) [171]. Due to its aqueous-friendly nature and the versatility of ligand

chemistry, thermolysis has been established as the synthetic method of choice for biological applications of lanthanide UCNPs.

2.1.3 Graphene Oxide

Graphene as a material has been increasingly studied and used since it was first described by Novoselov *et al.* (2004). [172] Most of this growing interest is due to its distinctly different properties, from its unique structural characteristics, mechanical strength and high planar surface area to its high thermal conductivity, electronic flexibility and optical properties. [173, 174] It is due to the latter two that graphene applications have expanded beyond electronic and chemical areas toward biomedical applications (for example, precise biosensing of different targets and cellular analysis and growth). [175, 176]

The most common form of graphene used in biosensing is graphene oxide (GO). The most used GO synthetic method is the Hummers method, which involves oxidation of graphite by treatment with potassium permanganate (KMnO4) and sulfuric acid (H2SO4). [177] The resulting graphite salts serve as precursors for GO by exfoliation in solvents with sonication. Over the years, this method has been improved to reduce dangerous by-products and improve the overall synthetic yield. [178, 179] The wide success of this method can be attributed to its simple solvent transfer process, easy scalability and inexpensive synthesis. [180] Despite the decreased in electronic quality of the graphene sheet by directly synthesising GO *via* the Hummers method when compared with other methods, the unique chemical structure of GO is extremely advantageous for biological applications. GO enables various chemical modifications [181] that allow the attachment of biomolecules such as proteins, oligonucleotides and antibodies. [175, 181, 182] Additionally, its excellent aqueous processability, amphiphilicity, surface enhanced Raman scattering (SERS) and fluorescence quenching properties make GO attractive for biosensing applications. [175, 183] These fascinating properties of GO are mainly derived from its unique chemical structures composed of small sp^2 carbon domains surrounded by sp^3 carbon domains and oxygen containing hydrophilic functional groups (Figure 2.5). This allows the GO structure to interact with polar reagents

through hydrogen bonding while keeping the optical properties that the sequential hexagonal ring structure characteristic of graphene provides.

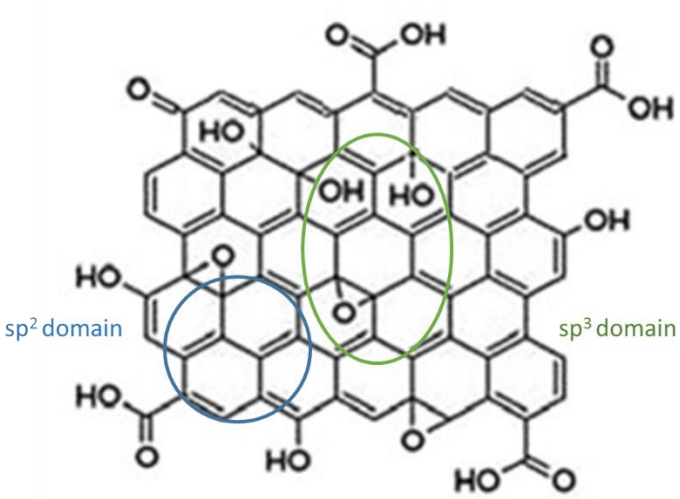

Figure 2.5. Chemical structure of graphene oxide (GO). GO is composed of sp^2 (blue) and sp^3 (green) domains. Sp^2 domains contribute to the optical properties of GO while sp^3 are usually enriched with hydrophilic functional groups (such as OH) to allow polar interactions and functionality

Graphene sheets in general are endowed with extensive p-orbitals above and below its crystalline honeycomb structure. [173, 183] This allows, amongst other things, the absorbance of photonic energy originated from fluorescent agents through Förster resonance energy transfer (FRET). FRET is the transfer of energy from one excited molecular fluorophore (the donor molecule) to another fluorophore (the acceptor molecule) via intermolecular dipole-dipole interactions. [184, 185] The FRET efficiency between two fluorophores is inversely proportional to the distance between the donor and acceptor (Equation 2.2.). [186]

$$E = \frac{1}{1 + (\frac{R}{R_0})^6}$$

Equation 2.2. Förster resonance energy transfer efficiency. Where *E* is efficiency of the FRET events, *R* is the distance between the acceptor and the donor fluorophores and R_0 is the Förster distance of the specific acceptor-donor pair (i.e. distance at which the energy transfer efficiency is 50%)

This distance dependence allows the creation of highly sensitive systems that either fluoresce or quench in the presence of targets (e.g. biomolecules) that influence the distance between the donor fluorophore and the GO, which acts as electronic energy acceptor. [187] This way, the detection of important biomolecules such as nucleic acids [183] and proteins [188] have been successfully demonstrated by using GO-fluorophore FRET pairs.

2.1.4 Oligonucleotides as nanomaterials

Since the discovery of nucleic acids in 1868[189], oligonucleotides have played a fundamental role in understanding basic cellular and biological mechanisms and pathways. However, oligonucleotides have transcended their biological role and have been used on nanotechnology applications of different natures due to four different key features [190–192]: 1) the quantitative understanding of DNA thermodynamics, which makes it possible to reliably predict how oligonucleotide molecules fold and interact with one another; 2) the high precision of its base-pairing system, making it a reliable tool for accurate structure formation; 3) the versatility of potential chemical modifications, leading to the synthesis of nucleic acids capable of incorporate fluorescent tags, cross-linkers and other useful complementary chemical features; and 4) the falling cost and increasing quality of DNA synthesis when compared with other nanoscale building blocks. All these key aspects are mostly related with the full understanding and versatile modification of the nucleotide bases, either naturally occurring or synthetically made.

There are essentially five different types of naturally occurring nucleotide bases: adenine (A), guanine (G), thymine (T) and cytosine (C) for DNA and uracil (U), which replaces T in RNA sequences. However, many more synthetic bases have been developed over the years to improve on certain aspects, such as resisting hydrolysis (e.g. morpholino [193]), increasing hybridization strength (e.g. locked nucleic acids – LNA [194] – and bridged nucleic acids – BNA [195]) or decreasing enzymatic degradation (e.g. peptide nucleic acid – PNA [196]). The variety of chemical structures of nucleic bases is the major factor behind its biggest advantages: highly precise base-pairing and sequence design. This sequence programmability has allowed the rational design of precisely defined structures ranging in size from nanometres to millimetres [197] and the *de novo* design of complex biomolecular systems. Some of these systems rely solely on the use of oligonucleotide for assembly and include functional aptamers [198], molecular beacons [199], DNA nanomachines [200] and drug delivery vehicles [201].

Pioneer work from groups such as Seeman and co-workers [202] provided the first demonstration of micro-sized DNA self-assembled lattices by using multiple oligonucleotides as building blocks. Rothemund and co-workers [203] further advanced structural DNA self-assembly by developing DNA origami, a technique that is straightforward to use, accommodates any two-dimensional (2D) structure of interest, and systematically produces high yield synthesis of the target structure [191]. DNA origami was rapidly and broadly adopted, and was soon generalized to the self-assembly of three-dimensional (3D) structures. [204, 205] Consequently, oligonucleotide nanostructures have been investigated as tools for drug delivery [206], sensing [207] and imaging [208], due to their programmable scaffolds for the attachment of functional groups (including therapeutic moieties), and because 3D structures can be designed to act as protective enclosures for a cargo of interest.

In biosensing applications particularly, functional nucleic acids such as DNAzymes [209] and aptamers [198] have been used extensively to detect the levels of various molecular species within cells. Pei *et al*. (2012) [210] constructed a set of tetrahedral DNA structures with one or two reconfigurable edges. By changing its shape in response to specific molecular signals and using FRET

reporter strategy, they showed that a reconfigurable oligonucleotide-based structure could be used to detect intracellular variables including protons, ATP and mercury ions. Along a similar line, Modi et al. (2009) [211] used a DNA-based sensor to map the pH of endosomal pathways in living cells. The design was based on two double helices connected with a flexible hinge with an incorporated G-quadruplex structure that acts as a pH-sensitive switch to open and close the tweezers. By taking advantage of a FRET reporter strategy and coupling the sensor to the protein transferrin, pH changes were mapped along a specific receptor-mediated endocytic pathway.

Further chemical and structural modifications have been used to improve the performance of live-cell imaging probes. Molecular beacons are one of the most reported class of probes for detecting mRNA in living cells [199]. Molecular beacons are stem-loop probes with a fluorophore and quencher attached to the stem. Fluorescence is quenched when the probe is delivered but becomes unquenched when the probe hybridizes to the target mRNA. Improvements on this basic design have been reported over the years. The addition of a longer double-stranded RNA domain sequence has been shown to result in active export of the probe from the nucleus to the cytoplasm, thus facilitating interactions with mRNA. [212, 213] Chemical modifications (e.g. methylation) have also been used to enhance probe stability by protecting against degradation by cellular nucleases. [214].

However, nanostructures based only on oligonucleotides for intracellular biosensing and imaging (e.g. molecular beacons) have some downfalls. For one, delivery of external oligonucleotides to a cell can be extremely challenging since foreign nucleic acids do not naturally enter the cellular membrane on their own. [215, 216] Various transfection agents have been used to deliver oligonucleotides into cells, including liposomes [217], viral vectors [218] and polymeric complexes [219]. Furthermore, once inside a cell the oligonucleotide structure needs to survive enzymatic and pH degradations that function as cellular defence mechanism from viral infections. [215] Even with chemical modifications to strengthen its overall stability (as discussed above), oligonucleotides are still prone to digestion from enzymes such as DNAse, RNAse and other nucleases. [220–224] Low pH

environments (such as in endosomes) have also been proven to deprotonate and destabilize oligonucleotide structures. [225–227] All these hurdles can render oligonucleotide nanostructures as less useful tools for in-cell biosensing and imaging. To tackle these problems, oligonucleotides have been combined with different types of nanoparticles (see section 2.2.1.).

2.2. Conjugates using multiple nano-blocks

Hybrid nanomaterials are capable of achieving far more than each component material acting independently. By combining biomolecules (e.g. oligonucleotides) with inorganic nanomaterials (e.g. AuNP), it is possible to develop multifunctional materials capable of targeted delivery to cells/tissues/organs, combined with sensing of specific analytes or endogenous properties/processes. [228] The biomolecule can provide the recognition, biocompatibility, active sensing and even drug activity while the inorganic component can host and display the biological component on its surface and provide optical properties (e.g. NIR fluorescence) to act as both a delivery and imaging tool. The next sections discuss the combination of inorganic nanoparticles (section 2.2.1.-2.) and graphene oxide (section 2.2.3.) with oligonucleotides.

2.2.1 Gold Nanoparticles and Oligonucleotide conjugates

As mentioned previously, AuNPs have been broadly studied as multifunctional carriers of biomolecules due to their ease of synthesis, excellent biocompatibility, well-defined surface chemistry, and facile molecular imaging utilising fluorescence resonance energy transfer (FRET). [229] Taking advantage of the sulphur-gold chemistry, a range of different biomolecules have been conjugated with gold, including oligonucleotides. [230] This conjugation with oligonucleotides has been described in a wide range of different applications, from the development of electrochemical sensors [231] to the direct assembly of DNA-directed crystalline

lattices [232]. However, it has been in the areas of bio-sensing, bio-imaging and drug and gene delivery that this gold-oligonucleotide conjugates have found some of its fastest growing applications.

In bio-sensing, pioneer work from Letsinger and co-workers (1998) [233] and Mirkin and co-workers (2000) [234] introduced the concept of linking two DNA-functionalized AuNPs based on the complementarity of the DNA strands displayed on the different particles. Since each nanoparticles can carry multiple copies of a DNA sequence on its surface, simple mixing can lead to uncontrolled aggregation. In turn, this affects the surface plasmon absorption band of the gold nanoparticles. This translates onto a colour change (usually red to purple) which can be quantitatively detected by colorimetric methods and has been the base of numerous DNA sensors. [235–237] The colour change in these aggregates is due to the intense plasmonic coupling between adjacent particles when the inter-particle distance is smaller than the diameter of the NPs. This type of colorimetric sensor has been shown to be a great alternative to more expensive and complex techniques such as PCR and fluorometric assays. [238–240]

This first description of gold-oligonucleotide conjugates paved the way for the investigation of this type of hybrid nanomaterials for other applications. For example, densely coated DNA functionalized AuNPs have also been employed as an intracellular probe for detecting and quantifying over- or under-expressed mRNA. [241, 242] Tang and co-workers developed a detection system where gold nanoparticles are covered with loop-based molecular beacons. [243] By having partially self-complementary sequences tagged with fluorophores, the whole sequence creates a loop which brings the fluorophore closer to the gold core. This allows quenching of the fluorophore *via* FRET mechanism. This looped sequence is designed to be complementary to a target mRNA. Therefore, in the presence of this target the loop is broken, since the complementarity of the target-beacon is greater than the self-complementarity of the beacon sequence. This brings the fluorophore away from the core, restoring its fluorescence properties, thus creating a sensitive and specific mRNA detector. Similarly, Mirkin and co-workers developed a system which they called ‘nano-flares’, where 13 nm AuNPs were functionalized with a

thiolated DNA comprising an 18-base recognition domain to a specific mRNA sequence. [71] This DNA sequence was partially hybridized to a short DNA sequence (flare strand) modified with Cy5 dye. In the absence of the target mRNA, the dye remained largely quenched by FRET due to the proximity of the AuNP surface. In the presence of the target, the dye-modified short oligonucleotide was released *via* strand displacement resulting in restoration of fluorescence. Both types of AuNP-oligonucleotide sensors have been the basis of multiple studies, advancing the sensing capability of this type of conjugates by increasing the number of targets detected at the same time. [244, 245]

The application of AuNP-oligonucleotide conjugates is not restricted to only imaging. These conjugates have been applied in drug and gene delivery over the years. [246, 247] Advantages of AuNPs-oligonucleotide conjugates include minimal toxicity[86, 248] and high cellular uptake despite negative ζ potential [248, 249]. These unique properties most likely originate from the display of a dense and highly oriented DNA layer, since conjugates with other than an AuNP core or even coreless hollow oligonucleotide shells display similarly high transfection properties. [250, 251]

In the area of drug delivery, for example, our group recently developed a theranostics AuNP-DNA conjugate [252], inspired in the design presented by Mirkin and co-workers. By taking advantage of the double helix formed when the thiolated and the flare strands are hybridized, we incorporated an anti-cancer drug (Doxorubicin). In the absence of the target mRNA, no fluorescence or drug leakage was detected. However, in the presence of the specific mRNA target, the flare strand is released *via* competitive hybridization and the drug is released in the process. This leads to a controlled release of the drug only in cells of interest while keeping the imaging capability of the whole AuNP-DNA conjugate.

Significant progress has also been made on the area of gene delivery using AuNP-oligonucleotide conjugates. Pioneer work conducted by Rosi and co-workers (2006) demonstrated the successful conjugation of siRNA with gold nanoparticles capable of knocking down enhanced green fluorescent protein (EGPF) expression. [253] This work showed that it was possible to deliver siRNA capable of triggering

the RNA-induced silencing complex (RISC) and successfully silencing a gene through the RNA interference (RNAi) pathway. [254] In a nutshell, the siRNA antisense strand enlists the help of a group of proteins and forms RISC complex. Those proteins chemically cleave the mRNA complementary to the antisense strand and prevent it from being transcribed into its consequent protein (Figure 2.6.).

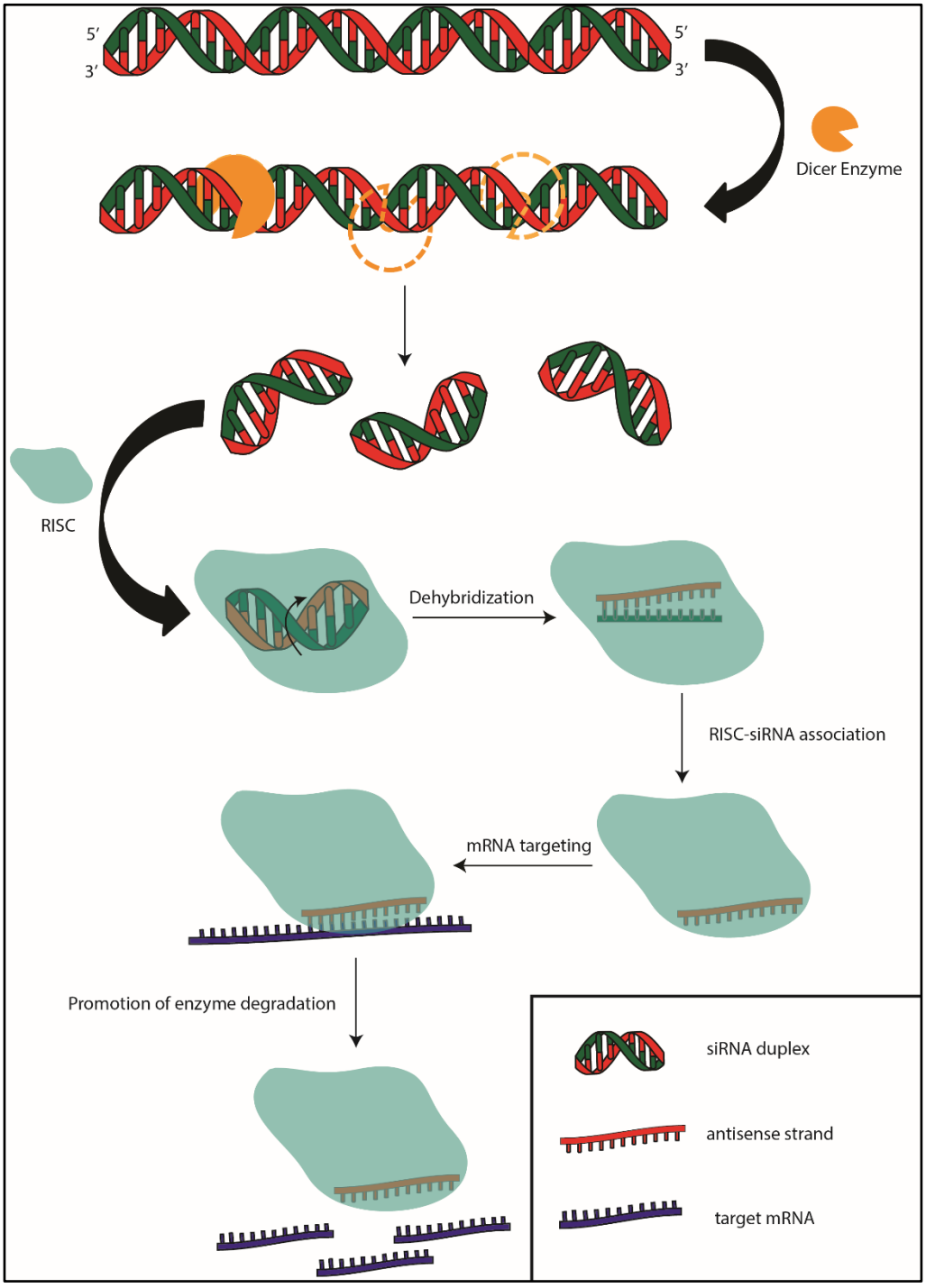

Figure 2.6. RNAi pathway and RISC-siRNA complex formation. The presence of RNA in a duplex form triggers the formation of the RNA inducing silencing complex (RISC), which unwinds and de-hybridizes the dsRNA in order to bind to the antisense strand. The RISC-RNA associate will then detect and bind to the complementary mRNA and induce degradation through enzymatic action, blocking the translation of the mRNA into the consequent protein and, therefore, silencing the gene that this specific mRNA represented.

Further work conducted by Mirkin and co-workers altered the silencing strategy by incorporating a dsDNA with complementarity to the mRNA sequence that codes for EGFP. [75] By intercepting the mRNA, the expression is reduced without actually inducing any silencing effect.

Since then, many different applications of silencing probes using AuNP-siRNA conjugation have been reported. For example, Ghosh *et al.* (2008) [255] coated gold nanoparticles with lysine-based headgroups to produce transfection vectors for siRNA that were approximately 28 times more effective than polylysine vectors. However, this study focused on the internalization of the conjugates and did not report any silencing efficiency experiments. Rhim *et al.* (2008) [256] opted to use liposomes as a delivery agent of the AuNP-siRNA conjugates. This facilitated the entering of the resulting complex into the cells without demonstrating any cytotoxic effects. Elbakry *et al.* (2009) [257] demonstrated a layer-by-layer coating of AuNPs with an alternating polyelectrolyte coating approach, using 21-mer siRNA and polyethylenimine (PEI) as polymers. This study showed that particles coated with PEI/siRNA/PEI layers entered the cell more efficiently than particles coated only with siRNA/PEI layers, thus demonstrating that overall net charge plays a role on the interaction of nanoparticulate systems designed for silencing with cells. This layer-by-layer system was shown to silence EGFP genes up to 80% when a specifically designed siRNA sequence was used. Further examples of genes silenced using AuNP-siRNA conjugates include β-galactosidase [258], galectin-1 [259] and ganglioside [260].

All the examples discussed in this section demonstrate that gold-oligonucleotide conjugates are in the forefront of not only silencing, but also imaging and sensing applications.

2.2.2 Lanthanide upconversion nanoparticles and oligonucleotide conjugates

As mentioned before, lanthanide upconversion nanoparticles (UCNPs) are an emerging class of fluorescent nanomaterials that display anti-Stokes emission upon irradiation with infrared light. In other words, they are capable of emitting higher energy photons from lower energy absorption. This is especially interesting for bio-imaging as they do not have drawbacks that commonly affect other fluorophores, such as photobleaching or high signal-to-noise ratios. [118, 150] Additionally, the infrared light required to excite UCNPs has a higher tissue penetration capability since it works outside of the biological window (see section 2.1.2.). Furthermore, due to its ladder electronic configuration and consequent sequential photon absorption, UCNPs do not require constant high power pulsed lasers.[261] Finally, unlike other fluorescent nanoparticles (e.g. quantum dots), emissions are not directly dependent of nanoparticle size. UCNPs emission can be carefully tuned depending on the lattice host, dopant and constituent ratios. [262]

All these properties make UCNPs a considerable alternative fluorophore in the development of both bio-sensing and bio-imaging systems. For example, Wang *et al.* (2005) demonstrated that biotin functionalized UCNPs were capable of detecting human avidin up to a concentration of 0.5 nM. [263] Another study conducted by Wang *et al.* (2009) demonstrated that UCNPs functionalized rabbit anti-goat IgG antibodies were capable of detecting the presence of goat IgG goat antibodies up to a limit of 0.88 µg/ml. [264] Finally, Zhang *et al.* (2009) demonstrated that an assembly of UCNPs with gold nanoparticles mediated by cysteine groups were capable of differentiating a range of pH solutions. [265] These examples demonstrate that combining UCNPs with biomolecules for sensing can be used for a range of different applications.

The combination of the fluorescence properties of UCNPs with the specificity of oligonucleotide detection has also been reported as the core mechanism of some types of sensing conjugates. One of the first descriptions of UCNPs-oligonucleotide conjugates was reported by Wheeler and co-workers (2006).[266] In this study, they reported a sandwich-type assay involving silica coated ytterbium (Yb^{3+}) and erbium (Er^{3+}) UCNPs for the detection of DNA. These particles were conjugated with amine-

modified DNA strands which were partly complementary to the target strand. In the presence of the target oligonucleotide, another reporter strand carrying a carboxytetramethylrhodamine (TAMRA) label was captured onto the UCNPs, triggering a FRET type of mechanism from the UCNPs to the TAMRA acceptor. This type of system minimalized the background signal and led to a sensitive detection limit of approximately 1.3 nM. Later Zhang and co-workers (2009) reported a simpler version without using a TAMRA reporter. [267] Instead, this study reported the use of EDC coupling chemistry to attach DNA onto UCNPs and using SYBR green as a FRET reporter. This intercalating dye is characterized by an enhanced fluorescence quantum yield upon binding to double stranded DNA. In the presence of the target, the SYBR green dye would be "activated" and could absorb the emission of the UCNPs. This type of system led to a lower detection limit of approximately 0.1 nM. These initial studies demonstrated that UCNP-oligonucleotide conjugates led the way for the application of UCNP-oligonucleotide conjugates for biosensing. More recent examples include FRET gold-aptamer and UCNPs sensors capable of detecting E.coli in a range of food and water samples [268], AuNP-UCNP FRET assemblies mediated with DNA for the detection of specific miRNA in living cells [269] and even UCNPs functionalized dsDNA molecules for photothermal therapy and delivery of anticancer drugs in HeLa cell models [270].

2.2.3 Graphene oxide as a platform for FRET sensing

The application of FRET sensing in biological settings has been of great interest in the past decade. One of the most commonly used electronic energy acceptors in FRET pairs has been graphene oxide (GO). [187] As mentioned in section 2.1.3, graphene oxide is the oxidised form of graphene sheets and is characterized by their honeycomb lattice of carbon atoms, its oxygen-linked functional groups (such as COOH) and its high solubility in aqueous solutions.[182] Due to its conducting sp^2 domains in a non-conducting sp^3 matrix, GO is ideal for quantum confinement of π electrons. This results in interesting photonic properties, such as its high capacity of electronic energy acceptance. [180] Furthermore, the sp3 domains of

GO permits specific interactions with biomolecules such as single stranded oligonucleotides via π-π stacking. [175] Interestingly, GO has been shown to specifically distinguish between ssDNA and dsDNA molecules due to unfavourable thermodynamics. [183, 271] The hydrogen bonded nucleotide bases in dsDNA block the sp^3 groups, reducing π-π interactions with GO and offering higher thermodynamic stability than π stacking of the constituent ssDNA on graphene can provide.

This unique interaction between ssDNA and GO has been exploited for the development of various analytical detection schemes. One of the first studies to describe this type of GO-DNA sensing was conducted by Lu and co-workers (2009). [175] In this study, a DNA sequence tagged with a fluorescein (FAM) fluorophore was adsorbed onto GO, resulting in almost complete quenching through FRET mechanism. In the presence of the target DNA (aimed for HIV1), a duplex formed which displaced the tagged DNA sequence from the GO surface and fluorescence is restored in the process. This type of FRET DNA-GO sensor has also been applied for the detection of different targets, ranging from multiple DNA sequences simultaneously[272], proteins (e.g. kinase [273] and endonuclease[274]), harmful metal ions (e.g. Hg(II) [275], Ag (I) [276] and Cu(II) [277]) and even cocaine compounds [278].

GO has also been used as a quencher in systems that use nanoparticle-oligonucleotide conjugates as the detection core. For example, Dong *et al.* (2010) reported quantum dot-molecular beacon complexes for the detection of specific DNA sequences. [279] Alternatively, Li *et al.* (2014) described ssDNA-coated gold nanoparticles in combination with GO for the detection of lead (Pb^{2+}) ions.[280] These nanoparticle-DNA-GO sensors have been applied in the different bio-sensing applications, from the detection of specific enzymes (e.g. nuclease [281] and caspase-3 [282]) and cancer biomarkers (e.g. BRCA1 [283]), to the development of immunoassays for the identification of potential biomarkers for different diseases[284].

2.3. Biological applications of conjugates

As seen by the various examples described throughout this chapter, the use of nano-conjugates in biological applications has been one of the main focus points of applied nanotechnology in the past few years. Nanomaterials are: 1) invaluable tools to understand basic biological mechanisms through sensing and imaging of the involved biological entities; 2) helpful agents for imaging of complex biological environments (such as tissue or organs); and 3) great alternative candidates for therapeutic methods. The work presented in this thesis reflects the broader aim of bionanotechnology as an area of applying different nanomaterials for a new look of different biological problems, mechanisms and events. Therefore, in order to test the applicability of different nanomaterials in biologically driven studies, two types of events were chosen as models to study: wound healing (section 2.3.1.) and biomarker detection (section 2.3.2.).

2.3.1 Wound healing and scarring

Skin is considered to be the human body's largest organ, and it serves as a protective barrier against external threats such as invasive species (e.g. viruses, bacteria, fungi, etc.), chemicals and other foreign materials and objects. [285] Therefore, any incision must be rapidly closed to avoid infection and invasion of such species into the body. The group of processes involved in the quick closure of a damaged area is called wound healing, and it is present not only in the skin but in different types of organs and tissues. [286] The wound healing process is divided into four stages across the different tissues: haemostasis, inflammation, proliferation and maturation (Figure 2.7). [286–289]

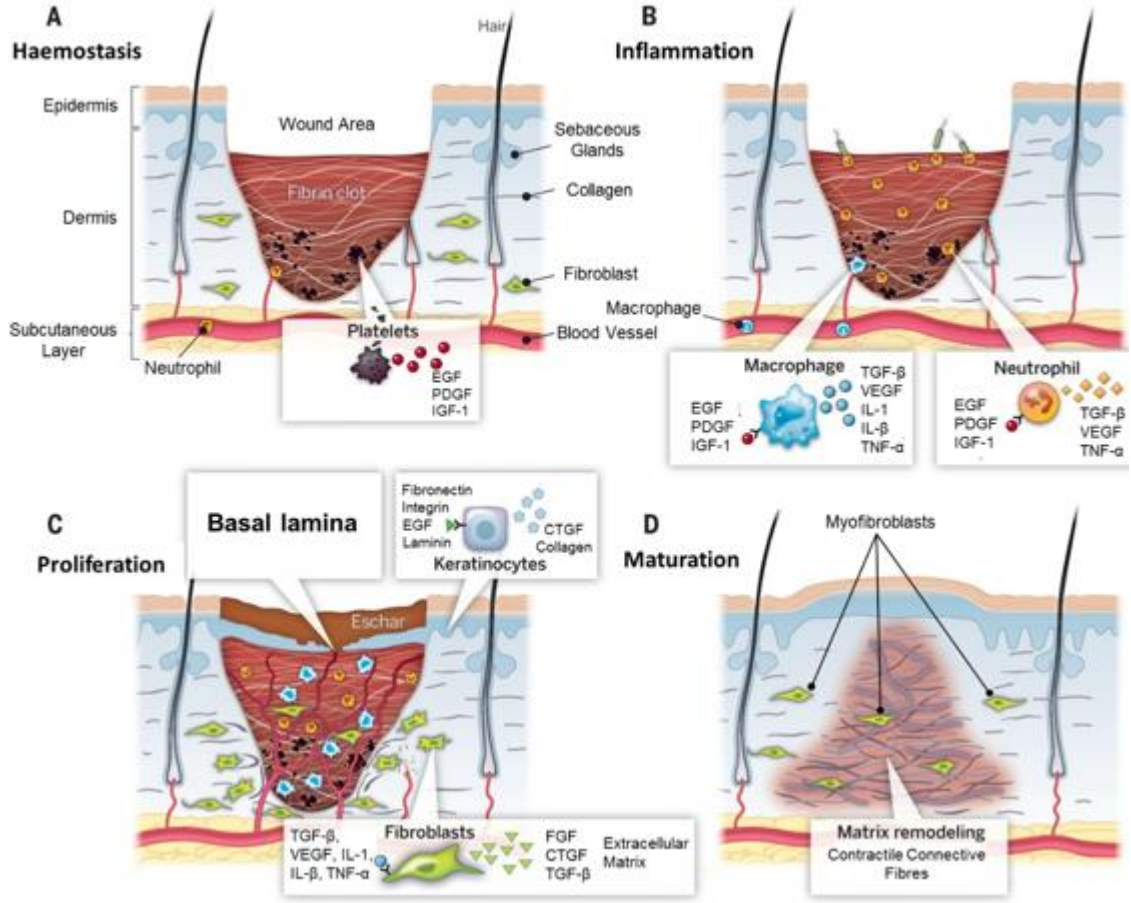

Figure 2.7. Wound healing mechanism. Upon damage, tissue goes through four stages to close the wound: (A) **haemostasis**, where a fibrin clot is formed to minimise invasion of opportunistic species; (B) **inflammation**, where immune cells rush onto the site to kill any damaged cells and invasive species (e.g. virus, bacteria); (C) **proliferation**, where fibroblasts migrate towards the wounded area and the basal lamina starts to form; and (D) **maturation**, where there is the remodelling of the tissue with the production of contractile connective fibres. Adapted from ref. [285, 286]

The first stage – haemostasis – is characterized by the formation of fibrin clots. Since most wounds usually cause damage to local blood vessels, blood leaks to the damaged area. Specific constituents of blood, most importantly platelets and fibrin, rush onto the wound in order to form a protective provisional matrix. Together with other fibres such as fibronectin, vitronectin and thrombospodin, these clots create not only a shield that tries to isolate exposed areas from the exterior environment,

but also a reservoir of cytokines and growth factors that are released as activated platelets go through degranulation. These include epidermal growth factors (EGF), platelet derived growth factors (PDGF) and insulin-like growth factor 1 (IGF-1). The presence of this mixture of cytokine and factors provides chemotactic cues to recruit circulating inflammatory cells to the wound site, thus initiating the second stage – inflammation.

In the second stage, immune cells such as neutrophils and monocytes are attracted from neighbouring circulating blood to the wound site by the aforementioned chemotactic signals. These include not only growth factors but also peptides cleaved from bacterial activity and by-products of proteolysis of fibrin[290]. Both macrophages and neutrophils have a role of clearing the invasion of contaminating species and/or materials and any other cells or matrix debris. In the process, these cells provide a source of pro-inflammatory cytokines and growth factors that recruit neighbouring keratinocytes and fibroblasts, including transforming growth factor beta family (TGF-β), vascular endothelial growth factors (VEGF), interleukin-1 and beta (IL-1 and IL- β) and tumour necrosis factors alpha (TNF-α). This new mixture of factors and cytokines induces neighbouring cells in the edges of the wound to migrate towards the middle in order to start the following stage – reepithelialisation or proliferation.

In this third stage, fibroblasts start to migrate toward the wound induced by the existing mixture of factors. Once they arrive, they start producing different proteins such as integrins, laminins and fribronectins. These fibre proteins create a niche matrix to accommodate the migration and anchoring of basal keratinocytes. At the same time, fibroblasts also produce a range of different factors, including fibroblast growth factors (FGF), connective tissue growth factor (CTGF) and TGF- β. These factors are produced in order to induce the migration of the surrounding keratinocytes towards the wound area to form a basal keratinocyte monolayer (i.e. basal lamina). During the formation of this layer, keratinocytes produce their own matrix rich in collagen and CTGF, mixing with the existing fibres and factors still lingering from fibroblast production. Once the wound surface has been covered by

this basal layer of keratinocytes, epidermal migration ceases and a new stratified epidermis begins to be established, starting the final stage – maturation.

In this final stage, mobilization factors (e.g. TGF-β) cease to be produced and the present keratinocytes undergo a differentiation process similar to the one seen in the outer layers of unwounded epidermis. At the same time, most of the remaining fibroblasts transform into myofibroblasts, which resemble closely muscle tissue cells with the capacity of generating strong contractile forces. These differentiation processes aim to connect both edges of the wound in order to fully close it from the inside, while still being protected by the initial clot formed. This is done through the production of a specific category of fibres: contractile connective fibres (e.g. integrin). These fibres are more rigid than fluid connective fibres, such as collagen, and are predominantly present in wounded regions in order to prevent any re-opening. Over time, the clot that filled the wound is replaced by all the involved agents – matrix and cells – up to the point where the wounded area is fully filled with this new layer of cells and matrix. At this point, the myofibroblasts start the process of contraction of the wound in order to fully close it, thus finishing the wound healing process.

The wound healing process as a whole is extremely efficient when it comes to the timing of closure. Usually, after about a week a wound can be almost completely closed. [287] However, when it comes to efficiency of reconstruction the process has some drawbacks. For instance, one of the core pathways present in wound healing is the (TGF-β) pathway. [289] TGF-β is a family of cytokines secreted by different cell types (including macrophages, fibroblasts). The major role of this cytokine family is to recruit different participants and, at the same time, to regulate the apoptosis of some of those same participants, giving the TGF-β a two directional role of both inhibition and promotion. As stated before, TGF-β is produced in three stages of the wound healing process. Consequently the overexpression or the prolonged lingering of TGF-β can lead to an abrupt and unbalanced apoptosis of matrix regulator agents (such as fibroblasts), which leads to a greater matrix deposition and a deficient remodelling of the tissue. This deficiency in the remodelling can, in short course, lead to scarring and, in extreme course, fibrosis,

necrosis and permanent organ damage. [291, 292] One of the pathways associated to the TGF-β-induced apoptosis is the SMAD pathway (Figure 2.8.). [289, 293] SMAD is a family of intracellular proteins that transduce extracellular signals to the nucleus and, consequently, activate downstream gene transcriptions. The R-SMAD 2 and 3 are of particular interest due to their participation in the dimer formation alongside with the co-SMAD 4. [294, 295] Together they form a promoter activator protein complex that leads to the production of mRNAs which are involved, amongst other things, in apoptosis mechanisms and extracellular matrix formation. [296] Based on reports such as Ashcroft *et al.* (1999) [297], who observed that SMAD 3 deficient mice had a better wound healing capability than wild type mice, or Tomikawa *et al.* (2012) where overexpression of SMAD2 led to a slower re-epitheliazation on wounded mice [298], it is hypothesised that the impact of the TGF-β-induced apoptosis is reduced by knocking down SMAD2 or SMAD3 expression.

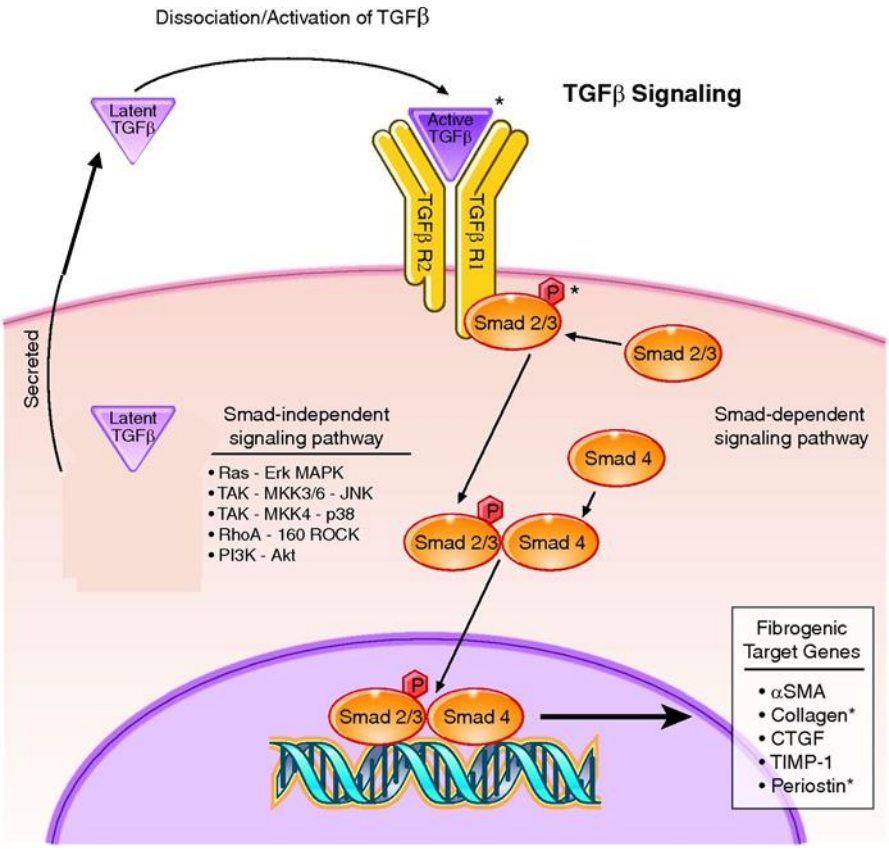

Figure 2.8. SMAD2/3 – TGF-β pathway. TGF-β is generally secreted as part of the wound healing mechanism at different stages. Active TGF-β binds its receptor to initiate SMAD-dependent and independent signalling. SMAD-dependent signalling regulates fibrogenic target genes such as α-smooth muscle actin (SMA), collagen, connective tissue growth factor (CTGF). TGF-β can also induce a number of SMAD-independent pathways such as Ras, TGF-β-activated kinase (TAK), RhoA, and phosphatidylinositol-3-kinase (PI3K). Adapted from ref. [292]

2.3.1.1 Nanoparticles for treatment of wounds

Wound treatment has its golden standard in the use of hydrogels, foams and cream emulsions in order to promote the regeneration of the skin by controlling different aspects such as moisture [299] and levels of biological agents (for example, growth factors and proteins [300]). In recent years, the inclusion of nanoparticles of both organic and inorganic nature has increased in order to better control this type

of treatments. For example, liposomes have been described as useful carriers of agents such as keratinocyte growth factor (KGF) in order to stimulate epithelial differentiation and proliferation. [301, 302] Other examples include micelles for the delivery of extracellular-mimicking polymers (e.g. chitosan) [303] and solid lipid nanoparticles (SNLs) for the delivery of anti-inflammatory agents [304]. Furthermore, organic delivery vehicles have been used to also delivery gene therapy agents, such as siRNAs [305], miRNAs [306] and gene transfection [307].

This type of organic-based nanoparticles are extremely biocompatible and multiple studies have reported their use in advanced clinical trials. [308] However, their use is limited only to the delivery of a specific agents (imaging requires further functionalization of the polymers used) and there is some degree of difficulty in controlling the dosage of delivery of those agents. [309]

As an alternative for a more theranostics approach, inorganic-based nanoparticles have also been applied for the treatment of wound. For example, silver and copper nanoparticles have been extensively studied as a complementary agent for wound dressings and hydrogels in order to prevent bacterial and fungal infections. [310–313] Titanium dioxide (TiO_2) and zinc oxide (ZnO) nanoparticles have also been incorporated in wound treatments in order to take advantage of their well-studied ability to absorb UV light and eliminate any pathological agents that are already present in the wounded area. [314, 315] This type of inorganic-based nanoparticles have the potential to be used as imaging tools, as well as treatment agents. [316] Nevertheless, the use of all these nanoparticles seems to be usually restricted to antibacterial studies due to their inherent toxicity to human cells. [317–320]

AuNPs have also emerged as a theranostics agent for wound healing due to their low toxicity and optical properties (see sections 2.1.1. and 2.2.1.). For example, Leu *et al.* (2012) demonstrated that wound healing could be accelerated by delivering AuNPs coated with a mixture of epigallocatechin gallate and α-lipoic acid. [321] Akturk *et al.* (2016) demonstrated that the use of AuNPs in a collagen rich scaffold improved both the stability and the efficiency of the complex in the promotion of cell proliferation in wounded skin. [322] Finally, Randeria *et al.* (2015)

showed that AuNP-siRNA conjugates are capable of penetrating the skin, altering the levels of GM3 and promoting accelerated wound healing in diabetic mice. [323] Therefore, AuNPs have a great potential as theranostic agents for the treatment of wounds.

2.3.2 Biomarkers for the detection of diseases

One of the most important aspects when studying a disease as a whole is the identification of biomarkers. Biomarkers are classified as any biological agent that can intrinsically point to a specific biological state. [324] These indicators can range from proteins [325], hormones [326], RNAs [327], factors [328] and specific cell phenotypes [329]. Biomarkers have been especially useful for the study and treatment of certain diseases (e.g. cardiovascular [330] or cancer [331]). For example, distinct subclasses of cancer may respond differently to various types of therapeutic interventions (e.g. BRAC1 therapeutics vs other types of breast cancer [332]). Biomarkers can also work as both indicators and targets. For example, specific gene mutations such as in BRAF (melanoma [333]) or HER2 (breast cancer [334]) can act as both the biomarker and the target of therapeutic action.

Therefore, the field of biomarker sensing has focused on three main points: study of new types of biomarkers for diagnosis and further understanding of both new and existing diseases; development of diagnostic tools capable of detecting multiple targets at the same time (e.g. bioarrays); and improvement of existing diagnostic tools by lowering the detection limit and investigating alternative methods of detection (e.g. *in vivo* vs *ex vivo*). Nanotechnology has helped in all these different focus points, with the development of high-throughput sensing arrays using gold nanoparticles, quantum dots or silica nanoparticles for the detection of diseases of autoimmune, infectious, neurodegenerative and even cancerous origin. [335]

For the work presented in this thesis, two different biomarkers were chosen to be investigated using combinatory nano-materials: Beta-secretase 1 (BACE-1) and Prostate Cancer Antigen 3 (PCA3).

BACE-1 is a protease important in the formation of myelin sheaths in peripheral nerve cells. [336, 337] The pattern and level of BACE-1 expression is largely consistent with those of β-secretase activity in cells and tissues [338, 339] and it has been shown to be required for beta-amyloid (Aβ) formation. [340, 341] Aβ is necessary for normal neuronal function [and is an important physiological regulator of potassium channel expression and neuronal excitability [343]. However, overproduction and long-term accumulation of Aβ can lead to the formation of cerebral plaques. [344, 345] Small clumps of Aβ have been shown to block cell-to-cell signaling at synapses and activate immune system cells that trigger inflammation in otherwise healthy neurons. [346] This plaque formation has been linked with a range of different neurological diseases, from cerebral amyloid angiopathy [347] to Alzheimer's Disease (AD) [346]. Treatments for AD in particular have focused on the removal of these accumulated plaques [348] or even early prevention of their formation [349].

Recent studies reported a lack of Aβ generation in the brains of BACE-1 deficient mice. Singer *et al.* (2005) silenced BACE1 gene expression and demonstrated that a partial reduction in BACE-1 production can improve the deposition of Aβ and cognitive deficits in mice. [350] Laird *et al.* (2005) demonstrated that Aβ production appears to be sensitive to BACE1 dosage in young animals, with Aβ levels reduced to approximately 60–70%. [351] Further findings have indicated that BACE1 deficiency might contribute to the treatment of other neurological disorders, from severe seizures [352] to hyperactivity [353] and anxious behaviour [354]. This indicates that BACE-1 is intrinsically connected with the production of cerebral Aβ levels and amyloid development. Consequently, the monitoring of BACE-1 expression has been shown to be a potential candidate for early diagnosis of AD. [355–357]

PCA3 (also known as differential display clone 3 – DD3) is a gene that expresses non-coding RNA and was firstly identified in 1999 to be highly overexpressed in 95% of primary prostate cancer specimens. [358] Additionally, low PCA3 expression was observed in normal prostate. This contrast of expression between healthy tissue and tumour led to PCA3 being identified as a biomarker for the diagnosis of prostate

cancer. [359] However, since this gene is a non-coding gene, the only molecule that can be targeted for diagnosis is PCA3 mRNA. Due to mRNA being prone to degradation, sensing PCA3 mRNA has a decreased sensitivity when compared with other types of targeted sensors (e.g. protein-based sensors). So far, reverse transcriptase polymerase chain reaction (rt-PCR) analysis has been one of the most used techniques for diagnosis of prostate cancer using PC3 as the biomarker. [360] Other studies have been conducted to assess the PCA3 expression with different methods used for the diagnostic of prostate cancer, such as the Gleason score, the pathological score and total tumour volume. [327, 361, 362] All studies point to a strong correlation between the overexpression of PCA3 and the incidence of malignant prostate cancer tumours.

However, in both BACE-1 and PCA3 cases, currently used methods have low sensitivities for the detection of the respective mRNA targets. Therefore, there is a need to develop sensors that can achieve a significant detection of low levels of mRNA expression for both PCA3 and BACE-1 in order to maximise the use of these biomarkers for diagnosis of the corresponding disease.

2.4. References

1. Melnik, A., & Shagalina, O. (2011). History of Nanotechnology. *Encyclopedia of Life Support Systems*. Retrieved from http://conf.sfu-kras.ru/sites/mn2011/thesis/s22/s22_024.pdf
2. John F. Mongillo. (2007). Nanotechnology 101. *Nanotechnology 101*, 63.
3. Novotny, L. (2006). *Principles of Nano-Optics*. *Nano Today* (Vol. 1). doi:10.1016/S1748-0132(06)70120-7
4. Natelson, D. (2006). Nanofabrication: Best of both worlds*. Nature Material, 5,* 853-854. doi:10.1038/nmat1769
5. Karmakar, S., Kumar, S., Rinaldi, R., & Maruccio, G. (2011). Nano-electronics and spintronics with nanoparticles. *Journal of Physics: Conference Series*, *292*, 12002. doi:10.1088/1742-6596/292/1/012002
6. Whitesides, G. M. (2005). Nanoscience, nanotechnology, and chemistry. *Small*, *1*(2), 172–179. doi:10.1002/smll.200400130
7. Salata, O. (2004). Applications of nanoparticles in biology and medicine. *Journal of Nanobiotechnology*, *2*(1), 3. doi:10.1186/1477-3155-2-3
8. Roco, M. C. (2003). Nanotechnology: Convergence with modern biology and medicine. *Current Opinion in Biotechnology*. doi:10.1016/S0958-1669(03)00068-5
9. Nouailhat, A. (2010). *An introduction to nanoscience and nanotechnology*. *An Introduction to Nanoscience and Nanotechnology*. doi:10.1002/9780470610954
10. Wang, Y., & Xia, Y. (2004). Bottom-up and top-down approaches to the synthesis of monodispersed spherical colloids of low melting-point metals. *Nano Letters*, *4*(10), 2047–2050. doi:10.1021/nl048689j
11. Ito, T., & Okazaki, S. (2000). Pushing the limits of lithography. *Nature*, *406*(6799), 1027–1031. doi:10.1038/35023233
12. Nakanishi, T., Hiraoka, T., Fujimoto, A., Saito, S., & Asakawa, K. (2006). Nano-patterning using an embedded particle monolayer as an etch mask. *Microelectronic Engineering*, *83*(4–9 SPEC. ISS.), 1503–1508. doi:10.1016/j.mee.2006.01.193
13. Brust, M., Fink, J., Bethell, D., Schiffrin, D. J., & Kiely, C. (1995). Synthesis and reactions of functionalised gold nanoparticles. *Journal of the Chemical Society, Chemical Communications*, (16), 1655. doi:10.1039/c39950001655
14. Liu, S., & Han, M. (2005). Synthesis, functionalization, and bioconjugation of monodisperse, silica-coated gold nanoparticles: Robust bioprobes. *Advanced Functional Materials*, *15*(6), 961–967. doi:10.1002/adfm.200400427
15. H, R. K., a, J. S., & Dhole S N. (2012). Solid Lipid Nanoparticle: A Review.

IOSR Journal of Pharmacy, *2*(6), 2250–3013. doi:10.9790/3013-26103444

16. Hawkins, M. J., Soon-Shiong, P., & Desai, N. (2008). Protein nanoparticles as drug carriers in clinical medicine. *Advanced Drug Delivery Reviews*, *60*(8), 876–885. doi:10.1016/j.addr.2007.08.044

17. Rao, C. N. R., Kulkarni, G. U., Thomas, P. J., & Edwards, P. P. (2000). Metal nanoparticles and their assemblies. *Chemical Society Reviews*, *29*(1), 27–35. doi:10.1039/a904518j

18. Tang, L., & Cheng, J. (2013). Nonporous silica nanoparticles for nanomedicine application. *Nano Today*, *8*(3), 290–312. doi:10.1016/j.nantod.2013.04.007

19. Hamidi, M., Azadi, A., & Rafiei, P. (2008). Hydrogel nanoparticles in drug delivery. *Advanced Drug Delivery Reviews*, *60*(15), 1638–1649. doi:10.1016/j.addr.2008.08.002

20. Faraji, A. H., & Wipf, P. (2009). Nanoparticles in cellular drug delivery. *Bioorganic and Medicinal Chemistry*. doi:10.1016/j.bmc.2009.02.043

21. Wilczewska, A., Niemirowicz, K., Markiewicz, K., & Car, H. (2012). [Review] Nanoparticles as drug delivery systems. *Pharmacological Reports*, *64*(5), 1864–1882. doi:10.1016/S1734-1140(12)70901-5

22. Wang, F., Banerjee, D., Liu, Y., Chen, X., & Liu, X. (2010). Upconversion nanoparticles in biological labeling, imaging, and therapy. *The Analyst*, *135*(8), 1839–54. doi:10.1039/c0an00144a

23. Parveen, S., Misra, R., & Sahoo, S. K. (2012). Nanoparticles: A boon to drug delivery, therapeutics, diagnostics and imaging. *Nanomedicine: Nanotechnology, Biology, and Medicine*. doi:10.1016/j.nano.2011.05.016

24. Pérez-López, B., & Merkoçi, A. (2011). Nanoparticles for the development of improved (bio)sensing systems. *Analytical and Bioanalytical Chemistry*. doi:10.1007/s00216-010-4566-y

25. Saha, K., Agasti, S. S., Kim, C., Li, X., & Rotello, V. M. (2012). Gold nanoparticles in chemical and biological sensing. *Chemical Reviews*. doi:10.1021/cr2001178

26. Bogart, L. K., Pourroy, G., Murphy, C. J., Puntes, V., Pellegrino, T., Rosenblum, D., Peer, D., Lévy, R. (2014). Nanoparticles for imaging, sensing, and therapeutic intervention. *ACS Nano*, *8*(4), 3107–3122. doi:10.1021/nn500962q

27. Patil, Y., & Panyam, J. (2009). Polymeric nanoparticles for siRNA delivery and gene silencing. *International Journal of Pharmaceutics*, *367*(1–2), 195–203. doi:10.1016/j.ijpharm.2008.09.039

28. Jain, P. K., ElSayed, I. H., & El-Sayed, M. A. (2007). Au nanoparticles target cancer. *Nano Today*. doi:10.1016/S1748-0132(07)70016-6

29. Mieszawska, A. J., Mulder, W. J. M., Fayad, Z. A., & Cormode, D. P. (2013).

Multifunctional gold nanoparticles for diagnosis and therapy of disease. *Molecular Pharmaceutics*. doi:10.1021/mp3005885

30. Thi, E. P., Mire, C. E., Lee, A. C. H., Geisbert, J. B., Zhou, J. Z., Agans, K. N., Snead, N. M., Deer, D. J., Barnard, T. R., Fenton, K. A., MacLachlan, I., Geisbert, T. W. (2015). Lipid nanoparticle siRNA treatment of Ebola-virus-Makona-infected nonhuman primates. *Nature*, *521*(7552), 362–5. doi:10.1038/nature14442

31. Kelly, K. L., Coronado, E., Zhao, L. L., & Schatz, G. C. (2003). The Optical Properties of Metal Nanoparticles: The Influence of Size, Shape, and Dielectric Environment. *J. Phys. Chem. B*. doi:10.1021/jp026731y

32. Liz-Marzán, L. M. (2004). Nanometals: Formation and color. *Materials Today*, *7*(2), 26–31. doi:10.1016/S1369-7021(04)00080-X

33. Gao, Y., Zhang, R., Cheng, J. C., Liaw, J. W., & Ma, C. (2013). Optical properties of plasmonic dimer, trimer, tetramer and pentamer assemblies of gold nanoboxes. *Journal of Quantitative Spectroscopy and Radiative Transfer*, *125*, 23–32. doi:10.1016/j.jqsrt.2013.04.014

34. Long, N. N., Vu, L. Van, Kiem, C. D., Doanh, S. C., Nguyet, C. T., Hang, P. T., Thien, N., Quynh, L. M. (2009). Synthesis and optical properties of colloidal gold nanoparticles. *Journal of Physics: Conference Series*, *187*(1), 12026. doi:10.1088/1742-6596/187/1/012026

35. Faraday, M. (1857). The Bakerian lecture: experimental relations of gold (and other metals) to light. *Philosophycal Transactions of the Royal Society of London*, *147*(0), 145–181. doi:10.1098/rstl.1857.0011

36. J. Turkevich; P.C. Stevenson; J. Hiller. (1951). Synthesis of Gold Nanoparticles Turkevich method. *Discussions of the Faraday Society*, *11*, 55–75.

37. Frens, G. (1972). Particle size and sol stability in metal colloids. *Kolloid-Zeitschrift & Zeitschrift für Polymere*, *250*(7), 736–741. doi:10.1007/BF01498565

38. Frens, G. (1973). Controlled Nucleation for the Regulation of the Particle Size in Monodisperse Gold Suspensions. *Nature Physical Science*, *241*(105), 20–22. doi:10.1038/physci241020a0

39. Zhao, P., Li, N., & Astruc, D. (2013). State of the art in gold nanoparticle synthesis. *Coordination Chemistry Reviews*. doi:10.1016/j.ccr.2012.09.002

40. Kimling, J., Maier, M., Okenve, B., Kotaidis, V., Ballot, H., & Plech, A. (2006). Turkevich method for gold nanoparticle synthesis revisited. *Journal of Physical Chemistry B*, *110*(32), 15700–15707. doi:10.1021/jp061667w

41. Bastús, N. G., Comenge, J., & Puntes, V. (2011). Kinetically controlled seeded growth synthesis of citrate-stabilized gold nanoparticles of up to 200 nm: Size focusing versus ostwald ripening. *Langmuir*, *27*(17), 11098–11105. doi:10.1021/la201938u

42. Ji, X., Song, X., Li, J., Bai, Y., Yang, W., & Peng, X. (2007). Size control of gold nanocrystals in citrate reduction: The third role of citrate. *Journal of the American Chemical Society*, *129*(45), 13939–13948. doi:10.1021/ja074447k

43. Kumar, S., Gandhi, K. S., & Kumar, R. (2007). Modeling of Formation of Gold Nanoparticles by Citrate Method. *Industrial & Engineering Chemistry Research*, *46*(10), 3128–3136. doi:10.1021/ie060672j

44. Xia, H., Bai, S., Hartmann, J., & Wang, D. (2010). Synthesis of monodisperse quasi-spherical gold nanoparticles in water via silver(I)-assisted citrate reduction. *Langmuir*, *26*(5), 3585–3589. doi:10.1021/la902987w

45. Xia, H., Xiahou, Y., Zhang, P., Ding, W., & Wang, D. (2016). Revitalizing the Frens Method to Synthesize Uniform, Quasi-Spherical Gold Nanoparticles with Deliberately Regulated Sizes from 2 to 330 nm. *Langmuir*, *32*(23), 5870–5880. doi:10.1021/acs.langmuir.6b01312

46. Libert, S., Gorshkov, V., Privman, V., Goia, D., & Matijević, E. (2003). Formation of monodispersed cadmium sulfide particles by aggregation of nanosize precursors. *Advances in Colloid and Interface Science*, *100–102*, 169–183. doi:10.1016/S0001-8686(02)00056-8

47. Li,G., Lauer, M.,, Schulz, A., Boettcher, C., Li, F., Fuhrhop, F. (2003). Spherical and Planar Gold(0) Nanoparticles with a Rigid Gold(I)−Anion or a Fluid Gold(0)−Acetone Surface.*Langmuir, 19*, 6483-6491 doi:10.1021/LA0300277

48. Majzik, A., Patakfalvi, R., Hornok, V., & Dékány, I. (2009). Growing and stability of gold nanoparticles and their functionalization by cysteine. *Gold Bulletin*, *42*(2), 113–123. doi:10.1007/BF03214921

49. Wuithschick, M., Birnbaum, A., Witte, S., Sztucki, M., Vainio, U., Pinna, N., … Polte, J. (2015). Turkevich in New Robes: Key Questions Answered for the Most Common Gold Nanoparticle Synthesis. *ACS Nano*, *9*(7), 7052–7071. doi:10.1021/acsnano.5b01579

50. Shi, W., Casas, J., Venkataramasubramani, M., & Tang, L. (2012). Synthesis and Characterization of Gold Nanoparticles with Plasmon Absorbance Wavelength Tunable from Visible to Near Infrared Region. *ISRN Nanomaterials*, *2012*, 1–9. doi:10.5402/2012/659043

51. Ivanov, M. R., Bednar, H. R., & Haes, A. J. (2009). Investigations of the mechanism of gold nanoparticle stability and surface functionalization in capillary electrophoresis. *ACS nano*, *3*(2), 386–94. doi:10.1021/nn8005619

52. George Thomas, K., Zajicek, J., & Kamat, P. V. (2002). Surface binding properties of tetraoctylammonium bromide-capped gold nanoparticles. *Langmuir*, *18*(9), 3722–3727. doi:10.1021/la015669d

53. Isaacs, S. R., Cutler, E. C., Park, J. S., Lee, T. R., & Shon, Y. S. (2005). Synthesis of tetraoctylammonium-protected gold nanoparticles with improved stability. *Langmuir*, *21*(13), 5689–5692. doi:10.1021/la050656b

54. Wang, W., Chen, Q., Jiang, C., Yang, D., Liu, X., & Xu, S. (2007). One-step synthesis of biocompatible gold nanoparticles using gallic acid in the presence of poly-(N-vinyl-2-pyrrolidone). *Colloids and Surfaces A: Physicochemical and Engineering Aspects*, *301*(1–3), 73–79. doi:10.1016/j.colsurfa.2006.12.037

55. Hoppe, C. E., Lazzari, M., Pardiñas-Blanco, I., & López-Quintela, M. A. (2006). One-step synthesis of gold and silver hydrosols using poly(N-vinyl-2-pyrrolidone) as a reducing agent. *Langmuir*, *22*(24), 7027–7034. doi:10.1021/la060885d

56. Jiang, P., Zhou, J.-J., Li, R., Wang, Z.-L., & Xie, S.-S. (2006). Poly(vinyl pyrrolidone)-capped five-fold twinned gold particles with sizes from nanometres to micrometres. *Nanotechnology*, *17*(14), 3533–3538. doi:10.1088/0957-4484/17/14/029

57. Sastry, M. (2004). Moving Nanoparticles Around : Phase-Transfer Processes in Nanomaterials Synthesis. *The Chemistry of Nanomaterials: Synthesis, Properties and Applications*, *1*(2), 31–50. doi:10.1002/352760247X.ch3

58. Hassinen, J., Liljeström, V., Kostiainen, M. A., & Ras, R. H. A. (2015). Rapid Cationization of Gold Nanoparticles by Two-Step Phase Transfer. *Angewandte Chemie International Edition*, *54*(27), 7990–7993. doi:10.1002/anie.201503655

59. Perrault, S. D., & Chan, W. C. W. (2009). Synthesis and surface modification of highly monodispersed, spherical gold nanoparticles of 50-200 nm. *Journal of the American Chemical Society*, *131*(47), 17042–17043. doi:10.1021/ja907069u

60. Zhong, J., Qu, J., Ye, F., Wang, C., Meng, L., & Yang, J. (2011). The bis(p-sulfonatophenyl)phenylphosphine-assisted synthesis and phase transfer of ultrafine gold nanoclusters. *Journal of Colloid and Interface Science*, *361*(1), 59–63. doi:10.1016/j.jcis.2011.05.017

61. Jin, P., Dai, Z., & Chang, T. (2015). The Role of Bis (p -Sulfonatophenyl) Phenylphosphine in Stabilizing Gold Nanoparticles, (Iea), 44–46.

62. Schmid, G., & Lehnert, A. (1989). The complexation of gold colloids. *Angew. Chem., Int. Ed.*, *28*(6), 780–781. doi:10.1002/anie.198907801

63. Sperling, R. A., & Parak, W. J. (2010). Surface modification, functionalization and bioconjugation of colloidal inorganic nanoparticles. *Philosophical Transactions of the Royal Society of London A: Mathematical, Physical and Engineering Sciences*, *368*(1915).

64. López-Cartes, C., Rojas, T. C., Litrán, R., Martínez-Martínez, D., de la Fuente, J. M., Penadés, S., Fernández, A. (2005). Gold Nanoparticles with Different Capping Systems: An Electronic and Structural XAS Analysis. *Journal of Physical Chemistry B, 109* (18)*,* pp 8761–8766 doi:10.1021/JP050184+

65. Bourg, M.-C., Badia, A., & Lennox, R. B. (2000). Gold−Sulfur Bonding in 2D and 3D Self-Assembled Monolayers: XPS Characterization. *The Journal of Physical Chemistry B*, *104*(28), 6562–6567. doi:10.1021/jp9935337

66. Häkkinen, H. (2012). The gold–sulfur interface at the nanoscale. *Nature Chemistry*, *4*(6), 443–455. doi:10.1038/nchem.1352

67. Mohamed, A. a., Abdou, H. E., Chen, J., Bruce, A. E., & Bruce, M. R. M. (2002). Perspectives in Inorganic and Bioinorganic Gold Sulfur Chemistry. *Comments on Inorganic Chemistry*, *23*(5), 321–334. doi:10.1080/02603590215003

68. Pelaz, B., del Pino, P., Maffre, P., Hartmann, R., Gallego, M., Rivera-Fernandez, S., de la Fuente, J., Parak, W. J. (2015). Surface Functionalization of Nanoparticles with Polyethylene Glycol: Effects on Protein Adsorption and Cellular Uptake. *ACS Nano*, *9*(7), 6996–7008. doi:10.1021/acsnano.5b01326

69. Wang, L., Liu, Y., Li, W., Jiang, X., Ji, Y., Wu, X., Qiu, Y., Zhao, K., Wei, T., Li, Y., Zhao, Y., Chen, C. (2011). Selective Targeting of Gold Nanorods at the Mitochondria of Cancer Cells: Implications for Cancer Therapy. *Nano Letters*, *11*(2), 772–780. doi:10.1021/nl103992v

70. Spindler, S., Ehrig, J., König, K., Nowak, T., Piliarik, M., Stein, H. E., Taylor, R., Garanger, E., Lecommandoux, S., Alves, I., Sandoghdar, V. (2016). Visualization of lipids and proteins at high spatial and temporal resolution via interferometric scattering (iSCAT) microscopy. *Journal of Physics D: Applied Physics*, *49*(27), 274002. doi:10.1088/0022-3727/49/27/274002

71. Seferos, D. S., Giljohann, D. A., Hill, H. D., Prigodich, A. E., & Mirkin, C. A. (2007). Nano-flares: Probes for transfection and mRNA detection in living cells. *Journal of the American Chemical Society*, *129*(50), 15477–15479. doi:10.1021/ja0776529

72. Pan, W., Li, Y., Wang, M., Yang, H., Li, N., Tang, B., (2016). FRET-based nanoprobes for simultaneous monitoring of multiple mRNAs in living cells using single wavelength excitation. *Chem. Commun.*, *52*(24), 4569–4572. doi:10.1039/C5CC10147F

73. Lee, J. S., Green, J. J., Love, K. T., Sunshine, J., Langer, R., & Anderson, D. G. (2009). Gold, poly(beta-amino ester) nanoparticles for small interfering RNA delivery. *Nano Letters*, *9*(6), 2402–2406. doi:10.1021/nl9009793

74. Shen, J., Kim, H. C., Mu, C., Gentile, E., Mai, J., Wolfram, J., Ji, L., Ferrari, M., Mao, Z., Shen, H. (2014). Multifunctional gold nanorods for siRNA gene silencing and photothermal therapy. *Advanced Healthcare Materials*, *3*(10), 1629–1637. doi:10.1002/adhm.201400103

75. Giljohann, D. A., Seferos, D. S., Prigodich, A. E., Patel, P. C., & Mirkin, C. A. (2009). Gene regulation with polyvalent siRNA-nanoparticle conjugates. *Journal of the American Chemical Society*, *131*(6), 2072–2073. doi:10.1021/ja808719p

76. Pan, B., Ao, L., Gao, F., Tian, H., He, R., & Cui, D. (2005). End-to-end self-assembly and colorimetric characterization of gold nanorods and nanospheres via oligonucleotide hybridization. *Nanotechnology*, *16*(9), 1776–1780. doi:10.1088/0957-4484/16/9/061

77. Coomber, D., Bartczak, D., Gerrard, S. R., Tyas, S., Kanaras, A. G., & Stulz, E. (2010). Programmed assembly of peptide-functionalized gold nanoparticles on DNA templates. *Langmuir*, *26*(17), 13760–13762. doi:10.1021/la1023554

78. Sanz, V., Conde, J., Hernández, Y., Baptista, P. V., Ibarra, M. R., & De La Fuente, J. M. (2012). Effect of PEG biofunctional spacers and TAT peptide on dsRNA loading on gold nanoparticles. *Journal of Nanoparticle Research*, *14*(6). doi:10.1007/s11051-012-0917-2

79. Eustis, S., & El-Sayed, M. A. (2006). Why gold nanoparticles are more precious than pretty gold: Noble metal surface plasmon resonance and its enhancement of the radiative and nonradiative properties of nanocrystals of different shapes. *Chem. Soc. Rev.*, *35*(3), 209–217. doi:10.1039/B514191E

80. Willets, K. A., & Van Duyne, R. P. (2007). Localized Surface Plasmon Resonance Spectroscopy and Sensing. *Annual Review of Physical Chemistry*, *58*(1), 267–297. doi:10.1146/annurev.physchem.58.032806.104607

81. Srivastava, A. K., Yadev, R., Rai, V. N., Ganguly, T., & Deb, S. K. (2012). Surface plasmon resonance in gold nanoparticles. *Solid State Physics: Proceedings of the 56th DAE Solid State Physics Symposium*, *1447*(1), 305–306. doi:10.1063/1.4710001

82. Mie, G. (1908). Beiträge zur Optik trüber Medien, speziell kolloidaler Metallösungen. *Annalen der Physik*, *330*(3), 377–445. doi:10.1002/andp.19083300302

83. Amendola, V., Pilot, R., Frasconi, M., Maragò, O. M., & Iatì, M. A. (2017). Surface plasmon resonance in gold nanoparticles: a review. *Journal of Physics: Condensed Matter*, *29*(20), 203002. doi:10.1088/1361-648X/aa60f3

84. Liu, J., & Lu, Y. (2004). Colorimetric biosensors based on DNAzyme-assembled gold nanoparticles. *Journal of Fluorescence*. doi:10.1023/B:JOFL.0000031816.06134.d3

85. Chah, S., Hammond, M. R., & Zare, R. N. (2005). Gold nanoparticles as a colorimetric sensor for protein conformational changes. *Chemistry and Biology*, *12*(3), 323–328. doi:10.1016/j.chembiol.2005.01.013

86. Alkilany, A. M., & Murphy, C. J. (2010). Toxicity and cellular uptake of gold nanoparticles: what we have learned so far? *Journal of nanoparticle research : an interdisciplinary forum for nanoscale science and technology*, *12*(7), 2313–2333. doi:10.1007/s11051-010-9911-8

87. Dreaden, E. C., Alkilany, A. M., Huang, X., Murphy, C. J., & El-Sayed, M. a. (2012). The golden age: gold nanoparticles for biomedicine. *Chemical Society Reviews*, *41*(7), 2740. doi:10.1039/c1cs15237h

88. Pan, Y., Neuss, S., Leifert, A., Fischler, M., Wen, F., Simon, U., … Jahnen-Dechent, W. (2007). Size-dependent cytotoxicity of gold nanoparticles. *Small*, *3*(11), 1941–1949. doi:10.1002/smll.200700378

89. Cho, E. C., Xie, J., Wurm, P. A., & Xia, Y. (2009). Understanding the role of surface charges in cellular adsorption versus internalization by selectively removing gold nanoparticles on the cell surface with a I 2/KI etchant. *Nano Letters*, *9*(3), 1080–1084. doi:10.1021/nl803487r

90. Pan, Y., Leifert, A., Ruau, D., Neuss, S., Bornemann, J., Schmid, G., Brandau, W., Simon, U., Jahnen-Dechent, W. (2009). Gold nanoparticles of diameter 1.4 nm trigger necrosis by oxidative stress and mitochondrial damage. *Small*, *5*(18), 2067–2076. doi:10.1002/smll.200900466

91. Tatur, S., MacCarini, M., Barker, R., Nelson, A., & Fragneto, G. (2013). Effect of functionalized gold nanoparticles on floating lipid bilayers. *Langmuir*, *29*(22), 6606–6614. doi:10.1021/la401074y

92. Zhang, Y., Xu, D., Li, W., Yu, J., & Chen, Y. (2012). Effect of size, shape, and surface modification on cytotoxicity of gold nanoparticles to human HEp-2 and Canine MDCK Cells. *Journal of Nanomaterials*, *2012*. doi:10.1155/2012/375496

93. Wang, L., Li, J., Pan, J., Jiang, X., Ji, Y., Li, Y., Qu, Y., Zhao, Y., Wu, X., Chen, C. (2013). Revealing the binding structure of the protein corona on gold nanorods using synchrotron radiation-based techniques: Understanding the reduced damage in cell membranes. *Journal of the American Chemical Society*, *135*(46), 17359–17368. doi:10.1021/ja406924v

94. Lewinski, N., Colvin, V., & Drezek, R. (2008). Cytotoxicity of nanoparticles. *Small (Weinheim an der Bergstrasse, Germany)*, *4*(1), 26–49. doi:10.1002/smll.200700595

95. Vijayakumar, S., & Ganesan, S. (2012). *In Vitro* Cytotoxicity Assay on Gold Nanoparticles with Different Stabilizing Agents. *Journal of Nanomaterials*, *2012*, 1–9. doi:10.1155/2012/734398

96. Soenen, S. J., Manshian, B., Montenegro, J. M., Amin, F., Meermann, B., Thiron, T., Cornelissen, M., Vanhaecke, F., Doak, S., Parak, W., de Smedt, S., Braeckmans, K. (2012). Cytotoxic Effects of Gold Nanoparticles: A Multiparametric Study. *ACS Nano*, *6*(7), 5767–5783. doi:10.1021/nn301714n

97. Shukla, R., Bansal, V., Chaudhary, M., Basu, A., Bhonde, R. R., & Sastry, M. (2005). Biocompatibility of gold nanoparticles and their endocytotic fate inside the cellular compartment: A microscopic overview. *Langmuir*. doi:10.1021/la0513712

98. Gu, Y.-J., Cheng, J., Lin, C.-C., Lam, Y. W., Cheng, S. H., & Wong, W.-T. (2009). Nuclear penetration of surface functionalized gold nanoparticles. *Toxicology and Applied Pharmacology*, *237*(2), 196–204. doi:10.1016/j.taap.2009.03.009

99. Villiers, C., Freitas, H., Couderc, R., Villiers, M.-B., & Marche, P. (2010). Analysis of the toxicity of gold nano particles on the immune system: effect on dendritic cell functions. *Journal of nanoparticle research : an interdisciplinary forum for nanoscale science and technology*, *12*(1), 55–60.

doi:10.1007/s11051-009-9692-0

100. Connor, E. E., Mwamuka, J., Gole, A., Murphy, C. J., & Wyatt, M. D. (2005). Gold Nanoparticles Are Taken Up by Human Cells but Do Not Cause Acute Cytotoxicity. *Small*, *1*(3), 325–327. doi:10.1002/smll.200400093

101. Hasan, T., Ortel, B., Moor, A. C. E., & Pogue, B. W. (2003). Photodynamic therapy of Cancer. *Holland-Frei Cancer Medicine*, 605–622. doi:10.3322/caac.20114

102. Kübler, A. C. (2005). Photodynamic therapy. *Medical Laser Application*. doi:10.1016/j.mla.2005.02.001

103. Castano, A., Mroz, P., & Hamblin, M. (2006). Photodynamic therapy and anti-tumour immunity. *Nature Reviews Cancer*, *6*(7), 535–545. doi:10.1038/nrc1894.Photodynamic

104. Jain, P. K., Huang, X., El-Sayed, I. H., & El-Sayed, M. A. (2008). Noble Metals on the Nanoscale: Optical and Photothermal Properties and Some Applications in Imaging, Sensing, Biology, and Medicine. *Accounts of Chemical Research*, *41*(12), 1578–1586. doi:10.1021/ar7002804

105. Li, C., Chen, T., Ocsoy, I., Zhu, G., Yasun, E., You, M., … Tan, W. (2014). Gold-Coated Fe3O4 nanoroses with five unique functions for cancer cell targeting, imaging, and therapy. *Advanced Functional Materials*, *24*(12), 1772–1780. doi:10.1002/adfm.201301659

106. Ray, P. C., Khan, S. A., Singh, A. K., Senapati, D., & Fan, Z. (2012). Nanomaterials for targeted detection and photothermal killing of bacteria. *Chemical Society Reviews*, *41*(8), 3193. doi:10.1039/c2cs15340h

107. Mantsch, H. H. (2006). Biomedical Spectroscopy: Introduction. In *Encyclopedia of Analytical Chemistry*. doi:10.1002/9780470027318.a0101

108. Chitra, K., & Annadurai, G. (2013). Fluorescent Silica Nanoparticles in the Detection and Control of the Growth of Pathogen. *Journal of Nanotechnology*, *2013*, 1–7. doi:10.1155/2013/509628

109. Tung, Y. T., Chang, C. C., Lin, Y. L., Hsieh, S. L., & Wang, G. J. (2016). Development of double-generation gold nanoparticle chip-based dengue virus detection system combining fluorescence turn-on probes. *Biosensors and Bioelectronics*, *77*, 90–98. doi:10.1016/j.bios.2015.09.007

110. Rane, T. D., Armani, A. M., Chan, W., Guan, Z., Zhao, T., & Zhou, N. (2016). Two-Photon Microscopy Analysis of Gold Nanoparticle Uptake in 3D Cell Spheroids. *PLOS ONE*, *11*(12), e0167548. doi:10.1371/journal.pone.0167548

111. Popović, Z., Liu, W., Chauhan, V. P., Lee, J., Wong, C., Greytak, A. B., Insin, N., Nocera, D., Fukumura, D., Jain, R., Bawendi, M. G. (2010). A nanoparticle size series for in vivo fluorescence imaging. *Angewandte Chemie (International ed. in English)*, *49*(46), 8649–52. doi:10.1002/anie.201003142

112. Albanese, A., Lam, A. K., Sykes, E. A., Rocheleau, J. V, & Chan, W. C. W.

(2013). Tumour-on-a-chip provides an optical window into nanoparticle tissue transport. *Nature communications*, *4*, 2718. doi:10.1038/ncomms3718

113. Waggoner, A. (2006). Fluorescent labels for proteomics and genomics. *Current Opinion in Chemical Biology*. doi:10.1016/j.cbpa.2006.01.005

114. Peng, F., Su, Y., Zhong, Y., Fan, C., Lee, S.-T., & He, Y. (2014). Silicon Nanomaterials Platform for Bioimaging, Biosensing, and Cancer Therapy. *Accounts of Chemical Research*, *47*(2), 612–623. doi:10.1021/ar400221g

115. Filonov, G. S., Piatkevich, K. D., Ting, L. M., Zhang, J., Kim, K., & Verkhusha, V. V. (2011). Bright and stable near-infrared fluorescent protein for in vivo imaging. *Nat Biotechnol*, *29*(8), 757–761. doi:10.1038/nbt.1918

116. Silva, A. K. A., Di Corato, R., Pellegrino, T., Chat, S., Pugliese, G., Luciani, N., Gazeau, F., Wilhem, C. (2013). Cell-derived vesicles as a bioplatform for the encapsulation of theranostic nanomaterials. *Nanoscale*, *5*(23), 11374–84. doi:10.1039/c3nr01541f

117. Dean, K. M., & Palmer, A. E. (2014). Advances in fluorescence labeling strategies for dynamic cellular imaging. *Nature Chemical Biology*, *10*(7), 512–523. doi:10.1038/nchembio.1556

118. Wolfbeis, O. S. (2015). An overview of nanoparticles commonly used in fluorescent bioimaging. *Chem. Soc. Rev.*, *44*(14), 4743–4768. doi:10.1039/C4CS00392F

119. Monici, M. (2005). Cell and tissue autofluorescence research and diagnostic applications. *Biotechnology Annual Review*. doi:10.1016/S1387-2656(05)11007-2

120. Eichler, J., Knof, J., & Lenz, H. (1977). Measurements on the depth of penetration of light (0.35-1.0 μm) in tissue. *Radiation and Environmental Biophysics*, *14*(3), 239–242. doi:10.1007/BF01323942

121. Yuan, F., Hu, C., Hu, X., Wei, D., Chen, Y., & Qu, J. (2011). Photodegradation and toxicity changes of antibiotics in UV and UV/H2O2 process. *Journal of Hazardous Materials*, *185*(2–3), 1256–1263. doi:10.1016/j.jhazmat.2010.10.040

122. Parrish, J. A., Jaenicke, K. F., & Anderson, R. R. (1982). Erythema And Melanogenesis Action Spectra Of Normal Human Skin. *Photochemistry and Photobiology*, *36*(2), 187–191. doi:10.1111/j.1751-1097.1982.tb04362.x

123. Gentile, M., Latonen, L., & Laiho, M. (2003). Cell cycle arrest and apoptosis provoked by UV radiation-induced DNA damage are transcriptionally highly divergent responses. *Nucleic Acids Research*, *31*(16), 4779–4790. doi:10.1093/nar/gkg675

124. Discussion, A. (2011). Near-infrared window in biological tissue. *Cell*, 9–12.

125. Escobedo, J. O., Rusin, O., Lim, S., & Strongin, R. M. (2010). NIR dyes for bioimaging applications. *Current Opinion in Chemical Biology*.

doi:10.1016/j.cbpa.2009.10.022

126. Hilderbrand, S. A., & Weissleder, R. (2010). Near-infrared fluorescence: application to in vivo molecular imaging. *Current Opinion in Chemical Biology*. doi:10.1016/j.cbpa.2009.09.029

127. Mantsch, H. H., & Chapman, D. (1996). *Infrared spectroscopy of biomolecules*. *Infrared Spectroscopy of Biomolecules*. doi:10.1016/0307-4412(96)82531-3

128. Ong, L. C., Gnanasammandhan, M. K., Nagarajan, S., & Zhang, Y. (2010). Upconversion: Road to El dorado of the fluorescence world. *Luminescence*, *25*(4), 290–293. doi:10.1002/bio.1229

129. Wang, F., & Liu, X. (2008). Upconversion multicolor fine-tuning: Visible to near-infrared emission from lanthanide-doped NaYF4 nanoparticles. *Journal of the American Chemical Society*, *130*(17), 5642–5643. doi:10.1021/ja800868a

130. DaCosta, M. V., Doughan, S., Han, Y., & Krull, U. J. (2014). Lanthanide upconversion nanoparticles and applications in bioassays and bioimaging: A review. *Analytica Chimica Acta*, *832*, 1–33. doi:10.1016/j.aca.2014.04.030

131. Chen, G., Qiu, H., Prasad, P. N., & Chen, X. (2013). Upconversion Nanoparticles : Design , Nanochemistry , and Applications in Theranostics. doi:10.1021/cr400425h

132. Pollnau, M., Gamelin, D. R., Lüthi, S. R., Güdel, H. U., & Hehlen, M. P. (2000). Power dependence of upconversion luminescence in lanthanide and transition-metal-ion systems. *Physical Review B*, *61*(5), 3337–3346. doi:10.1103/PhysRevB.61.3337

133. Suyver, J. F., Aebischer, A., García-Revilla, S., Gerner, P., & Güdel, H. U. (2005). Anomalous power dependence of sensitized upconversion luminescence. *Physical Review B*, *71*(12), 125123. doi:10.1103/PhysRevB.71.125123

134. Scheps, R. (1996). Upconversion laser processes. *Progress in Quantum Electronics*, *20*(4), 271–358. doi:10.1016/0079-6727(95)00007-0

135. Zhou, J., Liu, Q., Feng, W., Sun, Y., & Li, F. (2015). Upconversion luminescent materials: Advances and applications. *Chemical Reviews*. doi:10.1021/cr400478f

136. Zou, X., & Izumitani, T. (1993). Spectroscopic properties and mechanisms of excited state absorption and energy transfer upconversion for Er3+-doped glasses. *Journal of Non-Crystalline Solids*, *162*(1–2), 68–80. doi:10.1016/0022-3093(93)90742-G

137. Zhou, B., Shi, B., Jin, D., Liu, X., Ahmed, W. H., El-Nakla, M. A., Ismail, B. (2013). Controlling upconversion nanocrystals for emerging applications. *Nature nanotechnology*, *8*(3), 729–34. doi:10.1016/j.ijmultiphaseflow.2009.10.002

138. Sun, L.-D., Dong, H., Zhang, P.-Z., & Yan, C.-H. (2015). Upconversion of rare Earth nanomaterials. *Annual review of physical chemistry*, *66*(January), 619–42. doi:10.1146/annurev-physchem-040214-121344

139. Philipps, J. F., Tüpfer, T., Ebendorff-Heidepriem, H., Ehrt, D., & Sauerbrey, R. (2002). Energy transfer and upconversion in erbium-ytterbium-doped fluoride phosphate glasses. *Applied Physics B: Lasers and Optics*, *74*(3), 233–236. doi:10.1007/s003400200804

140. Jones, G. C., & Houde-Walter, S. N. (2005). Upconversion mechanisms in an erbium-doped transparent glass ceramic. *Journal of the Optical Society of America B: Optical Physics*, *22*(4), 825–830. doi:10.1364/JOSAB.22.000825

141. Dong, H., Sun, L.-D., & Yan, C.-H. (2015). Energy transfer in lanthanide upconversion studies for extended optical applications. *Chem. Soc. Rev.*, *44*(6), 1608–1634. doi:10.1039/C4CS00188E

142. Qiu, H., Yang, C., Shao, W., Damasco, J., Wang, X., Ågren, H., Prasad, P., Chen, G. (2014). Enhanced Upconversion Luminescence in Yb 3+ /Tm 3+ -Codoped Fluoride Active Core/Active Shell/Inert Shell Nanoparticles through Directed Energy Migration. *Nanomaterials*, *4*, 55–68. doi:10.3390/nano4010055

143. Boyer, J.-C., Cuccia, L. A., Capobianco, J. A. (2007). Synthesis of Colloidal Upconverting NaYF4: Er3+ /Yb3+ and Tm3+ /Yb3+ Monodisperse Nanocrystals. *Nano letters*, *7*(3), 847–852. doi:10.1021/nl070235+

144. Yi, G.-S., & Chow, G.-M. (2005). Colloidal LaF3:Yb,Er, LaF3:Yb,Ho and LaF3:Yb,Tm nanocrystals with multicolor upconversion fluorescence. *Journal of Materials Chemistry*, *15*(41), 4460. doi:10.1039/b508240d

145. Zhang, Q., Ding, J., Tang, B., Cheng, J. M., Qiao, Y. B., Zhou, Q. L., Qiu, J., Chen, Q., Chen, D. P. (2009). Optical properties of Yb3+ ions in SiO2-Al2O3-CaF2 glasses. *Journal of Physics D-Applied Physics*, *42*(23), 4. doi:235405\r10.1088/0022-3727/42/23/235405

146. Liu, C., Wang, H., Li, X., & Chen, D. (2009). Monodisperse, size-tunable and highly efficient β-NaYF4:Yb,Er(Tm) up-conversion luminescent nanospheres: controllable synthesis and their surface modifications. *Journal of Materials Chemistry*, *19*(21), 3546. doi:10.1039/b820254k

147. Chukalina, E. P., Popova, M. N., Korableva, S. L., & Abdulsabirov, R. Y. (2000). Fine structure of spectral lines in LiYF4:Er3+ due to isotopic disorder in the lattice. *Physics Letters, Section A: General, Atomic and Solid State Physics*, *269*(5–6), 348–350. doi:10.1016/S0375-9601(00)00273-5

148. He, F., Niu, N., Wang, L., Xu, J., Wang, Y., Yang, G., Gai, S., Yang, P. (2013). Influence of surfactants on the morphology, upconversion emission, and magnetic properties of β-NaGdF4:Yb3+,Ln3+ (Ln = Er, Tm, Ho). *Dalton Transactions*, *42*(27), 10019. doi:10.1039/c3dt00029j

149. Börjesson, K., Rudquist, P., Gray, V., & Moth-Poulsen, K. (2016). Photon

upconversion with directed emission. *Nature Communications*, *7*, 12689. doi:10.1038/ncomms12689

150. Wang, F., & Liu, X. (2009). Recent advances in the chemistry of lanthanide-doped upconversion nanocrystals. *Chemical Society Reviews*, *38*(4), 976. doi:10.1039/b809132n

151. Liu, C., & Chen, D. (2007). Controlled synthesis of hexagon shaped lanthanide-doped LaF3 nanoplates with multicolor upconversion fluorescence. *Journal of Materials Chemistry*, *17*(37), 3875. doi:10.1039/b707927c

152. Guo, H., Li, Y., Wang, D., Zhang, W., Yin, M., Lou, L., & Xia, S. (2004). Blue upconversion of cubic Gd2O3:Er produced by green laser. *Journal of Alloys and Compounds*, *376*(1–2), 23–27. doi:10.1016/j.jallcom.2003.12.020

153. Wang, Z., Wang, L., & Li, Z. (2011). A general method to NaLnF4 assemblies with ordered structures and strong emissions. *Materials Letters*, *65*(23–24), 3516–3518. doi:10.1016/j.matlet.2011.07.101

154. Wang, G., Qin, W., Wang, L., Wei, G., Zhu, P., Zhang, D., Ding, F. (2009). Enhanced ultraviolet upconversion in YF3:Yb3+/Tm3+ nanocrystals. *Journal of Rare Earths*, *27*(2), 330–333. doi:10.1016/S1002-0721(08)60245-8

155. Heer, S., Kömpe, K., Güdel, H. U., & Haase, M. (2004). Highly efficient multicolour upconversion emission in transparent colloids of lanthanide-doped NaYF4 nanocrystals. *Advanced Materials*, *16*(23–24), 2102–2105. doi:10.1002/adma.200400772

156. Qian, H., Li, Z., & Zhang, Y. (2008). Multicolor polystyrene nanospheres tagged with up-conversion fluorescent nanocrystals. *Nanotechnology*, *19*(25), 255601–255604. doi:10.1088/0957-4484/19/25/255601

157. Rinkel, T., Nordmann, J., Raj, A. N., & Haase, M. (2014). Ostwald-ripening and particle size focussing of sub-10 nm $NaYF_4$ upconversion nanocrystals. *Nanoscale*, *6*(23), 14523–14530. doi:10.1039/C4NR03833A

158. Chen, Z., Tian, Q., Song, Y., Yang, J., & Hu, J. (2010). PEG-mediated solvothermal synthesis of NaYF4:Yb/Er superstructures with efficient upconversion luminescence. *Journal of Alloys and Compounds*, *506*(2). doi:10.1016/j.jallcom.2010.07.087

159. Lin, X., Sorensen, C., & Klabunde, K. J. (2000). Digestive Ripening, Nanophase Segregation and Superlattice Formation in Gold Nanocrystal Colloids. *Journal of Nanoparticle Research*, *2*(2), 157–164. doi:10.1023/A:1010078521951

160. Zhao, J., Wu, W., Sun, J., & Guo, S. (2013). Triplet photosensitizers: from molecular design to applications. *Chem. Soc. Rev.*, *42*(12), 5323–5351. doi:10.1039/C3CS35531D

161. Monguzzi, A., & Meinardi, F. (2014). Second-order photochemical upconversion in organic systems. *Journal of Physical Chemistry A*, *118*(8),

1439–1442. doi:10.1021/jp5008957

162. Kim, D. Y., Song, D. W., Chopra, N., De Somer, P., & So, F. (2010). Organic infrared upconversion device. *Advanced Materials*, *22*(20), 2260–2263. doi:10.1002/adma.200903312

163. Zeng, J. H., Su, J., Li, Z. H., Yan, R. X., & Li, Y. D. (2005). Synthesis and upconversion luminescence of hexagonal-phase NaYF 4:Yb, Er3+ phosphors of controlled size and morphology. *Advanced Materials*, *17*(17), 2119–2123. doi:10.1002/adma.200402046

164. Zhao, J., Jia, T., Wang, X., & Kong, X. (2014). Controlled Synthesis of Water-Soluble $NaYF_4$:Yb^{3+}, Er^{3+} Nanoparticles with Surfactant Dependent Properties. *Journal of Nanomaterials*, *2014*, 1–7. doi:10.1155/2014/821706

165. Mai, H. X., Zhang, Y. W., Si, R., Yan, Z. G., Sun, L. D., You, L. P., & Yan, C. H. (2006). High-quality sodium rare-earth fluoride nanocrystals: Controlled synthesis and optical properties. *Journal of the American Chemical Society*, *128*(19), 6426–6436. doi:10.1021/ja060212h

166. Wang, F., Sun, L.-D., Gu, J., Wang, Y.-F., Feng, W., Yang, Y., Wang, J., Yan, C.-H. (2012). Selective Heteroepitaxial Nanocrystal Growth of Rare Earth Fluorides on Sodium Chloride: Synthesis and Density Functional Calculations. *Angewandte Chemie International Edition*, *51*(35), 8796–8799. doi:10.1002/anie.201203069

167. Yi, G., Peng, Y., & Gao, Z. (2011). Strong red-emitting near-infrared-to-visible upconversion fluorescent nanoparticles. *Chemistry of Materials*, *23*(11), 2729–2734. doi:10.1021/cm103175s

168. Shan, J., Qin, X., Yao, N., & Ju, Y. (2007). Synthesis of monodisperse hexagonal $NaYF_4$:Yb, Ln (Ln = Er, Ho and Tm) upconversion nanocrystals in TOPO. *Nanotechnology*, *18*(44), 445607. doi:10.1088/0957-4484/18/44/445607

169. Boyer, J. C., Manseau, M. P., Murray, J. I., & Van Veggel, F. C. J. M. (2010). Surface modification of upconverting NaYF4 nanoparticles with PEG-phosphate ligands for NIR (800 nm) biolabeling within the biological window. *Langmuir*, *26*(2), 1157–1164. doi:10.1021/la902260j

170. Nyk, M., Kumar, R., Ohulchanskyy, T. Y., Bergey, E. J., & Prasad, P. N. (2008). High Contrast in Vitro and in Vivo Photoluminescence Bioimaging Using Near Infrared to Near Infrared Up-Conversion in Tm 3+and Yb 3+Doped Fluoride Nanophosphors. *Nano Letters*, *8*(11), 3834–3838. doi:10.1021/nl802223f

171. Liu, C., Wang, Z., Wang, X., & Li, Z. (2011). Surface modification of hydrophobic NaYF4:Yb,Er upconversion nanophosphors and their applications for immunoassay. *Science China Chemistry*, *54*(8), 1292–1297. doi:10.1007/s11426-011-4319-6

172. Novoselov, K. S., Geim, A. K., Morozov, S. V, Jiang, D., Zhang, Y., Dubonos,

S. V, Grigorieva, I. V., Firsov, A. A. (2004). Electric field effect in atomically thin carbon films. *Science (New York, N.Y.)*, *306*(5696), 666–669. doi:10.1126/science.1102896

173. Geim, A. K., & Novoselov, K. S. (2007). The rise of graphene. *Nature Materials*, *6*(3), 183–191. doi:10.1038/nmat1849

174. Katsnelson, M. I. (2007). Graphene: carbon in two dimensions. *Materials Today*, *10*(1), 20–27. doi:10.1016/S1369-7021(06)71788-6

175. Lu, C. H., Yang, H. H., Zhu, C. L., Chen, X., & Chen, G. N. (2009). A graphene platform for sensing biomolecules. *Angewandte Chemie - International Edition*, *48*(26), 4785–4787. doi:10.1002/anie.200901479

176. Li, N., Su, X., & Lu, Y. (2015). Nanomaterial-based biosensors using dual transducing elements for solution phase detection. *The Analyst*, *140*(9), 2916–43. doi:10.1039/c4an02376e

177. Hummers, W. S., & Offeman, R. E. (1958). Preparation of Graphitic Oxide. *Journal of the American Chemical Society*, *80*(6), 1339–1339. doi:10.1021/ja01539a017

178. Marcano, D. C., Kosynkin, D. V., Berlin, J. M., Sinitskii, A., Sun, Z., Slesarev, A., Alemany, L., Lu, W., Tour, J. M. (2010). Improved synthesis of graphene oxide. *ACS Nano*, *4*(8), 4806–4814. doi:10.1021/nn1006368

179. Shahriary, L., & Athawale, A. a. (2014). Graphene Oxide Synthesized by using Modified Hummers Approach. *International Journal of Renewable Energy and Environmental Engineering*, *2*(1), 58–63.

180. Zhu, Y., Murali, S., Cai, W., Li, X., Suk, J. W., Potts, J. R., & Ruoff, R. S. (2010). Graphene and graphene oxide: Synthesis, properties, and applications. *Advanced Materials*, *22*(35), 3906–3924. doi:10.1002/adma.201001068

181. Gao, W. (2015). The chemistry of graphene oxide. In *Graphene Oxide: Reduction Recipes, Spectroscopy, and Applications* (pp. 61–95). doi:10.1007/978-3-319-15500-5_3

182. Chen, D., Feng, H., & Li, J. (2012). Graphene Oxide: Preparation, Functionalization, and Electrochemical Applications. *Chemical Reviews*, *112*(11), 6027–6053. doi:10.1021/cr300115g

183. Gao, L., Lian, C., Zhou, Y., Yan, L., Li, Q., Zhang, C., Chen, L., Chen, K. (2014). Graphene oxide-DNA based sensors. *Biosensors and Bioelectronics*, *60*, 22–29. doi:10.1016/j.bios.2014.03.039

184. Hussain, S. A. (2009). An Introduction to Fluorescence Resonance Energy Transfer (FRET). *Energy*, *132*(6), 4. doi:10.7237/sjp/268

185. Beljonne, D., Curutchet, C., Scholes, G. D., & Silbey, R. J. (2009). Beyond Förster Resonance Energy Transfer in Biological and Nanoscale Systems. *The Journal of Physical Chemistry B*, *113*(19), 6583–6599. doi:10.1021/jp900708f

186. Ha, T., Enderle, T., Ogletree, D. F., Chemla, D. S., Selvin, P. R., & Weiss, S. (1996). Probing the interaction between two single molecules: fluorescence resonance energy transfer between a single donor and a single acceptor. *Proceedings of the National Academy of Sciences*, *93*(13), 6264–6268. doi:10.1073/pnas.93.13.6264

187. Li, S., Aphale, A. N., MacWan, I. G., Patra, P. K., Gonzalez, W. G., Miksovska, J., & Leblanc, R. M. (2012). Graphene oxide as a quencher for fluorescent assay of amino acids, peptides, and proteins. *ACS Applied Materials and Interfaces*, *4*(12), 7069–7075. doi:10.1021/am302704a

188. Song, E., Cheng, D., Song, Y., Jiang, M., Yu, J., & Wang, Y. (2013). A graphene oxide-based FRET sensor for rapid and sensitive detection of matrix metalloproteinase 2 in human serum sample. *Biosensors and Bioelectronics*, *47*, 445–450. doi:10.1016/j.bios.2013.03.030

189. Dahm, R. (2008). Discovering DNA: Friedrich Miescher and the early years of nucleic acid research. *Human Genetics*. doi:10.1007/s00439-007-0433-0

190. Wengel, J. (2004). Nucleic acid nanotechnology-towards Angstrom-scale engineering. *Organic & biomolecular chemistry*, *2*(3), 277–80. doi:10.1039/b313986g

191. Kjems, J., Elena, F., & Gothelf, K. V. (2003). Nucleic Acid Nanotechnology. *Nucleic Acids and Molecular Biology*. doi:10.1007/978-3-642-38815-6

192. Michelotti, N., Johnson-Buck, A., Manzo, A. J., & Walter, N. G. (2012). Beyond DNA origami: The unfolding prospects of nucleic acid nanotechnology. *Wiley Interdisciplinary Reviews: Nanomedicine and Nanobiotechnology*, *4*(2), 139–152. doi:10.1002/wnan.170

193. Heasman, J. (2002). Morpholino Oligos: Making Sense of Antisense? *Developmental Biology*, *243*(2), 209–214. doi:10.1006/dbio.2001.0565

194. Singh, S. K., Koshkin, A. a., Wengel, J., & Nielsen, P. (1998). LNA (locked nucleic acids): synthesis and high-affinity nucleic acid recognition. *Chemical Communications*, (4), 455–456. doi:10.1039/a708608c

195. Obika, S., Rahman, S. M. A., Fujisaka, A., Kawada, Y., Baba, T., & Imanishi, T. (2010). Bridged nucleic acids: Development, synthesis and properties. *Heterocycles*, *81*(6), 1347–1392. doi:10.3987/REV-10-667

196. Hyrup, B., & Nielsen, P. E. (1996). Peptide Nucleic Acids (PNA): Synthesis, Properties and Potential Applications. *Bioorganic and Medicinal Chemistry*, *4*(1), 5–23. doi:10.1016/0968-0896(95)00171-9

197. Cutler, J. I., Zhang, K., Zheng, D., Auyeung, E., Prigodich, A. E., & Mirkin, C. A. (2011). Polyvalent nucleic acid nanostructures. *Journal of the American Chemical Society*, *133*(24), 9254–9257. doi:10.1021/ja203375n

198. Klussmann, S. (2006). *The Aptamer Handbook: Functional Oligonucleotides and Their Applications*. doi:10.1002/3527608192

199. Wang, K., Tang, Z., Yang, C. J., Kim, Y., Fang, X., Li, W., Wu, Y., Medley, C., Cao, Z., Li, J., Colon, P., Lin H., Tan, W. (2009). Molecular engineering of DNA: Molecular beacons. *Angewandte Chemie - International Edition*, *48*(5), 856–870. doi:10.1002/anie.200800370

200. Bath, J., & Turberfield, A. J. (2007). DNA nanomachines. *Nature Nanotechnology*, *2*(5), 275–284. doi:10.1038/nnano.2007.104

201. Narayan, S. P., Choi, C. H. J., Hao, L., Calabrese, C. M., Auyeung, E., Zhang, C., Goor, O., Mirkin, C. A. (2015). The Sequence-Specific Cellular Uptake of Spherical Nucleic Acid Nanoparticle Conjugates. *Small*, *11*(33), 4173–4182. doi:10.1002/smll.201500027

202. Seeman, N. C. (1982). Nucleic acid junctions and lattices. *Journal of Theoretical Biology*, *99*(2), 237–247. doi:10.1016/0022-5193(82)90002-9

203. Rothemund, P. W. K. (2005). Design of DNA origami. In *IEEE/ACM International Conference on Computer-Aided Design, Digest of Technical Papers, ICCAD* (Vol. 2005, pp. 470–477). doi:10.1109/ICCAD.2005.1560114

204. Dai, G., Lu, X., Chen, Z., Meng, C., Ni, W., & Wang, Q. (2014). DNA origami-directed, discrete three-dimensional plasmonic tetrahedron nanoarchitectures with tailored optical chirality. *ACS Applied Materials and Interfaces*, *6*(8), 5388–5392. doi:10.1021/am501599f

205. Endo, M., Yang, Y., & Sugiyama, H. (2013). DNA origami technology for biomaterials applications. *Biomater. Sci.*, *1*(4), 347–360. doi:10.1039/C2BM00154C

206. De Vries, J. W., Zhang, F., & Herrmann, A. (2013). Drug delivery systems based on nucleic acid nanostructures. *Journal of Controlled Release*, *172*(2), 467–483. doi:10.1016/j.jconrel.2013.05.022

207. Giannetti, A., Tombelli, S., & Baldini, F. (2013). Oligonucleotide optical switches for intracellular sensing Optical Nanosensing in Cells. *Analytical and Bioanalytical Chemistry*. doi:10.1007/s00216-013-7086-8

208. Zeng, Z., Parekh, P., Li, Z., Shi, Z. Z., Tung, C. H., & Zu, Y. (2014). Specific and sensitive tumor imaging using biostable oligonucleotide aptamer probes. *Theranostics*, *4*(9), 945–952. doi:10.7150/thno.9246

209. Yang, C., Lates, V., Prieto-Simón, B., Marty, J. L., & Yang, X. (2012). Aptamer-DNAzyme hairpins for biosensing of Ochratoxin A. *Biosensors and Bioelectronics*, *32*(1), 208–212. doi:10.1016/j.bios.2011.12.011

210. Pei, H., Liang, L., Yao, G., Li, J., Huang, Q., & Fan, C. (2012). Reconfigurable three-dimensional DNA nanostructures for the construction of intracellular logic sensors. *Angewandte Chemie - International Edition*, *51*(36), 9020–9024. doi:10.1002/anie.201202356

211. Modi, S., M. G., S., Goswami, D., Gupta, G. D., Mayor, S., & Krishnan, Y. (2009). A DNA nanomachine that maps spatial and temporal pH changes inside living cells. *Nature Nanotechnology*, *4*(5), 325–330.

doi:10.1038/nnano.2009.83

212. Chen, A. K., Davydenko, O., Behlke, M. A., & Tsourkas, A. (2010). Ratiometric bimolecular beacons for the sensitive detection of RNA in single living cells. *Nucleic acids research*, *38*(14), e148. doi:10.1093/nar/gkq436

213. Mhlanga, M. M., Vargas, D. Y., Fung, C. W., Kramer, F. R., & Tyagi, S. (2005). tRNA-linked molecular beacons for imaging mRNAs in the cytoplasm of living cells. *Nucleic Acids Research*, *33*(6), 1902–1912. doi:10.1093/nar/gki302

214. Tsourkas, A., Behlke, M. A., & Bao, G. (2002). Hybridization of 2′-O-methyl and 2-deoxy molecular beacons to RNA and DNA targets. *Nucleic Acids Research*. doi:10.1093/nar/gkf635

215. Elsabahy, M., Nazarali, A., & Foldvari, M. (2011). Non-Viral Nucleic Acid Delivery: Key Challenges and Future Directions. *Current Drug Delivery*, *8*(3), 235–244. doi:10.2174/156720111795256174

216. Xu, L., & Anchordoquy, T. (2011). Drug delivery trends in clinical trials and translational medicine: Challenges and opportunities in the delivery of nucleic acid-based therapeutics. *Journal of Pharmaceutical Sciences*, *100*(1), 38–52. doi:10.1002/jps.22243

217. Banga, R. J., Chernyak, N., Narayan, S. P., Nguyen, S. T., & Mirkin, C. A. (2014). Liposomal spherical nucleic acids. *Journal of the American Chemical Society*, *136*(28), 9866–9869. doi:10.1021/ja504845f

218. Choi, C. H. J., Hao, L., Narayan, S. P., Auyeung, E., & Mirkin, C. A. (2013). Mechanism for the endocytosis of spherical nucleic acid nanoparticle conjugates. *Proceedings of the National Academy of Sciences*, *110*(19), 7625–7630. doi:10.1073/pnas.1305804110

219. Zhao, M., Hu, B., Gu, Z., Joo, K. Il, Wang, P., & Tang, Y. (2013). Degradable polymeric nanocapsule for efficient intracellular delivery of a high molecular weight tumor-selective protein complex. *Nano Today*, *8*(1), 11–20. doi:10.1016/j.nantod.2012.12.003

220. Hoffmann, P. J. (1981). Mechanism of degradation of duplex DNA by the DNase induced by herpes simplex virus. *Journal of virology*, *38*(3), 1005–14. Retrieved from http://www.ncbi.nlm.nih.gov/pubmed/6264148

221. Monia, B. P., Johnston, J. F., Sasmor, H., & Cummins, L. L. (1996). Nuclease resistance and antisense activity of modified oligonucleotides targeted to Ha-ras. *Journal of Biological Chemistry*, *271*(24), 14533–14540. doi:10.1074/jbc.271.24.14533

222. Evans, C. J., & Aguilera, R. J. (2003). DNase II: Genes, enzymes and function. *Gene*. doi:10.1016/j.gene.2003.08.022

223. Frazão, C., McVey, C. E., Amblar, M., Barbas, A., Vonrhein, C., Arraiano, C. M., & Carrondo, M. A. (2006). Unravelling the dynamics of RNA degradation by ribonuclease II and its RNA-bound complex. *Nature*, *443*(7107), 110–114. doi:10.1038/nature05080

224. Hernandez, F. J., Stockdale, K. R., Huang, L., Horswill, A. R., Behlke, M. A., & McNamara, J. O. (2012). Degradation of Nuclease-Stabilized RNA Oligonucleotides in Mycoplasma-Contaminated Cell Culture Media. *Nucleic Acid Therapeutics (Formerly Oligonucleotides)*, 120109070352007. doi:10.1089/nat.2011.0316

225. Varkouhi, A. K., Scholte, M., Storm, G., & Haisma, H. J. (2011). Endosomal escape pathways for delivery of biologicals. *Journal of Controlled Release*. doi:10.1016/j.jconrel.2010.11.004

226. Martens, T. F., Remaut, K., Demeester, J., De Smedt, S. C., & Braeckmans, K. (2014). Intracellular delivery of nanomaterials: How to catch endosomal escape in the act. *Nano Today*, *9*(3), 344–364. doi:10.1016/j.nantod.2014.04.011

227. Juliano, R. L., & Carver, K. (2015). Cellular uptake and intracellular trafficking of oligonucleotides. *Advanced Drug Delivery Reviews*. doi:10.1016/j.addr.2015.04.005

228. Samanta, A., & Medintz, I. L. (2016). Nanoparticles and DNA – a powerful and growing functional combination in bionanotechnology. *Nanoscale*, *8*(17), 9037–9095. doi:10.1039/C5NR08465B

229. Zhong, W. (2009). Nanomaterials in fluorescence-based biosensing. *Analytical and Bioanalytical Chemistry*. doi:10.1007/s00216-009-2643-x

230. Sperling, R. a, & Parak, W. J. (2010). Surface modification, functionalization and bioconjugation of colloidal inorganic nanoparticles. *Philosophical transactions. Series A, Mathematical, physical, and engineering sciences*, *368*(1915), 1333–1383. doi:10.1098/rsta.2009.0273

231. Zhang, J., Song, S., Wang, L., Pan, D., & Fan, C. (2007). A gold nanoparticle-based chronocoulometric DNA sensor for amplified detection of DNA. *Nature Protocols*, *2*(11), 2888–2895. doi:10.1038/nprot.2007.419

232. Macfarlane, R. J., Lee, B., Jones, M. R., Harris, N., Schatz, G. C., & Mirkin, C. A. (2011). Nanoparticle Superlattice Engineering with DNA. *Science*, *334*(6053), 204–208. doi:10.1126/science.1210493

233. Mucic, R. C., Storhoff, J. J., Mirkin, C. A., & Letsinger, R. L. (1998). DNA-directed synthesis of binary nanoparticle network materials [5]. *Journal of the American Chemical Society*. doi:10.1021/ja982721s

234. Demers, L. M., Mirkin, C. A., Mucic, R. C., Reynolds, R. A., Letsinger, R. L., Elghanian, R., & Viswanadham, G. (2000). Based Method for Determining the Surface Coverage and Hybridization Efficiency of Thiol - Capped Oligonucleotides Bound to Gold Thin Films and Nanoparticles. *Analytical Chemistry*, *72*(22), 5535–5541.

235. Lee, J. S., Han, M. S., & Mirkin, C. A. (2007). Colorimetric detection of mercuric ion (Hg2+) in aqueous media using DNA-functionalized gold nanoparticles. *Angewandte Chemie - International Edition*, *46*(22), 4093–4096. doi:10.1002/anie.200700269

236. Xu, X., Daniel, W. L., Wei, W., & Mirkin, C. A. (2010). Colorimetric Cu2+ detection using DNA-modified gold-nanoparticle aggregates as probes and click chemistry. *Small*, *6*(5), 623–626. doi:10.1002/smll.200901691

237. Zhao, W., Chiuman, W., Brook, M. A., & Li, Y. (2007). Simple and rapid colorimetric biosensors based on DNA aptamer and noncrosslinking gold nanoparticle aggregation. *ChemBioChem*, *8*(7), 727–731. doi:10.1002/cbic.200700014

238. Liu, P., Yang, X., Sun, S., Wang, Q., Wang, K., Huang, J., Liu, J., He, L. (2013). Enzyme-Free Colorimetric Detection of DNA by Using Gold Nanoparticles and Hybridization Chain Reaction Amplification. *Analytical Chemistry*, *85*(16), 7689–7695. doi:10.1021/ac4001157

239. Jae-Seung Lee, Pirmin A. Ulmann, Min Su Han, Mirkin, C. A. (2008). A DNA−Gold Nanoparticle-Based Colorimetric Competition Assay for the Detection of Cysteine. doi:10.1021/NL0727563

240. Li, B., Du, Y., Dong, S. (2009). DNA based gold nanoparticles colorimetric sensors for sensitive and selective detection of Ag(I) ions. *Analytica Chimica Acta*, *644*(1–2), 78–82. doi:10.1016/j.aca.2009.04.022

241. Li, N., Chang, C., Pan, W., & Tang, B. (2012). A Multicolor Nanoprobe for Detection and Imaging of Tumor-Related mRNAs in Living Cells. *Angewandte Chemie International Edition*, *51*(30), 7426–7430. doi:10.1002/anie.201203767

242. Rosi, N. L., Giljohann, D. A., Thaxton, C. S., Lytton-Jean, A. K. R., Han, M. S., Mirkin, C. A.. (2006). Oligonucleotide-Modified Gold Nanoparticles for Intracellular Gene Regulation. *Science*, *312*(5776), 1027–1030. doi:10.1126/science.1125559

243. Qiao, G., Gao, Y., Li, N., Yu, Z., Zhuo, L., & Tang, B. (2011). Simultaneous detection of intracellular tumor mRNA with bi-color imaging based on a gold nanoparticle/molecular beacon. *Chemistry - A European Journal*, *17*(40), 11210–11215. doi:10.1002/chem.201100658

244. Prigodich, A. E., Randeria, P. S., Briley, W. E., Kim, N. J., Daniel, W. L., Giljohann, D. A., & Mirkin, C. A. (2012). Multiplexed nanoflares: MRNA detection in live cells. *Analytical Chemistry*, *84*(4), 2062–2066. doi:10.1021/ac202648w

245. Luan, M., Li, N., Pan, W., Yang, L., Yu, Z., Tang, B., (2017). Simultaneous detection of multiple targets involved in the PI3K/AKT pathway for investigating cellular migration and invasion with a multicolor fluorescent nanoprobe. *Chem. Commun.*, *53*(2), 356–359. doi:10.1039/C6CC07605J

246. Kim, H. J., Takemoto, H., Yi, Y., Zheng, M., Maeda, Y., Chaya, H., Hayashi, K., Mi, P., Pittella, F., Christie, R., Toh, K., Matsumoto, Y., Nishiyama, N., Miyata, K., Kataoka, K. (2014). Precise engineering of siRNA delivery vehicles to tumors using polyion complexes and gold nanoparticles. *ACS Nano*, *8*(9), 8979–8991. doi:10.1021/nn502125h

247. Kayal, S., & Ramanujan, R. V. (2009). Anti-Cancer Drug Loaded Iron–Gold Core–Shell Nanoparticles (Fe@Au) for Magnetic Drug Targeting. *Journal of Nanoscience and Nanotechnology*, *10*(xx), 1–13. doi:10.1166/jnn.2010.2461

248. Massich, M. D., Giljohann, D. A., Schmucker, A. L., Patel, P. C., & Mirkin, C. a. (2010). Cellular response of polyvalent oligonucleotide-gold nanoparticle conjugates. *ACS nano*, *4*(10), 5641–5646. doi:10.1021/nn102228s

249. Randeria, P. S., Briley, W. E., Chinen, A. B., Guan, C. M., Petrosko, S. H., & Mirkin, C. A. (2015). Nanoflares as probes for cancer diagnostics. *Cancer Treatment and Research*, *166*, 1–22. doi:10.1007/978-3-319-16555-4_1

250. Cutler, J. I., Auyeung, E., & Mirkin, C. A. (2012). Spherical Nucleic Acids (SNAs). *Journal of the American Chemical Society*, *134*, 1376–1391. doi:10.1021/ja209351u

251. Young, K. L., Scott, A. W., Hao, L., Mirkin, S. E., Liu, G., & Mirkin, C. A. (2012). Hollow spherical nucleic acids for intracellular gene regulation based upon biocompatible silica shells. *Nano Letters*, *12*(7), 3867–3871. doi:10.1021/nl3020846

252. Heuer-Jungemann, A., El-Sagheer, A. H., Lackie, P. M., Brown, T., & Kanaras, A. G. (2016). Selective killing of cells triggered by their mRNA signature in the presence of smart nanoparticles. *Nanoscale*, *8*(38), 16857–16861. JOUR. doi:10.1039/C6NR06154K

253. Rosi, N. L., Giljohann, D. a, Thaxton, C. S., Lytton-Jean, A. K. R., Han, M. S., & Mirkin, C. a. (2006). Oligonucleotide-modified gold nanoparticles for intracellular gene regulation. *Science (New York, N.Y.)*, *312*(5776), 1027–1030. doi:10.1126/science.1125559

254. Kim, D. H., & Rossi, J. J. (2008). RNAi mechanisms and applications. *BioTechniques*. doi:10.2144/000112792

255. Ghosh, P. S., Kim, C. K., Han, G., Forbes, N. S., & Rotello, V. M. (2008). Efficient gene delivery vectors by tuning the surface charge density of amino acid-functionalized gold nanoparticles. *ACS Nano*, *2*(11), 2213–2218. doi:10.1021/nn800507t

256. Rhim, W. K., Kim, J. S., & Nam, J. M. (2008). Lipid-gold-nanoparticle hybrid-based gene delivery. *Small*, *4*(10), 1651–1655. doi:10.1002/smll.200800628

257. Elbakry, A., Zaky, A., Liebl, R., Rachel, R., Goepferich, A., & Breunig, M. (2009). Layer-by-layer assembled gold nanoparticles for sirna delivery. *Nano Letters*, *9*(5), 2059–2064. doi:10.1021/nl9003865

258. Kim, S. T., Chompoosor, A., Yeh, Y. C., Agasti, S. S., Solfiell, D. J., & Rotello, V. M. (2012). Dendronized gold nanoparticles for siRNA delivery. *Small*, *8*(21), 3253–3256. doi:10.1002/smll.201201141

259. Reynolds, J. L., Law, W. C., Mahajan, S. D., Aalinkeel, R., Nair, B., Sykes, D. E., Yong, K. T., Hui R., Prasad, P. N., Schwartz, S. A. (2012). Nanoparticle based galectin-1 gene silencing, implications in methamphetamine regulation

of HIV-1 infection in monocyte derived macrophages. *Journal of neuroimmune pharmacology : the official journal of the Society on NeuroImmune Pharmacology*, *7*(3), 673–85. doi:10.1007/s11481-012-9379-7

260. Wang, X.-Q., Lee, S., Wilson, H., Seeger, M., Iordanov, H., Gatla, N., Whittington, A., Bach, D., Lu, J., Paller, A. S. (2013). Ganglioside GM3 Depletion Reverses Impaired Wound Healing in Diabetic Mice by Activating IGF-1 and Insulin Receptors. *The Journal of investigative dermatology*, *134*(5), 1–10. doi:10.1038/jid.2013.532

261. X., L. (2008). Upconversion Multicolor Fine-Tuning: Visible to Near-Infrared Emission from Lanthanide-Doped NaYF4 Nanoparticles. *J. Am. Chem. Soc.*, *130*, 5642.

262. Muhr, V., Wilhelm, S., Hirsch, T., & Wolfbeis, O. S. (2014). Upconversion nanoparticles: From hydrophobic to hydrophilic surfaces. *Accounts of Chemical Research*, *47*(12), 3481–3493. doi:10.1021/ar500253g

263. Wang, L., Yan, R., Huo, Z., Wang, L., Zeng, J., Bao, J., Wang, X., Peng, Q., Li, Y. (2005). Fluorescence Resonant Energy Transfer Biosensor Based on Upconversion-Luminescent Nanoparticles. *Angewandte Chemie International Edition*, *44*(37), 6054–6057. doi:10.1002/anie.200501907

264. Wang, M., Hou, W., Mi, C.-C., Wang, W.-X., Xu, Z.-R., Teng, H.-H., Mao, C., Xu, S.-K. (2009). Immunoassay of Goat Antihuman Immunoglobulin G Antibody Based on Luminescence Resonance Energy Transfer between Near-Infrared Responsive $NaYF_4$:Yb, Er Upconversion Fluorescent Nanoparticles and Gold Nanoparticles. *Analytical Chemistry*, *81*(21), 8783–8789. doi:10.1021/ac901808q

265. Zhang, S.-Z., Sun, L.-D., Tian, H., Liu, Y., Wang, J.-F., & Yan, C.-H. (2009). Reversible luminescence switching of NaYF4:Yb,Er nanoparticles with controlled assembly of gold nanoparticles. *Chemical Communications*, (18), 2547. doi:10.1039/b823453a

266. Zhang, P., Rogelj, S., Nguyen, K., Wheeler, D. (2006). Design of a Highly Sensitive and Specific Nucleotide Sensor Based on Photon Upconverting Particles. doi:10.1021/JA0644024

267. Kumar, M., & Zhang, P. (2009). Highly sensitive and selective label-free optical detection of DNA hybridization based on photon upconverting nanoparticles. *Langmuir*, *25*(11), 6024–6027. doi:10.1021/la900936p

268. Jin, B., Wang, S., Lin, M., Jin, Y., Zhang, S., Cui, X., Gong, Y., Li, A., Xu, F., Lu, T. J. (2017). Upconversion nanoparticles based FRET aptasensor for rapid and ultrasenstive bacteria detection. *Biosensors and Bioelectronics*, *90*, 525–533. doi:10.1016/j.bios.2016.10.029

269. Li, S., Xu, L., Ma, W., Wu, X., Sun, M., Kuang, H., Wang, L., Kotov, N., Xu, C. (2016). Dual-Mode Ultrasensitive Quantification of MicroRNA in Living Cells by Chiroplasmonic Nanopyramids Self-Assembled from Gold and Upconversion Nanoparticles. *Journal of the American Chemical Society*,

138(1), 306–312. doi:10.1021/jacs.5b10309

270. Li, L., Hao, P., Wei, P., Fu, L., Ai, X., Zhang, J., & Zhou, J. (2017). DNA-assisted upconversion nanoplatform for imaging-guided synergistic therapy and laser-switchable drug detoxification. *Biomaterials*, *136*, 43–55. doi:10.1016/j.biomaterials.2017.05.006

271. Wu, M., Kempaiah, R., Huang, P. J. J., Maheshwari, V., & Liu, J. (2011). Adsorption and desorption of DNA on graphene oxide studied by fluorescently labeled oligonucleotides. *Langmuir*, *27*(6), 2731–2738. doi:10.1021/la1037926

272. Dong, H., Zhang, J., Ju, H., Lu, H., Wang, S., Jin, S., Hao, K., Du, H., Zhang, X. (2012). Highly sensitive multiple microRNA detection based on fluorescence quenching of graphene oxide and isothermal strand-displacement polymerase reaction. *Analytical Chemistry*, *84*(10), 4587–4593. doi:10.1021/ac300721u

273. Zhou, J., Xu, X., Liu, W., Liu, X., Nie, Z., Qing, M., Nie, L., Yao, S. (2013). Graphene oxide-peptide nanocomplex as a versatile fluorescence probe of protein kinase activity based on phosphorylation protection against carboxypeptidase digestion. *Analytical Chemistry*, *85*(12), 5746–5754. doi:10.1021/ac400336u

274. Li, W., Wu, P., Zhang, H., & Cai, C. (2012). Signal amplification of graphene oxide combining with restriction endonuclease for site-specific determination of DNA methylation and assay of methyltransferase activity. *Analytical Chemistry*, *84*(17), 7583–7590. doi:10.1021/ac301990f

275. Huang, J., Gao, X., Jia, J., Kim, J. K., & Li, Z. (2014). Graphene oxide-based amplified fluorescent biosensor for Hg2+ detection through hybridization chain reactions. *Analytical Chemistry*, *86*(6), 3209–3215. doi:10.1021/ac500192r

276. Wen, Y., Xing, F., He, S., Song, S., Wang, L., Long, Y., Li, D., Fan, C. (2010). A graphene-based fluorescent nanoprobe for silver(i) ions detection by using graphene oxide and a silver-specific oligonucleotide. *Chemical Communications*, *46*(15), 2596. doi:10.1039/b924832c

277. Zhou, L., Shen, Q., Zhao, P., Xiang, B., Nie, Z., Huang, Y., & Yao, S. (2013). Fluorescent detection of copper(II) based on DNA-templated click chemistry and graphene oxide. *Methods*, *64*(3), 299–304. doi:10.1016/j.ymeth.2013.09.001

278. Qiu, L., Zhou, H., Zhu, W., Qiu, L., Jiang, J., Shen, G., & Yu, R. (2013). A novel label-free fluorescence aptamer-based sensor method for cocaine detection based on isothermal circular strand-displacement amplification and graphene oxide absorption. *New Journal of Chemistry*, *37*(12), 3998. doi:10.1039/c3nj00594a

279. Dong, H., Gao, W., Yan, F., Ji, H., & Ju, H. (2010). Fluorescence resonance energy transfer between quantum dots and graphene oxide for sensing biomolecules. *Analytical Chemistry*, *82*(13), 5511–5517.

doi:10.1021/ac100852z

280. Li, C., Wei, L., Liu, X., Lei, L., & Li, G. (2014). Ultrasensitive detection of lead ion based on target induced assembly of DNAzyme modified gold nanoparticle and graphene oxide. *Analytica Chimica Acta*, *831*, 60–64. doi:10.1016/j.aca.2014.05.001

281. Lin, X., Cui, L., Huang, Y., Lin, Y., Xie, Y., Zhu, Z., Yin, B., Chen, X., Yang, C. J. (2014). Carbon nanoparticle-protected aptamers for highly sensitive and selective detection of biomolecules based on nuclease-assisted target recycling signal amplification. *Chemical Communications*, *50*(57), 7646. doi:10.1039/c4cc02184c

282. Huang, X., Liang, Y., Ruan, L., & Ren, J. (2014). Chemiluminescent detection of cell apoptosis enzyme by gold nanoparticle-based resonance energy transfer assay. *Analytical and Bioanalytical Chemistry*, *406*(23), 5677–5684. doi:10.1007/s00216-013-7611-9

283. Rasheeda, P. A. and Sandhyarani, N.(2015). A highly sensitive DNA sensor for attomolar detection of the BRCA1 gene: signal amplification with gold nanoparticle clusters. *The Analyst*, *140*(8), 2713–2718. doi:10.1039/C5AN00004A

284. Wang, Y., Li, M., Zhu, Y., Ge, S., Yu, J., Yan, M., Song, X. (2013). A visible light photoelectrochemical sensor for tumor marker detection using tin dioxide quantum dot?graphene as labels. *The Analyst*, *138*(23), 7112. doi:10.1039/c3an01410j

285. Venus, M., Waterman, J., & McNab, I. (2011). Basic physiology of the skin. *Surgery*, *29*(10), 471–474. doi:10.1016/j.mpsur.2011.06.010

286. Gantwerker, E. A., & Hom, D. B. (2012). Skin: Histology and physiology of wound healing. *Clinics in Plastic Surgery*. doi:10.1016/j.cps.2011.09.005

287. Singer, A. J., & Clark, R. A. (1999). Cutaneous wound healing. *The New England journal of medicine*, *341*(10), 738–46. doi:10.1056/NEJM199909023411006

288. Martin, P. (1997). Wound healing--aiming for perfect skin regeneration. *Science (New York, N.Y.)*, *276*(5309), 75–81. doi:10.1126/science.276.5309.75

289. Faler, B. J., Macsata, R. A., Plummer, D., Mishra, L., & Sidawy, A. N. (2006). Transforming growth factor-beta and wound healing. *Perspectives in vascular surgery and endovascular therapy*, *18*(1), 55–62. Retrieved from http://www.ncbi.nlm.nih.gov/pubmed/16628336

290. Werner, S., & Grose, R. (2003). Regulation of wound healing by growth factors and cytokines. *Physiological reviews*, *83*(3), 835–870. doi:10.1152/physrev.00031.2002

291. Klass, B. R., Grobbelaar, A. O., & Rolfe, K. J. (2009). Transforming growth factor beta1 signalling, wound healing and repair: a multifunctional cytokine

with clinical implications for wound repair, a delicate balance. *Postgraduate medical journal*, *85*(999), 9–14. doi:10.1136/pgmj.2008.069831

292. Leask, A. (2004). TGF-Beta signaling and the fibrotic response. *The FASEB Journal*, *18*(7), 816–827. doi:10.1096/fj.03-1273rev

293. Meng, X. M., Huang, X. R., Chung, A. C. K., Qin, W., Shao, X., Igarashi, P., Ju, W., Bottinger, E., Lan, H. Y. (2010). Smad2 protects against TGF-beta/Smad3-mediated renal fibrosis. *Journal of the American Society of Nephrology : JASN*, *21*(9), 1477–1487. doi:10.1681/ASN.2009121244

294. Derynck, R., & Zhang, Y. E. (2003). Smad-dependent and Smad-independent pathways in TGF-beta family signalling. *Nature*, *425*(6958), 577–584. doi:10.1038/nature02006

295. Cheng, E., Souza, R. F., & Spechler, S. J. (2012). Tissue remodeling in eosinophilic esophagitis. *American Journal of Physiology - Gastrointestinal and Liver Physiology*, *303*(11). Retrieved from http://ajpgi.physiology.org/content/303/11/G1175

296. Zi, Z., Chapnick, D. A., & Liu, X. (2012). Dynamics of TGF-β/Smad signaling. *FEBS letters*, *586*(14), 1921–8. doi:10.1016/j.febslet.2012.03.063

297. Ashcroft, G. S., Yang, X., Glick, A. B., Weinstein, M., Letterio, J. L., Mizel, D. E., Anzano, M., Greenwell-Wild, T., Wahl, S., Deng, C., Roberts, A. B. (1999). Mice lacking Smad3 show accelerated wound healing and an impaired local inflammatory response. *Nature cell biology*, *1*(5), 260–6. doi:10.1038/12971

298. Tomikawa, K., Yamamoto, T., Shiomi, N., Shimoe, M., Hongo, S., Yamashiro, K., Yamaguchi, T., Maeda, H., Takashiba, S. (2012). Smad2 Decelerates Re-epithelialization during Gingival Wound Healing. *Journal of Dental Research*, *91*(8), 764–770. doi:10.1177/0022034512451449

299. Okan, D., Woo, K., Ayello, E. a, & Sibbald, G. (2007). The role of moisture balance in wound healing. *Advances in skin & wound care*, *20*(1), 39-53–5. doi:10.1097/00129334-200701000-00014

300. Boateng, J. S., Matthews, K. H., Stevens, H. N. E., & Eccleston, G. M. (2008). Wound healing dressings and drug delivery systems: A review. *Journal of Pharmaceutical Sciences*. doi:10.1002/jps.21210

301. Jeschke, M. G., Richter, G., Höfstädter, F., Herndon, D. N., Perez-Polo, J.-R., Jauch, K.-W. (2002). Non-viral liposomal keratinocyte growth factor (KGF) cDNA gene transfer improves dermal and epidermal regeneration through stimulation of epithelial and mesenchymal factors. *Gene therapy*, *9*(16), 1065–1074. doi:10.1038/sj.gt.3301732

302. Pereira, C. T., Herndon, D. N., Rocker, R., & Jeschke, M. G. (2007). Liposomal Gene Transfer of Keratinocyte Growth Factor Improves Wound Healing by Altering Growth Factor and Collagen Expression. *Journal of Surgical Research*, *139*(2), 222–228. doi:10.1016/j.jss.2006.09.005

303. Bonferoni, M. C., Sandri, G., Dellera, E., Rossi, S., Ferrari, F., Mori, M., &

Caramella, C. (2014). Ionic polymeric micelles based on chitosan and fatty acids and intended for wound healing. Comparison of linoleic and oleic acid. *European Journal of Pharmaceutics and Biopharmaceutics*, *87*(1), 101–106. doi:10.1016/j.ejpb.2013.12.018

304. Küchler, S., Wolf, N. B., Heilmann, S., Weindl, G., Helfmann, J., Yahya, M. M., Stein, C., Schäfer-Korting, M. (2010). 3D-Wound healing model: Influence of morphine and solid lipid nanoparticles. *Journal of Biotechnology*, *148*(1), 24–30. doi:10.1016/j.jbiotec.2010.01.001

305. Nelson, C. E., Gupta, M. K., Adolph, E. J., Guelcher, S. A., & Duvall, C. L. (2013). siRNA Delivery from an Injectable Scaffold for Wound Therapy. *Advances in Wound Care*, *2*(3), 93–99. doi:10.1089/wound.2011.0327

306. Banerjee, J., & Sen, C. K. (2015). microRNA and Wound Healing. In *Advances in Experimental Medicine and Biology* (Vol. 888, pp. 291–305). doi:10.1007/978-3-319-22671-2_15

307. Petrie, N. C., Yao, F., & Eriksson, E. (2003). Gene therapy in wound healing. *The Surgical clinics of North America*, *83*(3), 597–616, vii. doi:10.1016/S0039-6109(02)00194-9

308. Kalashnikova, I., Das, S., & Seal, S. (2015). Nanomaterials for wound healing: Scope and advancement. *Nanomedicine*, *10*(16), 2593–2612. doi:http://dx.doi.org/10.2217/nnm.15.82

309. Tocco, I., Zavan, B., Bassetto, F., & Vindigni, V. (2012). Nanotechnology-based therapies for skin wound regeneration. *Journal of Nanomaterials*. doi:10.1155/2012/714134

310. Abedini, F., Ahmadi, A., Yavari, A., Hosseini, V., & Mousavi, S. (2013). Comparison of silver nylon wound dressing and silver sulfadiazine in partial burn wound therapy. *International Wound Journal*, *10*(5), 573–578. doi:10.1111/j.1742-481X.2012.01024.x

311. Maneerung, T., Tokura, S., & Rujiravanit, R. (2008). Impregnation of silver nanoparticles into bacterial cellulose for antimicrobial wound dressing. *Carbohydrate Polymers*, *72*(1), 43–51. doi:10.1016/j.carbpol.2007.07.025

312. Cady, N. C., Behnke, J. L., & Strickland, A. D. (2011). Copper-based nanostructured coatings on natural cellulose: Nanocomposites exhibiting rapid and efficient inhibition of a multi-drug resistant wound pathogen, A. baumannii, and mammalian cell biocompatibility in vitro. *Advanced Functional Materials*, *21*(13), 2506–2514. doi:10.1002/adfm.201100123

313. Cioffi, N., Torsi, L., Ditaranto, N., Tantillo, G., Ghibelli, L., Sabbatini, L., Bleve-Zachio, T., D'Alessio, M., Zambonin, G., Traversa, E. (2005). Copper nanoparticle/polymer composites with antifungal and bacteriostatic properties. *Chemistry of Materials*, *17*(21), 5255–5262. doi:10.1021/cm0505244

314. Jones, N., Ray, B., Ranjit, K. T., & Manna, A. C. (2008). Antibacterial activity

of ZnO nanoparticle suspensions on a broad spectrum of microorganisms. *FEMS Microbiology Letters*, *279*(1), 71–76. doi:10.1111/j.1574-6968.2007.01012.x

315. Sankar, R., Dhivya, R., Shivashangari, K. S., & Ravikumar, V. (2014). Wound healing activity of Origanum vulgare engineered titanium dioxide nanoparticles in Wistar Albino rats. *Journal of Materials Science: Materials in Medicine*, *25*(7), 1701–1708. doi:10.1007/s10856-014-5193-5

316. Janib, S. M., Moses, A. S., & MacKay, J. A. (2010). Imaging and drug delivery using theranostic nanoparticles. *Advanced Drug Delivery Reviews*. doi:10.1016/j.addr.2010.08.004

317. Park, M. V. D. Z., Neigh, A. M., Vermeulen, J. P., de la Fonteyne, L. J. J., Verharen, H. W., Briedé, J. J., van Loveren, H., de Jong, W. H. (2011). The effect of particle size on the cytotoxicity, inflammation, developmental toxicity and genotoxicity of silver nanoparticles. *Biomaterials*, *32*(36), 9810–9817. doi:10.1016/j.biomaterials.2011.08.085

318. Gaetke, L. M., & Chow, C. K. (2003). Copper toxicity, oxidative stress, and antioxidant nutrients. *Toxicology*. doi:10.1016/S0300-483X(03)00159-8

319. Li, S. Q., Zhu, R. R., Zhu, H., Xue, M., Sun, X. Y., Yao, S. De, & Wang, S. L. (2008). Nanotoxicity of TiO2 nanoparticles to erythrocyte in vitro. *Food and Chemical Toxicology*, *46*(12), 3626–3631. doi:10.1016/j.fct.2008.09.012

320. Zhao, X., Wang, S., Wu, Y., You, H., & Lv, L. (2013). Acute ZnO nanoparticles exposure induces developmental toxicity, oxidative stress and DNA damage in embryo-larval zebrafish. *Aquatic Toxicology*, *136–137*, 49–59. doi:10.1016/j.aquatox.2013.03.019

321. Leu, J. G., Chen, S. A., Chen, H. M., Wu, W. M., Hung, C. F., Yao, Y. D., Tu, C. S., Liang, Y. J. (2012). The effects of gold nanoparticles in wound healing with antioxidant epigallocatechin gallate and α-lipoic acid. *Nanomedicine: Nanotechnology, Biology, and Medicine*, *8*(5), 767–775. doi:10.1016/j.nano.2011.08.013

322. Akturk, O., Kismet, K., Yasti, A. C., Kuru, S., Duymus, M. E., Kaya, F., Caydere, M., Hucumenoglu, S., Keskin, D. (2016). Collagen/gold nanoparticle nanocomposites: A potential skin wound healing biomaterial. *Journal of Biomaterials Applications*, *31*(2), 283–301. doi:10.1177/0885328216644536

323. Randeria, P. S., Seeger, M. A., Wang, X.-Q., Wilson, H., Shipp, D., Mirkin, C. A., & Paller, A. S. (2015). siRNA-based spherical nucleic acids reverse impaired wound healing in diabetic mice by ganglioside GM3 synthase knockdown. *Proceedings of the National Academy of Sciences of the United States of America*, *112*(18), 5573–8. doi:10.1073/pnas.1505951112

324. Strimbu, K., & Tavel, J. A. (2010). What are biomarkers? *Current opinion in HIV and AIDS*, *5*(6), 463–6. doi:10.1097/COH.0b013e32833ed177

325. Natesan, M., & Ulrich, R. G. (2010). Protein microarrays and biomarkers of infectious disease. *International Journal of Molecular Sciences*.

doi:10.3390/ijms11125165

326. Santi, A., Duarte, M. M. M. F., Moresco, R. N., Menezes, C., Bagatini, M. D., Schetinger, M. R. C., & Loro, V. L. (2010). Association between thyroid hormones, lipids and oxidative stress biomarkers in overt hypothyroidism. *Clinical Chemistry and Laboratory Medicine*, *48*(11), 1635–1639. doi:10.1515/CCLM.2010.309

327. Nilsson, R. J. A., Balaj, L., Hulleman, E., Van Rijn, S., Pegtel, D. M., Walraven, M., Widmark, A., Gerritsen, W. R., Verheul, H. M., Vandertop, W. P., Noske, D. P., Skog, J., Würdinger, T. (2011). Blood platelets contain tumor-derived RNA biomarkers. *Blood*, *118*(13), 3680–3683. doi:10.1182/blood-2011-03-344408

328. Albert, M. A. (2011). Biomarkers and heart disease. *Journal of Clinical Sleep Medicine*. doi:10.5664/JCSM.1342

329. Chang, S.-H., Worley, L. A., Onken, M. D., & Harbour, J. W. (2008). Prognostic biomarkers in uveal melanoma: evidence for a stem cell-like phenotype associated with metastasis. *Melanoma Research*, *18*(3), 191–200. doi:10.1097/CMR.0b013e3283005270

330. Gerszten, R. E., & Wang, T. J. (2008). The search for new cardiovascular biomarkers. *Nature*, *451*(7181), 949–952. doi:10.1038/nature06802

331. Henry, N. L., & Hayes, D. F. (2012). Cancer biomarkers. *Molecular Oncology*. doi:10.1016/j.molonc.2012.01.010

332. Kaufman, B., Shapira-Frommer, R., Schmutzler, R. K., Audeh, M. W., Friedlander, M., Balmaña, J., Mitchell, G., Fried, G., Stemmer, S. M., Hubert, A., Rosengarten, O., Steiner, M., Loman, N., Bowen, K., Fielding, A. Domchek, S. M. (2015). Olaparib monotherapy in patients with advanced cancer and a germline BRCA1/2 mutation. *Journal of clinical oncology : official journal of the American Society of Clinical Oncology*, *33*(3), 244–50. doi:10.1200/JCO.2014.56.2728

333. Lin, L., Asthana, S., Chan, E., Bandyopadhyay, S., Martins, M. M., Olivas, V.,Yan, J., Pham, L., Wang, M., Bollag, G., Solit, D., Collisson, E., Rudin, C., Taylor, B., Bivona, T. G. (2014). Mapping the molecular determinants of BRAF oncogene dependence in human lung cancer. *Proceedings of the National Academy of Sciences*, *111*(7), E748–E757. doi:10.1073/pnas.1320956111

334. Gohring, J. T., Dale, P. S., & Fan, X. (2010). Detection of HER2 breast cancer biomarker using the opto-fluidic ring resonator biosensor. *Sensors and Actuators, B: Chemical*, *146*(1), 226–230. doi:10.1016/j.snb.2010.01.067

335. Ray, S., Reddy, P. J., Choudhary, S., Raghu, D., & Srivastava, S. (2011). Emerging nanoproteomics approaches for disease biomarker detection: A current perspective. *Journal of Proteomics*. doi:10.1016/j.jprot.2011.04.027

336. Zhao, J., Paganini, L., Mucke, L., Gordon, M., Refolo, L., Carman, M., Sinha, S., Oltersdorf, T., Lieberburg, I., McConlogue, L. (1996). Beta-secretase

processing of the beta-amyloid precursor protein in transgenic mice is efficient in neurons but inefficient in astrocytes. *The Journal of biological chemistry*, *271*(49), 31407–31411. doi: 10.1074/jbc.271.49.31407

337. Citron, M., Teplow, D. B., & Selkoe, D. J. (1995). Generation of amyloid β protein from its precursor is sequence specific. *Neuron*, *14*(3), 661–670. doi:10.1016/0896-6273(95)90323-2

338. Vassar, R. (1999). Beta-Secretase Cleavage of Alzheimer's Amyloid Precursor Protein by the Transmembrane Aspartic Protease BACE. *Science*, *286*(5440), 735–741. doi:10.1126/science.286.5440.735

339. Yan, R., Bienkowski, M. J., Shuck, M. E., Miao, H., Tory, M. C., Pauley, A., M., Brashler, J. R., Stratman, N. C., Mathews, W. R., Buhl, A. E., Carter, D. B., Tomasselli, A. G., Parodi, L., A., Heinrikson, R. L., Gurney, M. E. (1999). Membrane-anchored aspartyl protease with Alzheimer's disease beta-secretase activity. *Nature*, *402*(6761), 533–7. doi:10.1038/990107

340. Li, Q. M., & Sudhof, T. C. (2004). Cleavage of amyloid-beta precursor protein and amyloid-beta precursor-like protein by BACE 1. *Journal of Biological Chemistry*, *279*(11), 10542–10550. doi:10.1074/jbc.M310001200

341. Li, R., Lindholm, K., Yang, L.-B., Yue, X., Citron, M., Yan, R., Beach, T., Sue, L., Sabbagh, M., Cai, H., Wong, P., Price, D., Shen, Y. (2004). Amyloid beta peptide load is correlated with increased beta-secretase activity in sporadic Alzheimer's disease patients. *Proceedings of the National Academy of Sciences of the United States of America*, *101*(10), 3632–3637. doi:10.1073/pnas.0205689101

342. Yu, H., Saura, C. A., Choi, S. Y., Sun, L. D., Yang, X., Handler, M., Kawarabayashi, T., Younkin, L., Fedeles, B., Wilson, M. A., Younkin, S:, Kander, E. R., Kirwood, A., Shen, J. (2001). APP processing and synaptic plasticity in presenilin-1 conditional knockout mice. *Neuron*, *31*(5), 713–726. doi:10.1016/S0896-6273(01)00417-2

343. Parihar, M. S., & Brewer, G. J. (2010). Amyloid-beta as a modulator of synaptic plasticity. *J Alzheimers Dis*, *22*(3), 741–763. doi:10.3233/JAD-2010-101020

344. LaFerla, F. M., Green, K. N., & Oddo, S. (2007). Intracellular amyloid-beta in Alzheimer's disease. *Nature Reviews. Neuroscience*, *8*(7), 499–509. doi:10.1038/nrn2168

345. Hardy, J. (2002). The Amyloid Hypothesis of Alzheimer's Disease: Progress and Problems on the Road to Therapeutics. *Science*, *297*(5580), 353–356. doi:10.1126/science.1072994

346. Querfurth, H. W., & Laferla, F. M. (2010). Alzheimer's disease: mechanism of disease. *The New England Journal of Medicine*, *362*(4), 329–344. doi:10.1016/B978-0-12-803699-0.00045-1

347. Kinnecom, C., Lev, M. H., Wendell, L., Smith, E. E., Rosand, J., Frosch, M. P., & Greenberg, S. M. (2007). Course of cerebral amyloid angiopathy-related

inflammation. *Neurology*, *68*(17), 1411–1416. doi:10.1212/01.wnl.0000260066.98681.2e

348. Bard, F., Cannon, C., Barbour, R., Burke, R. L., Games, D., Grajeda, H., Guido, T., Hu, K., Huang, J., Johnson-Wood, K., Khan, K., Kholodenko, D., Lee, M., Lieberburg, I., Motter, R., Nguyen, M., Soriano, F., Vasquez, N., Weiss, K., Welch, B., Seubert, P., Schenk, D., Yednock, T. (2000). Peripherally administered antibodies against amyloid beta-peptide enter the central nervous system and reduce pathology in a mouse model of Alzheimer disease. *Nature Medicine*, *6*(8), 916–919. doi:10.1038/78682

349. Karran, E., Mercken, M., & Strooper, B. De. (2011). The amyloid cascade hypothesis for Alzheimer's disease: an appraisal for the development of therapeutics. *Nature Reviews Drug Discovery*, *10*(9), 698–712. doi:10.1038/nrd3505

350. Singer, O., Marr, R. A., Rockenstein, E., Crews, L., Coufal, N. G., Gage, F. H., Verma, I. M., Masliah, E. (2005). Targeting BACE1 with siRNAs ameliorates Alzheimer disease neuropathology in a transgenic model. *Nature Neuroscience*, *8*(10), 1343–1349. doi:10.1038/nn1531

351. Laird, F. M., Cai, H., Savonenko, A. V, Farah, M. H., He, K., Melnikova, T., Wen, H., Chiang, H.-C., Zu, G., Koliatsos, V. E., Borchelt, D. R., Pricel, D. L., Lee, H.-K., Wong, P. C. (2005). BACE1, a Major Determinant of Selective Vulnerability of the Brain to Amyloid- Amyloidogenesis, is Essential for Cognitive, Emotional, and Synaptic Functions. *Journal of Neuroscience*, *25*(50), 11693–11709. doi:10.1523/JNEUROSCI.2766-05.2005

352. Kobayashi, D., Zeller, M., Cole, T., Buttini, M., McConlogue, L., Sinha, S., Freedman, S., Morris, R. G., Chen, K. S. (2008). BACE1 gene deletion: Impact on behavioral function in a model of Alzheimer's disease. *Neurobiology of Aging*, *29*(6), 861–873. doi:10.1016/j.neurobiolaging.2007.01.002

353. Dominguez, D., Tournoy, J., Hartmann, D., Huth, T., Cryns, K., Deforce, S., Serneels, L., Camacho, I. E., Marjaux, E., Craessaerts, K., Roebroek, A. J. M., Schwake, M., D'Hooge, R., Bach, P., Kalinke, U., Moechars, D., Alzeimer, C., Reiss, K., Saftig, P., De Strooper, B. (2005). Phenotypic and biochemical analyses of BACE1- and BACE2-deficient mice. *Journal of Biological Chemistry*, *280*(35), 30797–30806. doi:10.1074/jbc.M505249200

354. Harrison, S. M., Harper, A. J., Hawkins, J., Duddy, G., Grau, E., Pugh, P. L., Winter, P. H., Shilliam, C. S., Hughes, Z. A., Dawson, L. A., Gonzalez, M. I., Upton, N., Pangalos, M. N., Dingwall, C. (2003). BACE1 (beta-secretase) transgenic and knockout mice: identification of neurochemical deficits and behavioral changes. *Molecular and cellular neurosciences*, *24*(3), 646–55. doi.org/10.1016/S1044-7431(03)00227-6

355. Cole, S. L., Vassar, R. (2007). The Alzheimer's disease Beta-secretase enzyme, BACE1. *Molecular Neurodegeneration*, *2*(1), 22. doi:10.1186/1750-1326-2-22

356. Cole, S. L., Vassar, R. (2008). The role of amyloid precursor protein processing by BACE1, the beta-secretase, in Alzheimer disease pathophysiology. *The Journal of biological chemistry*, *283*(44), 29621–5. doi:10.1074/jbc.R800015200

357. Zetterberg, H., Andreasson, U., Hansson, O., Wu, G., Sankaranarayanan, S., Andersson, M. E., Buchhave, P., Londos, E., Umek, R. M., Minthon, L., Simon, A. J., Blennow, K. (2008). Elevated cerebrospinal fluid BACE1 activity in incipient Alzheimer disease. *Archives of neurology*, *65*(8), 1102–7. doi:10.1001/archneur.65.8.1102

358. Bussemakers, M. J. G., Van Bokhoven, A., Verhaegh, G. W., Smit, F. P., Karthaus, H. F. M., Schalken, J. A., Debruyne, F. M. J., Ru, N., Isaacs, W. B. (1999). DD3: A new prostate-specific gene, highly overexpressed in prostate cancer. *Cancer Research*, *59*(23), 5975–5979. doi:10.1038/ncb2161

359. De Kok, J. B., Verhaegh, G. W., Roelofs, R. W., Hessels, D., Kiemeney, L. A., Aalders, T. W., Swinkes, D. W., Schalken, J. A. (2002). DD3PCA3, a very sensitive and specific marker to detect prostate tumors. *Cancer Research*, *62*(9), 2695–2698. doi:10.1016/s0022-5347(01)65160-7

360. Marks, L. S., & Bostwick, D. G. (2008). Prostate Cancer Specificity of PCA3 Gene Testing: Examples from Clinical Practice. *Reviews in urology*, *10*(3), 175–81. Retrieved from http://www.pubmedcentral.nih.gov/articlerender.fcgi?artid=2556484&tool=pmcentrez&rendertype=abstract

361. Perdonà, S., Bruzzese, D., Ferro, M., Autorino, R., Marino, A., Mazzarella, C., Perruolo, G., D'Esposito, V., Cosimato, V., Buonerba, C., Di Lorenzo, G., Musi, G., De Cobelli, O., Chun, F. K., Terracciano, D. (2013). Prostate health index (phi) and prostate cancer antigen 3 (PCA3) significantly improve diagnostic accuracy in patients undergoing prostate biopsy. *Prostate*, *73*(3), 227–235. doi:10.1371/journal.pone.0067687

362. Crawford, E. D., Rove, K. O., Trabulsi, E. J., Qian, J., Drewnowska, K. P., Kaminetsky, J. C., Huisman, T.K., Bilowus, M. L., Freedman, S. J., Glover, W. L. Jr, Bostwick, D. G. (2012). Diagnostic performance of PCA3 to detect prostate cancer in men with increased prostate specific antigen: A prospective study of 1,962 cases. *Journal of Urology*, *188*(5), 1726–1731. doi:10.1016/j.juro.2012.07.023

Chapter 3: Experimental Procedures

In this chapter, the syntheses (sections 3.1-3.2) and surface modifications (section 3.4) of both gold and lanthanide upconversion nanoparticles are elucidated. The bio-informatic investigation of the oligonucleotide sequences (section 3.3) and their consequent conjugation with inorganic nanoparticles (section 3.4) is also explained. The methodology for *in vitro* (3.5.1-2), *ex vivo* (3.5.3) and *in vivo* (3.6) studies is described. Finally, all the characterization methods used for any study are discussed in section 3.7.

3.1. Synthesis of spherical 13 nm gold nanoparticles

Gold nanospheres were synthesised using the citrate reduction method, first established by Turkevich [1, 2] and subsequently optimised by Frens [3]. In detail, an aqueous solution of sodium tetrachloroaurate(III) (100 mL, 1 mM, 99% purity, Sigma-Aldrich) was brought to boiling under stirring. Once boiling, a hot aqueous solution of sodium citrate (1) (see Figure 3.1.) (5 mL, 2% wt/v, ≥99% purity, Sigma-Aldrich) was added to the gold solution. The formation of particles was confirmed by a colour change, from yellow to colourless, to blue and finally to red. [1–4] The boiling solution was then stirred 15 min and subsequently allowed to cool to room temperature under stirring. To increase the stability of the particles for the attachment of DNA strands, a ligand exchange was performed. The citrate ligand was exchanged with bis(p-sulfonatophenyl)phenyl phosphine dihydrate dipotassium salt (BSPP, 97% purity, 1 mg/mL, Sigma-Aldrich) (see Figure 3.1.). BSPP (20mg, 97% purity, 1 mg/mL, Sigma-Aldrich) were added to the solution [5–8] once it reached room temperature. After stirring overnight, an oversaturated solution of sodium chloride (NaCl, 99% purity, Sigma-Aldrich) was used to aggregate the nanoparticles in a controlled manner via charge screening in the presence of Na^+ ions. This aggregation was confirmed by a colour change from red to blue [9–12]. Three rounds of centrifugation (5000 rpm, 10 min) followed by decantation and re-dispersion via sonication were performed to remove excess ligands. Particles were finally re-dispersed in Milli-Q water and purified by filtration (0.2 μm Nylon syringe filter, VWR). Particles were characterized using TEM (section 3.6.3), UV-

spectroscopy (section 3.6.1.1) and ζ-potential (section 3.6.4.) and finally stored at 4ºC prior to further functionalization.

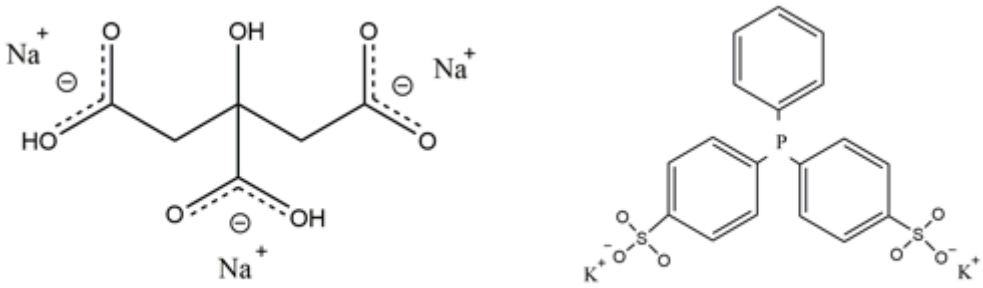

Figure 3.1. Chemical structures of Sodium Citrate (1) and BSPP (2)

3.2. Synthesis of $NaYF_4$:Yb Upconversion Nanoparticles

Lanthanide upconversion nanoparticles were synthesised by following a well reported thermal decomposition protocol. [13–15] The crystal matrix was formed using yttrium(III) chloride hexahydrate (236.62 mg, 0.78 mmol, Sigma-Aldrich). Ytterbium(III) chloride hexahydrate (77.5 mg, 0.20 mmol, Sigma-Aldrich) was used as the sensitizer. As emitters, either erbium(III) chloride hexahydrate (7.63 mg, 0.02 mmol, Sigma-Aldrich) or thulium(III) chloride hexahydrate (7.67 mg, 0.02 mol, Sigma-Aldrich) were used. The ratio of matrix/sensitizer/emitter was kept as 78%/20%/2% for both erbium and thulium.

All the salts were dissolved in a three-necked round-bottom flask with oleic acid (6 mL of 90% purity solution, 19 mmol, Sigma-Aldrich) and 1-octadecene (15 mL of 90% purity solution, 46.9 mmol) and heated at 160°C for 1 h and 30 min under nitrogen at atmospheric pressure. After this time, a solution of sodium hydroxide (100 mg, 2.5 mmol, ≥98% purity, Sigma-Aldrich) and ammonium fluoride (148.16 mg, 4 mmol, 98% purity, Sigma-Aldrich) dissolved in 10 mL of methanol (99% purity, VWR) was added dropwise in the reaction under vigorous stirring. This mixture was

slowly heated to 100°C for 2 h under nitrogen gas at atmospheric pressure and then 30 more minutes under vacuum. Next, the flask containing the mixture was set up with a thermometer, a reflux condenser, and nitrogen atmosphere and was placed in a heating mantle. The temperature was raised to 300°C and left to react for 1 h and 30 min. Subsequently, the mixture was left to cool to room temperature, and the NaYF4:Yb,Er nanoparticles were collected by centrifugation (8500 rpm, 10 min) with a mixture of hexane, ethanol, and water (2:1:1 v/v). The pellet was re-dispersed with 5 mL of ethanol and centrifuged in a mixture of ethanol and water (1:1 v/v). This process was repeated three times.

Finally, the purified NaYF4:Yb upconversion nanoparticles were dried overnight at 80 °C in an oven for prolonged storage. The mass of the resulting nanoparticles was then measured, and the particles (10 mg/ml) were stored in hexane at room temperature until further use.

3.3. Oligonucleotide synthesis for specific targets

All the oligonucleotide sequences used (Table 3.1.) were synthesised according to a comparison to the specific targets (e.g. Vimentin) used for the different types of applications (courtesy of AtdBio®, Southampton, UK). The gene sequences of each target was taken from the NCBI (http://www.ncbi.nlm.nih.gov/nucleotide/) and the Gene Cards (http://www.genecards.org) databases. Sequences were then analysed for alignments with other sequences (i.e. similarities) using the NCBI's Basic Local Alignment Search Tool (BLAST) (www.ncbi.nlm.nih.gov/BLAST.cgi). This tool is an algorithm constructed to compare sequence information such as amino acids, proteins or nucleotides using published databases[16]. Here the nucleotide-specific blastn was utilized. The following settings were applied: Database: RefSeq RNA; Entrez Query: all[filter] NOT predicted[title]; Expect threshold: 10; Match/Mismatch scores: 2/-3. Appropriate sequence targets were then chosen with the following criteria: Length of sense strand: 20-23 bases, melting temperature > 45 °C, GC

content < 50 % (in accordance with previous literature reports) [17–20], E value < 0.05, E value of nearest match > 1. The oligonucleotides were chemically altered to have different functional groups (Figure 3.2.), and different dyes (Figure 3.3.). For attachment to gold nanoparticles, all sequences integrated a thiol functional group /Figure 3.2.B), while for the functionalization of upconversion lanthanide nanoparticles the sequences incorporated an aminohexyl group (Figure 3.2.A). Cyanine dyes (Cy3 and Cy5, Figure 3.3.A and B respectively) were incorporated for some of the sequences for fluorescence studies, as well as for the imaging of mRNA presence in different models (see Chapter 5).

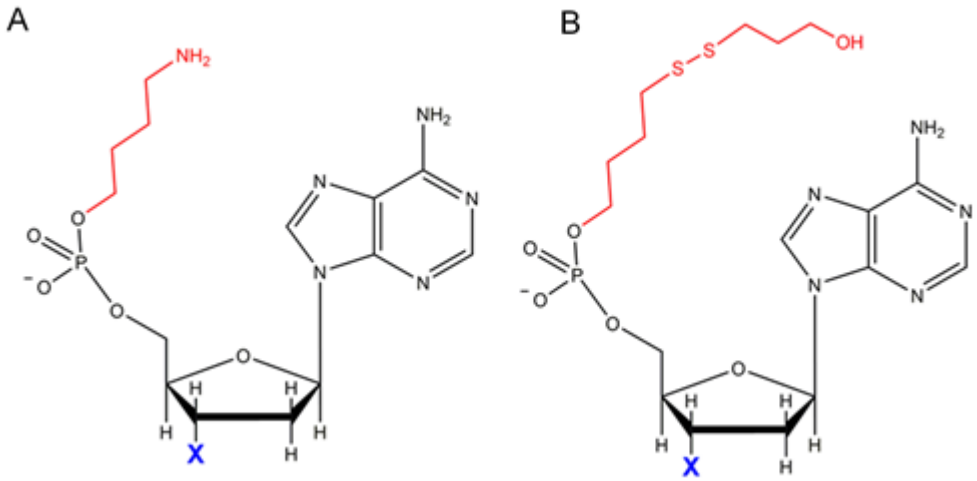

Figure 3.2. Chemical modifications to the oligonucleotide sequences. Both functional groups (red) were attached to either the 5' end (represented) or the 3' end (not represented). Aminohexyl (A) was used for EDC/sulfo-NHS coupling while the thiol group (B) was used for S-Au coupling. The functional groups were attached to the last amino acid of the sequence (represented by the blue X).

Study	***Target***	***Oligonucleotide***	***Sequences (5' - 3') and modifications***
Imaging	Vimentin Sense	DNA	Cy3-CTT TGC TCG AAT GTG CGG ACT T - $(A)_8$ - **S1**
	Vimentin Flare	DNA	Cy5-AAG TCC GCA CA
	Vimentin Perfect Target	DNA	AAG TCC GCA CAT TCG AGC AAA G
	Vimentin 1 mismatch target	DNA	AAG TTC GCA CAT TCG AGC AAA G
	Vimentin 2 mismatch target	DNA	AAG TTC GAC CAT TCG AGC AAA G
	Scramble control Sense	DNA	Cy3- GGT GGT CTT CGT ATG AAT AC $(A)_8$ - **S1**
	Scramble control Flare	DNA	Cy5-GTA TTC ATA CGA AG
	Vimentin Forward Primer	DNA	TGT CCA AAT CGA TGT GGA TGT TTC
	Vimentin Reverse Primer	DNA	TTG TAC CAT TCT TCT GCC TCC TG
Silencing	SMAD3 sense	RNA	**S1**- $(A)_{10}$ - UUG GAG AAG UUG UAA UGG AGC
	SMAD3 antisense	RNA	GCU CCA UUA CAA CUU CUC CAA
	SMAD3 sense (tagged)	RNA	**S1**- $(A)_{10}$ - UUG GAG AAG UUG UAA UGG AGC-Cy3
	SMAD3 antisense (tagged)	RNA	GCU CCA UUA CAA CUU CUC CAA-Cy5
	Scramble Control Sense	RNA	**S1**- $(A)_{10}$ – CAC AGU AUC AAU CUC AAG CCC
	Scramble Control Antisense	RNA	GGG CUU GAG UUG AUA CUG UG

	TGF-β Forward Primer	DNA	GGT TCA TGT CAT GGA TGG TGC
	TGF-β Reverse Primer	DNA	TGA CGT CAC TGG AGT TGT ACG G
	SMAD1 Forward Primer	DNA	GGA CTA CAA GGA CGA CGA TGA CA
	SMAD1 Reverse Primer	DNA	TTT GGT TCC TCA TAA GCA ACC G
	SMAD3 Forward Primer	DNA	TTG CAT AGT CAG GAG CAT CTT C
	SMAD3 Reverse Primer	DNA	CAG GGT GGA AGC CAA GTA TAA G
Sensing	BACE-1 sense	DNA	**S2** - $(A)_5$ - CAA CCT TCG TTT GCC CAA GA
	BACE-1 target	DNA	TCT TGG GCA AAC GAA GGT TG
	PCA3 sense	DNA	**S2** - $(A)_5$ - TGT TCA AAG ACC CTT CGT GT
	PCA3 target	DNA	ACA CGA AGG GTC TTT GAA CA
	Poly T sense (tagged)	DNA	**S2** - TTT TTT TTT TTT TTT TTT TT - Cy3
	Poly T sense	DNA	**S2** - TTT TTT TTT TTT TTT TTT TT
	Poly T target	DNA	AAA AAA AAA AAA AAA AAA AA

Table 3.1. Oligonucleotide sequences used in different types of studiesS1 – Thiol termination group ($C_2H_4OC_3H_6S$-$SC_3H_6OC_2H_4$, Figure 3.2.B); S2 – Aminohexyl termination group ($C_6H_{14}N$, Figure 3.2.A); Cy 3 – Cyanine 3 (Figure 3.3.A); Cy 5 – Cyanine 5 (Figure 3.3.B)

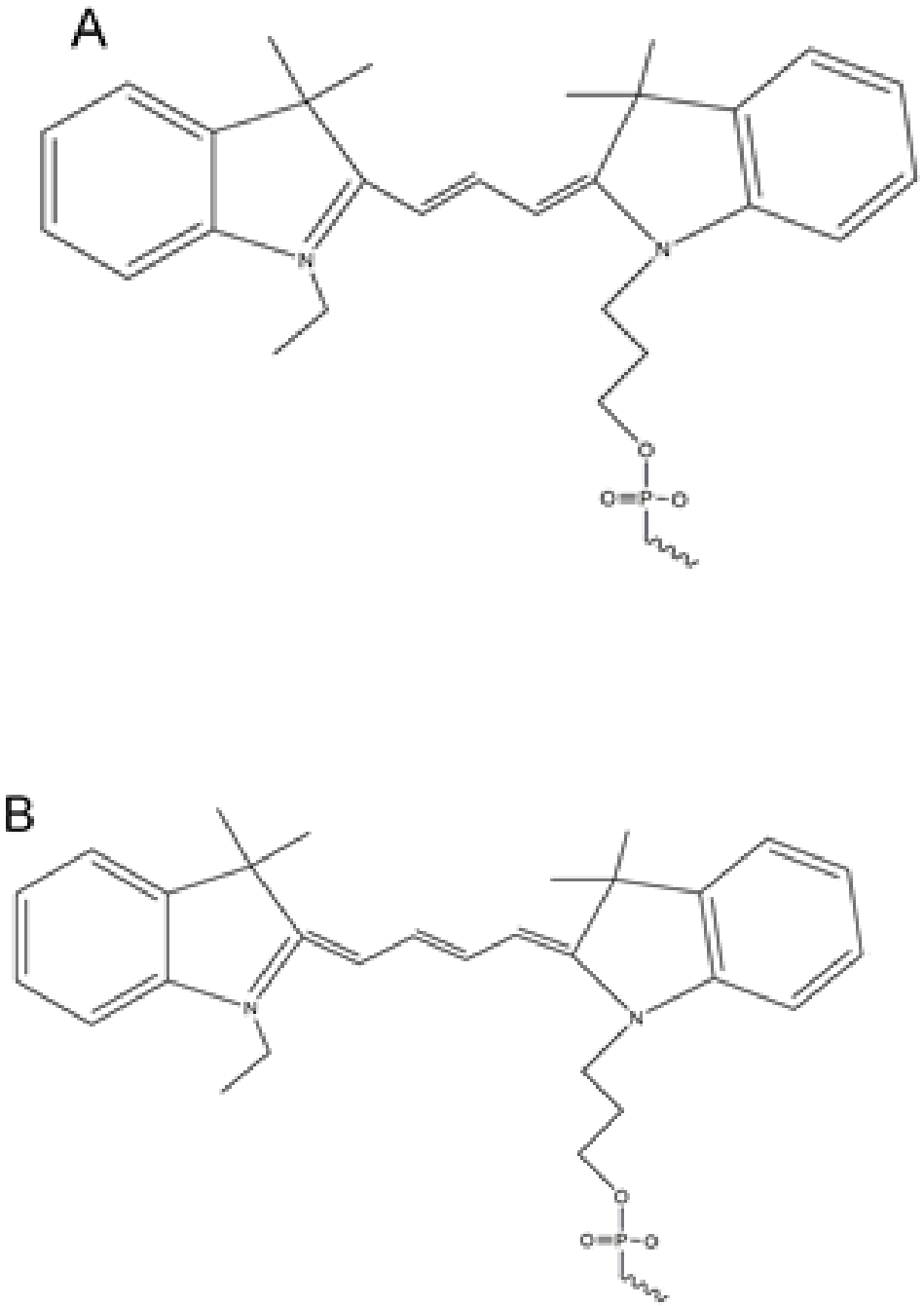

Figure 3.3. Cyanine dyes used as fluorescent tags. Cy3 (A) and Cy5 (B) were usedas fluorescent tags for the oligonucleotide sequences showed in Table 3.1.

3.4. Surface modification of nanoparticles

3.4.1 Oligonucleotide attachment to 13 nm gold nanoparticles

Gold nanoparticles were used as a core for the attachment of oligonucleotides due to their optical properties, their promptness for thiol-mediated conjugation and their biocompatibility (see section 2.1.1.). Various oligonucleotides were used depending on the application (see section 4 for imaging and section 5 for silencing). Therefore, the following sections (3.4.1.1 and 3.4.1.2) describe in detail the different attachment strategies to nanoparticle surfaces for both DNA and RNA strands.

3.4.1.1 DNA

The successful conjugation of thiol-terminated DNA strands on gold nanoparticles was achieved using a previously reported “salt aging” protocol. [18, 21, 22] Salt aging is required to screen repulsive negative charges between the DNA phosphate backbones and the particle surface covered with negatively charged BSPP. This ensures a high loading of oligos onto the nanoparticle surface. In detail, BSPP-coated 13nm AuNPs (1mL, 10 nM) were left shaking (1000 rpm) overnight at room temperature with 3 nmol of the DNA sense thiol-terminated sequence (Vimentin and Scramble Control in Table 3.1.). Afterwards, BSPP (1 mg/20 µL, 10 µL) was added to reduce the disulphide group on the oligonucleotide to the reactive thiol form. [23] After 10 mins of incubation while sonicating, phosphate buffer (0.1 M, pH 7.4), and sodium dodecyl sulfate (SDS, Sigma) (10%) were added to obtain final concentrations of 0.01 M phosphate and 1% SDS. Next, NaCl (2 M) was added six times over a period of 8h in order to obtain a final concentration of 0.2 M. The solution was left shaking (1000 rpm) overnight at RT.

Non-specifically bound oligonucleotide strands were removed after three steps of centrifugation (16400 rpm, 4 °C, 10 min). The resultant oligonucleotide-coated AuNPs were re-dispersed in 1 mL of hybridization buffer (0.5 M Na_2PO4 pH 6.8, 10 mM EDTA, 2% SDS). The corresponding flare strand was then added in a ratio of 60 Flare strands : 1 AuNP (10 mL, 600 nM) and the solution was heated to 80 °C for 2 minutes. The solution was left to cool down to room temperature. Non-

hybridised flare strands were removed after three steps of centrifugation (16400 rpm, 4 °C, 10 min) and the final AuNP-Sense-Flare conjugate was re-dispersed in PBS buffer and stored at 4 °C until further characterization (see Section 5).

3.4.1.2 siRNA

The attachment of siRNA onto AuNPs required a different approach since the RNA interference pathway requires a dsRNA sequence to be triggered [24, 25] (see section 2.2.1. for more detail). Therefore, it was necessary to hybridize the sense strand (the mRNA sequence targeted by the siRNA duplex) and the antisense strand (complimentary to the mRNA) before attaching the siRNA duplex onto the AuNPs surface. Hybridization took place in a buffer (30 mM Hepes, 100 mM of potassium acetate, pH 7.5, 100 µL total volume) using a 1:1 ratio of oligonucleotide strands. The solution containing both strands was heated to 85 ºC for 10 mins, and then it was slowly cooled to RT overnight. The initial solution containing the hybridized siRNA duplex was added to a solution of BSPP-coated nanoparticles (10 nM, 1 mL) and Tween 20 (0.2% v/v) and left for shaking overnight (500 rpm, RT). Finally, the salt aging was done by adding NaCl (2 M) divided into six additions over 8h. After the final salt addition, the solution was left shaking overnight (500 rpm, RT). The solution was then brought to a solution thiolated polyethylene glycol (1 mL, 10µM 10 kDa, (PEG; Prochimia) and allowed to shake for 4 h (500 rpm, RT). The solution was then centrifuged 3x for purification (16400 rpm, 4 ºC) and the resultant pellet was re-suspended in 1x PBS. The AuNPs-siRNA conjugates were stored at 4 °C until further characterization or use.

3.4.2 DNA attachment to upconversion nanoparticles

Oleic acid-coated lanthanide upconversion nanoparticles (section 3.2 for synthesis) were used as the fluorescent component in our experiments (Chapter 6). However, in order to use the nanoparticles both the conjugation with the oligonucleotide sequences and for the sensor use in biological samples, there was a need to first transfer the nanoparticles to an aqueous medium. Two strategies

were used in order to obtain water-soluble UCNPs: silanization of nanoparticles (3.4.2.1.1) or ligand exchange with a hydrophilic polymer (polyacrylic acid).(3.4.2.1.2).

3.4.2.1 Phase transfer of upconversion nanoparticles

3.4.2.1.1 Silica Coated upconversion nanoparticles

One of the most well-studied phase transfer strategies to bring non-polar nanoparticles into polar solvents (e.g. water) is to coat these particles with a silica shell (silanization). [26, 27] In detail, the silanization of UCNPs was achieved by a base catalysed polymerisation of TEOS in a reverse micro-emulsion. The surfactant IGEPAL CO-520 (240 mg, Sigma-Aldrich) was dissolved in 5 mL of hexane containing 5 mg/ mL of UCNPs and mixed via sonication. Afterwards, ammonium hydroxide solution (40 µl, 30% v/v, Sigma Aldrich) was added to increase the overall pH from 6 to 9. The solution turned transparent upon addition of the ammonia solution, indicating the formation of microspheres that surround the UCNPs. The silanization reaction was then initiated by adding a range of volumes (10 – 50 µl) of silane compound (TEOS), which anchors itself on the nanoparticles' surfaces via hydrophilic/hydrophobic interactions and forms silica-oxygen (Si-O) bonds, gradually creating a silica shell around each particle. The shell thickness was dependent on the amount of TEOS added (see chapter 6 for details). Finally, silica coated UCNPs were purified from excess reagents through centrifugation (3x, 5000 rpm, RT). Consequently, since the silica shell is hydrophilic, the nanoparticles become soluble in polar solvents allowing further silane based functionalization (e.g. amino-silylation) for the DNA attachment Therefore, silica coated-UCNPs were re-dispersed in ethanol and stored at 4 ºC until further characterization (see sections 3.6) and functionalization (see 3.4.2.2.).

3.4.2.1.2 Polyacrylic acid coating

Another strategy to transfer OA-coated UCNPs was to perform a ligand exchange with a more polar ligand. [28–30] Polyacrylic acid (PAA) was chosen not

only for its polarity but also for the several carboxylic groups present (Figure 3.4). In detail, ligand exchange was achieved by centrifuging OA-coated UCNPs (7000 rpm, 10 mins) and re-dispersing them in THF (7 ml). THF works as an intermediate solvent for both polar and non-polar compounds and allows the particles and the new ligand to come to close proximity within the same phase. PAA (0.25g, 1.8 kDa, Sigma Aldrich) was separately added to 3 ml of THF and sonicated until completely dissolved. Both solutions were mixed for a total volume of 10 mL and left stirring (500 rpm, RT) overnight to allow the ligand exchange to happen. The final PAA-coated UCNPs solution was heated to 80 °C under argon until the solvent was completely evaporated. The powder was then re-dispersed in 1:1 mix of Hexane/ethanol and centrifuged (7000 rpm, 10 mins). The resultant pellet was washed with ethanol (7000 rpm, 10 mins, 3x) to remove the residual OA and excess PAA. The final PAA-coated particles was re-dispersed in water and stored at 4 °C until further characterization (see section 3.6) and functionalization (see section 3.4.2.2.)

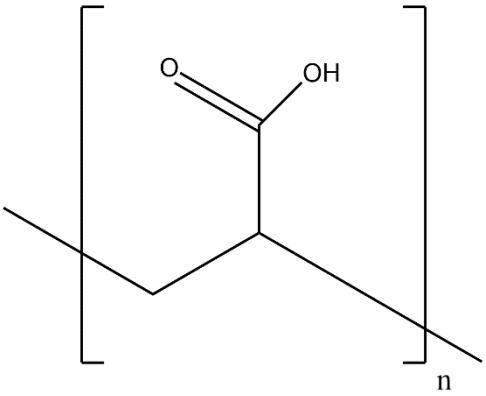

Figure 3.4. Polyacrylic acid monomer. The polymer form can be used to phase transfer nanoparticles and to incorporate COOH groups onto their surface

3.4.2.2 EDC/sulfo-NHS coupling

To functionalize the carboxylic groups on PAA with amine-modifiied oligonucleotides we employed an EDC coupling strategy. [31–33] This type of coupling relies on the presence of a reactive carbodiimide (e.g. EDC) that interacts with the COOH groups in a compound and forms an unstable intermediate o-acylisourea ester. This intermediate compound can then react with the sulfo-NHS, which is semi-stable and is prone to react with primary amine groups. Therefore, it

is possible to covalently bind two different molecules provided that one has a COOH group and the other has a NH_2 group.

Knowing that all the chosen oligonucleotide sequences were synthesised with a free NH_2 group on the 5' end (see Table 3.1.), it was only a matter of covering the UCNPs' surfaces with COOH groups in order to proceed to the coupling. PAA used in the ligand exchange (see section 3.4.2.1.2.) had already been chosen for that purpose. However, with the silica coating approach, there was a need for further functionalization of the surface before proceeding to the EDC/sulfo-NHS coupling. Therefore, a two-step functionalization of the silica-covered UCNPs was done. An amino-silylation[34] was conducted by adding an amino enriched silane reagent - APTMS (150 µl, 0.68 mmol, Sigma-Aldrich) - to the silica coated UCNPs (see section 3.4.2.1.1.) dissolved in a total volume of 5 ml. The APTMS reacts with the Si-O on the surface of the silica shell to covalently attach an amino group to the surface of the particles. The mixture was stirred (500 rpm, RT) overnight and purified in DMF via centrifugation (7000 rpm, RT, 3x). The resultant pellet was re-dispersed in 5 ml of ethanol for characterization or in 5 ml of DMF (99.8%, Sigma-Aldrich) for further functionalization.

In the second stage of functionalization, succinic anhydride (150 mg, 1.49 mmol, Sigma-Aldrich) was dissolved in 3 mL of DMF and was added dropwise to the DMF solution containing the NH_2-functionalized UCNPs (total volume 7 ml). The succinic anhydride reacts with the amine group and, through a ring opening reaction [35, 36], creates a carboxylic acid group ready to be used for the attachment of oligonucleotides. The final COOH-functionalized particles were purified with several washes of ethanol. The final COOH-silica coated UCNPs were dispersed in milli-Q water. With both the PAA and the silica coated UCNPs having a COOH group, the EDC/sulfo-NHS coupling with the NH_2-terminated oligonucleotide sequences was completed. This was achieved by re-dispersing the COOH-silica coated UCNPs in borate buffered solution (1 mM) at a concentration of 2 mg/ml. The EDC (1.15 mg, Sigma-Aldrich) was then dissolved in 20 µl MES buffered solution (99.6%, pH 6, Sigma-Aldrich) to obtain a final solution of 0.3M concentration. Sulfo-NHS (2.6 mg, ≥98%, Sigma-Aldrich) was also dissolved in MES buffered solution (20 µl) to obtain the same concentration. Both were mixed and sonicated (1 min, RT) and then

injected to the borate buffered solution containing the UCNPs. This mixture was shaken (500 rpm, 5 min, RT) and then the oligonucleotide of choice (Table 3.1.) was added in excess (30-50 µl). This final mixture was stirred overnight.

Finally, the oligonucleotide-functionalized UCNPs were purified by centrifugation (2x, 16400 rpm, 20 min, 4ºC) using milli-Q water. The purified particles were collected with PBS solution (0.01 M, pH 7.4, Sigma-Aldrich) and stored at 4ºC until further characterization or until used for sensing applications (see Chapter 6).

3.5. Culture of cells and tissue

3.5.1 Human Cells

Human bronchial epithelial cells (16HBE) and human fetal lung fibroblasts (MRC-5) were cultured in Corning cell culture flasks using Dulbecco's Modified Eagle's Medium (DMEM, Gibco) (see Appendix A for formulation) supplemented with 1% penicillin/streptomycin (Gibco), 1 % L-glutamine (Gibco), 1 mL nystatin (Gibco) and 10% foetal bovine serum (FBS, Sigma Aldrich). Cells were kept at 37 °C, 5% CO_2 atmosphere in a Sanyo CO_2 incubator (model MCO-17AI). Cells were grown to 90% confluency and then passaged once a week. In all experiments cells from passages < 30 were used. All human cell culture stocks were received from Dr Peter Lackie, Southampton General Hospital. For passaging, cells were incubated with Hank's Balanced Salt Solution (HBSS) (10 mL) for 5 min and subsequently detached using trypsin (5 mL, 0.25 % trypsin, 0.01% EDTA solution). Trypsin was then inhibited by the addition of full serum growth medium (13 mL). The resulting cell suspension was pelleted by centrifugation (1000 rpm, 5 min). The supernatant was decanted off and the resulting cell pellet was re-suspended in a small amount of media (400 – 600 µL). A small portion of this (100 µL) was then seeded into a new cell culture flask containing full serum DMEM growth medium (13 mL). This formed the cell stock. The remainder of the cells was used in further experiments.

3.5.2 Mouse Cells

Mouse embryonic fibroblasts (MEFs) were harvested following a standard protocol. [37] In detail, mouse embryos were harvested from albino HsdOla:MF1 females (12-30 weeks old) at day 13.5 after the appearance of the copulation plug. After euthanizing the female *via* cervical dislocation, an incision was made in the abdominal area, the uterus was surgically removed and the embryos were pressed out of one of the open ends, removing placental and other maternal tissues in the process. An average of 6-10 embryos were harvested per female. The embryos were transferred to a 10 cm cell culture dish with PBS (w/o Ca^{2+} or Mg^{2+}, Gibco) and the heads, heart and lungs were carefully removed. The rest of the embryonic bodies were placed in separate 10 cm cell culture dishes (3/4 per dish) with 2 mL of trypsin (0.25%, 0.01% EDTA) and minced using fresh razor blade for each dish. The dishes were then placed in a Sanyo CO_2 incubator (model MCO-17AI) at 37 ºC/5% CO_2 for 30-45 mins to allow the trypsin to act.

The trypsin activity was then stopped by adding 3 mL of MEF media (DMEM - see Appendix A for formulation, supplemented with 10% FCS and 1% Pen/Strep) and the mix was pipetted 20-30 times using a 20G syringe to break up tissues. The cellular suspension was then transferred to a new 10 cm cell culture dish and 7 ml of MEF media was added. The dishes were placed in the incubator at 37 ºC/5% CO_2 overnight and the leftover tissue was removed on the next day. New MEF media was added and the dishes were left incubating at 37 ºC/5% CO_2 for 3-4 days to allow the cells to replicate. Afterwards, the medium was aspirated and disposed of and the dishes were rinsed with 10 ml of PBS. Trypsin (3mL) was then added to each dish and left incubating for 5 min. The trypsin activity was once more stopped by adding 5 mL of MEF media and the cell suspension was passed to a falcon tube (50 mL, VWR) and centrifuged (1000 rpm, 5 min). The cell pellet was recovered by re-suspending in MEF media (1 ml). After cell counting, cells were either frozen down ($2x10^6$ cell/vial) in liquid nitrogen or were kept for 2 more passages for maturation before being used for further experiments.

3.5.3 Mouse *ex vivo* skin

Dorsal skin was harvested from new born wild type C57BL/6 mice (1-4 days old). Each skin tissue piece was roughly cut to be 2 x 1.5 cm^2 in area. Straight after harvest, the skin was washed 3x with PBS and a punch biopsy was done using a circular blade (6 mm diameter) to ensure that the *ex vivo* samples were all of equal size. These samples were then positioned in a Corning® Transwell® (Polyester membrane, 12 mm, 0.4 µm pore) in 24 well plates with 2ml of MEM skin medium (see Appendix A for formulation) supplemented with 1% penicillin/streptomycin (Gibco), 1% L-gluthamine (Gibco) and 10% foetal bovine serum (FBS, Sigma Aldrich). The samples were used for studying the interaction of AuNPs-DNA with *ex vivo* models and were left incubating at 37 ºC/5% CO_2 no more than 6h after harvesting.

3.5.4 *In vivo* wound healing model

A total of 9 male wild type C57BL/6 mice (12-16 weeks old) were used as wound healing models for the *in vivo* studies. Mice were kept in the Biomedical Research Facilities (BRF, upper level Southampton General Hospital) with conditions aligned with the Animals Scientific Procedures Act (ASPA, 1986). These conditions included individual cages, kept in a ventilated room, constant temperature (18-23 ºC) and humidity (~50%), 12h light/12h dark cycle and normal dietary plans (see Appendix A for formulation of chow).

Experiments were conducted under the project license 30/2971 and the Personal License number IC73F2D5B and all mice for *in vivo* were used for wound healing studies only. Mice were prepared for surgery by following a standard wounding protocol.[38, 39] In detail, each mouse was anesthetized using 5% isoflurane in 100% oxygen (flow rate 1L/min) until unconscious. The isoflurane percentage was reduced to 2% to maintain anesthesia. The deep pedal reflexes of the mouse were checked to ensure full anesthesia. The dorsal fur was removed using clipper from the base of the neck to 6 cm further down the back and between the two should blades. Depilatory cream was applied for 1 min to remove any unclipped fur. The skin was then wiped with 70% ethanol solution and sterilized using a 10% povidone-iodine.

A sterile 6 mm biopsy punch blade was used to create a full-thickness subcutaneous wound on each side of the back of the mouse (see Figure 3.5.). In the left wound a scramble AuNP-siRNA control solution (2 ml, 100 nM,) was applied, whilst on the right wound the SMAD3 knockdown AuNP-siRNA solution was used (2ml ,100 nM). In both cases, a petroleum based cream matrix (Aquaphor®, Eucerin) was used to facilitate the application of the nanoparticles (dilution of 1% v/wt of particles in cream). After the application of the AuNP-siRNA conjugates, the wound was covered with a transparent occlusive dressing (3M Tegaderm). Each mouse was injected with Carprofen (5mg/kg) as an analgesic and kept on heating mats until fully recovered.

The mice were kept on a normal diet with a carprofen enriched water as a pain reliever. The wounds were monitored from day 0 *via* photography and the AuNP-siRNA conjugates were reapplied on the wound every 2 days until day 15, when the wound was totally closed. Mice were regularly shaved to keep the wounds from infecting and to provide cleared pictures. After 15 days, the mice were euthanized via neck dislocation, carefully made in order to avoid distortions of the wounded regions. A sterile 8mm biopsy punch was then used to remove three samples from each mouse: the region treated with the scramble control, the region treated with the SMAD3 AuNP-siRNA conjugate and a non-wounded region to use as a control on the histological analysis. The tissue biopsies were carefully placed in a wax platform to keep the skin intact and stretched. Finally, each biopsy was incubated in a 4% paraformaldehyde (in PBS) at 4 ºC overnight. The tissue was then transferred to a 10% neutral buffered formalin solution until used for histological preparation and analysis.

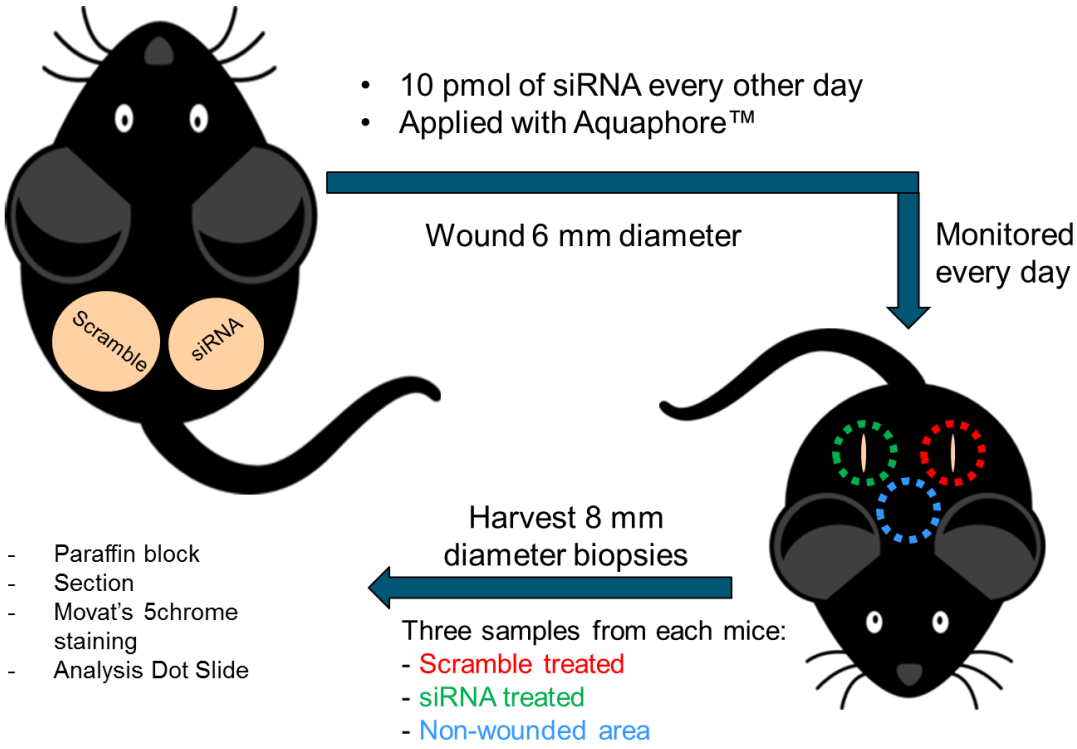

Figure 3.5.Summary of the *in vivo* experiment. Male C57BL/6 mice were wounded (6 mm diameter) on the dorsal part. The left wound was treated with AuNP-siRNA scramble control solution, whilst the right wound was treated with a knockdown AuNP-siRNA solution. After 15 days of monitoring, three skin areas were harvested on each mice (two controls and one treatment), before taking the tissues to paraffin embedding and consequent histological analysis (section 3.9.5.2)

3.6. Characterization techniques for nanoparticle-oligonucleotide conjugates

3.6.1 Spectroscopy

3.6.1.1 UV-Visible Spectroscopy

All samples were analysed using a black low volume quartz cuvette (1 cm path length, Hellma Analytics) on a Cary 300 Bio UV-Vis Spectrometer.

3.6.1.1.1 Determination of AuNPs concentration

The concentrations of colloidal AuNP solutions were determined from the absorption spectrum at the peak maxima (~520 nm) using the Beer-Lamber law (equation X):

$$c = \frac{AD}{\varepsilon l}$$

Equation 3.1.Beer-Lambert law for the determination of concentrations

c = concentration (mol/L), A = absorbance at the peak maximum (0<A<1 a.u.), l = path length of light (cm) and ε = extinction coefficient (L mol^{-1} cm^{-1})

The extinction coefficient for the calculation of 13 nm AuNPs concentration is: 2.27 x 10^8 L mol^{-1} cm^{-1}. [40] Sample calculation can be found on Appendix B.

3.6.1.1.2 Determination of oligonucleotide loading on AuNPs

The determination of oligonucleotide loading on nanoparticles was done following two different approaches. For AuNPs, a KI/I_2 etchant was used (see Figure 3.6. for mechanism). In detail, to a solution of AuNP-oligonucleotide with a known concentration (200 µl, 10 nM) a solution of KI/I_2 (ratio of I_2 to KI = 1:6, 200 µl, 34 mM) was added. [41] A colour change from red to yellow indicated the dissolution of colloidal gold. [1, 3, 42, 43]

$I_2 + I^- \rightarrow I_3^-$

$I_3^- + 2e^- \rightarrow 3I^-$

$2I^- + Au \rightarrow AuI_2 + 2e^-$

Figure 3.6. Etching of gold mechanism

Using a KI/I_2 solution (ratio 6:1) it is possible to dissolve gold forming gold iodine with a series of RedOx reactions.

The gold etching solution was made up to 1 ml with Milli-Q water and the oligonucleotides were purified by running the resulting solution through a desalting NAP™-10 column (GE Healthcare). The purified oligonucleotides were eluted from the column with 1.5 ml of Milli-Q water and collected in an eppendorf tube. The oligonucleotide optical density (O.D.) was determined (at 260 nm) on a Cary 300 Bio UV-Vis Spectrophotometer. This data, together with the initial O.D. given on the accompanying oligonucleotide data sheet (prepared by Dr. Afaf El-Sagheer) allowed for the determination of the concentration of oligonucleotides in solution. This concentration, together with the fluorescence calibration curves (see sections 4.2. and 5.1), permitted the determination of the number of oligonucleotide-loading on the surface of AuNPs.

3.6.1.1.3 Determination of oligonucleotide loading on UCNPs

For the lanthanide UCNPs, the oligonucleotide loading was determined either *via* direct measurement of the absorbance at 260 nm (for PAA coated particles) in a 1 ml solution of known nanoparticle concentration (10 mg/ml) or through dissolution of the silica shell using a strong base (NaOH, 1 M, pH = 9.5). [44] For the latter, a 10:1 ratio between UCNPs and NaOH was used to break the Si-O-Si bonds and form a soluble Si-OH product. The oligonucleotides were then purified from the uncovered UCNPs through centrifugation (16400 rpm, RT) and the absorbance spectrum of the supernatant was taken to calculate the O.D. (at 260 nm) correspondent to the oligonucleotide sequence.

3.6.1.2 Fluorescence Spectroscopy

Samples were analysed using a black low volume fluorescence quartz cuvette (Hellma Analytics) on a Cary Eclipse Fluorescence Spectrophotometer.

3.6.1.2.1 Determination of oligonucleotide loading on AuNPs

Gold nanoparticles were etched with a solution of KI/I_2 in a 1:1 ratio (see 3.7.1.1.2. for details). Oligonucleotides were purified using a desalting NAP-10 column and eluted with 1.5 ml Milli-Q water. The fluorescence spectrum of the resulting solution was taken for the specific dyes attached to the correspondent oligonucleotide sequences (see Table 3.1. for sequences). A calibration curve was done with pure oligonucleotide solutions (0-5 µM concentration, 1 mL) and the fluorescence spectrum was compared with the corresponding calibration curve (see sections 4.2. and 5.1.). This data allowed to the determination of the number of oligonucleotide strands coating the surface of the AuNPs.

3.6.1.2.2 Quality control of sequence hybridization

The successful design of the sequences was confirmed using fluorescence melting curves. In detail, a mix of the complementary oligonucleotides (see Table 3.1.) was made in a 1:1 ratio (e.g. 10 pmol of SMAD3 sense and 10 pmol SMAD3 antisense strand). The oligonucleotide sequences were dispersed in hybridization buffer (80 mM phosphate, pH 7, total volume 1 ml) and the SYBR® Green II Dye was added (5 µL, 1x Conc.). The solution was heated from 20 to 80 ºC at a rate of 0.1 ºC/min. Readings were taken at a rate of 0.1 ºC/min (excitation wavelength: 493 nm; emission wavelength: 520 nm).

3.6.1.2.3 Determination of target specificity

The determination of the specificity of mRNA detection (Chapter 4) was done by incubating assembled AuNP-DNA nanoprobes with target sequences for vimentin (see Table 3.1.). Perfect, 1 mismatch and 2 mismatch targets were added in excess to a solution of AuNP-DNA probes (150 µl, 2.5 nM) in PBS. Fluorescence readings were taken immediately until a plateau was reached and the corresponding spectra were recorded (excitation wavelengths: 543 nm (Cy3) or 635 (Cy5); emission wavelengths: 563 nm (Cy3) or 662 nm (Cy5)).

3.6.1.2.4 Gluthathione assay

DNA-AuNP and siRNA-AuNP conjugates suspended in PBS (150 µl, 2.5 nM) were incubated at 37 ºC with gluthathione 3 (5 nM) to test their stability in cells in the presence of another thiolated molecule (Figure 3.7.). The samples were incubated for 4 different periods (3h, 6h, 12h and 24h) and purified via centrifugation (16400 rpm, 15min, 4ºC). The resultant supernatant was collected and analysed for fluorescence (excitation wavelengths: 543 nm (Cy3) or 635 (Cy5); emission wavelengths: 563 nm (Cy3) or 662 nm (Cy5)) to monitor any thiol displacement of the oligonucleotide strands.

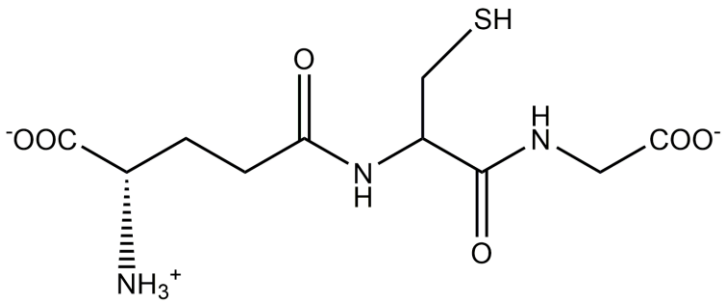

Figure 3.7. Chemical structure of glutathione

3.6.1.2.5 Nuclease Assay

The stability of the AuNP-oligonucleotide conjugates in intracellular conditions was also tested by incubating them with two different types of nucleases: DNAseI and DNAseII. [45] For both, AuNP-oligonucleotide conjugates (150 µl, 2.5 nM) in PBS were incubated at 37 ºC with 0.38 mg/ml of enzyme. For DNAseI (from bovine pancreas, Sigma-Aldrich), the incubation of conjugate and enzyme was done at pH 7.6 in the presence of $CaCl_2$ (0.50 mM, Sigma-Aldrich) and $MgCl_2$ (2.5 mM, Sigma-Aldrich). For DNaseII (from porcine spleen, Sigma-Aldrich), the incubation was done

only in PBS at pH 4.6. Both type of incubations were done over 24h and the fluorescence (excitation wavelengths: 543 nm (Cy3) or 635 (Cy5); emission wavelengths: 563 nm (Cy3) or 662 nm (Cy5)) was monitored every at different timepoints (0h, 2h, 4h, 6h, 8h, 12h, 18h and 24h) to detect any degradation.

3.6.1.2.6 Cell culture media stability assay

AuNP-oligonucleotide conjugates (150 µl, 2.5 nM) were dispersed in 1 mL of different cell culture media (DMEM and MEF media, see Appendix A for formulations). The mixture was incubated at 37 ºC for 24h and the fluorescence (excitation wavelengths: 543 nm (Cy3) or 635 (Cy5); emission wavelengths: 563 nm (Cy3) or 662 nm (Cy5)) was monitored at different timepoints (0h, 2h, 4h, 6h, 8h, 12h, 18h and 24h) to detect any degradation.

3.6.1.3 Energy Dispersive X-Ray Spectroscopy

The elemental analysis of lanthanide UCNPs was performed using energy dispersive x-ray (EDX) spectroscopy. In detail, a droplet of UCNP solution (1 mg/ml) was air dried on a 400 mesh formvar-coated copper grip (SPI) and analysed on a FEI Technai12 transmission electron microscope (bias voltage: 75 kV, EDX detector incorporated). The analysis was conducted in selected parts of the grid containing nanoparticles at high magnification (100,000x).

3.6.1.4 Fourier Transforming Infrared Spectroscopy

The successful ligand exchange and DNA attachment *via* EDC/sulfo-NHS coupling was confirmed via Fourier transforming infrared (FTIR) spectroscopy. In detail, solutions of PAA-coated UCNPs (1 mg/ml) and DNA-coated UCNPs (1 mg/ml) were analysed on a Nicolet iS5 FT-IR Spectrometer (Thermo Fisher). Milli-Q water was used for background correction and each spectrum was taken at room temperature, 10s scan time.

3.6.2 Gel Electrophoresis

Agarose gels were prepared by dissolving agarose (1.75% wt/V) in 0.5x TBE buffer (45 mM Tri-borate, 1 mM EDTA), followed by microwave heating. [46, 47] Once all the agarose dissolved, the resulting gel was cast into the gel construct and a comb was inserted to form wells. After setting for 1h the gel was placed in the electrophoresis buffer chamber containing 0.5x TBE buffer. Samples were mixed with Ficoll solution (15% in 3x TBE) to increase the sample density before loading into the wells of the gel. The loaded gel was then electrophoresed at 9 V/cm. After a successful run (average 45 min – 1h), the gel was taken out and pictures were taken. For pure DNA, ethidium bromide (1/10000 dilution, Sigma-Aldrich) was added to the gel solution before microwave heating as a staining agent and imaging was conducted on a white background in a Syngene G.BOX under UV illumination.

3.6.3 Transmission Electron microscopy

Nanomaterials were visualized by transmission electron microscopy (Hitachi H7000 Tem, bias voltage: 75 kV). Sample droplets were air dried on a 400 mesh formvar-coated copper grid (SPI). Size distribution histograms were generated from statistical analyses of relevant representative images using ImageJ software.

3.6.4 ζ-Potential

Net charges of nanomaterials were measured on a Malvern Zetasizer Nano ZS using disposable capillary cells. Average net charges were determined from at least three independent measurements.

3.7. Characterization techniques for imaging of *in vitro* and *ex vivo* models using AuNP-DNA conjugates

3.7.1 Microscopy

3.7.1.1 Confocal Microscopy

The investigation of mRNA detection using AuNPs-DNA conjugates was done in both human (see section 3.5.1) and mouse (see section 3.5.2) cell lines and *ex vivo* skin biopsies (see section 3.5.3).

Cells were grown on square glass coverslips in 6-well plates. Once cells were ~90% confluent, media was exchanged with fresh media containing AuNP-DNA conjugates (2 ml, 1 nM) for 18h. Cells were incubated with Hoechst 33342 (5 µl) for 1h as a nuclear stain. For imaging the glass coverslip was removed and washed with PBS. The coverslip was then mounted on a glass slide with a drop of PBS in order to keep cells alive. The edges around the coverslip were sealed using double-sided tape. All imaging was carried out on a Leica SP8 confocal microscope at 37ºC.

Ex vivo murine dorsal skin was harvested from new born hairless mice (see section 3.5.3). Straight after harvest, the skin was washed 3 x with PBS and injected with a Micro-Fine™ syringe, 0.5 mL, 0.3mm x 4 mm (BD, Europe), in a ~30° angle with a solution containing AuNP-DNA (2 ml, 10 nM). After 6h incubation in a transwell using MEM-L-glutamine enriched medium (see section 3.5.3), the skin was removed, washed 3x with PBS and fixed in Formalin Buffer salin fixative. Afterwards, skin samples were incubated with DAPI (1 µg/mL) for 30 mins. Each sample was embedded in paraffin blocks using a standard dehydration protocol. [48] In detail, the tissue is processed gradually in an automated machine that processed the tissue in graded alcohols (70/90/100% v/v), then in xylene and finally in paraffin ready to be embedded. The embedding was done in a Leica HistoCore Arcadia™ machine. The blocks were then sectioned in 2µm thick sections and the excess paraffin was removed using a standard hydration/dehydration protocol. [48] Briefly, the paraffin was removed by subjecting the sections to various steps of first xylene and then graded alcohols (100/90/70% v/v), 10 minutes on each step. Once the final alcohol step was done, the sections were then moved back up the graded alcohols and

finally the xylene, before being mounted in the slide using Sub-X mounting agent (Leica Biosystems). All imaging was carried out on a Leica SP8 confocal microscope. Fluorescence intensity was analysed using the Leica Application Suite X software and statistical analysis was performed using GraphPad Prism 7 software.

3.7.1.2 Light sheet Microscopy

Ex vivo murine dorsal skin was harvested (see section 3.5.3) and incubated at different time points (0h, 1h, 2h, 3h, 4h, 5h and 6h) with different solutions (see section 3.8.1.1 for detailed experimental). Conditions were kept constant across experiments. RhodB was chosen as a counter-dye for the determination of the injection site, since it interacts with the elastic fibres of the skin [49] without interfering with the other two channels used for DAPI (405nm) and for the smart nanoparticles (640nm). The clearing of the skin samples for the analysis using light sheet microscopy was done following progressive dehydration procedure. [50] In detail, each sample was embedded in 1% Agarose block after the respective incubation time with the respective solutions. The blocks were cut suitably to fit a small vial.

Each block was then submerged in an increasingly hydrophobic solvent (50/50 Water: THF initially, then 80% THF, 96% THF and finally 2x 100% THF), with each step taking 6h. After the final 100% THF step, the solvent was removed and the sample was submerged in 2 mL of DCM and left until it sank to the bottom of the vial (approximately 2h). Afterwards, the solvent was disposed of and two steps (6h each) of DBE clearing were performed. The complete clearing of the skin block was observed by the transparency of both the blocks and the samples. Finally, the block was submerged in fresh DBE. Images were taken using an Olympus MVX10, with excitation at 405 nm, 561 nm and 640 nm. Images were taken using a 1.6x magnification, with a section size of 3 µm per stage step. Resulting images were processed using ImageJ to combine for a 3D projection. For fluorescence intensity analysis, the controls (PBS, RhodB only and scramble control) where used to measure the “background” levels of fluorescence of each channel (405nm, 561nm and 640nm). This was done using ImageJ to extract the grey value histogram of

each pixel and have plot of average of fluorescence intensity against area of the image. The mean grey values were also taken into consideration. Each sample had is fluorescence of the 405nm and 561nm taken and used for “sample-to-sample” variation adjustment. Finally, the value at 640nm fluorescence was taken and adjusted using all the aforementioned correction values and plotted in percentage of relative fluorescence increase relative to the controls. Statistical analysis was performed using GraphPad Prism 7 software.

3.7.2 Wound closure Assessment

3.7.2.1 Cell migration Assay

Epithelial human cells (see section 3.5.1) were grown on square glass coverslips in 6-well plates with supplemented DMEM (see Appendix A for formulation). The wound assay was performed once cells were ~90 % confluent by scratching off the cells in a grid pattern using a 1 ml pipette tip. At the same point, the solution was exchanged with fresh media containing AuNP-DNA conjugates (2 ml, 1 nM) and left incubating for 18h at 37 °C, 5% CO_2 atmosphere in an incubator (Sanyo MCO-17AI). Cells were incubated with Hoechst 33342 (5 µl) for 1h as a nuclear stain. For imaging the glass coverslip was removed and washed with PBS. The coverslip was then mounted on a glass slide with a drop of PBS in order to keep cells alive. The edges around the coverslip were sealed using double-sided tape. All imaging was carried out on a Leica SP8 confocal microscope at 37ºC. Statistical analysis was performed using GraphPad Prism 7 software.

3.7.2.2 Real-Time Quantitative Polymerase Chain Reaction (qPCR)

Epithelial human cells (see section 3.5.1) were grown on 6-well plates with supplemented DMEM (see Appendix A for formulation). The wound assay was performed once cells were ~90 % confluent by scratching off the cells in a grid pattern using a 1 ml pipette tip. The cells were left to “recover” for 18h at 37 °C, 5% CO_2 atmosphere in an incubator (Sanyo MCO-17AI). Afterwards, cells were lifted

using trypsin (5 mL, 0.25 % trypsin, 0.01% EDTA solution) and its activity was inhibited by the addition of medium (13 mL). After centrifuging the cells once (3000 rpm, 4 °C, 10 min), the resulting pellet was re-dispersed in 200µl of 1x lysis buffer (25 mM Tris, 50 mM Glycerol Phosphate, 50 mM potassium chloride, 1% Triton, 1 mM DTT, 1x Protease inhibitor Tablet). Lysis of the cells was conducted by pipetting the cells through a 0.6 µm syringe to facilitate the breakdown of the cells. Finally, the resulting solution was centrifuged again (15000 rpm, 4 °C, 10 min), and the final supernatant was transferred to a fresh Eppendorf tube. The RNA was extracted using an All prep DNA/RNA mini kit (Qiagen, USA) following the recommended protocol. The resulting RNA was quantified using a Nanodrop 1000 (Thermo Scientific, USA). Finally, the PCR reaction was done using a Precision 2X qPCR Mastermix (PrimerDesign, UK), following the recommended protocol and using a MiniOpticon Real-Time PCR system (Biorad). The primers used were described previously [50] (see Table 3.1.) and obtained from AtdBio. The qPCR conditions included an initial increase of temperature to 95°C (10 mins at this temperature), followed by 95 °C for 15 s, 60 °C for 60 s and data collection (repeated 50x), and finally one final step with temperature increase from 45-95 °C for a melting curve. Statistical analysis was performed using GraphPad Prism 7 software.

3.8. Characterization techniques for silencing studies of *in vitro* and *in vivo* models using AuNP-siRNA conjugates

3.8.1 Microscopy

To investigate the effectiveness of AuNP-siRNA conjugates as gene knockdown agents for murine cells, three types of microscopy were used: light microscopy (section 3.8.1.1) to evaluate the rate of recovery of cells when wounded; epifluorescence (section 3.9.1.2) for visual assessment of protein expression and transmission electron microscopy (section 3.9.1.3) as a characterization method of the internalization of AuNP-siRNA conjugates.

3.8.1.1 Light Microscopy

MEF cells were seeded in 6-well plates at a cell concentration of 0.3 x 10^6 cell/well and kept at 37 °C, 5% CO_2 atmosphere in an incubator (Sanyo MCO-17AI). Once cells were ~90% confluent, a wound was created by scratching off the cells in a grid pattern using a 1 ml pipette tip. At the same time, media was exchanged with fresh media containing AuNP-siRNA conjugates (2 ml, 10 nM) and left incubating for 18h at 37 °C, 5% CO_2 atmosphere in an incubator (Sanyo MCO-17AI). The wound healing was monitored for a period of 5 days and pictures were taken with a Canon 60D. The processing was carried out on ImageJ software to assess the rate of wound closure across the time period.

3.8.1.2 Epifluorescence Microscopy

MEF cells were seeded in 6-well plates at a cell concentration of 0.3 x 10^6 cells/well and kept at 37 °C, 5% CO_2 atmosphere in an incubator (Sanyo MCO-17AI). Once cells were ~90% confluent, media was exchanged with fresh media containing either AuNP-siRNA conjugates at different concentrations (2 mL, 0.1-10 nM) or different control solutions (media alone, BSPP-coated AuNPs – 2 ml, 10 nM – or scramble control – 2 ml, 10 nM) for 24h.Cells were fixed by aspirating the corresponding media and covering them in ice-cold 100% methanol for 15 mins at -20ºC. The fixative solution was then aspirated and the cells were rinsed with 0.1 M PBS (3x) for 5 minutes each. The cells were then incubated with blocking buffer (1% Bovine Serum Albumin, Sigma-Adrich, in 0.1 M PBS) shaking for 30 minutes (200 rpm, RT). The solution was aspirated and the cells were incubated for 45 mins with a solution containing the primary antibody (Rabbit polyclonal Anti-Mouse SMAD3, AB28379, Abcam, 1:3000 dilution in 0.1 M PBS plus 0.1% BSA). The cells were then washed with 0.1 M PBS with 1% BSA (3x, 5 min each, 200 rpm, RT) and after the third wash a solution containing the secondary antibody (Goat Anti-Rabbit Cy3, AB6939, Abcam, 1:200 dilution in 0.1 M PBS with 1% BSA) was added for 45 min. After aspiration of the secondary antibody solution followed by three washing steps (0.1 M PBS with 1% BSA), the cells were incubated with DAPI (0.1 mg/ml, Sigma-Adrich) for 1h as a nuclear stain. Three last washes (5 mins each, 200 rpm, RT)

were done and the excess buffer was absorbed using a tissue. The mounting agent (Mowiol 4-88, 31 kDa, Sigma-Aldrich) was added and the cells were mounted in the wells using round cover slips. The final fixed cells were imaged on the 380 nm channel (DAPI) and the 550 nm channel (TRITC) using an Olympus IX81 inverted fluorescence microscope (for further processing see 3.9.2.1).

3.8.1.3 Transmission Electron Microscopy

To investigate the intracellular fate of AuNP-siRNA conjugates, cells were embedded in resin, cut into ultrathin sections and visualised by transmission electron microscopy. Resin embedding ensures the preservation of cell structure and intracellular compartments and allows specimens to be viewed in small sections with highly detailed resolution [51]. For this purpose, cells were seeded on cellulose transwell inserts in 12-well plates at cell concentrations of approximately 1×10^5 cells/mL. Once MEF cells had grown to ~90% confluency they were incubated with AuNP-siRNA for 24h, after which they were fixed for 1h in 3% glutaraldehyde / 4 % formaldehyde in 0.1 M piperazine-1,4-bis(2-ethanesulfonic acid) (PIPES buffer 0.1 M, pH 7.2). Three washing steps (10 min each) were done. Cells were subsequently treated with osmium tetroxide (1% in PIPES buffer 0.1M, pH 7.2) for 1h for staining. After a further three washing steps with PIPES buffer and one brief 30s wash with deionised water, cells were stained with a 2% aqueous solution of uranyl acetate for 20 min. The sample was then dehydrated by treatment with increasing percentages of ethanol dilutions (30, 50, 70 and 90%) for 10 min each. (N.B.: After treatment with 50% ethanol, transwell inserts were cut from the plastic in order to avoid plastic dissolution in high % ethanol. From this point onwards transwell membranes were placed in a small glass vial). After treatment with 90% ethanol, the sample was finally fully dehydrated by two consecutive washes in absolute ethanol (20 min each). In order to prepare for resin embedding, samples were then treated with acetonitrile for 10 min followed by 1:1 acetonitrile : SPURR resin overnight. The sample was subsequently fully emerged in pure SPURR resin for 6h for complete infiltration in order to ensure the removal of acetonitrile. After 6h the transwells were cut in half and each embedded in fresh SPURR resin in small embedding capsules and polymerised at 60 °C for 24 h. Resin blocks were then cut using a Leica RM 2255

ultramicrotome. Ultrathin (~100 nm) sections were collected on TEM grids (200 mesh) prior to imaging on a Hitachi H7000 transmission electron microscope (operating bias voltage of 75 kV).

3.8.2 Protein Expression Assays

3.8.2.1 Fluorescence Imaging

Epifluorescence images were taken as described in the previous section (3.9.1.2). For any sample under analysis, images were taken in two channels: 380 nm for DAPI nuclear staining and 550 nm for TRITC dye attached on the secondary antibody. Fluorescence analysis was then conducted using the software ImageJ. DAPI images had the respective overall intensity in grey value extracted and these values were used as a normalizer factor for sample-to-sample variation. The fluorescence from the TRITC images was also converted to grey values and these were normalized using the aforementioned DAPI values. Samples were compared to the control samples and the SMAD3 relative was expressed in percentage. For each different sample, three experiments were conducted and the average of the grey value was used. Statistical analysis was performed using GraphPad Prism 7 software.

3.8.2.2 Western Blot

MEF cells were seeded in 10 cm cell culture dishes (Thermofisher) at a cell concentration of 2 x 10^6 cells/dish and kept at 37 °C, 5% CO_2 atmosphere in an incubator (Sanyo MCO-17AI). Once cells were ~90% confluent, media was exchanged with fresh media containing either AuNP-siRNA conjugates at different concentrations (2 mL, 0.1-10 nM) or different control solutions (media alone, particles alone – 2 ml, 10 nM – or scramble control – 2 ml, 10 nM) for 24h. Afterwards, the media was disposed of and the cells were washed with ice cold PBS to remove an excess media. While the cell culture dish was placed on ice, the PBS was aspirated and an ice-cold RIPA lysis buffer (1 ml per dish, see Appendix A for formulation) was added and left incubating on ice for 5 mins. The adherent cells

were scraped off the dish and the cell suspension was gently transferred into a centrifuge tube (1.5 ml, Eppendorf).

Lysis was ensured by using a 0.6 µm syringe to facilitate the breakdown of the cells. The suspension was kept in agitation (30 min, 4 ºC) and was centrifuged (10000 rpm, 20 min, 4 ºC). The supernatant (i.e. lysate) was transferred to a fresh centrifuge tube and any cell debris in the pellet was discarded. 10 µl of each different lysate was used to perform a standard Bradford assay [52] to determine the protein concentration on each lysate. Next, 20 µg of each sample was taken and an equal volume of 2x Laemmli sample buffer (see Appendix A for formulation) was added. Each Laemmli-lysate solution was boiled (95 ºC, 5 min) for protein denaturation and the resulting boiled solution was centrifuged (10000 rpm, 1 min, RT).

Each sample was loaded to a different well on a 10% SDS-PAGE gel (see Appendix A for formulation) alongside a molecular weight marker (Precision Plus Protein™, Biorad). The gel was placed on a fitting electrophoresis tank (Biorad) filled with running buffer (see Appendix A for formulation) and a pre-run was conducted (5 min, 50 V) to ensure a perfect alignment of all the lanes of the gel. Once the pre-run was finished, the voltage was increased to 125 V and the separation was left to occur for 1h. Once the separation was concluded, the gel was placed in a 1x Transfer buffer solution (see Appendix A for formulation) to prepare the protein transfer sandwich. This sandwich consisted of a clamping cassette, a sponge on inside of each end of the cassette, followed by two pieces of filter paper (0.8mm Whatman, GE Lifesciences), the SDS-PAGE gel where the proteins were separated and membrane (0.2 µm PVDF, ThermoFisher) where the proteins would bind once diffused out of the gel. Due to the hydrophobicity of the PVDF material, the membrane was pre-soaked in methanol (100%) for activation. Both the gel and the membrane were located in the middle of the sandwich (see Figure 3.8.). The gel was ensured to be on the cathode side (i.e. negative), whilst the membrane was on the anode side (i.e. positive). N.B. During the assembling of the protein transfer sandwich, each element was added while ensuring that no air bubbles were formed to avoid “blind transfer” spots. The cassette was placed on a transfer tank (Biorad) filled with 1x transfer buffer (see Appendix A for formulation). The transfer was done at 4 ºC overnight at a constant current of 100 mA.

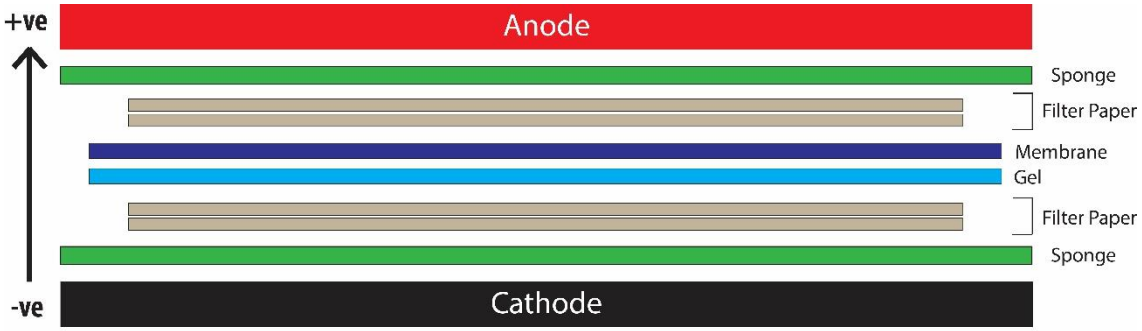

Figure 3.8. Protein transfer sandwich assembling

Once the transfer was finished, the successfulness of the blot (located on the membrane) was confirmed using Ponceau dye solution (see Appendix A for formulation). The Ponceau stained blot was then rinsed with three washes of TBST (see Appendix A for formulation) to remove the dye and the membrane was blocked using a solution of 3% BSA in TBST (1h, RT). The blocking solution was discarded and the blot was incubated overnight (4 ºC, 100 rpm) with a solution (3% BSA in TBST) containing the primary antibody (SMAD3 - Rabbit polyclonal Anti-Mouse, AB28379, Abcam, 1:50 dilution; GAPDH – Mouse monoclonal to GAPDH, AB8245, Abcam, 1:250 dilution). On the next day the blot was rinsed 5x with TBST to remove any unbound primary antibody. The blot was then incubated with a solution (3% BSA in TBST) containing the secondary antibody (IRDye® 800 CW Goat anti-Mouse or Donkey anti-Rabbit, Li-Cor 1:10000 dilution). The imaging of the blots was conducted using an Odyssey® Infrared imaging system and processing of intensity was done using ImageJ software. Statistical analysis was performed using GraphPad Prism 7 software.

3.8.2.3 *In cell* western blotting

In cell western blotting was used for a less disruptive and quicker assessment of the silencing capability of the AuNP-siRNA conjugates. [53, 54] In detail, MEF cells (see section 3.5.2) were grown on 48 well plates with conical bottom (Sigma-Aldrich) with a concentration of 1 x 10^5 cells/well at 37 °C, 5% CO_2 atmosphere in

an incubator (Sanyo MCO-17AI) using MEF culture media (see Appendix A for formulation). Once the cells were ~90% confluent on the top of the conical bottom (centre of each well), the media was discarded and a new media was added containing either AuNP-siRNA conjugates (0.1-10 pmol, 3 ml) or different control solutions (scramble control or only BSPP-AuNPs, 10 pmol, 3 ml). The cells were left incubating with the respective solutions for 24h. Afterwards, the solutions were aspirated and the cells were immediately fixed by the addition of 4% formaldehyde in PBS solution for 20 mins (150µl, 200 rpm, RT). The fixing solution was carefully added to avoid detachment of the cells from the well. The fixing solution was removed and disposed and then the cells were permeabilized (0.1% Triton X-100 in PBS, 200 µl, 200 rpm, 5x, 5 min each wash).

After the last step, the permeabilization solution was disposed of and the cells were blocked using a provided Odyssey® Blocking buffer (150 µl each well, 1.5h, 200 rpm, RT) on a plate shaker. The primary antibody (SMAD3 - Rabbit polyclonal Anti-Mouse, AB28379, Abcam, 1:50 dilution) was diluted in blocking buffer and 50 µl of the solution was added to all wells except the secondary antibody control wells (to which 50 µl of pure blocking buffer was added as a control for unspecific cross-reaction). The cells were incubated with this primary antibody solution overnight at 4 ºC with gentle shacking (200 rpm).

On the next day, the plate was washed with a solution of 0.1% Tween 20 in PBS (5x, 5 min each, 200 rpm) to remove excess unbound primary antibodies. After the last washing step, the secondary antibody (IRDye® 800 CW Donkey anti-Rabbit, Li-Cor 1:1000 dilution) was diluted in blocking buffer containing also a CellTag 700 nuclear staining dye (0.2 µM final concentration). Only secondary antibody control wells were not exposed to the primary antibody for normalization purposes. The final volume added to each well was 50 µl and the cells were left incubating with the respective solution (1h, 200 rpm, RT) in dark conditions to avoid photobleaching of both the nuclear stain dye and the tagged secondary antibody. Finally, the excess secondary antibodies were washed away (200 µl, 0.1% Tween 20 in PBS, 5x, 5 min each, 200 rpm, RT) and the plate was inverted carefully over a paper towel to dry the excess washing buffer. The plate was then either immediately scanned using an Odyssey® Infrared imaging system or stored at 4 ºC in dark conditions.

The scans were conducted for both the 700 nm and 800 nm channels for 7 min with an intensity setting of 7 for both channels across all samples. Results were processed in the Odyssey® Image Studio™ software, using the secondary antibody only control as a normalization factor for any unspecific fluorescence. Statistical analysis was performed using GraphPad Prism 7 software.

3.8.2.4 qPCR

MEF cells were grown on 6-well plates at a cell concentration of 1 x 10^5 cells/well at 37 °C, 5% CO_2 atmosphere in an incubator (Sanyo MCO-17AI). Some of the cells were incubated with either a scramble control solution or a SMAD3 siRNA conjugate solution (see Table 3.1. for sequences) for 18h. Afterwards, cells were lifted using trypsin (5 mL, 0.25 % trypsin, 0.01% EDTA solution) and its activity was inhibited by the addition of medium (13 mL). After centrifuging the cells once (3000 rpm, 4 °C, 10 min), the resulting pellet was re-dispersed in 200µl of 1x RIPA lysis buffer (see Appendix A for formulation). Lysis of the cells was conducted by pipetting the cells through a 0.6 µm syringe to facilitate the breakdown of the cells. Finally, the resulting solution was centrifuged again (15000 rpm, 4 °C, 10 min), and the final supernatant was transferred to a fresh Eppendorf tube. The RNA was extracted using an All prep DNA/RNA mini kit (Qiagen) following the recommended protocol. The resulting RNA was quantified using a Nanodrop 1000 (Thermo Scientific, USA). Finally, the PCR reaction was done using a Precision 2X qPCR Mastermix (PrimerDesign), following the recommended protocol and using a MiniOpticon Real-Time PCR system (Biorad). The primers used were described previously[55–57] (see Table 1) and obtained from AtdBio. qPCR was performed with an initial increase of temperature to 95°C (10 mins at this temperature), followed by 95 °C for 15 s, 60 °C for 60 s and data collection (repeated 50x), and finally one final step with temperature increase from 45-95 °C for a melting curve. Statistical analysis was performed using GraphPad Prism 7 software.

3.8.3 MTT Viability Assay

To test the potential toxicity of gold nanoparticles and AuNP-siRNA conjugates, a MTT viability assay was performed. [58, 59] In detail, MEF cells were plated in 48-well plates at a cell concentration of 1 x 10^4 cells/well at 37 °C, 5% CO_2 atmosphere in an incubator (Sanyo MCO-17AI) using MEF media (see Appendix A for formulation). Once the cells were ~75% confluent the media was exchanged for solutions containing either AuNP-siRNA conjugates (0.1- 50 nM), AuNP-DNA (1-50 nM), particles only (0.1-50 nM) or just fresh MEF media. The cells were incubated with the respective solutions for 24h. Afterwards, the solutions were disposed of and fresh MEF media was added to each well, and 10 µl of MTT reagent was added (12 mM in PBS).

Live and active cells convert the MTT reagent (3-(4,5-dimethylthiazol-2-yl)-2,5-diphenyltetrazolium bromide) into an insoluble formazan salt ((*E,Z*)-5-(4,5-dimethylthiazol-2-yl)-1,3-diphenylformazan) through mitochondrial reductase activity (see Scheme X). This chemical reduction can be seen from the change of colour from yellow (MTT) to purple (formazan salt). By solubilizing the formazan salt and determining the optical density at 570nm, it is possible to determine the viability of cells when compared with healthy untreated cells. [60]

Cells were incubated with the MTT reagent for 3 hours at 37 ºC. Once this time has passed and the purple salt was visibly formed, 100 µl of DMSO was added to dissolve the formazan salt and the plate was incubated for 2h at room temperature in dark conditions. Later the plate was taken to a Microplate Reader (Model 680, Biorad) and the O.D. at 570nm was taken for the whole plate. The reading was deemed optimal if the blank wells had an absorbance value close to zero and the overall readings were between 0.75-1.25 of absorbance. The final values for the viability percentages were obtained by subtracting the blank values from all the other values and using the control untreated cells as 100%. All the other wells were compared to this control. Statistical analysis was performed using GraphPad Prism 7 software.

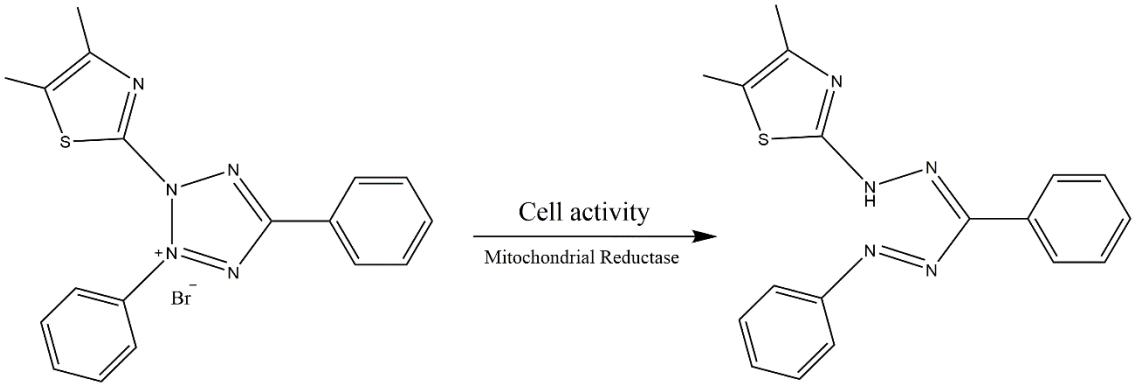

Figure 3.9. Chemical representation of MTT reduction to formazan through cell activity

3.8.4 *In vivo* wound closure assessment

3.8.4.1 Photography

The wound closure in *in vivo* models was monitored via photography from day 0 (the day the wound was created on the mice). Every day each mouse was anesthetized using 5% isoflurane in 100% oxygen (flow rate 1L/min) until unconscious. Afterwards, the isoflurane percentage was reduced to 2% to maintain anesthesia. The deep pedal reflexes of the mouse were checked to ensure full anesthesia. The unconscious mouse was then shaved using electrical clipper to clear the wounded area and placed close to a ruler for scale. Photographs of each wound were taken every day (0-15) approximately at the same time of the day. On the 15th day, once the wound was visually closed, the mice were euthanized via neck dislocation (see section 3.6) and skin biopsies were taken for histological processing (see section 3.9.4.2). The photographs were analysed using ImageJ software for wound diameter measurements using the ruler as a scale. Statistical analysis was performed using GraphPad Prism 7 software.

3.8.4.2 Histology

Skin biopsies obtained from the *in vivo* wound model mice had been stored in 10% neutral formalin buffered solution before being embedded in paraffin blocks. This was done using a standard dehydration protocol. [48] In detail, the tissue is processed gradually in an automated machine that processed the tissue in graded alcohols (70/90/100% v/v), then in xylene and finally in paraffin ready to be embedded. The embedding was done in a Leica HistoCore Arcadia™ machine. The blocks were then sectioned in 2µm thick sections and the excess paraffin was removed using a standard hydration/dehydration protocol. [48] The paraffin was removed by subjecting the sections to various steps of first xylene and then graded alcohols (100/90/70% v/v), 10 minutes on each step. Once the final alcohol step was done, the tissue sections were stained for histological analysis.

The Movat's pentachrome stain was chosen due to its ability to stain various constituents of skin tissue in different colours, thus making it possible to distinguish between collagen and stiff fibres formation and consequently assess the level of scarring.[61, 62] In detail, the slides containing the skin sections were firstly stained for ground substance by submerging the sections in alcian blue (2% Aniline blue, 2% glacial acetic acid, 100 ml total volume distilled water) for 20 mins. Afterwards, the sections were washed for 10 min under running tap water and the slides were places in alkaline alcohol (0.2% KOH in 80% alcohol) for 1h to fix the alcian blue by converting it into monastral fast blue. Once this was done, the slides were once again washed under running tap water for 10 min and rinsed 3x in deionised water. Nuclei and elastic fibres were then stained by submerging the slides in Verheoff's haematoxylin solution (see Appendix A for formulation) for 15 min. The excess haematoxylin solution was removed by rinsing several time with deionised water. Afterwards, the tissue staining was differentiated (i.e. removal of non-specific binding) by submerging the slides in a ferric chloride solution (2% ferric chloride in deionised water). The differentiation was ensured by agitating the slides gently while submerged in the ferric solution and quickly stopping it by submerging the slides in tap water. The staining was checked under a light microscope and the differentiation step was repeated until the elastic fibres were clearly visible. Once the last differentiation repeat was done, the slides were places in sodium thiosulfate (5% in

deionised water) for 1 min. The slides were then washed under running tap water for 5 min and rinsed in deionised water straight after. The muscle tissue was subsequently stained using a crocein scarlet-acid fuchsin (8:2) solution (see Appendix A for formulation). The slides were kept in this solution for 1.5 min and the excess stain was removed by rinsing several times using deionised water first and in 0.5% acetic acid water after. The muscle tissue stain was differentiated in 5% aqueous phosphotungstic acid for 7.5 min and the differentiation was stopped by rinsing the slides using 0.5% acetic acid water first and absolute alcohol after (3x). Finally, the last staining step consisted of submerging the slides in a saffron solution (70% w/v solution in absolute alcohol) for 30 min to dye the collagen fibres present in the tissue. The excess saffron solution was removed by rinsing the slides three times using absolute alcohol.

The slides were then moved back up the graded alcohols (100/90/70% v/v) and finally the xylene, before being mounted in the slide using Sub-X mounting agent (Leica Biosystems). Imaging of the slides was done using an Olympus Dotslide system. Measurements of the wounded area and collagen levels were done using ImageJ software by comparing the control tissue from each mouse against the AuNP-siRNA SMAD3 treated wound and the scramble control treated wound. Statistical analysis was performed using GraphPad Prism 7 software.

3.9. Characterization of the sensor based on lanthanide upconversion nanoparticles-DNA conjugates and graphene oxide

3.9.1 Laser Set-up

For the characterization of the UCNP-DNA-GO sensor, a homemade laser setup was built (Figure 3.10.) with the help of Prof. Otto Muskens. In detail, the laser source (980 nm, 500 mW, Top-Lasers) was located outside of the setup area, pointing to a fixed silver-coated mirror (97% reflectance, Thorlabs). This mirror directed the laser irradiation into a plano-convex lens (AR 650-1050 nm, Thorlabs) which focus the beam into the sample in a unidirectional manner, thus avoiding interferences from backscattered light. Samples were always measured in a quartz

micro cuvette (3 mm path length, 1 ml volume, Aireka Cells). By having a 90º configuration from the sample to the detectors any unwanted interference from the laser source was avoided. In addition, any irradiation that did not interact with the sample solution was blocked by a beam blocker. The irradiated fluorescence light originated by the UCNPs was then focused by a bi-convex lens (AR 350-800nm, Thorlabs) to a removable silver-coated mirror (97% reflectance, Thorlabs). In the absence of the mirror, the light would continue to another bi-convex lens that focused the emitted fluorescence from the sample to the spectrophotometer detector (350-1000 nm USB2000+, OceanOptics) for spectrometric analysis (2.000 ms of integration time and 100 scans to average; resulting data was processed using Origin 9.1 software). Alternatively, the presence of the mirror would redirect the emitted fluorescence from the UCNPs into a different plano-convex lens (AR 350-800 nm, Thorlabs). This lens would focus the emitted fluorescent light to the photon detector, while making it pass through a bandpass filter (540 ± 2 nm, Thorlabs) to ensure that any photons detected would be at the wavelength of interest. This ensured the specificity of the signal while increasing the lower detection limit of the whole system for photon analysis (count rate <200 counts/sec; resulting data was processed using Origin 9.1 software). Statistical analysis was performed using GraphPad Prism 7 software.

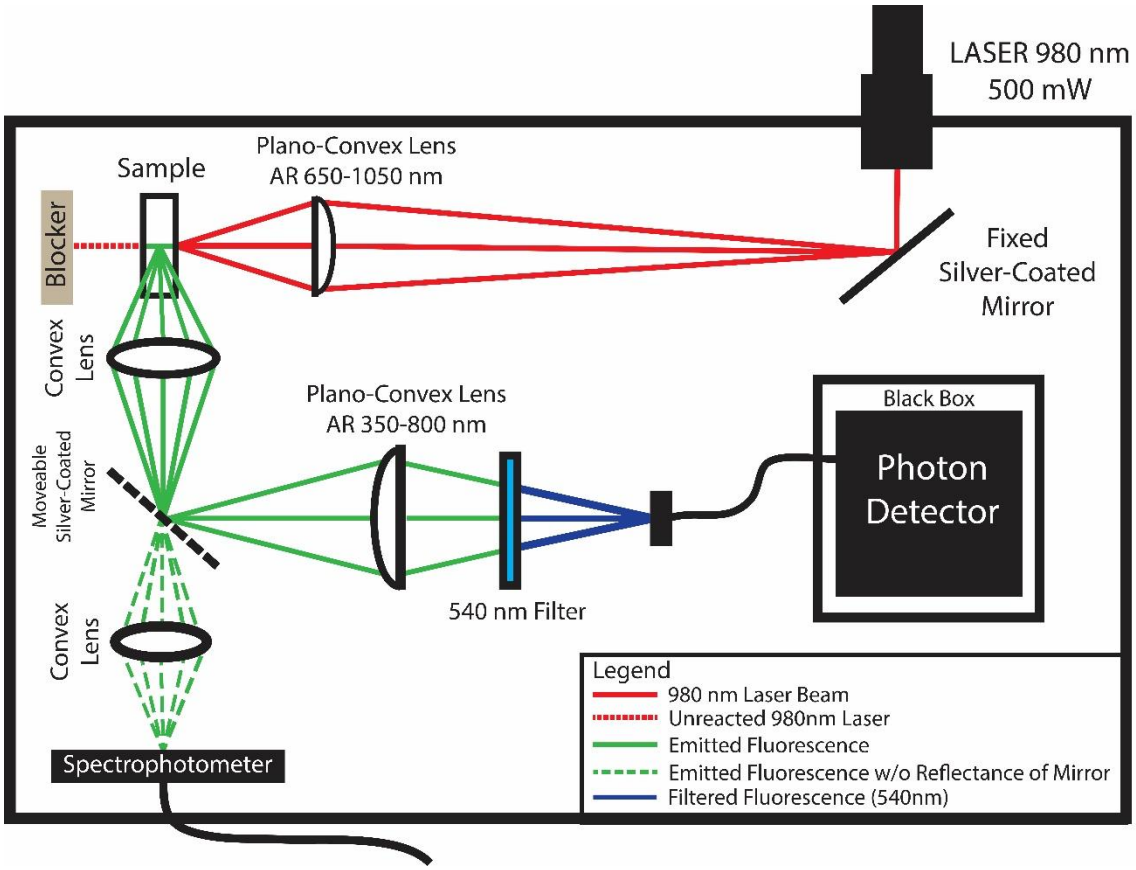

Figure 3.10. Laser setup for the analysis of UCNP-DNA-GO sensor. A 980nm laser light was directed to the sample under analysis. If the sample reacted with the light, it emitted fluorescent light which would be either re-directed to a photon detector or to a spectrophotometer, depending on the aim of the analysis.

3.10. References

1. J. Turkevich; P.C. Stevenson; J. Hiller. (1951). Synthesis of Gold Nanoparticles Turkevich method. *Discussions of the Faraday Society*, *11*, 55–75. doi: 10.1039/DF9511100055
2. Turkevich, J., Stevenson, P., & Hillier, J. (1953). The formation of colloidal gold. *The Journal of Physical Chemistry*, *57*, 670. doi:10.1021/j50508a015
3. Frens, G. (1973). Controlled Nucleation for the Regulation of the Particle Size in Monodisperse Gold Suspensions. *Nature Physical Science*, *241*(105), 20–22. doi:10.1038/physci241020a0
4. Kimling, J., Maier, M., Okenve, B., Kotaidis, V., Ballot, H., & Plech, A. (2006). Turkevich method for gold nanoparticle synthesis revisited. *Journal of Physical Chemistry B*, *110*(32), 15700–15707. doi:10.1021/jp061667w
5. Schmid, G., & Lehnert, A. (1989). The complexation of gold colloids. *Angew. Chem., Int. Ed.*, *28*(6), 780–781. doi:10.1002/anie.198907801
6. Lin, X., Sorensen, C., & Klabunde, K. J. (2000). Digestive Ripening, Nanophase Segregation and Superlattice Formation in Gold Nanocrystal Colloids. *Journal of Nanoparticle Research*, *2*(2), 157–164. doi:10.1023/A:1010078521951
7. Mangeney, C., Ferrage, F., Aujard, I., Artzner, V., Jullien, L., Ouari, O., Rekai, E. D., Laschewsky, A., Vikholm, I.,Sadowski, J. W. (2002). Synthesis and properties of water-soluble gold colloids covalently derivatized with neutral polymer monolayers. *Journal of the American Chemical Society*, *124*(20), 5811–5821. doi:10.1021/ja010796h
8. Wang, S., Qian, K., Bi, X., & Huang, W. (2009). Influence of speciation of aqueous HAuCl4 on the synthesis, structure, and property of Au colloids. *Journal of Physical Chemistry C*, *113*(16), 6505–6510. doi:10.1021/jp811296m
9. Verano-Braga, T., Miethling-Graff, R., Wojdyla, K., Rogowska-Wrzesinska, A., Brewer, J. R., Erdmann, H., Kjeldsen, F., (2014). Insights into the cellular response triggered by silver nanoparticles using quantitative proteomics. *Acs Nano*, 8 (3), 2161–2175. Retrieved from http://pubs.acs.org/doi/abs/10.1021/nn4050744
10. Turkevich, J. (1985). Colloidal gold. Part I. *Gold Bulletin*, *18*(4), 125–131. doi:10.1007/BF03214694
11. Xia, Y., Gates, B., Yin, Y., & Lu, Y. (2000). Monodispersed colloidal spheres: Old materials with new applications. *Advanced Materials*, *12*(10), 693–713. doi:10.1002/(SICI)1521-4095(200005)12:10<693::AID-ADMA693>3.0.CO;2-J
12. Long, N. N., Vu, L. Van, Kiem, C. D., Doanh, S. C., Nguyet, C. T., Hang, P. T., Thien, N. D., Quynh, L. M. (2009). Synthesis and optical properties of colloidal gold nanoparticles. *Journal of Physics: Conference Series*, *187*(1), 12026. doi:10.1088/1742-6596/187/1/012026
13. Li, Z., & Zhang, Y. (2008). An efficient and user-friendly method for the synthesis of hexagonal-phase NaYF(4):Yb, Er/Tm nanocrystals with

controllable shape and upconversion fluorescence. *Nanotechnology*, *19*(34), 345606–345610. doi:10.1088/0957-4484/19/34/345606

14. Liu, C., Wang, H., Li, X., & Chen, D. (2009). Monodisperse, size-tunable and highly efficient β-NaYF4:Yb,Er(Tm) up-conversion luminescent nanospheres: controllable synthesis and their surface modifications. *Journal of Materials Chemistry*, *19*(21), 3546. doi:10.1039/b820254k
15. Ye, X., Collins, J. E., Kang, Y., Chen, J., Chen, D. T. N., Yodh, A. G., & Murray, C. B. (2010). Morphologically controlled synthesis of colloidal upconversion nanophosphors and their shape-directed self-assembly. *Proceedings of the National Academy of Sciences of the United States of America*, *107*(52), 22430–22435. doi:10.1073/pnas.1008958107
16. Altschul, S. F., Gish, W., Miller, W., Myers, E. W., & Lipman, D. J. (1990). Basic local alignment search tool. *Journal of Molecular Biology*, *215*(3), 403–10. doi:10.1016/S0022-2836(05)80360-2
17. Seferos, D. S., Giljohann, D. A., Hill, H. D., Prigodich, A. E., & Mirkin, C. A. (2007). Nano-flares: Probes for transfection and mRNA detection in living cells. *Journal of the American Chemical Society*, *129*(50), 15477–15479. doi:10.1021/ja0776529
18. Giljohann, D. A., Seferos, D. S., Patel, P. C., Millstone, J. E., Rosi, N. L., & Mirkin, C. A. (2007). Oligonucleotide loading determines cellular uptake of DNA-modified gold nanoparticles. *Nano Letters*, *7*(12), 3818–3821. doi:10.1021/nl072471q
19. Giljohann, D. A., Seferos, D. S., Prigodich, A. E., Patel, P. C., & Mirkin, C. A. (2009). Gene regulation with polyvalent siRNA-nanoparticle conjugates. *Journal of the American Chemical Society*, *131*(6), 2072–2073. doi:10.1021/ja808719p
20. Jensen, S. A., Day, E. S., Ko, C. H., Hurley, L. A., Luciano, J. P., Kouri, F. M., Merkel, T. J., Luthi, A. J., Patel, P. C., Cutler, J. I., Daniel, W. L., Scott, A. W., Rotz, M. W., Meade, T. J., Giljohann, D. A., Mirkin, C. A., Stegh, A. H. (2013). Spherical nucleic acid nanoparticle conjugates as an RNAi-based therapy for glioblastoma. *Science translational medicine*, *5*(209), 209ra152. doi:10.1126/scitranslmed.3006839
21. Hurst, S. J., Lytton-Jean, A. K. R., & Mirkin, C. A. (2006). Maximizing DNA loading on a range of gold nanoparticle sizes. *Analytical Chemistry*, *78*(24), 8313–8318. doi:10.1021/ac0613582
22. Heuer-Jungemann, A., El-Sagheer, A. H., Lackie, P. M., Brown, T., & Kanaras, A. G. (2016). Selective killing of cells triggered by their mRNA signature in the presence of smart nanoparticles. *Nanoscale*, *8*(38), 16857–16861. JOUR. doi:10.1039/C6NR06154K
23. Claridge, S. A., Mastroianni, A. J., Au, Y. B., Liang, H. W., Micheel, C. M., Fréchet, J. M. J., & Alivisatos, A. P. (2008). Enzymatic ligation creates discrete multinanoparticle building blocks for self-assembly. *Journal of the American Chemical Society*, *130*(29), 9598–9605. doi:10.1021/ja8026746
24. Novina, C. D., & Sharp, P. a. (2004). The RNAi revolution. *Nature*, *430*(6996), 161–164. doi:10.1038/430161a
25. Kim, D. H., & Rossi, J. J. (2008). RNAi mechanisms and applications.

BioTechniques. doi:10.2144/000112792

26. Liu, S., & Han, M. Y. (2010). Silica-coated metal nanoparticles. *Chemistry - An Asian Journal*. doi:10.1002/asia.200900228
27. Guerrero-Martínez, A., Pérez-Juste, J., & Liz-Marzán, L. M. (2010). Recent progress on silica coating of nanoparticles and related nanomaterials. *Advanced Materials*, *22*(11), 1182–1195. doi:10.1002/adma.200901263
28. Sperling, R. a, & Parak, W. J. (2010). Surface modification, functionalization and bioconjugation of colloidal inorganic nanoparticles. *Philosophical transactions. Series A, Mathematical, physical, and engineering sciences*, *368*(1915), 1333–1383. doi:10.1098/rsta.2009.0273
29. Ling, D., Hackett, M. J., & Hyeon, T. (2014). Surface ligands in synthesis, modification, assembly and biomedical applications of nanoparticles. *Nano Today*, *9*(4), 457–477. doi:10.1016/j.nantod.2014.06.005
30. Palui, G., Aldeek, F., Wang, W., & Mattoussi, H. (2014). Strategies for interfacing inorganic nanocrystals with biological systems based on polymer-coating. *Chemical Society reviews*, *44*, 193–227. doi:10.1039/c4cs00124a
31. Staros, J. V., Wright, R. W., & Swingle, D. M. (1986). Enhancement by N-hydroxysulfosuccinimide of water-soluble carbodiimide-mediated coupling reactions. *Analytical Biochemistry*, *156*(1), 220–222. doi:10.1016/0003-2697(86)90176-4
32. Fischer, M. J. (2010). Amine coupling through EDC/NHS: a practical approach. *Methods in molecular biology (Clifton, N.J.)*, *627*, 55–73. doi:10.1007/978-1-60761-670-2_3
33. Bartczak, D., & Kanaras, A. G. (2011). Preparation of peptide-functionalized gold nanoparticles using one pot EDC/Sulfo-NHS coupling. *Langmuir*, *27*(16), 10119–10123. doi:10.1021/la2022177
34. Pasternack, R. M., Amy, S. R., & Chabal, Y. J. (2008). Attachment of 3-(aminopropyl)triethoxysilane on silicon oxide surfaces: Dependence on solution temperature. *Langmuir*, *24*(22), 12963–12971. doi:10.1021/la8024827
35. Maréchal, P., Coppens, G., Legras, R., & Dekoninck, J.-M. (1995). Amine/anhydride reaction versus amide/anhydride reaction in polyamide/anhydride carriers. *Journal of Polymer Science Part A: Polymer Chemistry*, *33*(5), 757–766. doi:10.1002/pola.1995.080330501
36. Patil, M. M., & Rajput, S. S. (2014). Innovare Academic Sciences SUCCINIMIDES : SYNTHESIS , REACTION AND BIOLOGICAL ACTIVITY, 8–14.
37. Xu, J. (2005). Preparation, culture, and immortalization of mouse embryonic fibroblasts. *Current protocols in molecular biology / edited by Frederick M. Ausubel*, *Chapter 28*, Unit 28.1. doi:10.1002/0471142727.mb2801s70
38. Galiano, R. D., Michaels V, J., Dobryansky, M., Levine, J. P., & Gurtner, G. C. (2004). Quantitative and reproducible murine model of excisional wound healing. *Wound Repair and Regeneration*, *12*(4), 485–492. doi:10.1111/j.1067-1927.2004.12404.x

39. Dunn, L., Prosser, H. C. G., Tan, J. T. M., Vanags, L. Z., Ng, M. K. C., & Bursill, C. A. (2013). Murine model of wound healing. *Journal of visualized experiments : JoVE*, (75), e50265. doi:10.3791/50265

40. Haiss, W., Thanh, N. T. K., Aveyard, J., & Fernig, D. G. (2015). Determination of Size and Concentration of Gold Nanoparticles from UV − Vis Spectra Determination of Size and Concentration of Gold Nanoparticles from UV - Vis Spectra, *79*(October), 4215–4221. doi:10.1021/ac0702084

41. Cho, E. C., Xie, J., Wurm, P. A., & Xia, Y. (2009). Understanding the role of surface charges in cellular adsorption versus internalization by selectively removing gold nanoparticles on the cell surface with a I 2/KI etchant. *Nano Letters*, *9*(3), 1080–1084. doi:10.1021/nl803487r

42. Dielacher, B., Tiefenauer, R. F., Junesch, J., & Vörös, J. (2015). Iodide sensing via electrochemical etching of ultrathin gold films. *Nanotechnology*, *26*(2), 25202. doi:10.1088/0957-4484/26/2/025202

43. Zhou, X., Xu, H., Cheng, J., Zhao, N., & Chen, S.-C. (2015). Flexure-based Roll-to-roll Platform: A Practical Solution for Realizing Large-area Microcontact Printing. *Scientific reports*, *5*, 10402. doi:10.1038/srep10402

44. Fertani-Gmati, M., Brahim, K., Khattech, I., & Jemal, M. (2014). Thermochemistry and kinetics of silica dissolution in NaOH solutions: Effect of the alkali concentration. *Thermochimica Acta*, *594*, 58–67. doi:10.1016/j.tca.2014.09.003

45. Zhang, Y., & Ying, J. Y. (2015). Homogeneous Immunochemical Assay on the Lateral Flow Strip for Measurement of DNase i Activity. *Analytical Chemistry*, *87*(20), 10193–10198. doi:10.1021/acs.analchem.5b02658

46. Voytas, D. (2001). Agarose Gel Electrophoresis. *Current protocols in Molecular Biology*, *Chapter 2*(1), 2.5A.1-2.5A.9. doi:10.1002/0471142727.mb0205as51

47. Lee, P. Y., Costumbrado, J., Hsu, C.-Y., & Kim, Y. H. (2012). Agarose gel electrophoresis for the separation of DNA fragments. *Journal of visualized experiments : JoVE*, (62), 1–5. doi:10.3791/3923

48. Redi, C. (2010). Histology protocols. *European Journal of Histochemistry*, *54*(2), 211–225. doi:10.1007/978-1-60327-345-9

49. Rossetti, F. C., & Depieri, L. V. (2013). Confocal Laser Scanning Microscopy as a Tool for the Investigation of Skin Drug Delivery Systems and Diagnosis of Skin Disorders. *Intech*, 99–140. doi:10.5772/55995

50. Renier, N., Wu, Z., Simon, D. J., Yang, J., Ariel, P., & Tessier-Lavigne, M. (2014). IDISCO: A simple, rapid method to immunolabel large tissue samples for volume imaging. *Cell*, *159*(4), 896–910. doi:10.1016/j.cell.2014.10.010

51. Bozzola, J. J., & Russell, L. D. (1999). *Electron Microscopy: Principles and Techniques for Biologists*. Jones and Barlett.

52. Harlow, E., & Lane, D. (2006). Bradford assay. *CSH protocols*. doi:10.1101/pdb.prot4644

53. Aguilar, H. N., Zielnik, B., Tracey, C. N., Mitchell(2010). Quantification of Rapid Myosin Regulatory Light Chain Phosphorylation Using High-Throughput In-Cell Western Assays: Comparison to Western Immunoblots.

PLoS ONE, *5*(4), e9965. doi:10.1371/journal.pone.0009965

54. Hoffman, G. R., Moerke, N. J., Hsia, M., Shamu, C. E., & Blenis, J. (2010). A high-throughput, cell-based screening method for siRNA and small molecule inhibitors of mTORC1 signaling using the In Cell Western technique. *Assay and drug development technologies*, *8*(2), 186–99. doi:10.1089/adt.2009.0213

55. Liu, Z., Shi, W., Ji, X., Sun, C., Jee, W. S. S., Wu, Y., Mao, Z., Nagy, T. R., Li, Q., Cao, X. (2004). Molecules Mimicking Smad1 Interacting with Hox Stimulate Bone Formation. *Journal of Biological Chemistry*, *279*(12), 11313–11319. doi:10.1074/jbc.M312731200

56. Meng, X. M., Huang, X. R., Chung, A. C. K., Qin, W., Shao, X., Igarashi, P., Bottinger, E. P., Lan, H. Y. (2010). Smad2 protects against TGF-beta/Smad3-mediated renal fibrosis. *Journal of the American Society of Nephrology : JASN*, *21*(9), 1477–1487. doi:10.1681/ASN.2009121244

57. Letterio, J. J., & Roberts, a B. (1998). Regulation of immune responses by TGF-beta. *Annual review of immunology*, *16*(1), 137–161. doi:10.1146/annurev.immunol.16.1.137

58. Alkilany, A. M., & Murphy, C. J. (2010). Toxicity and cellular uptake of gold nanoparticles: what we have learned so far? *Journal of nanoparticle research : an interdisciplinary forum for nanoscale science and technology*, *12*(7), 2313–2333. doi:10.1007/s11051-010-9911-8

59. Riss, T. L., Niles, A. L., & Minor, L. (2015). Cell Viability Assays. In *Assay Guidance Manual [Internet]* (pp. 1–23). doi:10.1016/j.acthis.2012.01.006

60. Marquis, B. J., Love, S. A., Braun, K. L., & Haynes, C. L. (2009). Analytical methods to assess nanoparticle toxicity. *The Analyst*, *134*(3), 425. doi:10.1039/b818082b

61. Jacobsen, J. N., Steffensen, B., Häkkinen, L., Krogfelt, K. A., & Larjava, H. S. (2010). Skin wound healing in diabetic β6 integrin-deficient mice. *APMIS : acta pathologica, microbiologica, et immunologica Scandinavica*, *118*(10), 753–64. doi:10.1111/j.1600-0463.2010.02654.x

62. McGee, H. M., Schmidt, B. A., Booth, C. J., Yancopoulos, G. D., Valenzuela, D. M., Murphy, A. J., Stevens, S., Flavell, R. A., Horsley, V. (2013). IL-22 promotes fibroblast-mediated wound repair in the skin. *The Journal of investigative dermatology*, *133*(5), 1321–9. doi:10.1038/jid.2012.463

Chapter 4: Detection of Vimentin mRNA in *in vitro* and *ex vivo* skin models using gold nanoparticle-oligonucleotide conjugates

Wound healing is a group of naturally occurring processes that initiate in every type of tissue upon injury. These processes start a cascade of events that aim to regenerate the tissue as promptly as possible in order to close the open wound and, consequently, reduce the risk of infection by bacterial, viral or fungal agents. [1] This can involve inflammatory signals, vasodilating and vasoconstriction agents, as well as proliferation and cell regulation factors. [2, 3]

Many of the steps in these cascade mechanisms are controlled by the regulation of different proteins. For example, transforming growth factor (TGF)-β and connective tissue growth factor (CTGF) are upregulated in order to induce cell proliferation [4–6], while oscillations of Notch expression in intercellular sites-of-contact shapes tube formation and cell alignment. [7] The mechanisms involved in wound healing are highly influenced by the location of certain proteins and the respective mRNAs at different stages of the process. [8–10] Therefore, the dynamic visualization of mRNA is a crucial part for a deeper comprehension of the wounding mechanisms and any related dysfunctions.

Various methods have been introduced to visualize protein-encoding mRNA, which can infer information about protein production and, within tissue samples to some extent spatial localisation [11–13]. Nevertheless, the detection of mRNA in live cells and more complex systems such as tissue is extremely challenging. Common strategies used to monitor mRNA rely on fixation of cells (thus imaging only static time-points on the cell's life) [14, 15], sectioning of the cells/tissue (limiting the spatial information gathered) [16] and/or genetic fluorescence tagging (which take several cellular generations to act) [17, 18]. For example, fluorescence in situ hybridization (FISH), the most commonly used technique for spatial distribution studies of RNA, requires a lengthy cell processing and fixing protocol before analysis.[16] This results in a loss of dynamic spatial information, since the data gathered is restricted to a single time point.

Hybrid nanomaterials based on the combination of inorganic nanoparticles and biomolecules (proteins [19–21] , antibodies [22–24], oligonucleotides [25–27] , etc) have had an ever growing impact in a range of different applications, from nano-optics [28–30] and electronics [31, 32], to pharmaceutical [33, 34], sensing [35–37] and bioimaging [38–41]. In the latter for example, hybrid nanomaterials have been used to tackle some fundamental biological events, such as telomerisation [42], enzymatic activity [43, 44], DNA hybridization [45, 46] and cell differentiation [47–50], amongst others. Pioneering work from groups such as Mirkin *et al.* and Tang *et al.* have used gold nanoparticle-oligonucleotide conjugates in order to detect intracellular mRNA in real-time. Therefore, AuNP-oligonucleotide conjugates were presented as alternative imaging tools for the monitoring of protein-encoding mRNAs in cellular environments.

In this chapter, the synthesis of gold nanoparticles-dsDNA conjugates and its application for imaging of both cell and tissue models is presented. Gold nanoparticles (AuNPs) were synthesised and characterized (section 4.1.) before the attachment of specially designed oligonucleotide sequences. The successful formulation of the AuNP-DNA was confirmed *via* a range of techniques (section 4.2.) and the resulting conjugates were tested under different conditions for their stability (section 4.3.) and specificity (section 4.4.). These conjugates were then applied to *in vitro* models for the detection of Vimentin mRNAs (section 4.5.). Finally, AuNP-DNA conjugates were ultimately applied in *ex vivo* models of the skin (section 4.6.) for the 2D and 3D tracking of mRNA in complex tissue environment.

4.1. Synthesis and characterization of 13 nm AuNP

Gold nanoparticles (AuNPs) have several optical and chemical characteristics that make them ideal as a core for the attachment of fluorescent oligonucleotides. On the one hand, nanosized gold has a characteristic localized surface plasmon resonance (LSPR), in which, depending on the size of the nanoparticles, specific wavelengths of light are greatly absorbed. This renders AuNPs useful for the development of on/off fluorescent probes, as shown in previously reported literature

[51–53]. On the other hand, the versatile and straightforward chemistry of gold-sulphur bonding permits the conjugation of a variety of biomolecules onto gold surfaces, including AuNPs [54] (see section 2.1.1). Finally, gold has been shown to have low toxicity and to be non-reactive in cells, leading to is application in a wide variety of studies of inorganic NPs in biological applications. [55–59]

The main objective of this chapter involves the preparation and employment of advanced types of DNA-coated gold nanoparticles in bio-imaging. The sequences used were altered with two different cyanine dyes (Cy3 and Cy5), depending on their application (see Table 3.1. for full sequences). Both dyes have specific emission wavelengths: Cy3 – 570 nm and Cy5 –662 nm. Therefore, the gold core had to be synthesised at particle sizes that translated to plasmon bands that overlapped with the emission wavelengths of the dyes. Reports such as Fernig *et al.* (2007) [60] and El-Sayed *et al.* (2006) [61] demonstrated that to quench the wavelengths of interest (570/662 nm), 12-15 nm sized nanoparticles would be the most indicated. Therefore, gold nanoparticles were aimed to be synthesised at 13 nm in size. For that, the Turkevich-Frens method [62, 63] were used, in which the reduction of gold salt in the presence of a mild reduction agent such as sodium citrate leads to the controlled synthesis of monodisperse nanoparticles. In this type of synthesis, citrate molecules also act as coating agents that protect and stabilize the particles. However, citrate-coated particles are generally susceptible to irreversible aggregation, due to insufficiently strong electrostatic stabilisation of the nanoparticle core by citrate. [64, 65] Therefore, to increase their stability, nanoparticles were coated with Bis(*p*-sulfonatophenyl)phenylphosphine (BSPP, 1 mg/mL) [66, 67] prior to the attachment of synthetic oligonucleotides.

Figure 4.1.A demonstrates that gold nanoparticles were spherical and indeed monodisperse. Size distribution analysis (Figure 4.1.B) demonstrated that BSPP-coated AuNP were approximately 13 ± 1 nm in size (Figure 4.1.B). Consequently, analysis of the absorbance spectrum of the gold nanoparticles confirmed that the absorbance peaks at 522 nm, optimal for quenching of both Cy3 and C5 dyes (Figure 4.1.C).

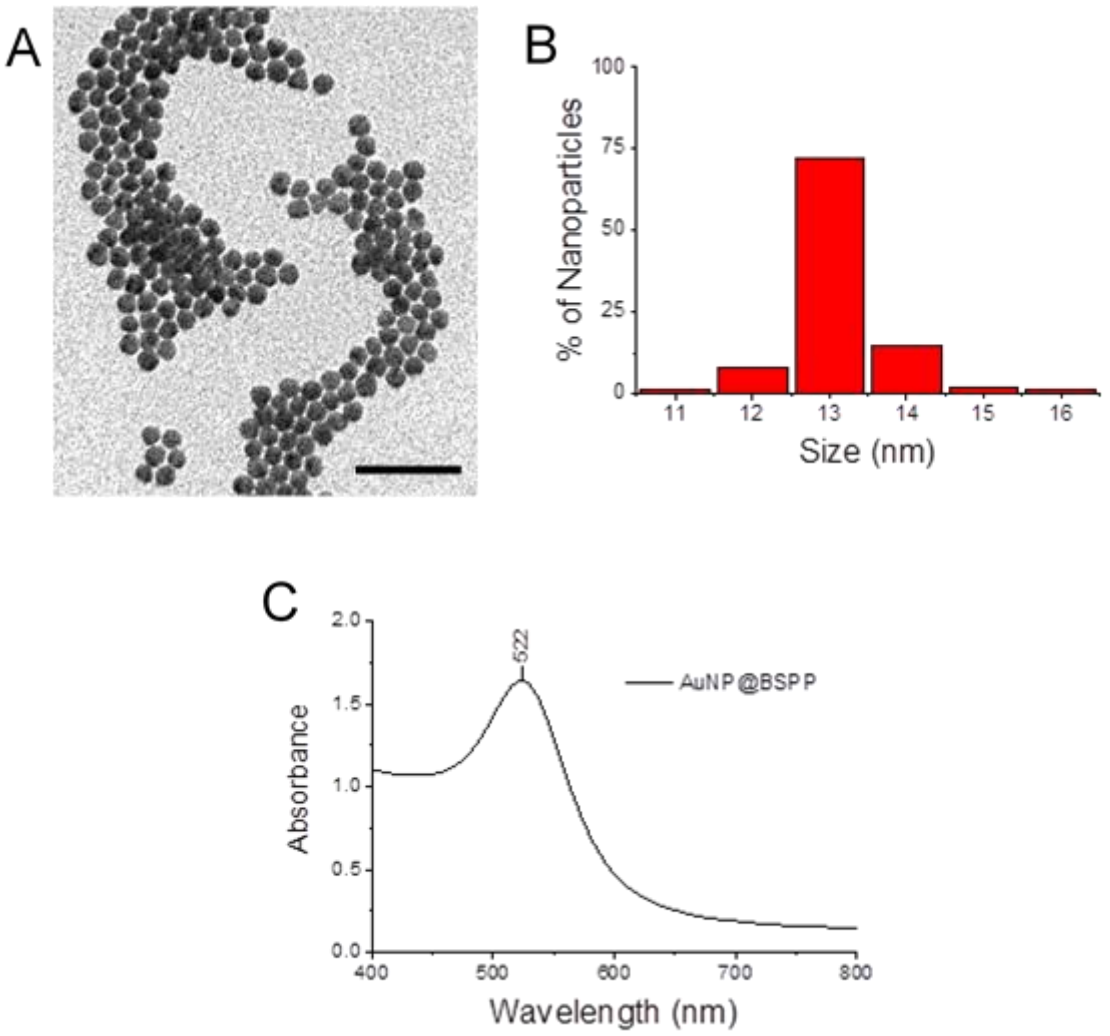

Figure 4.1. Characterization of BSPP-coated gold nanoparticles (AuNP@BSPP). (A) Gold nanoparticles were synthesized using the Turkevich-Frens method and observed by TEM (Scale bar = 100 nm). Synthesized particles were spherical, monodispersed and (B) with an average size of 13 ± 1 nm. (C) UV-Vis spectra of gold nanoparticle absorbance, with the peak absorbance at 522 nm. (Approximately 2000 particles counted)

4.2. Conjugation of oligonucleotides with AuNPs

The design of the AuNP-DNA conjugates was obtained based on previously reported work [68–70]. In detail, a Cy3 tagged ssDNA sequences complementary

to the mRNA target of interest are attached to the nanoparticles (sense strands) *via* a sulphur-gold bond. This bond is formed due to the proximity of the thiol group localized in the 5' end of the synthetic oligonucleotides. Another ssDNA sequence that mimics a smaller region of the target mRNA and is tagged with Cy5 (flare strands) is hybridized with the sense strands attached to the nanoparticles. At this point, due to the close proximity of the dyes in both strands to the gold core, their fluorescence is quenched and the conjugate is considered to be "off". However, in the presence of the target mRNA, the flare strand is released due to competitive hybridization, since the target mRNA has higher complementarity to the sense strand. With this release, the distance from the flare strands and the gold core increases, which restores the fluorescence of the Cy5 dye and the conjugate is "on". Additionally, Cy3-tagged sense strand serves as a reporter for any type of unspecific release (e.g. enzymatic degradation).

Therefore, since the fluorescence signal is highly visible in the presence of the target mRNA, the AuNP-DNA conjugates are "off-on" types of fluorescent sensors capable of in cell mRNA detection. Figure 4.2. schematically represents the process of detection as a whole.

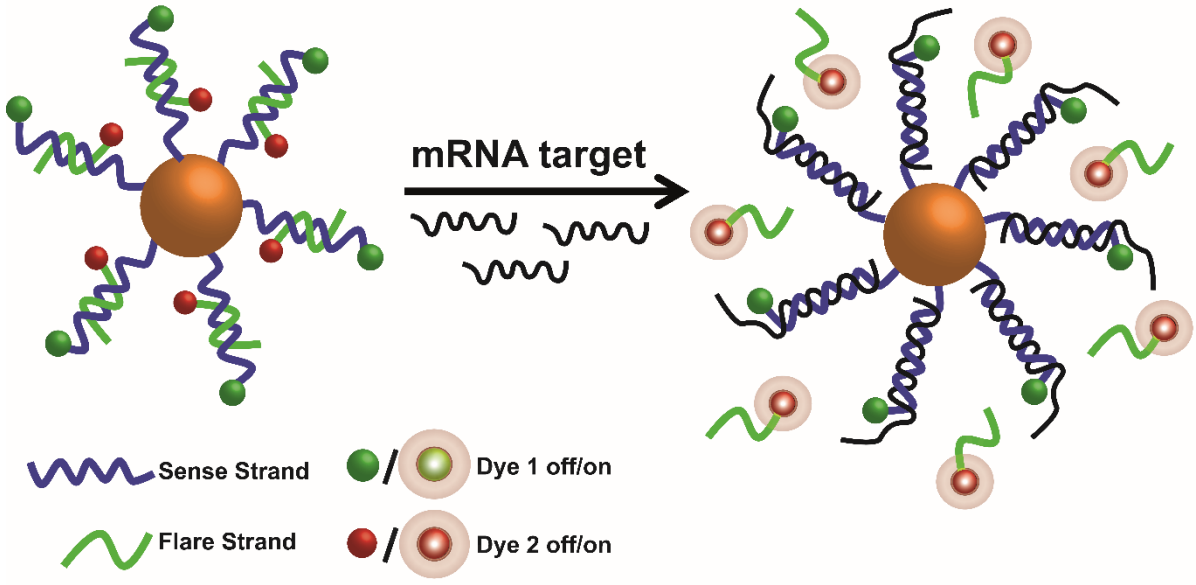

Figure 4.2. Schematic representation of the working principle of DNA-coated nanoparticles for the detection of mRNA. The DNA-coated nanoparticles are constituted by a dsDNA (sense + flare strands). When in close proximity to the AuNP core,

the two dyes in both strands are quenched. However, in the presence of the target mRNA, the flare strand is released due to competitive hybridisation and its fluorescence is restored.

In order to apply the AuNP-DNA conjugates for mRNA monitoring in different models (see sections 4.6-7.), Vimentin mRNA was chosen as a specific target to detect. Vimentin is an intermediate filament protein involved in the regulation of cell elasticity and movement. Consequently, Vimentin is highly expressed during the epithelial to mesenchymal transition (EMT). [71–73] As such, Vimentin mRNA sequences were chosen and analysed using the National Centre for Biotechnology Information's (NCBI) Basic Local Alignment Search Tool (BLAST) (see section 3.3.). The final sequences were designed by Dr. Amelie Heuer-Jungemann and kindly synthesised by ATDBio (Southampton, UK).

In order to conjugate the sense strands (Vimentin Sense - Cy3-CTT TGC TCG AAT GTG CGG ACT TAA AAA AAA - Thiol Group **OR** Scramble Control Sense - Cy3- GGT GGT CTT CGT ATG AAT ACA AAA AAA A - Thiol Group; for more detail please refer to Table 3.1) to the gold nanoparticles, both were incubated in the presence of increasing concentrations of salt (i.e. salt-aging) (see section 3.4.1.1.). The final conjugates were characterized using four different techniques: electron microscopy (Figure 4.3.A), ζ-potential (Figure 4.3.B) and UV-Vis (Figure 4.3.C-D) and fluorescence spectroscopy (Figure 4.3.E)

Figure 4.3.A shows the TEM micrograph of DNA-coated gold nanoparticles. Although no significant size difference between these conjugates and the BSPP-coated AuNP showed in Figure 4.1.A was observable, there is an increased separation between the gold nanoparticles. This is an indication that the DNA shell is present, since the highly negative backbone of the DNA strands induces a significantly higher electrostatic repulsion between AuNP-DNA conjugates.

This was confirmed by looking at the ζ-potential (Figure 4.3.B) where the exchange between citrate and BSPP in gold nanoparticles was observable through the shift of the overall net charge from −4 mV (blue) to −18 mV (red). Moreover, when the DNA sense strands were attached to the AuNPs, the net charge decreased even further to −32 mV. This effect is induced by the negative phosphate backbone of the DNA strands.

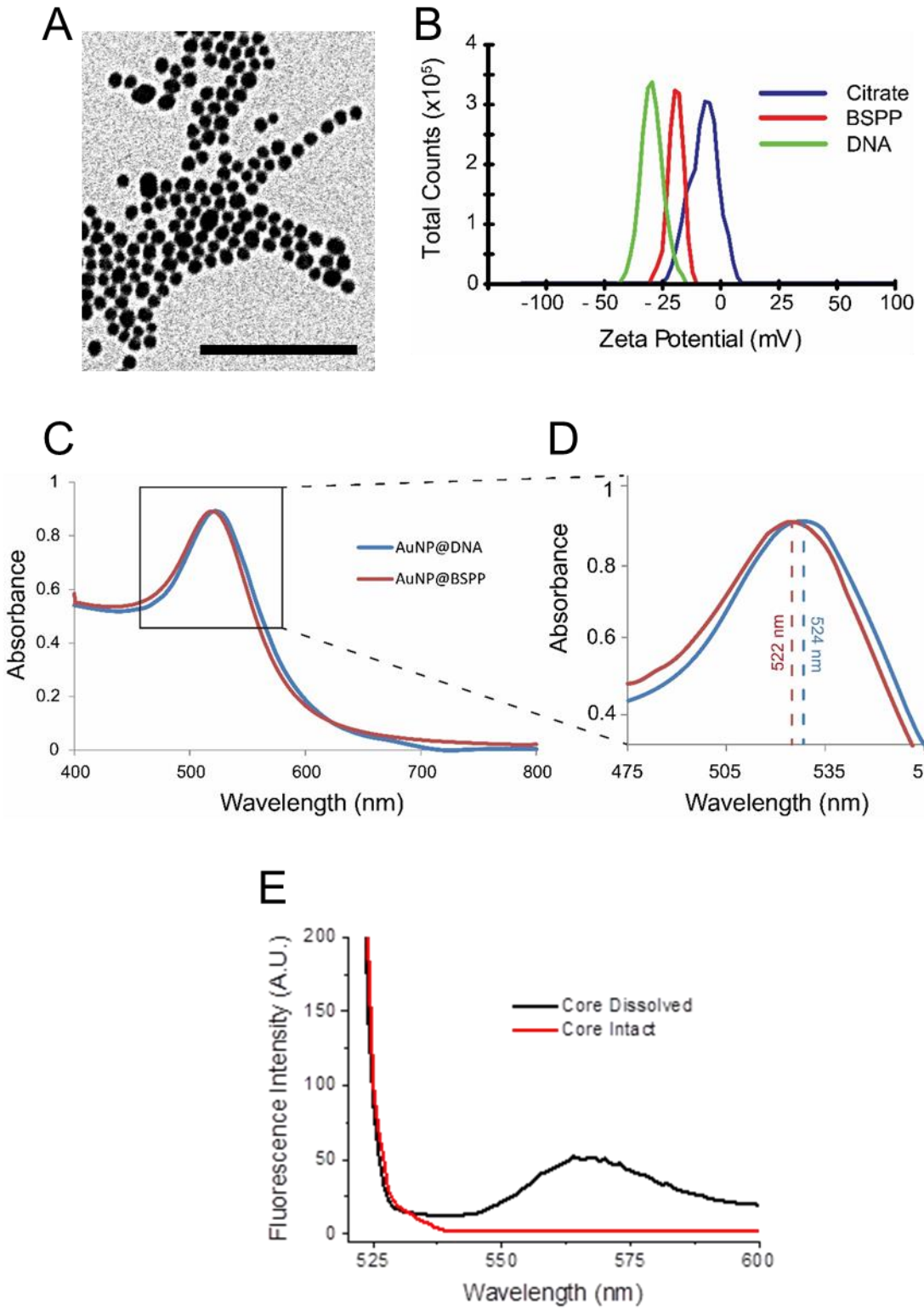
A
B
Total Counts (x10⁵)
Citrate
BSPP
DNA
Zeta Potential (mV)
C
D
Absorbance
AuNP@DNA
AuNP@BSPP
Wavelength (nm)
522 nm
524 nm
E
Fluorescence Intensity (A.U.)
Core Dissolved
Core Intact
Wavelength (nm)

Figure 4.3. Characterization of the DNA attachment to the AuNP's surface. The attachment of thiol-modified ssDNA strands (Vimentin Sense - Cy3-CTT TGC TCG AAT GTG CGG ACT TAA AAA AAA - Thiol Group; 3 nmol of DNA) was observed to have a small effect on the inter-particle distance when investigated under TEM (A) (Scale bar = 150 nm). Additionally, the ζ-potential analysis of the particles showed that not only the BSPP exchange was successful – visible from the shift from citrate at −4 mV (blue) to BSPP at −18 mV (red) – but also that the DNA lowered the overall net charge to −32 mV (black). UV-Vis analysis (C-D) demonstrated a slight shift from 522 nm (red) to 524 nm (blue) when the ssDNA was attached to the AuNPs. Finally, fluorescence spectrum of Cy3 (E) tagged strands after gold core dissolution shows the appearance of a 570 nm peak associated with the presence of the DNA strands.

Furthermore, UV-Vis analysis (Figure 4.3.C-D) demonstrated the successful attachment of DNA strands through a shift from the usual absorbance peak of BSPP-coated nanoparticles (red) from 522 nm to 524 nm (blue). This is a direct effect from the increase of the hydrodynamic radius of the particles when coated with DNA sequences. By having bigger molecules surrounding the nanoparticles, the radii of the particles is dynamically bigger, leading to a slight difference in their interaction with light. This translates to an absorbance peak that is slightly red-shifted in the resulting UV-Vis spectrum.

Finally, taking advantage of the Cy3 dyes in the sense strands, fluorescence spectroscopy was used to confirm the attachment of DNA sense strands. This was done by dissolving the gold core using an iodine etching method and purifying the oligonucleotide strands from the resulting solutions (see section 3.6.1.1.2). Since the gold core is what quenches the Cy3 dyes, the dissolution of the core corresponded to a restore of the fluorescence signal. Figure 4.3.E demonstrates that the fluorescence signal is observable after the gold core is etched (black). A characteristic 570 nm peak appears in the absence of the core, demonstrating that the strands are present in the nanoparticles. However, when the core is intact (red), the fluorescence peak is not present, confirming the quenching capability of the gold core.

Next, the characterization of the complete nano-probes (sense+flare) was performed. Therefore, flare strands were hybridized in an optimal ratio of 2:1 sense/flare, as reported by Mirkin and co-workers (2012) [74], prior to any further characterization. After dissolving the core, the sense strand detected by the appearance of a fluorescence peak at 662 nm after excitation at 645 nm. Figure 4.4.A shows the idiosyncratic emission profile of Cy5 present in hybridized AuNP-DNA nano-probes (black). However, in the absence of the flare strand (red), there was no visible peak for Cy5. Furthermore, the fluorescence analysis of both types of strands (sense and flare) permitted the calculation of the average number of strands on each nanoparticle. Calibration curves for both the sense (Figure 4.4.B) and flare (Figure 4.4.C) strands were plotted on a concentration range from 10 nM to 10 µM for the respective sequence. Using the obtained equations, it was possible to determine that the average number of sense strands detected was 97 ± 2 strands/particle and the average number of flare strands was 47 ± 2 strands/particle (see Appendix B.2. for example calculation).

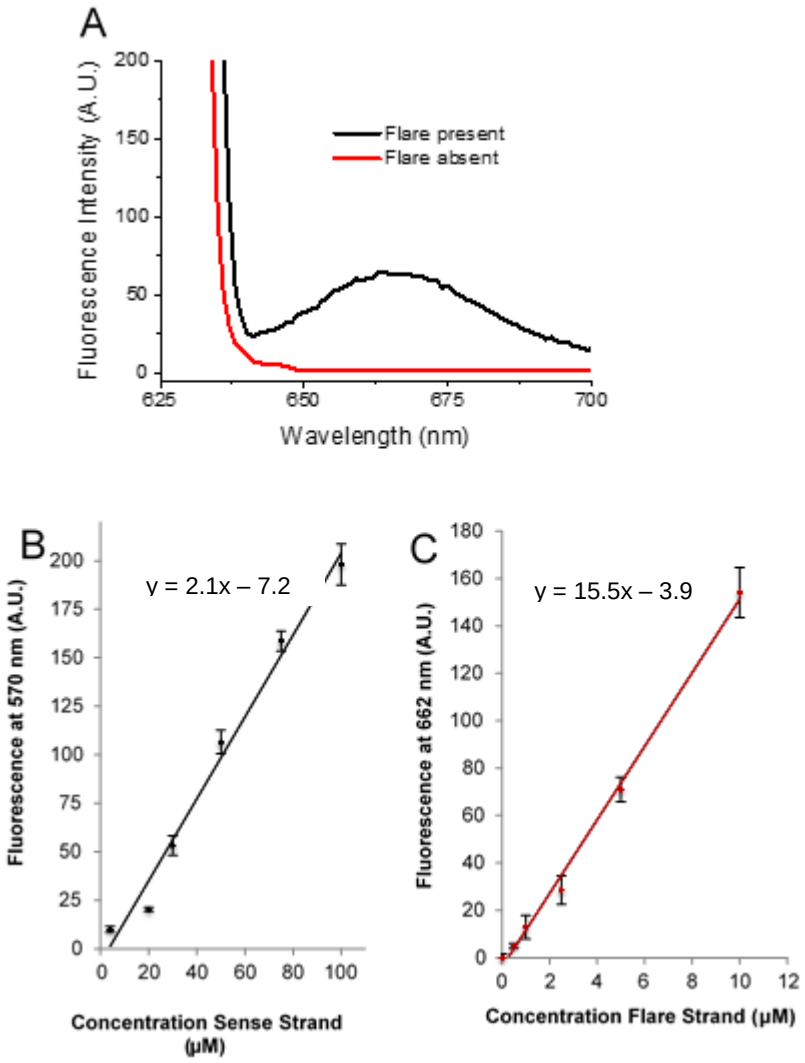

Figure 4.4. Characterization of hybridized sense/flare AuNP-DNA conjugates. The presence of the flare strand (Vimentin Flare - Cy5-AAG TCC GCA CA) for 10 nM of AuNP-DNA conjugates was confirmed via fluorescence spectroscopy (A) where a characteristic peak for Cy5 at 662 nm appears when the flares are hybridized to the sense strands. In addition, by obtaining calibration curves for different concentrations of sense (B) and flare (C) strands, it was possible to calculate the average number of each type of strand on the nanoparticles: sense – 97 ± 2 strands/particle; flare – 47 ± 2 strands/particle.

4.3. Stability of oligonucleotide-gold nanoparticle conjugates

In order to evaluate the stability of the AuNP-DNA conjugates, four assays were used: melting curve (section 4.3.1.), gluthathione assay (section 4.3.2.), DNAseI/II assay (section 4.3.3.) and incubation with cell media (section 4.3.4.).

4.3.1 Thermal stability

The melting temperature of an oligonucleotide duplex dictates at what temperature 50% of the strands are de-hybridised. This was relevant to test for the nano-probes in order to understand if there was the possibility of false-positive results upon incubating them in optimal cell culture conditions (i.e. at 37 ºC). Taking advantage of the dyes present in both sense and flare strands, the thermal stability was investigated by monitoring the fluorescence of the nano-probes in gradually increasing temperatures. Figure 4.5. reflects the melting curves for the sense (black) and the flare (red) strands.

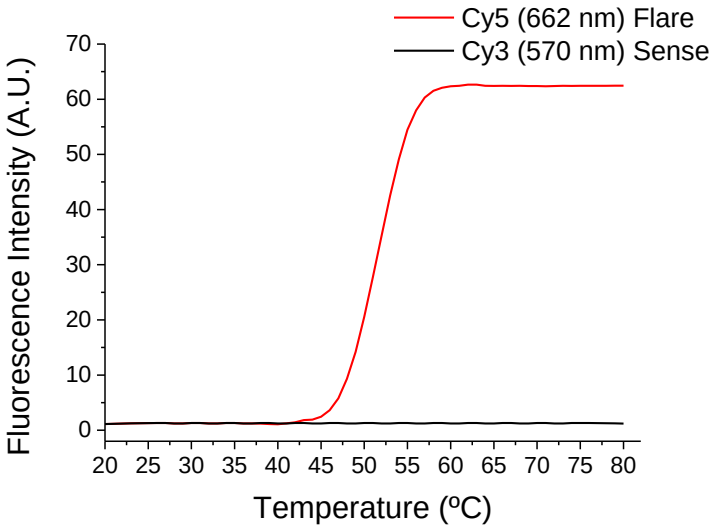

Figure 4.5. Thermal stability of complete AuNP-DNA conjugates. By subjecting nano-probes (10 nM) to increasingly higher temperatures, the fluorescence of both sense (570 nm, Vimentin Sense - Cy3-CTT TGC TCG AAT GTG CGG ACT TAA AAA AAA - Thiol Group) and flare (662 nm, Vimentin Flare - Cy5-AAG TCC GCA CA) strands were monitored. The melting temperature for the flare strand was at 52 ºC. On the other hand, the sense strand did not detach from the gold core, thus no fluorescence was detected.

The melting temperature (Tm) of the sense-flare duplex was approximately 52 ºC. As this temperature is higher than the one at which human cells are maintained (37 ºC) no unspecific release should be observed when incubating the conjugates with cell models. Additionally, the sense strand showed the same fluorescence intensity at all tested temperatures. This indicates that the sulfur-gold bond between the sense strands and the gold core is not affected by temperature. These results are in accordance with the work reported by Bhatt *et al* (2011), were it was shown that DNA attached to gold nanospheres is extremely resistant to a range of different conditions. [75]

Both results demonstrate the inherent stability of the nano-probes in optimal temperatures for cell culture and re-inforce the overall robustness of the conjugate.

4.3.2 Gluthathione assay

Glutathione (GSH) is a biomolecule that behaves as a sulfhydryl buffer as well as an antioxidant in mammalian cells. [76] Due to its free thiol group in the form of a cysteine residue, it is possible for GSH to cause DNA release *via* ligand replacement on the nanoparticle surface. To test the resistance of AuNP-DNA conjugates to DNA strand displacement, the nano-probes were treated with high concentrations of GSH (5 mM, typical intracellular concentrations vary from 0.5 to 5 mM [77]). The fluorescence of Cy3 and Cy5 of the duplex was closely monitored for 24 h (Figure 4.6).

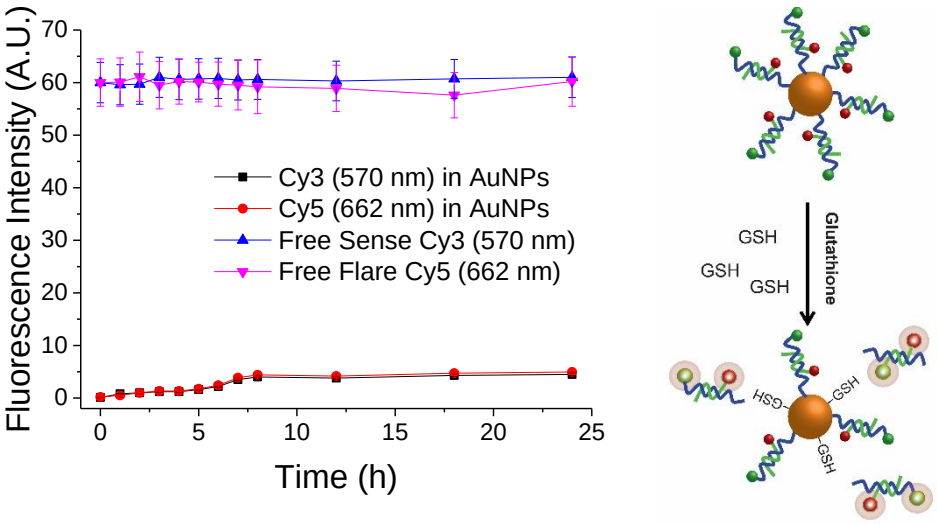

Figure 4.6. Stability of AuNP-DNA conjugates in glutathione rich environment. The nano-probes (2.5 nM) with both sense (Cy3-CTT TGC TCG AAT GTG CGG ACT TAA AAA AAA - Thiol Group) and flare strands (Cy5-AAG TCC GCA CA) were incubated with 5 mM of glutathione (GSH) and the fluorescence was monitored over 24h (left). In the event of displacement (right), the strands would come away from the nanoparticles and fluorescence would be restored. When compared with free strand solutions (blue and pink), the fluorescence signal of the strands attached to the nanoparticles (red and black) did not significantly change over time.

As shown, even at the high end of the intracellular concentration range of GSH, the nano-probes had more than 95% of sense strands still remaining on the nanoparticles surfaces, pointing to a high stability of this type of nano-probes in conditions mimicking the intracellular environment.

4.3.3 DNAse assays

A common concern with oligonucleotide-based intracellular probes is their susceptibility to degradation by nuclease enzymes. However, studies have suggested that probes based on DNA-AuNP conjugates show an increased stability towards nuclease digestion, especially by DNAse I [78, 79], an endonuclease present within the cytoplasm of cells [80, 81].

In order to determine the stability of our nano-probes against enzymatic degradation, dsDNA Vimentin nano-probes were incubated with DNAse I at 37 °C in optimal conditions. The fluorescence of both the sense and the flare strand was monitored for 36 h (Figure 4.7.).

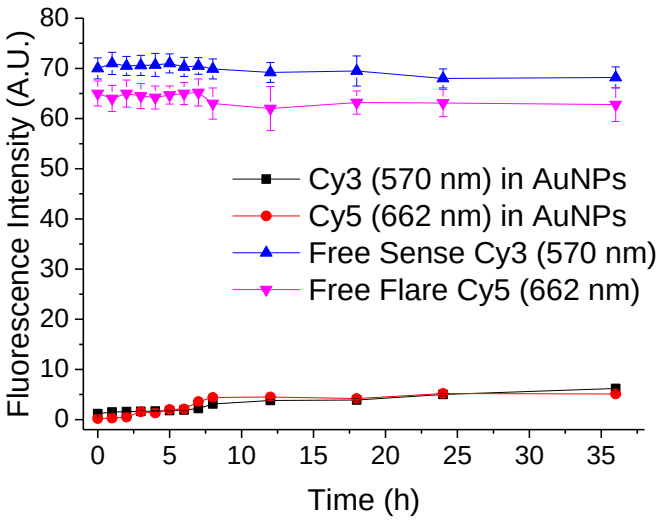

Figure 4.7. Stability of AuNP-DNA conjugates in the presence of DNAseI. 2.5 nM of hybridized nano-probes (with sense (Cy3-CTT TGC TCG AAT GTG CGG ACT TAA AAA AAA - Thiol Group) and flare (Cy5-AAG TCC GCA CA)) were incubated in the presence of 1 nM of DNAseI at 37 ºC. Fluorescence spectra was monitored over 36h. When compared with free strand solutions (blue and pink), both the sense (black) and the flare (red) strands were not detected in significant values, therefore showing the stability of the conjugates towards DNAseI enzymatic activity.

Figure 4.7. shows the fluorescence profile of both sense and flare strands in the presence of DNAseI. In comparison to 'free' sense or flare strands (obtained by particle dissolution), no significant increase of fluorescence in either the flare or the sense strands was observed when these were attached to the particles. This suggests that these nano-probes are not susceptible to degradation by DNAse I, as previously shown by Tang *et al.* (2012) [82].

Additionally, recent work by Mirkin *et al.* (2014) suggested that DNA-AuNP conjugates, although resistant towards digestion by DNAse I, could be aggregated

by DNAse II [78]. DNAse II exhibits optimal activity at acidic pH (common in lysosomes [83, 84]), and studies suggest that its main function is the degradation of exogenous DNA [85, 86]. To test the resistance of our probes to DNAse II-induced degradation, fully assembled probes were incubated with the enzyme at pH 4.5 and the fluorescence of both sense and flare strands was monitored for 24 h (Figure 4.8.)

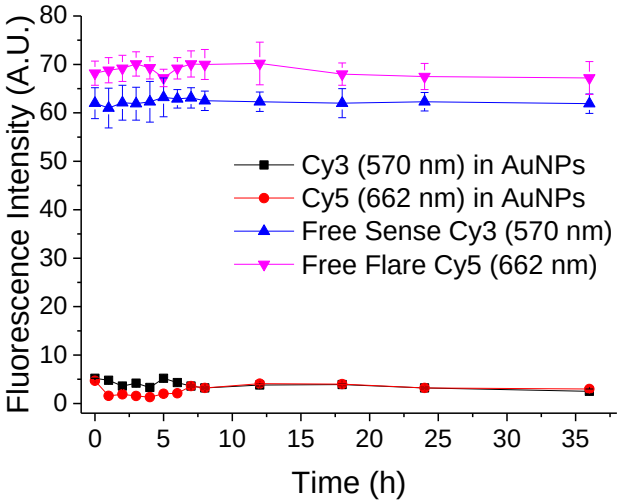

Figure 4.8. Stability of AuNP-DNA conjugates in the presence of DNAseII. 2.5 nM of hybridized nano-probes (with sense (Cy3-CTT TGC TCG AAT GTG CGG ACT TAA AAA AAA - Thiol Group) and flare (Cy5-AAG TCC GCA CA)) were incubated in the presence of 1 nM of DNAseII at 37 ºC. Fluorescence spectra was monitored over 36h. When compared with free strand solutions (blue and pink), both the sense (black) and the flare (red) strands were not detected in significant values, therefore showing the stability of the conjugates towards DNAseI enzymatic activity.

In these conditions, the fluorescence of the flare and sense was unaltered, thus showing that these probes are resistant to DNAse II. These results are in accordance with recently published work from our group, were a range of different nano-probes were incubated with DNAseII in lysomal mimicking conditions without any observable degradation. [70]

A possible explanation for this observable resistance to enzymatic activity could be that oligonucleotides attached to the nanoparticle surface adopt a slightly altered

conformation compared to their natural form as suggested by Pellegrino *et al.* (2007) [87]. In addition, a dense shell of DNA compacted onto the nanoparticles' surface can obstruct the enzymatic access in order to break down the dsDNA. [88] Therefore, both factors might inhibit the activity of DNAseI and DNAseII due to inaccessibility of the enzyme to the action sites. Nonetheless, more evidence needs to be gathered in order to understand the mechanism of protection that DNA coated gold nanoparticles have from DNAse enzymatic activity.

4.3.4 Incubation with cell media

Several groups have investigated the interactions of nanoparticles with cell culture media with serum. [89, 90] Several components found within these media such as salts and proteins can interact with the nanoparticles and alter their interaction with cells. [91–93] In order to test the stability of the nano-probes in cell culture media, probes were incubated with DMEM and MEM (see Appendix A for formulation) and the fluorescence of both strands was monitored for up to 18h. UV-Vis spectroscopy was also used to investigate the level of particle aggregation after 18h.

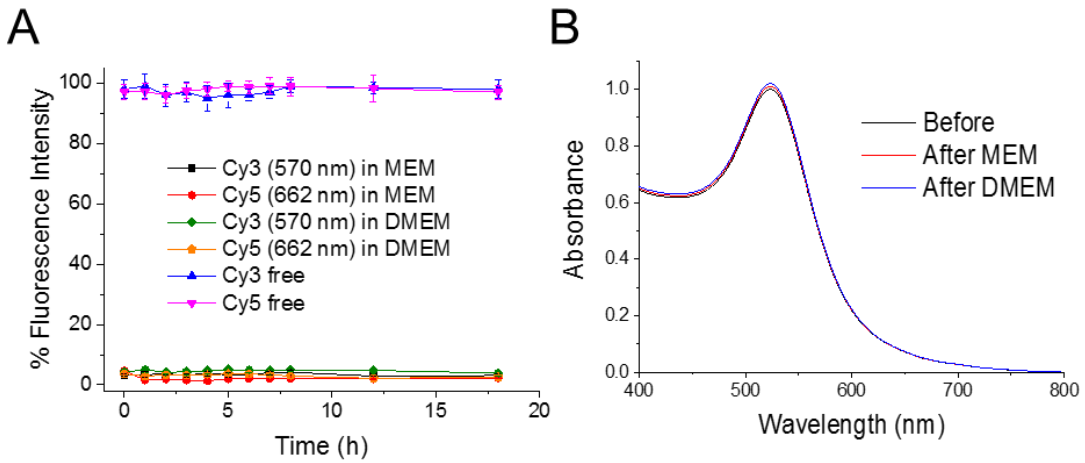

Figure 4.9. Stability of AuNP-DNA conjugates in cell culture media. 2.5 nM of fully hybridized nano-probes were incubated with both MEM and DMEM media for 18h. Fluorescence analysis (A) showed that no significant degradation of the strands was

observed. Additionally, UV-Vis analysis (B) demonstrated no significant aggregation of the AuNP-DNA conjugates.

As shown in Figure 4.9., probe stability was not affected by incubation with cell culture media. Both sense and flare strands remained attached to the nano-particles in the presence of both MEM and DMEM (Figure 4.9.A) and no signs of nanoparticle aggregation were observed, as determined by the unchanged plasmon peak at 524 nm (Figure 4.9B).

4.4. Specificity tests of AuNP-DNA conjugates

To determine the response rate and specificity of oligonucleotide coated nanoparticles against Vimentin mRNA, AuNP-DNA conjugates were incubated with synthetic Vimentin mRNA targets (AAG TCC GCA CAT TCG AGC AAA G; see Table 3.1. for more details). The fluorescence of the flare strand was measured over a period of 160 min. Representative maximum fluorescence intensities are shown in Figure 4.10.A. Further studies were also conducted to test the specificity of the probe. AuNP-DNA conjugates were incubated with artificial Vimentin mRNA targets containing one or two mismatched bases (see section 3.3.) and incubated for 1 h. Resulting spectra are depicted in Figure 4.10.B.

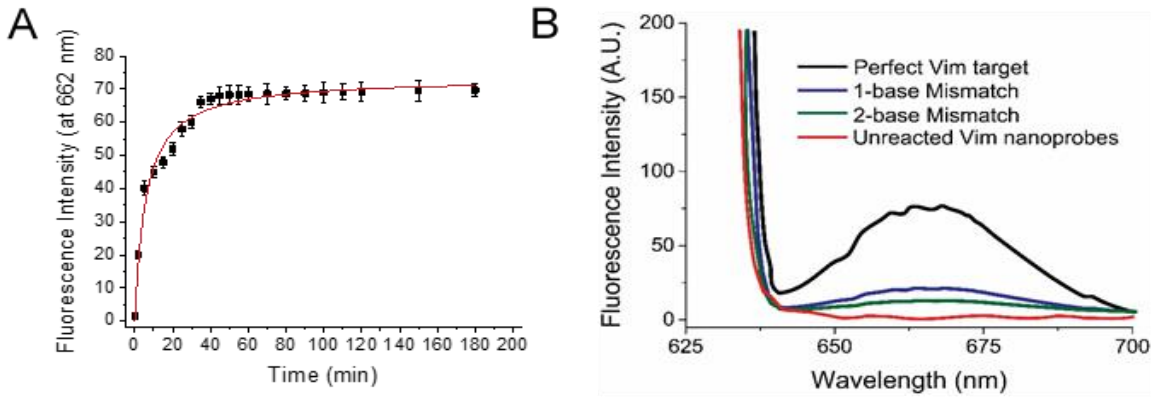

Figure 4.10. Specificity of Vimentin nano-probes. Vimentin nano-probes (10 nM) were incubated with an artificially designed complete target (AAG TCC GCA CAT TCG AGC AAA G; 100 nmol) and the fluorescence of the flare strand (662 nm; Cy5-AAG TCC GCA CA) was observed over 180 min (A). It was possible to observe a fluorescent signal after just 2 mins. Additionally, at 45 mins most of the flare strands had been displaced. On the

other hand, the specific detection of perfect Vimentin targets was investigated using UV-Vis spectroscopy (B). In the presence of non-perfect targets (1-base mismatch (AAG TTC GCA CAT TCG AGC AAA G) in blue and 2-base mismatch (AAG TTC GAC CAT TCG AGC AAA G) in green) the fluorescence signal is significantly lower (5x for 1-mismatch and 8x for 2-mismatch).

Figure 4.10.A shows a fast response rate, with a fluorescent signal detected increasing more than 40x in 5 min. Finally, a plateau was reached after 40 min, suggesting that most of the flare strands had been released at this time.

Additionally, the spectra presented in Figure 4.10.B show that incubation with mismatched targets (blue and green) induced minimal fluorescence increases. When compared to the complete sequence target, one-base mismatch was 5x lower, while a two-base mismatch sequence was 8x lower. The specificity of the probe in detecting the desired target was, therefore, demonstrated and the full probes were deemed optimal for application onto different models (sections 4.5-6.).

4.5. Application of AuNP-DNA conjugates in different *in vitro* models

In order to analyse the ability of the AuNP-DNA probes to recognize Vimentin in physiological conditions, these were applied in two human cell lines: 16-HBE (epithelial) and MRC-5 (fibroblasts). Since Vimentin is an intermediate filament protein associated with cell motility, this protein is oppositely expressed in the two different cell lines. On the one hand, fibroblasts are highly mobile cells, which translate to a high degree of Vimentin expression [94]; on the other hand, epithelial cells are mostly stagnant and fit closely packed together. Thus, the need for Vimentin in fully confluent epithelial cells is minimal [95]. Therefore, the imaging of mRNA in these cells lines was expected to be completely contrasting to each other.

Consequently, Vimentin nano-probes (1 nM concentration, Sense strand - AAG TCC GCA CAT TCG AGC AAA G - Thiol Group; flare strand (Cy5-AAG TCC GCA CA))were incubated with both 16HBE and MRC-5 cells once these were 90% confluent. After 18h, fluorescence images were taken and analysed (Figure 4.11.)

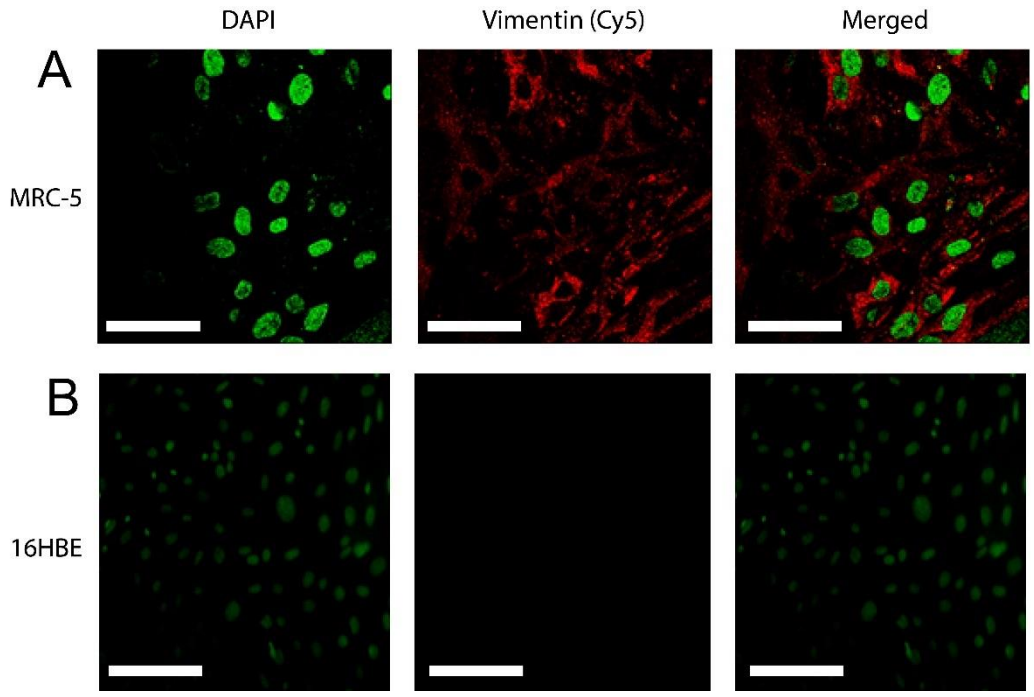

Figure 4.11. Incubation of Vimentin nano-probes with human cells. Fully assembled Vim conjugates (1 nM) were incubated with confluent cells for 18h and images were taken *via* confocal microscopy. While fibroblasts (MRC-5) (A) showed a fluorescent signal due to the presence of Vimentin mRNA (red), fully confluent epithelial cells (16HBE) (B) had no significant signal detected. (Scale bar = 50 µm)

Figure 4.11. shows that Vimentin is expressed differently in the two cells lines. Fibroblasts demonstrate a high degree of Vimentin mRNA expression (Fig. 4.11.A). This is seen from the fluorescence signal (red) present majorly localized in the cytoplasm. Oppositely, Vimentin mRNA expression was minimal in epithelial cells (Fig. 4.11.B), with no significant fluorescent signal detected. These results are in aggreement with recently published work by our group.[70] In the referred study, the capability of this type of AuNP-DNA conjugates for the specific delivery of Doxorubicin based on the presence of different mRNA targets in different human cells was investigated. There was a clear imaging of unique mRNA targets specific to different types of cells such as Keratin-8 for epithelial cells and Vimentin for fibroblasts. Therefore, alongside the mismatch experiments the nanoprobes were demonstrated to be specific in their detection of Vimentin mRNA. To further analyse

the localization of the fluorescence signal in the cytoplasm, optical cross-sectioning images were taken (Figure 4.12.).

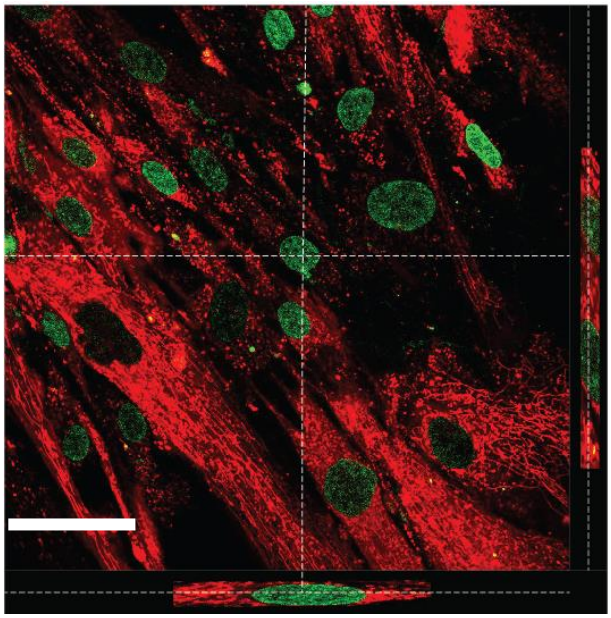

Figure 4.12. Spatial localization of the Vim flare strands. By doing an optical Z-stack, it was possible to observe that the red signal (consequent of the presence of Vim mRNA) was located in the same plane as the DAPI counterstain (green). (Scale bar = 20 µm)

It is possible to observe that the fluorescence signal (red) resulting from the release of the flare strand (i.e. the presence of Vimentin mRNA) was localized in the same focal plane as the signal from the nuclear stain (green). Therefore, this confirmed that the fluorescent signal was intracellular and not consequent of any extracellular artefact.

The main aim for the use of these nano-probes was to detect changes of Vimentin mRNA in wounded tissue. Vimentin is highly expressed for the movement of cells and plays a significant role in wound healing [72, 73]. Highly mobile cells such as fibroblasts demonstrate a natural high level of Vimentin[94]. However, upon damage, epithelial cells are also induced to move and Vimentin was shown to have an important role in their movement [71, 95, 96]. This mobilization of epithelial cells

in wound healing is mostly related with EMT, which is extremely important for a quick closure and covering of the wounded area [97].

To test if Vimentin mRNA significantly increases during wound healing, scratch assays were performed in both fibroblasts and epithelial cells. In this type of assay, cells are incubated until fully confluent and wound conditions are created by scratching the surface of the plate in a grid pattern. This type of migration assay has been reported to be a good translational model for wound healing in *in vitro* models, specifically in epithelial cells, since it thoroughly captures most of the intra- and intercellular pathways and agents involved in wound healing. [98–100]

Fully confluent cells were scratched in a grid pattern and incubated with the nano-probes (1 nM) for 18h. Confocal images were taken for fibroblasts (Figure 4.13) and for epithelial (Figure 4.14) cells.

As expected, fibroblasts have high levels of detected Vimentin mRNA, both close and away from the wound edge (Figure 4.13.) due to their motile nature. However, Vimentin mRNA levels are slightly increased near the wound site (5x higher). Therefore, even though the difference is not statistically significant, this is a visual representation of the sensitivity of the nano-probes.

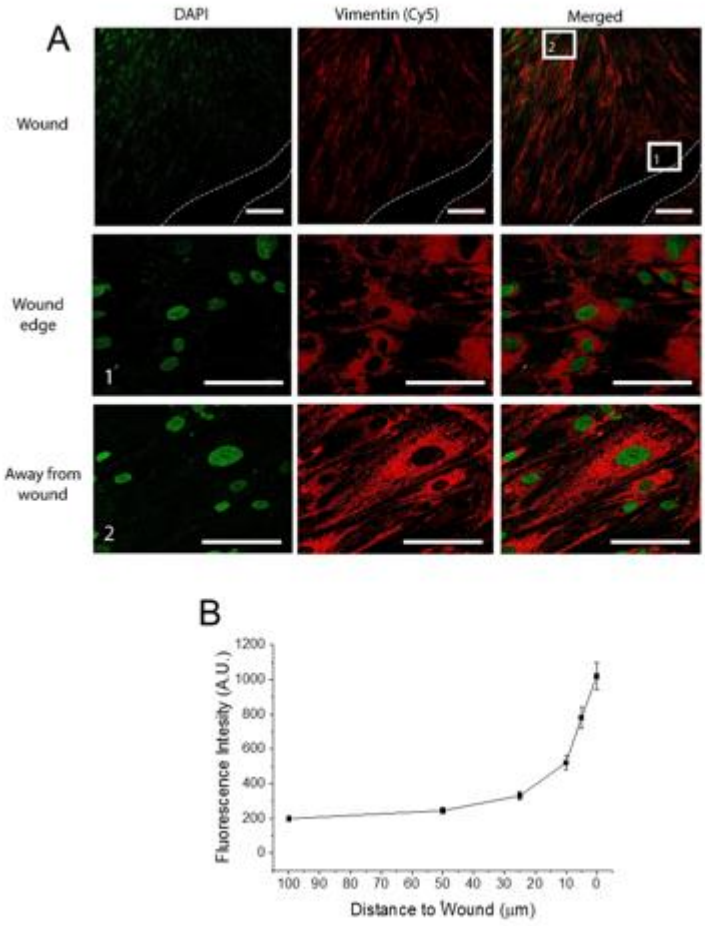

Figure 4.13. Scratch assay in human fibroblasts incubated with Vimentin nano-probes. After 18h of incubation with Vim conjugates (1 nM), a scratch assay was performed in human fibroblasts (A). Initial observations seem to indicate that the distribution of red signal is almost even across the cell layer (top), independently of the distance to the wounded area (depicted with white dotted lines). However, when zoomed in (middle and bottom), it is possible to see that the fibroblasts closer to the wound edge (1) have a slightly less intense and more sparse fluorescent signal when compared with cells away from the wound edge (2). By analysing the relative fluorescence intensities correlated with the distance to the wound site (B), it is possible to see that this difference, although small, it is detectable. (Scale bar = 50 µm)

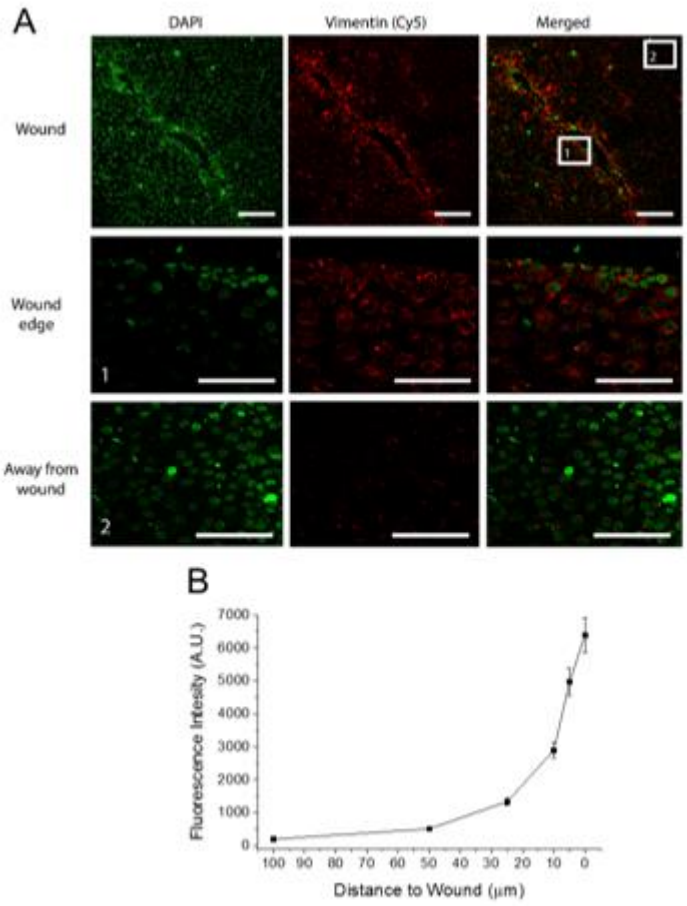

Figure 4.14. Scratch assay in human epithelial cells incubated with Vimentin nano-probes. After 18h of incubation with Vim conjugates (1 nM), a scratch assay was performed in human epithelial cells (A). A high fluorescent signal corresponding to the detection of Vimentin mRNA was observed near the wound site (1). Away from the wound site (2) a significantly weaker fluorescent signal was measured. Comparing relative fluorescence intensities (B) showed that the fluorescence signal intensity was lowest approximately 100 μm away from the wound edge and got progressively stronger away closer to the wound site, reaching values 1000x higher in cells right next to the wounded area (1) than farther away from it (2). (Scale bar = 50 μm)

In contrast, wounded areas of the grid pattern in epithelial cells shown a significant increase of the fluorescence signal. As seen from Figure 4.14.A, most of the wounded area is tinted with a red colour on the edges of the scratch. Furthermore, when zoomed in, it is possible to see that the area closer to the wound (1) is significantly brighter than the area away from the wound (2). Through

fluorescence analysis (Figure 4.14.B), it is possible to observe that the fluorescence signal increases the closer the cells are to the wounded site.

Moreover, when normalizing the data against the DAPI signal, wounded cells have 1000x higher detect Vimentin mRNA than confluent cells (Figure 4.15.A). To further investigate this result, qPCR was performed to quantify Vimentin mRNA levels in fully confluent epithelial cells versus wounded cells (Figure 4.15.B.). Vimentin mRNA levels from fully confluent fibroblasts was used as a control.

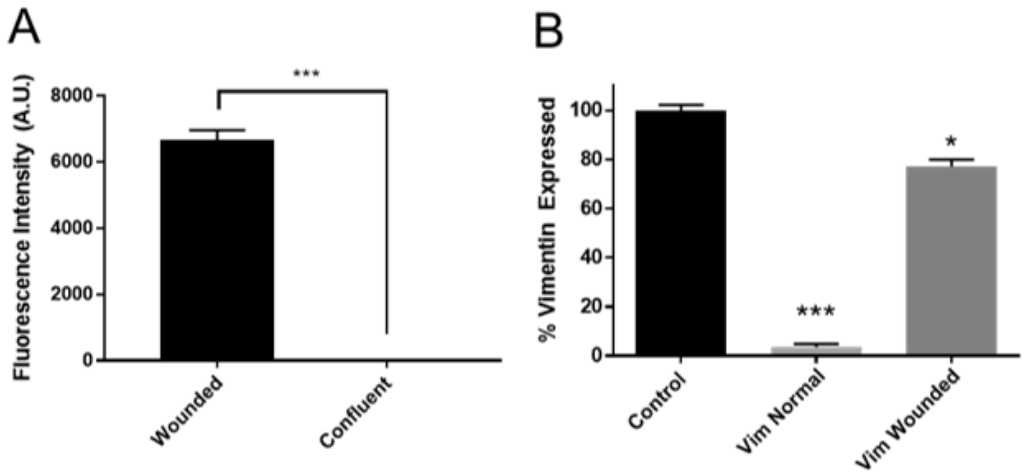

Figure 4.15. Vimentin expression levels on epithelial cells (wounded vs non wounded). Relative fluorescence intensity analysis between wounded epithelial cells and confluent (A) showed that expression of vimentin mRNA was 1000x higher in wounded cells than in confluent. Additionally, qPCR (B) demonstrated that wounded cells showed a significant increase (78%) of vimentin expression compared with fully confluent (normal, 6%). In addition, the levels were almost as high as the control (fully confluent fibroblasts) (*p<0.05,***p<0.001. Student's t-test)

As expected, epithelial cells from wounded areas express significantly higher levels of Vimentin mRNA then fully confluent cells (78% vs 6%). In fact, the levels of Vimentin mRNA in damaged epithelial cells are almost comparable with levels of naturally expressed in highly mobile cells.

The combined set of results for both epithelial and fibroblast cells demonstrated that this type of Vimentin nano-probe excels not only in spatially detecting the presence of Vimentin mRNA in different cell lines, but also when the same type of cell lines are subjected to external factors (such as signalled migration, for example). Therefore this type of detection method has the potential for applications in complex models such as whole tissue.

Nonetheless, since the *ex vivo* models used in this chapter (shown in section 4.6.) were based on *mus musculus* specimens, there was a need to examine the performance of the AuNP-DNA conjugates in murine cells. For that, the same type of sequence used previously on human cells was checked for overlapping regions using NCBI's BLAST. It was found that there was a significant conservation between species in the encoding region of the sequence, thus rendering the sequences used in human cells also useful for murine cells.

Before proceeding to a mouse model of wound healing, the Vimentin probes were tested in mouse embryonic fibroblasts (MEFs) to verify if the same sense and flare strands can recognize mouse Vimentin mRNA. Fully confluent MEFs were incubated with Vimentin conjugates and confocal images were taken after 18h (Figure 4.16).

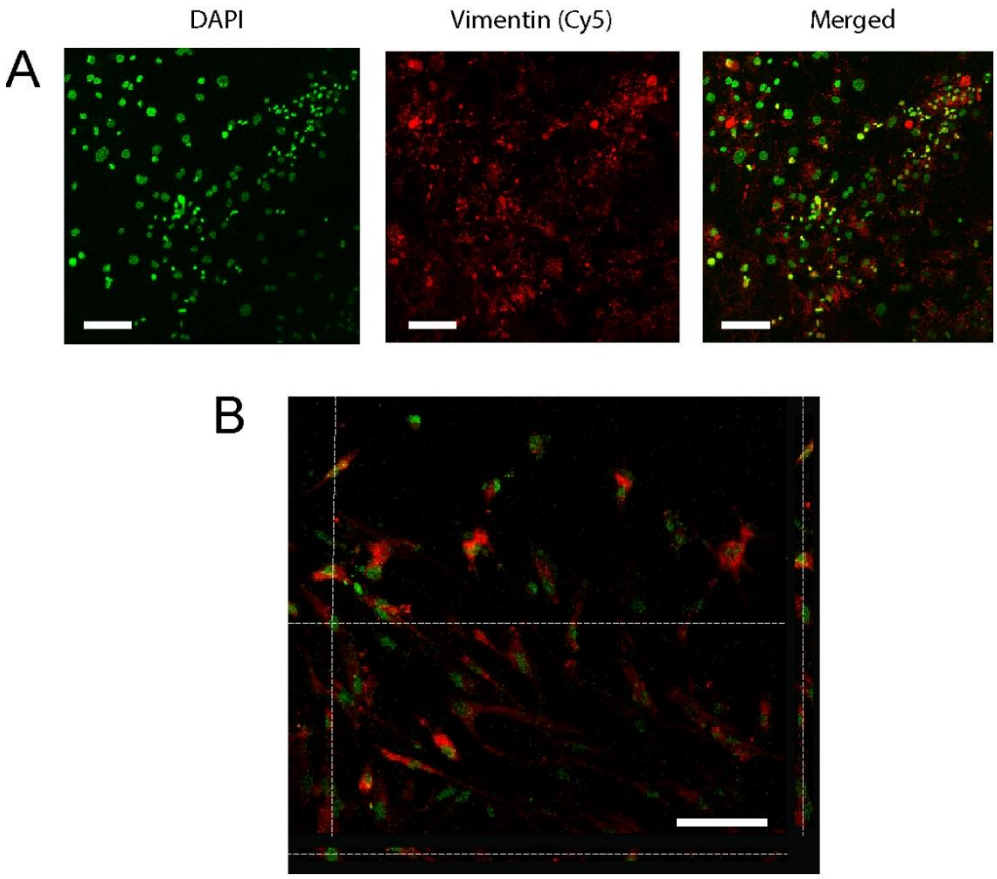

Figure 4.16. Incubation of Vimentin nano-probes with mouse embryonic fibroblasts. Fully assembled Vim conjugates (1 nM) were incubated with confluent MEFs for 18h and images were taken *via* confocal microscopy (A). Fluorescent signal correspondent to the presence of Vimentin was observed across the cells. Using a Z-stack image (B) it was possible to observe that the red fluorescence signal was localised in the same focal plane as the cell nucleus (green) (Scale bar = 50 µm)

It was observed that, as with the human cell lines, the Vimentin AuNP-DNA conjugates successfully recognized Vimentin mRNA (Figure 4.16.A). Additionally, when performing a Z-stack analysis of the confocal images (Figure 4.16.B), it is possible to see that the fluorescence is also located in the cytoplasm. Therefore, the nano-probes were observed to function both in murine and human cell models.

Despite their recurrent use in the development of delivery agents, some controversy exists regarding the possible cellular toxicity of gold nanoparticles. Groups such as Brandenberge *et al.* (2010) [101] and Chithrani *et al.* (2010) [102]

has shown that gold nanoparticles can accumulate intracellular in lysosomes without having a negative impact on cells. Contrastingly, recent work conducted by Yao *et al.* (2015) [103] demonstrated that epithelial cells are more prone to be affected by the presence of gold nano-spheres than fibroblasts. Additionally, Gunduz *et al.* (2017) [104] reported that a low dose exposure of vascular endothelial cells to gold nanoparticles can lead to their accumulation in the endoplasmic reticulum and induce cellular stress. Nonetheless, it has been shown previously that different aspects such as coating agents significantly contribute to the uptake and toxicity of gold nanoparticles. [57, 105]

Therefore, there was an interest to study the toxicity of our conjugates in the three different cell lines used (Figure 4.17.). For that, different concentrations of conjugates (0.1-10 nM) were added to the cells and an MTT assay was performed.

Figure 4.17. shows that no significant toxicity was observed in cells treated with Vimentin nano-probes, independent of their concentration.

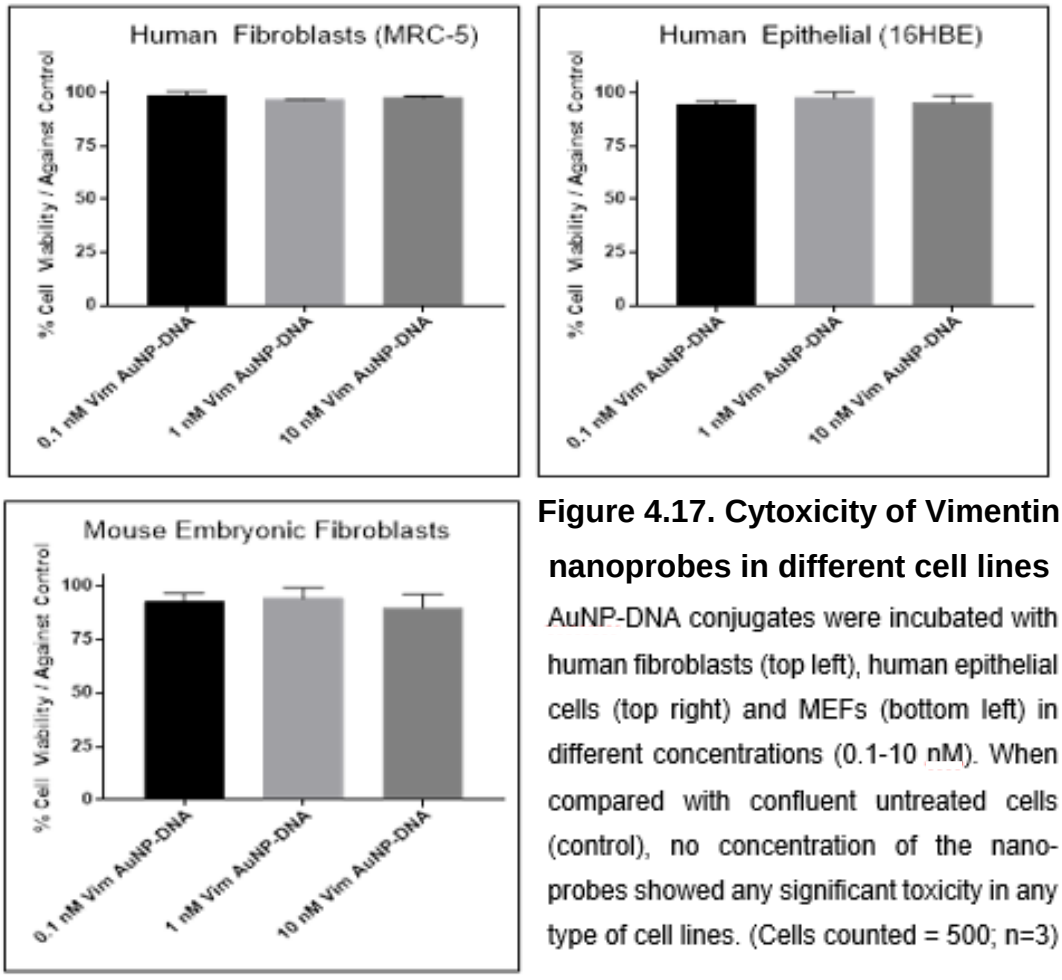

Figure 4.17. Cytoxicity of Vimentin nanoprobes in different cell lines

AuNP-DNA conjugates were incubated with human fibroblasts (top left), human epithelial cells (top right) and MEFs (bottom left) in different concentrations (0.1-10 nM). When compared with confluent untreated cells (control), no concentration of the nano-probes showed any significant toxicity in any type of cell lines. (Cells counted = 500; n=3)

4.6. Application of Vimentin AuNP-DNA conjugates in *ex vivo* murine models

Having successfully demonstrated the ability of the nano-probes to visualise Vimentin mRNA expression in both stationary and migrating cells, the next step was to investigate the conjugates' response in complex tissue environments. For this, dorsal murine skin of new-born mice was used as a tissue model. Skin was chosen because it is one of the most affected organs by wounding and the easiest one to investigate. [106] Additionally, skin tissue not only represents accurately the wound healing process as a whole, but some of its most prominent cell constituents include epithelial cells and fibroblasts. [107, 108] Consequently, Vimentin nano-probes were

injected into the dermis region of the skin, creating a wound in the process and simultaneously exposing the tissue to the probes. After 6 h of incubation, the skin was fixed, embedded and sectioned. To determine the viable regions of the skin biopsies, cell nuclei were stained with DAPI for analysis by confocal microscopy. Figure 4.18 shows wounded regions of the skin where the presence of Vimentin mRNA is observed.

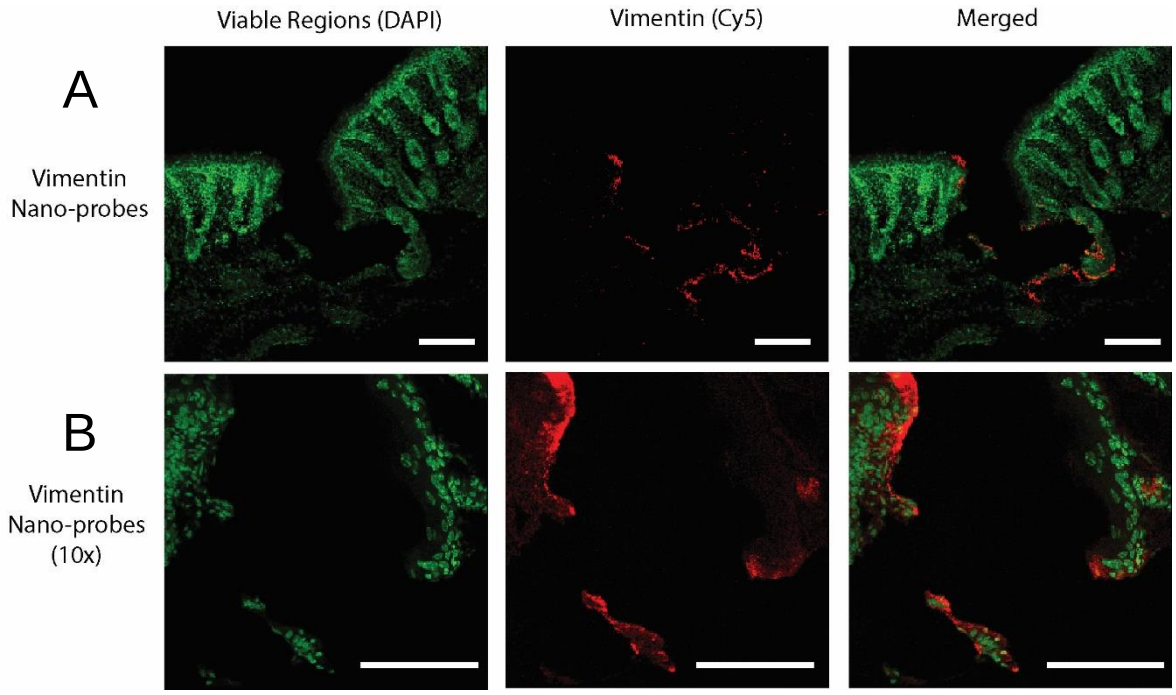

Figure 4.18. Confocal imaging *ex vivo* murine skin incubated with Vim nano-probes. *Ex vivo* dorsal skin was injected with 100 nM of Vimentin nano-probes and incubated for 6h. After wax embedding, 2 µm sections were taken and counter-stained with DAPI to mark the viable regions of the sample (green). A high fluorescent signal was possible to be observed in the red channel (A). In fact, when zoomed in (B), the regions of the red fluorescence were overlapping with viable regions of the skin (green) (Scale bar = 500 µm for A, 1 mm for B)

At higher magnification (Figure 4.18.B.) it is possible to observe that the fluorescent signal localizes at the edges of the cellular regions (i.e. regions where cells are present). Furthermore, when skin samples were injected with a scramble control (i.e. a similar type of conjugate with a non-specific and non-active sequence, see Figure B.1 in Appendix B) no signal was observed. These results correlate with

the results obtained from in vitro models, where wounded regions were significantly more fluorescent than the confluent regions and where no unspecific release of flare strands was observed.

However, imaging of cross-sections of skin has limitations. For example, current processing methods for confocal analysis of tissue (such as mechanical sectioning) can lead to loss of spatial information. While this type of analysis creates a specific spatial snapshot, dynamic processes involved in wound healing in the tissue as a whole can be masked or even completely undetected. [109, 110] To overcome these issues and gain a better understanding of the interaction of the nano-probes with the wounded region, light sheet fluorescence microscopy (LSFM) was used. [111, 112] Briefly, this recently described technique consists of two controlled opposite lasers that scan samples that were made transparent *via* dehydration bleaching [113]. This type of bleaching permits the performance of a vertical optical sectioning, which allows for the extraction of the fluorescence profile of each section (which can have thicknesses in the range of a few nanometres to micrometres). By combining the whole set of images originated from those sections, it is possible to precisely reconstruct a three dimensional map of the fluorescence in the whole tissue piece.

Firstly, it was necessary to understand if DAPI could still be used as a marker for the viable regions. For that, a piece of skin was incubated with 1 mg/ml of DAPI counter stain solution for 10 mins. The optical sectioning was then performed and fluorescence images were taken. Finally, by combining the whole set of images, a three dimensional picture was formed (Figure 4.19.).

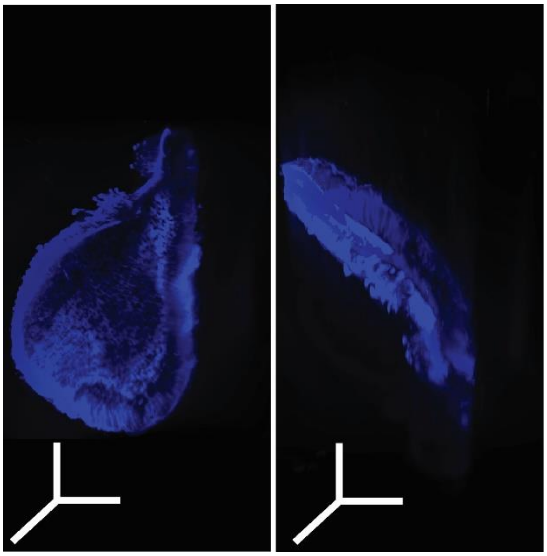

Figure 4.19. 3D-LSFM images of dorsal skin stained with DAPI. Skin was made translucent *via* dehydration bleaching and incubated with 1 µg/mL of DAPI. The 3D projection of the whole set of images taken demonstrated that it was possible to clearly visualize the viable parts of the skin (Scale bar = 1x1x1 mm in xyz axis)

As seen in Figure 4.19., DAPI indeed marked the viable regions of the skin, with clear staining of the cells' nuclei being visible (blue – 405 nm). The 3D model demonstrated the potential of this type of approach to visualize spatially the fluorescence signals from the sample. Therefore, for future experiments DAPI was used as a staining agent to identify the viable regions of each sample.

Secondly, in order to precisely locate the wounded region, Rhodamine B (RhodB) was incorporated in the injected solution as a marker of the injection site. RhodB has been demonstrated to interact specifically with the elastic fibres of the skin [114] without interfering with the other two channels used for DAPI (405nm) and for the flare strand of the nano-probes (640nm). Figure 4.20. shows the successful three-dimensional imaging of the injection site using RhodB. It is possible to see the appearance of the second fluorescent signal (here labelled in green) coming from the RhodB counter dye.

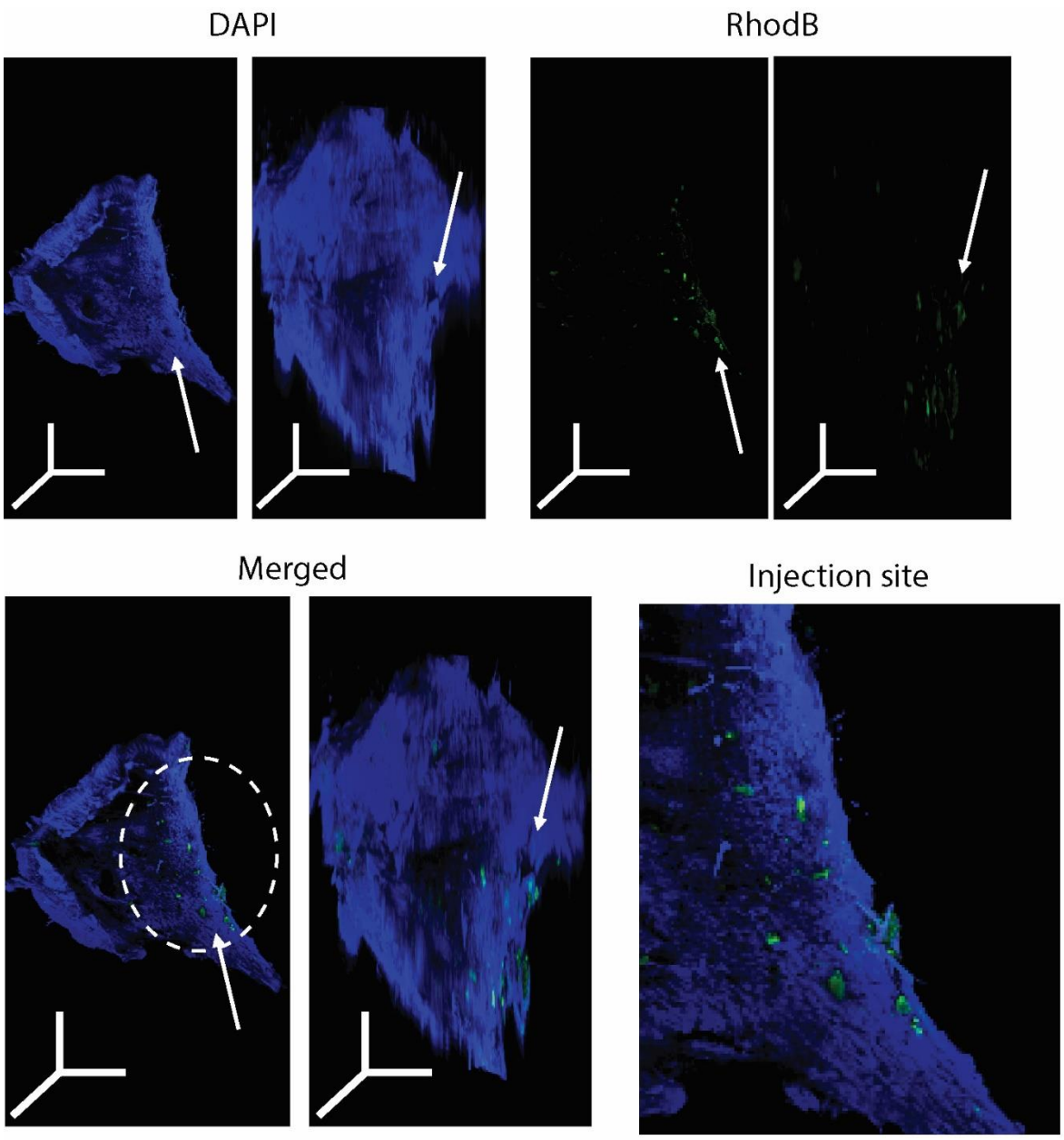

Figure 4.20. 3D-LSFM visualization of injection site in *ex vivo* skin. When using RhodamineB as a counter-stain for the injection site, it was possible to observe the appearance of a new signal (shown in green) localized in the injection site (Arrows indicate the direction of injection; 3D scale bar = 1x1x1 mm in xzy axis)

One final control experiment was conducted by injecting a solution of AuNP-DNA conjugates incorporated with a scramble sequence. Figure 4.21 shows that no significant signal was observed in the red channel (662 nm). This clearly shows that the release of the flare strand only happens in specific conditions. Furthermore, any

other element of the nano-probe (core or sense strands) did not show any effect on any of the channels.

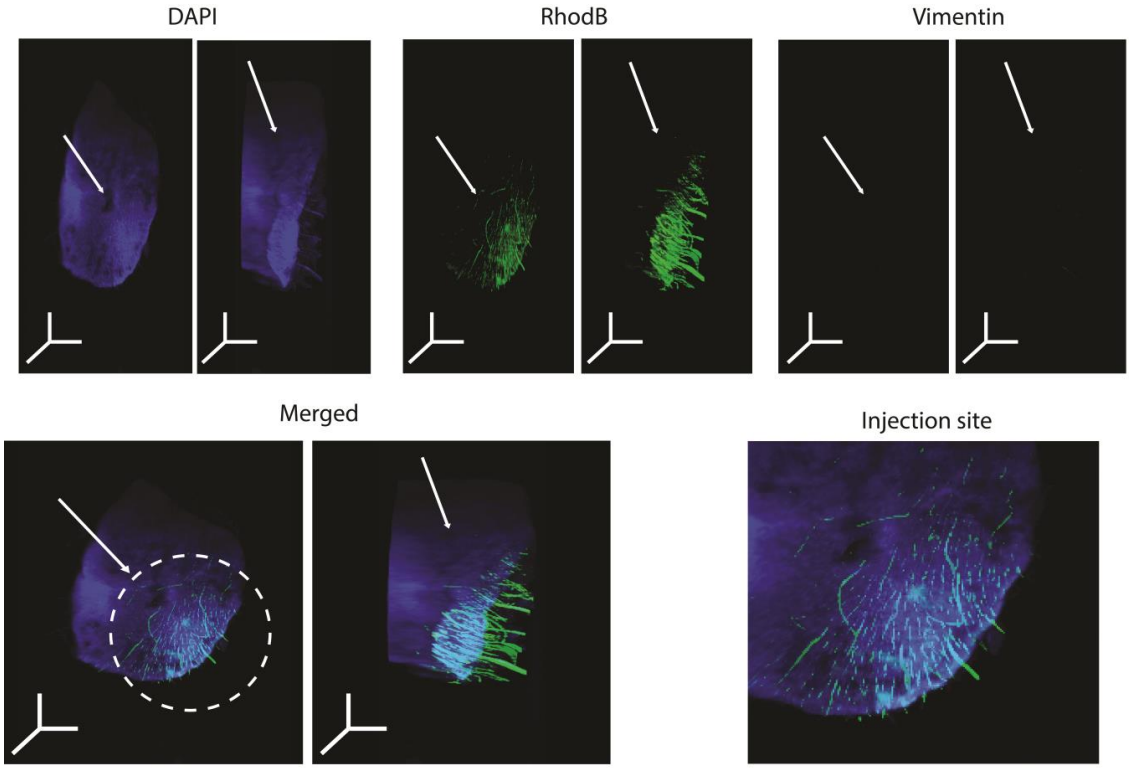

Figure 4.21. 3D-LSFM visualization of *ex vivo* skin injected with scramble control solution. Skin samples were incubated with 100 nM of scramble control DNA-coated nanoparticles and the counter dye RhodB. After 6h the vimentin expression (red channel) was not detectable, whilst RhodB counter dye (green channel) was visile. The green channel overlapped with the viable regions of the skin (shown using DAPI counter stain and represented by the blue channel). (Arrows indicate the direction of injection; 3D scale bar = 1x1x1 mm in xzy axis)

Imaging the tissue itself and the injection site was therefore successfully shown. Additionally, with the demonstration of no false-positive results from the the scramble control experiments, the injection of Vimentin nano-probes was performed and imaged in two instances: straight after injection (0h) and after six hours of incubation. Figure 4.22. represents the LSFM images obtain from that experiment.

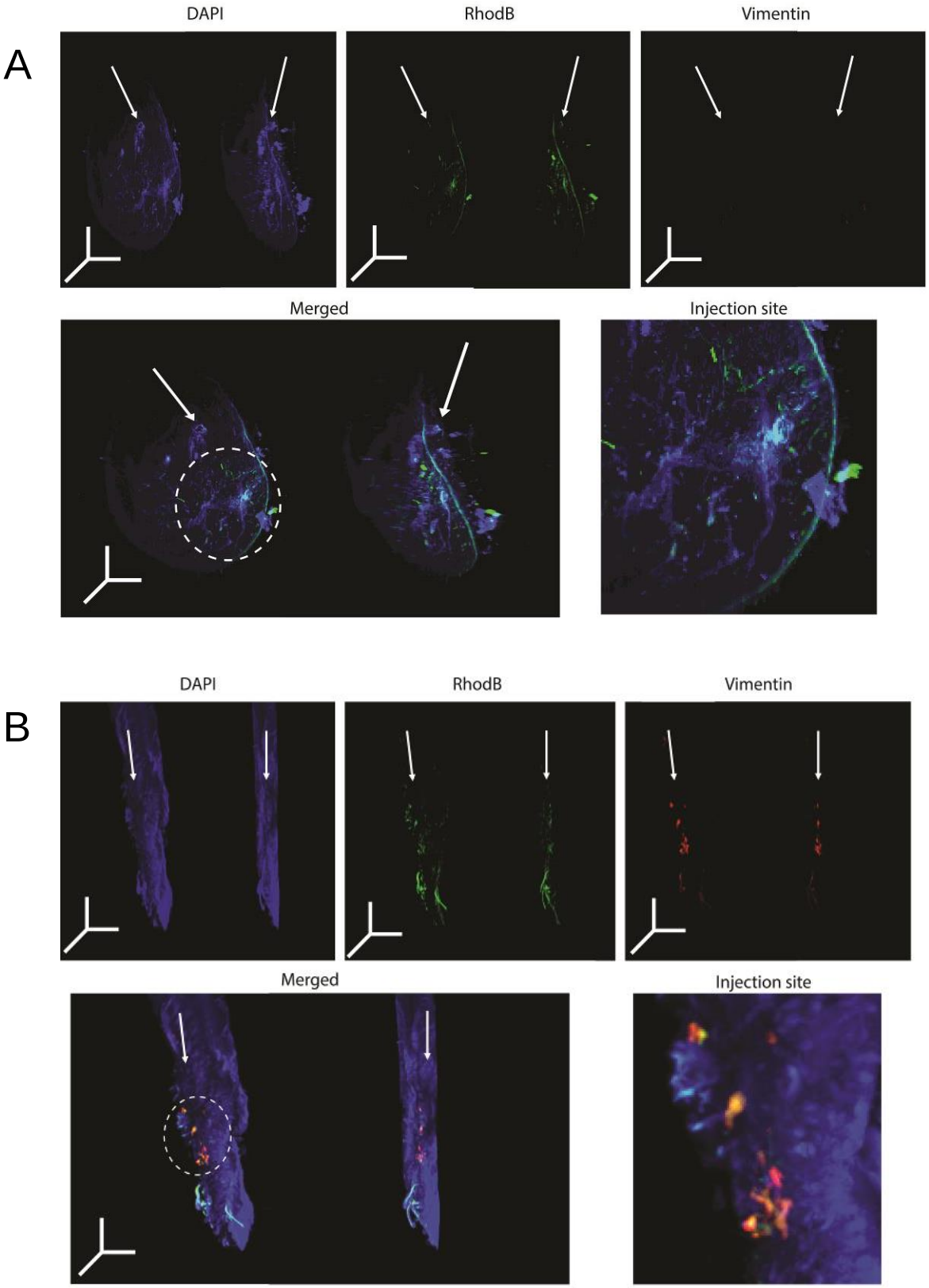

Figure 4.22. 3D-LSFM visualization of *ex vivo* skin injected with Vim nano-probes at 0h and 6h. Skin samples were injected with 100 nM of DNA-coated

nanoparticles and RhodB. DAPI was used for counter stain of the viable regions of the tissue. At 0h (A), no Vimentin mRNA expression was detectable (red) even though the injection site was visible from the RhodB counter dye (green). However, after 6h (B) an increase in the red fluorescence was observable, indicating a successful detection of the expression of vimentin in a skin biopsy. The expression was overlapping with both the viable regions of the skin (blue channel) and the injection site (green channel). (Arrows indicate the direction of injection; 3D scale bar = 1x1x1 mm in xzy axis)

Figure 4.22.A demonstrates that the wound site could be precisely detected immediately after injection, with an evident co-localization between the nuclear counterstain DAPI and RhodB. No fluorescent signal from the nano-probes could be detected at this point, even when zoomed in on the injection site (Figure 4.22.A. bottom right). This is possibly due to the time taken for the particles to be endocytosed by the different cells present in the tissue. Reported studies demonstrated that inorganic nanoparticles covered with biological agents tend to take between two and six hours to be uptaken into the cells [103, 115, 116].

After 6 h of incubation, a strong red fluorescent signal from Vimentin nano-probes was observed (Figure 4.22.B). Moreover, a clear overlap between the DAPI, RhodB and flare signals is seen when zoomed in (Figure 4.22.B bottom right). This was an indication that the Vimentin mRNA was detected not only in the viable region of the skin (shown from the DAPI in blue colour) but also close to the injection site (shown by RhodB in gree colour). When compared with the controls discussed earlier (Figure 4.21), where no fluorescent signal for the Vimentin nano-probes was detected, the red fluorescent signal was concluded to be from the presence of Vimentin mRNA.

However, this three-dimensionally representation of the presence of Vimentin mRNA had only been for an initial and final time point (at 6h). This type of AuNP-DNA conjugates were shown to be a good tool for live cell imaging, due to, amongst other things, their inherent reduced background signal [70, 117, 118]. Therefore, it was hypothesised that the development of the fluorescent signal, and consequently the Vimentin mRNA expression, could also be monitored over time to provide a

more complete dynamic representation of the process. For that, a time-lapse experiment was conducted, investigating the expression of Vimentin mRNA over a period of 6h in the skin biopsies. Two sets of biopsies were injected with the same concentration of nano-probes (100 nM) and left incubating for up to 6 h, with images being acquired after each hour. Figure 4.23. shows the first time point at which the red signal was detectable (at 2hr mark). Representative images for each of additional time points (1/3/4/5 hr) can be found in Appendix II.

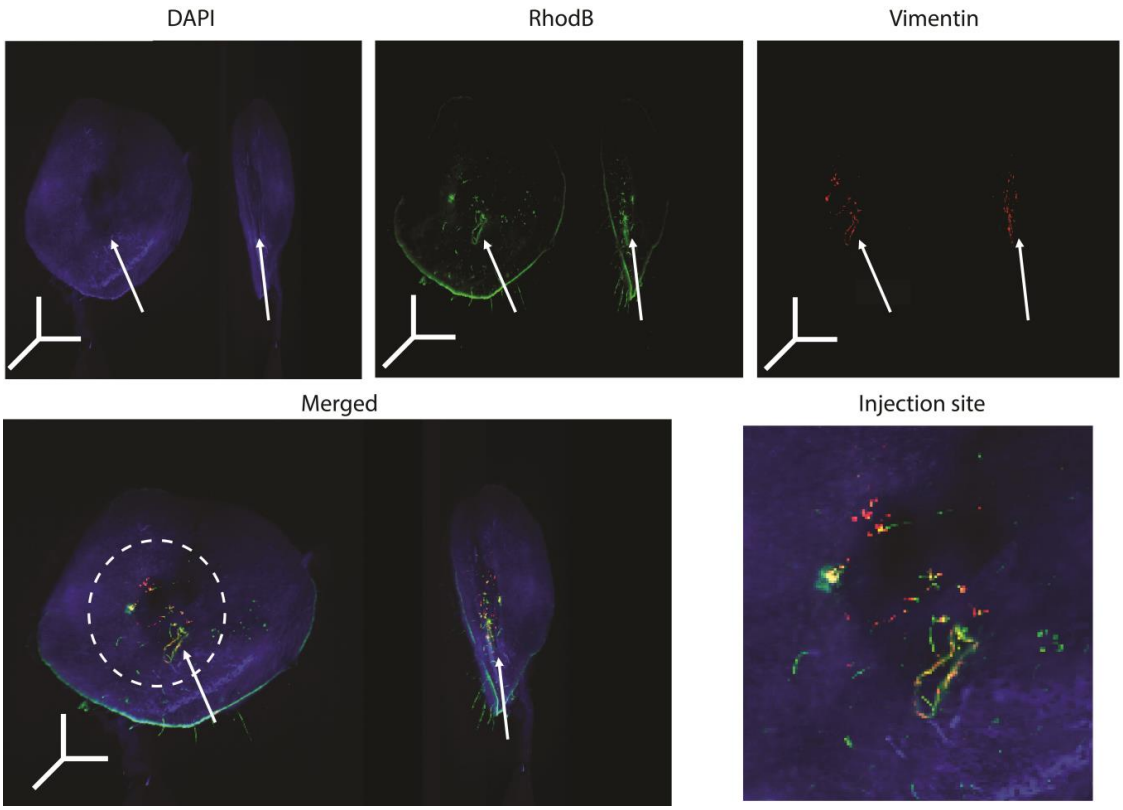

Figure 4.23. 3D-LSFM visualization of *ex vivo* skin injected with a Vim nano-probes solution at 2h. After 2h, a significant fluorescence signal in the red channel (top right) was detected arising from the detection of Vimentin mRNA expression. This signal was overlapping with the viable regions of the skin (represented by the blue channel due to DAPI) and the injection site (represented by the green channel due to RhodB) - (Arrows indicate the direction of injection; 3D scale bar = 1x1x1 mm in xzy axis).

Using the reconstructed 3D projections of the biopsies, it was possible to analyse the development of Vimentin mRNA expression after injection. No significant signal

could be observed in the first two time points – 0h (Figure 4.22.A) and 1h (Fig.B2 in Appendix B). However, after the second hour (Figure 4.23.), the appearance of a strong red signal was noticed, corresponding to the detection of Vimentin mRNA. This signal increased steadily over time (Fig. B 2-5 in Appendix B), hitting its maximum fluorescence intensity at 6h (Figure 4.22B).

Since RhodB and DAPI fluorescence intensities were stable immediately after injection, they were used as a normalisation factor to determine the relative fluorescence intensity arising from the Vimentin nano-probes at different time points (Figure 4.24.).

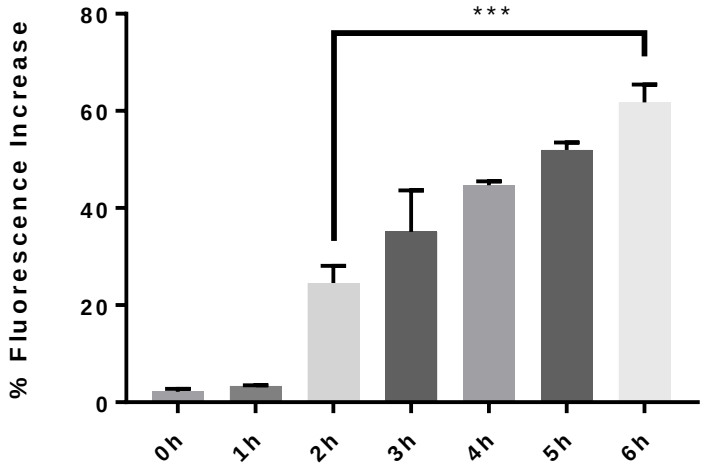

Figure 4.24. Relative fluorescence analysis of Vimentin mRNA expression in skin samples. When comparing the different 3D models for all the time points, the relative fluorescence intensity was significantly higher after 2h. The fluorescence signal consequent of the Vimentin expression increased over time, with the final time-point (6h) being approximately 70% higher than the initial signal. (***p<0.0001 Two-Way ANOVA)

As observed, Vimentin mRNA was detected 2 h after injection (30% when compared time 0 h). Moreover, after 6 h there was a relative fluorescence increase of about 70%. This increase of the detection signal over time can be explained by either the increasing levels of Vimentin mRNA expressed in the wound and/or the increasing uptake of nano-probes by the cells surrounding the wound site.

In summary, the application of DNA-coated nanoparticles capable of detecting Vimentin mRNA expression both in vitro and ex vivo was successfully demonstrated in this chapter. The presence of Vimentin mRNA was studied in 2D cell models and 2D and 3D tissue models. The use of Vimentin AuNP-DNA conjugates with cell models demonstrated that the expression was specific to the target mRNA. Furthermore, it was possible to use this type of detection system to detect the mRNA expression in complex biological processes such as cell migration during wound healing. When applying these nano-probes to a more complex environment (i.e. whole skin biopsies), it was possible to observe that in both 2D models (using confocal microscopy) and 3D models (using LSFM) the expression of Vimentin mRNA was localised in the expected wounded site. In addition, the time-lapse localization analysis showed that mRNA was detected as early as 2 h after the injection of the nano-probes. This suggests that DNA-coated nanoparticles can be employed to investigate the temporal and spatial features of mRNA expression in more complex models such as the whole tissue. This opens up new directions in understanding important biological mechanisms using advanced design of nanoparticles as biomarkers and demonstrates that hybrid materials can be useful tools to overcome imaging difficulties.

4.7. References

1. Shaw, T. J., & Martin, P. (2009). Wound repair at a glance. *Journal of Cell Science*, *122*(Pt 18), 3209–3213. doi:10.1242/jcs.031187

2. Werner, S., & Grose, R. (2003). Regulation of wound healing by growth factors and cytokines. *Physiological Reviews*, *83*(3), 835–870. doi:10.1152/physrev.00031.2002

3. Barrientos, S., Stojadinovic, O., Golinko, M. S., Brem, H., & Tomic-Canic, M. (2008). Growth factors and cytokines in wound healing. *Wound Repair and Regeneration*. doi:10.1111/j.1524-475X.2008.00410.x

4. Carvajal-Gonzalez, J. M., Roman, A. C., Cerezo-Guisado, M. I., Rico-Leo, E. M., Martin-Partido, G., & Fernandez-Salguero, P. M. (2009). Loss of dioxin-receptor expression accelerates wound healing in vivo by a mechanism involving TGFbeta. *Journal of Cell Science*, *122*, 1823–1833. doi:10.1242/jcs.047274

5. Sisco, M., Kryger, Z. B., O'Shaughnessy, K. D., Kim, P. S., Schultz, G. S., Ding, X. Z., Roy, N. K., Dean, N. M., Mustoe, T. A. (2008). Antisense inhibition of connective tissue growth factor (CTGF/CCN2) mRNA limits hypertrophic scarring without affecting wound healing in vivo. *Wound Repair and Regeneration*, *16*(5), 661–673. doi:10.1111/j.1524-475X.2008.00416.x

6. Klass, B. R., Grobbelaar, A. O., & Rolfe, K. J. (2009). Transforming growth factor beta1 signalling, wound healing and repair: a multifunctional cytokine with clinical implications for wound repair, a delicate balance. *Postgraduate Medical Journal*, *85*(999), 9–14. doi:10.1136/pgmj.2008.069831

7. Chigurupati, S., Arumugam, T. V., Son, T. G., Lathia, J. D., Jameel, S., Mughal, M. R., Tang, S.-C., Jo, D.-G., Camandola, S., Giunta, M., Rakova, I., McDonnel, N., Miele, L., Mattson, M. P., Poosala, S. (2007). Involvement of Notch Signaling in Wound Healing. *PLoS ONE*, *2*(11), e1167. doi:10.1371/journal.pone.0001167

8. Daniels, J. T., Geerling, G., Alexander, R. A., Murphy, G., Khaw, P. T., &

Saarialho-Kere, U. (2003). Temporal and spatial expression of matrix metalloproteinases during wound healing of human corneal tissue. *Experimental Eye Research*, *77*(6), 653–664. doi:10.1016/j.exer.2003.08.010

9. Kibe, Y., Takenaka, H., & Kishimoto, S. (2000). Spatial and temporal expression of basic fibroblast growth factor protein during wound healing of rat skin. *British Journal of Dermatology*, *143*(4), 720–727. doi:10.1046/j.1365-2133.2000.03824.x

10. Attia-Vigneau, J., Terryn, C., Lorimier, S., Sandre, J., Antonicelli, F., & Hornebeck, W. (2013). Regeneration of Human Dermis by a Multi-Headed Peptide. *The Journal of Investigative Dermatology*, *134*(1), 58–67. doi:10.1038/jid.2013.290

11. Raj, A., van den Bogaard, P., Rifkin, S. A., van Oudenaarden, A., & Tyagi, S. (2008). Imaging individual mRNA molecules using multiple singly labeled probes. *Nature Methods*, *5*(10), 877–879. doi:10.1038/nmeth.1253

12. Rodriguez, A. J., Condeelis, J., Singer, R. H., & Dictenberg, J. B. (2007). Imaging mRNA movement from transcription sites to translation sites. *Seminars in Cell and Developmental Biology*. doi:10.1016/j.semcdb.2007.02.002

13. Wang, C., Han, B., Zhou, R., & Zhuang, X. (2016). Real-Time Imaging of Translation on Single mRNA Transcripts in Live Cells. *Cell*, *165*(4), 990–1001. doi:10.1016/j.cell.2016.04.040

14. Bratu, D. P., Cha, B.-J., Mhlanga, M. M., Kramer, F. R., & Tyagi, S. (2003). Visualizing the distribution and transport of mRNAs in living cells. *Proceedings of the National Academy of Sciences of the United States of America*, *100*(23), 13308–13. doi:10.1073/pnas.2233244100

15. Bann, D. V, & Parent, L. J. (2012). Application of live-cell RNA imaging techniques to the study of retroviral RNA trafficking. *Viruses*, *4*(6), 963–79. doi:10.3390/v4060963

16. McIsaac, R. S., Silverman, S. J., Parsons, L., Xu, P., Briehof, R., McClean, M.

N., & Botstein, D. (2013). Visualization and analysis of mRNA molecules using fluorescence in situ hybridization in Saccharomyces cerevisiae. *Journal of Visualized Experiments : JoVE*, (76), e50382. doi:10.3791/50382

17. Tyagi, S. (2009). Imaging intracellular RNA distribution and dynamics in living cells. *Nature Methods*, *6*(5), 331–338. doi:10.1038/nmeth.1321

18. Weil, T. T., Parton, R. M., & Davis, I. (2010). Making the message clear: visualizing mRNA localization. *Trends in Cell Biology*, *20*(7), 380–90. doi:10.1016/j.tcb.2010.03.006

19. Long, M. S., & Keating, C. D. (2006). Nanoparticle conjugation increases protein partitioning in aqueous two-phase systems. *Analytical Chemistry*, *78*(2), 379–386. doi:10.1021/ac051882t

20. Aubin-Tam, M.-E., & Hamad-Schifferli, K. (2008). Structure and function of nanoparticle–protein conjugates. *Biomedical Materials*, *3*(3), 34001. doi:10.1088/1748-6041/3/3/034001

21. Rana, S., Yeh, Y. C., & Rotello, V. M. (2010). Engineering the nanoparticle-protein interface: Applications and possibilities. *Current Opinion in Chemical Biology*. doi:10.1016/j.cbpa.2010.10.001

22. Kumar, S., Aaron, J., & Sokolov, K. (2008). Directional conjugation of antibodies to nanoparticles for synthesis of multiplexed optical contrast agents with both delivery and targeting moieties. *Nature Protocols*, *3*(2), 314–320. doi:10.1038/nprot.2008.1

23. Yeom, S. H., Han, M. E., Kang, B. H., Kim, K. J., Yuan, H., Eum, N. S., & Kang, S. W. (2013). Enhancement of the sensitivity of LSPR-based CRP immunosensors by Au nanoparticle antibody conjugation. *Sensors and Actuators, B: Chemical*, *177*, 376–383. doi:10.1016/j.snb.2012.10.099

24. Ke, R., Yang, W., Xia, X., Xu, Y., & Li, Q. (2010). Tandem conjugation of enzyme and antibody on silica nanoparticle for enzyme immunoassay. *Analytical Biochemistry*, *406*(1), 8–13. doi:10.1016/j.ab.2010.06.039

25. Dougan, J. A., Karlsson, C., Smith, W. E., & Graham, D. (2007). Enhanced

oligonucleotide-nanoparticle conjugate stability using thioctic acid modified oligonucleotides. *Nucleic Acids Research*, *35*(11), 3668–3675. doi:10.1093/nar/gkm237

26. Parak, W. J., Pellegrino, T., Micheel, C. M., Gerion, D., Williams, S. C., & Alivisatos, A. P. (2003). Conformation of oligonucleotides attached to gold nanocrystals probed by gel electrophoresis. *Nano Letters*, *3*(1), 33–36. doi:10.1021/nl025888z

27. Ackerson, C. J., Sykes, M. T., & Kornberg, R. D. (2005). Defined DNA/nanoparticle conjugates. *Proceedings of the National Academy of Sciences*, *102*(38), 13383–13385. doi:10.1073/pnas.0506290102

28. Jahns, J., Cao, Q., & Sinzinger, S. (2008). Micro- and nanooptics - An overview. *Laser and Photonics Reviews*. doi:10.1002/lpor.200810009

29. Lebeau, B., & Innocenzi, P. (2011). Hybrid materials for optics and photonics. *Chemical Society Reviews*, *40*(2), 886–906. doi:10.1039/c0cs00106f

30. Bettotti, P. (2014). Hybrid Materials for Integrated Photonics. *Advances in Optics*, *2014* (September), 1–24. doi:10.1155/2014/891395

31. Mitzi, D. B. (2004). Hybrid organic-inorganic electronics*. Functional. Hybrid Materials,.* doi:10.1002/3527602372.ch10

32. Duan, X., Fu, T. M., Liu, J., & Lieber, C. M. (2013). Nanoelectronics-biology frontier: From nanoscopic probes for action potential recording in live cells to three-dimensional cyborg tissues. *Nano Today*, *8*(4), 351–373. doi:10.1016/j.nantod.2013.05.001

33. Salata, O. (2004). Applications of nanoparticles in biology and medicine. *Journal of Nanobiotechnology*, *2*(1), 3. doi:10.1186/1477-3155-2-3

34. Gasparyan, V. (2013). Preparation and application of various nanoparticles in biology and medicine. *Nanotechnology Development*, *3*(1), 2. doi:10.4081/nd.2013.e2

35. Luo, X., Morrin, A., Killard, A. J., & Smyth, M. R. (2006). Application of

nanoparticles in electrochemical sensors and biosensors. *Electroanalysis*. doi:10.1002/elan.200503415

36. Uehara, N. (2010). Polymer-functionalized gold nanoparticles as versatile sensing materials. *Analytical sciences : the International Journal of the Japan Society for Analytical Chemistry*, *26*(12), 1219–1228. doi:10.2116/analsci.26.1219

37. Saha, K., Agasti, S. S., Kim, C., Li, X., & Rotello, V. M. (2012). Gold nanoparticles in chemical and biological sensing. *Chemical Reviews*. doi:10.1021/cr2001178

38. Sharma, P., Brown, S., Walter, G., Santra, S., & Moudgil, B. (2006). Nanoparticles for bioimaging. *Advances in Colloid and Interface Science*. doi:10.1016/j.cis.2006.05.026

39. Li, Z., Sun, Q., Zhu, Y., Tan, B., Xu, Z. P., & Dou, S. X. (2014). Ultra-small fluorescent inorganic nanoparticles for bioimaging. *Journal of Materials Chemistry B*, *2*(19), 2793. doi:10.1039/c3tb21760d

40. Akerman, M. E., Chan, W. C. W., Laakkonen, P., Bhatia, S. N., & Ruoslahti, E. (2002). Nanocrystal targeting in vivo. *Proceedings of the National Academy of Sciences of the United States of America*, *99*(20), 12617–12621. doi:10.1073/pnas.152463399

41. Frangioni, J. V. (2003). In vivo near-infrared fluorescence imaging. *Current Opinion in Chemical Biology*. doi:10.1016/j.cbpa.2003.08.007

42. Fernando Patolsky, Ron Gill, Yossi Weizmann, Taleb Mokari, Uri Banin, and, & Willner, I. (2003). Lighting-Up the Dynamics of Telomerization and DNA Replication by CdSe−ZnS Quantum Dots. *Journal of the American Chemical Society,* 125 (46), 13918-13919, doi:10.1021/JA035848C

43. Weissleder, R., Tung, C. H., Mahmood, U., & Bogdanov, a. (1999). In vivo imaging of tumors with protease-activated near-infrared fluorescent probes. *Nature Biotechnology*, *17*(4), 375–378. doi:10.1038/7933

44. Tung, C. H., Mahmood, U., Bredow, S., & Weissleder, R. (2000). In vivo

imaging of proteolytic enzyme activity using a novel molecular reporter. *Cancer Research*, *60*(17), 4953–4958. doi: unavailable

45. Wu, Z.-S., Jiang, J.-H., Fu, L., Shen, G.-L., & Yu, R.-Q. (2006). Optical detection of DNA hybridization based on fluorescence quenching of tagged oligonucleotide probes by gold nanoparticles. *Analytical Biochemistry*, *353*(1), 22–29. doi:10.1016/j.ab.2006.01.018

46. Son, A., Dosev, D., Nichkova, M., Ma, Z., Kennedy, I. M., Scow, K. M., & Hristova, K. R. (2007). Quantitative DNA hybridization in solution using magnetic/luminescent core-shell nanoparticles. *Analytical Biochemistry*, *370*(2), 186–194. doi:10.1016/j.ab.2007.08.001

47. Bulte, J. W., Douglas, T., Witwer, B., Zhang, S. C., Strable, E., Lewis, B. K., Zywicke, H., Miller, B., van Gelderen, P., Moskowitz, B. M., Duncan, I. D., Frank, J. A. (2001). Magnetodendrimers allow endosomal magnetic labeling and in vivo tracking of stem cells. *Nature biotechnology*, *19*(12), 1141–7. doi:10.1038/nbt1201-1141

48. Berman, S. C., Walczak, P., & Jeff W.M. Bulte. (2011). Tracking stem cells using magnetic nanoparticles. *Wiley Interdisciplinary Reviews: Nanomedicine and Nanobiotechnology*, *3*, 343–355. doi:10.1002/wnan.140.

49. Bezuidenhout, M., Liu, P., Singh, S., Kiely, M., Ryan, K. M., & Kiely, P. A. (2014). Promoting Cell Proliferation Using Water Dispersible Germanium Nanowires. *PLoS ONE*, *9*(9), e108006. doi:10.1371/journal.pone.0108006

50. Paviolo, C., Chon, J. W. M., & Clayton, A. H. A. (2015). Inhibiting EGFR Clustering and Cell Proliferation with Gold Nanoparticles. *Small*, *11*(14), 1638–1643. doi:10.1002/smll.201402701

51. Bunz, U. H. F., & Rotello, V. M. (2010). Gold nanoparticle-fluorophore complexes: Sensitive and discerning “noses” for biosystems sensing. *Angewandte Chemie - International Edition*. doi:10.1002/anie.200906928

52. Swierczewska, M., Lee, S., & Chen, X. (2011). The design and application of fluorophore–gold nanoparticle activatable probes. *Physical Chemistry*

Chemical Physics, *13*(21), 9929. doi:10.1039/c0cp02967j

53. Wang, J., Moore, J., Laulhe, S., Nantz, M., Achilefu, S., & Kang, K. A. (2012). Fluorophore–gold nanoparticle complex for sensitive optical biosensing and imaging. *Nanotechnology*, *23*(9), 95501. doi:10.1088/0957-4484/23/9/095501

54. Sheng, H., & Ye, B. C. (2009). Different strategies of covalent attachment of oligonucleotide probe onto glass beads and the hybridization properties. *Applied Biochemistry and Biotechnology*, *152*(1), 54–65. doi:10.1007/s12010-008-8245-9

55. Connor, E. E., Mwamuka, J., Gole, A., Murphy, C. J., & Wyatt, M. D. (2005). Gold Nanoparticles Are Taken Up by Human Cells but Do Not Cause Acute Cytotoxicity. *Small*, *1*(3), 325–327. doi:10.1002/smll.200400093

56. Patra, H. K., Banerjee, S., Chaudhuri, U., Lahiri, P., & Dasgupta, A. K. (2007). Cell selective response to gold nanoparticles. *Nanomedicine: Nanotechnology, Biology and Medicine*, *3*(2), 111–119. doi:10.1016/j.nano.2007.03.005

57. Alkilany, A. M., & Murphy, C. J. (2010). Toxicity and cellular uptake of gold nanoparticles: what we have learned so far?, *Journal of Nanoparticle Research, 12*(7), 2313–2333. doi:10.1007/s11051-010-9911-8

58. Villiers, C., Freitas, H., Couderc, R., Villiers, M.-B., & Marche, P. (2010). Analysis of the toxicity of gold nano particles on the immune system: effect on dendritic cell functions. *Journal of Nanoparticle Research*, *12*(1), 55–60. doi:10.1007/s11051-009-9692-0

59. Fratoddi, I., Venditti, I., Cametti, C., & Russo, M. V. (2015). How toxic are gold nanoparticles? The state-of-the-art. *Nano Research*, *8*(6), 1771–1799. doi:10.1007/s12274-014-0697-3

60. Haiss, W., Thanh, N. T. K., Aveyard, J., & Fernig, D. G. (2007). Determination of size and concentration of gold nanoparticles from UV-Vis spectra. *Analytical Chemistry*, *79*(11), 4215–4221. doi:10.1021/ac0702084

61. Jain, P. K., Lee, K. S., El-Sayed, I. H., & El-Sayed, M. A.,. Calculated

Absorption and Scattering Properties of Gold Nanoparticles of Different Size, Shape, and Composition: Applications in Biological Imaging and Biomedicine. *The Journal of Physical Chemistry B,* 110 (14), 7238-7248, doi:10.1021/jp057170o

62. J. Turkevich; P.C. Stevenson; J. Hiller. (1951). Synthesis of Gold Nanoparticles Turkevich method. *Discussions of the Faraday Society*, *11*, 55–75.

63. Kimling, J., Maier, M., Okenve, B., Kotaidis, V., Ballot, H., & Plech, A. (2006). Turkevich method for gold nanoparticle synthesis revisited. *Journal of Physical Chemistry B*, *110*(32), 15700–15707. doi:10.1021/jp061667w

64. Ghosh, P., Han, G., De, M., Kim, C. K., & Rotello, V. M. (2008). Gold nanoparticles in delivery applications. *Advanced Drug Delivery Reviews*, *60*(11), 1307–1315. doi:10.1016/j.addr.2008.03.016

65. Tiwari, P. M., Vig, K., Dennis, V. a., & Singh, S. R. (2011). Functionalized Gold Nanoparticles and Their Biomedical Applications. *Nanomaterials*, *1*(1), 31–63. doi:10.3390/nano1010031

66. Zhong, J., Qu, J., Ye, F., Wang, C., Meng, L., & Yang, J. (2011). The bis(p-sulfonatophenyl)phenylphosphine-assisted synthesis and phase transfer of ultrafine gold nanoclusters. *Journal of Colloid and Interface Science*, *361*(1), 59–63. doi:10.1016/j.jcis.2011.05.017

67. Bidault, S., & Polman, A. (2012). Water-Based Assembly and Purification of Plasmon-Coupled Gold Nanoparticle Dimers and Trimers. *International Journal of Optics*, *2012*, 1–5. doi:10.1155/2012/387274

68. Seferos, D. S., Giljohann, D. A., Hill, H. D., Prigodich, A. E., & Mirkin, C. A. (2007). Nano-flares: Probes for transfection and mRNA detection in living cells. *Journal of the American Chemical Society*, *129*(50), 15477–15479. doi:10.1021/ja0776529

69. Jensen, S. A., Day, E. S., Ko, C. H., Hurley, L. A., Luciano, J. P., Kouri, F. M., Merkel, T. J., Luthi, A. J., Patel, P. C., Cutler, J. I., Daniel, W. L., Scott, A. W.,

Rotz, M. W., Meade, T. J., Giljohann, D. A., Mirkin, C. A., Stegh, A. H. (2013). Spherical nucleic acid nanoparticle conjugates as an RNAi-based therapy for glioblastoma. *Science Translational Medicine*, *5*(209), 209ra152. doi:10.1126/scitranslmed.3006839

70. Heuer-Jungemann, A., El-Sagheer, A. H., Lackie, P. M., Brown, T., & Kanaras, A. G. (2016). Selective killing of cells triggered by their mRNA signature in the presence of smart nanoparticles. *Nanoscale*, *8*(38), 16857–16861, doi:10.1039/C6NR06154K

71. Gilles, C., Polette, M., Zahm, J. M., Tournier, J. M., Volders, L., Foidart, J. M., & Birembaut, P. (1999). Vimentin contributes to human mammary epithelial cell migration. *Journal of Cell Science*, 112 (2), 4615–4625. doi: unavailable

72. Eckes, B., Colucci-Guyon, E., Smola, H., Nodder, S., Babinet, C., Krieg, T., & Martin, P. (2000). Impaired wound healing in embryonic and adult mice lacking vimentin. *Journal of Cell science*, *113*, 2455–2462. doi: unavailable

73. Rogel, M. R., Soni, P. N., Troken, J. R., Sitikov, A., Trejo, H. E., & Ridge, K. M. (2011). Vimentin is sufficient and required for wound repair and remodeling in alveolar epithelial cells. *FASEB Journal , 25*(11), 3873–83. doi:10.1096/fj.10-170795

74. Prigodich, A. E., Randeria, P. S., Briley, W. E., Kim, N. J., Daniel, W. L., Giljohann, D. A., & Mirkin, C. A. (2012). Multiplexed nanoflares: MRNA detection in live cells. *Analytical Chemistry*, *84*(4), 2062–2066. doi:10.1021/ac202648w

75. Bhatt, N., Jimmy Huang, P.-J., Dave, N., & Liu, J. (2011). Dissociation and Degradation of Thiol-Modified DNA on Gold Nanoparticles in Aqueous and Organic Solvents. *Langmuir,* 27 (10), 6132-6137, doi:10.1021/la200241d

76. Meister, A., & Anderson, M. E. (1983). Glutathione. *Annual Review of Biochemistry*, *52*(1), 711–760. doi:10.1146/annurev.bi.52.070183.003431

77. Lushchak, V. I., & I., V. (2012). Glutathione Homeostasis and Functions: Potential Targets for Medical Interventions. *Journal of Amino Acids*, *2012*, 1–26. doi:10.1155/2012/736837

78. Wu, X. A., Choi, C. H. J., Zhang, C., Hao, L., & Mirkin, C. A. (2014). Intracellular fate of spherical nucleic acid nanoparticle conjugates. *Journal of the American Chemical Society*, *136*(21), 7726–7733. doi:10.1021/ja503010a

79. Lee, D. S., Qian, H., Tay, C. Y., & Leong, D. T. (2016). Cellular processing and destinies of artificial DNA nanostructures. *Chemical Society Reviews*, *45*(15), 4199–4225. doi:10.1039/C5CS00700C

80. Edge, L. (2013). Innate Immune DNA-Sensing Pathways. *Cell*, *152*, 375–377. doi:10.1016/j.cell.2013.01.026

81. Paludan, S., & Bowie, A. (2013). Immune Sensing of DNA. *Immunity*. doi:10.1016/j.immuni.2013.05.004

82. Li, N., Chang, C., Pan, W., & Tang, B. (2012). A Multicolor Nanoprobe for Detection and Imaging of Tumor-Related mRNAs in Living Cells. *Angewandte Chemie International Edition*, *51*(30), 7426–7430. doi:10.1002/anie.201203767

83. Fischer, H., Scherz, J., Szabo, S., Mildner, M., Benarafa, C., Torriglia, A., Tschadler, E., Eckhart, L. (2011). Dnase 2 is the main DNA-degrading enzyme of the stratum corneum. *PLoS ONE*, *6*(3). doi:10.1371/journal.pone.0017581

84. Lan, Y. Y., Londoño, D., & Hacohen, N. (2016). Lysosomal DNaseII degrades nuclear DNA and prevents self DNA recognition, *The Journal of Immunology*, *188*(1 Supplement), 159.17; doi: unavaible

85. Evans, C. J., & Aguilera, R. J. (2003). DNase II: Genes, enzymes and function. *Gene*. doi:10.1016/j.gene.2003.08.022

86. Pinto-González Howell, D., Krieser, R. J., Eastman, A., & Barry, M. A. (2003). Deoxyribonuclease II is a lysosomal barriers to transfection. *Molecular Therapy*, *8*(6), 957–963. doi:10.1016/j.ymthe.2003.09.011

87. Pellegrino, T., Sperling, R. A., Alivisatos, A. P., & Parak, W. J. (2007). Gel Electrophoresis of Gold-DNA Nanoconjugates, *2007*. doi:10.1155/2007/

88. Yevdokimov, Y., Skuridin, S. G., Salyanov, V. I., Shtykova, E. V., Dadinova, L. A., Volkov, V. V., Khlebtsov, N. G., Komarov, P. V., Kats, E. I. (2015). Negatively Charged Gold Nanoparticles Control Double-Stranded DNAs Spatial Packing. *Journal of Material Science & Nanotechnology*, *4*(41). doi:10.15744/2348-9812.3.201

89. Petri-Fink, A., Steitz, B., Finka, A., Salaklang, J., & Hofmann, H. (2008). Effect of cell media on polymer coated superparamagnetic iron oxide nanoparticles (SPIONs): Colloidal stability, cytotoxicity, and cellular uptake studies. *European Journal of Pharmaceutics and Biopharmaceutics*, *68*(1), 129–137. doi:10.1016/j.ejpb.2007.02.024

90. Buyens, K., Meyer, M., Wagner, E., Demeester, J., De Smedt, S. C., & Sanders, N. N. (2010). Monitoring the disassembly of siRNA polyplexes in serum is crucial for predicting their biological efficacy. *Journal of Controlled Release*, *141*(1), 38–41. doi:10.1016/j.jconrel.2009.08.026

91. Smith, P. J., Giroud, M., Wiggins, H. L., Gower, F., Thorley, J. A., Stolpe, B., Mazzolini, J., Dyson, R. J., Rappoport, J. Z. (2012). Cellular entry of nanoparticles via serum sensitive clathrin-mediated endocytosis, and plasma membrane permeabilization. *International Journal of Nanomedicine*, *7*, 2045–2055. doi:10.2147/IJN.S29334

92. Wang, W., Huang, Y., Zhao, S., Shao, T., & Cheng, Y. (2013). Human serum albumin (HSA) nanoparticles stabilized with intermolecular disulfide bonds. *Chemical Communications*, *49*(22), 2234–6. doi:10.1039/c3cc38397k

93. Cifuentes-Rius, A., De Puig, H., Kah, J. C. Y., Borros, S., & Hamad-Schifferli, K. (2013). Optimizing the properties of the protein corona surrounding nanoparticles for tuning payload release. *ACS Nano*, *7*(11), 10066–10074. doi:10.1021/nn404166q

94. Laurila, P., Virtanen, I., Lehto, V. P., Vartio, T., & Stenman, S. (1982). Expression and distribution of vimentin and keratin filaments in heterokaryons of human fibroblasts and amnion epithelial cells. *Journal of Cell Biology*, *94*(2), 308–315. doi:10.1083/jcb.94.2.308

95. Mørk, C., van Deurs, B., & Petersen, O. W. (1990). Regulation of vimentin expression in cultured human mammary epithelial cells. *Differentiation, 43*, 146–156. doi:10.1111/j.1432-1033.1992.tb17449.x

96. Mendez, M. G., Kojima, S.-I., & Goldman, R. D. (2010). Vimentin induces changes in cell shape, motility, and adhesion during the epithelial to mesenchymal transition. *FASEB Journal* , *24*(6), 1838–51. doi:10.1096/fj.09-151639

97. Vuoriluoto, K., Haugen, H., Kiviluoto, S., Mpindi, J.-P., Nevo, J., Gjerdrum, C., Tiron, C., Lorens, J. B., Ivaska, J. (2011). Vimentin regulates EMT induction by Slug and oncogenic H-Ras and migration by governing Axl expression in breast cancer. *Oncogene*, *30*(12), 1436–48. doi:10.1038/onc.2010.509

98. Liang, C. C., Park, A. Y., & Guan, J. L. (2007). In vitro scratch assay: a convenient and inexpensive method for analysis of cell migration in vitro. *Nature Protocols*, *2*(2), 329–333. doi:nprot.2007.30

99. Goetsch, K. P., & Niesler, C. U. (2011). Optimization of the scratch assay for in vitro skeletal muscle wound healing analysis. *Analytical Biochemistry*, *411*(1), 158–160. doi:10.1016/j.ab.2010.12.012

100. Chen, Y. (2013). Scratch Wound Healing Assay. *Journal of Chemical Information and Modeling*. doi:10.1017/CBO9781107415324.004

101. Brandenberger, C., Mühlfeld, C., Ali, Z., Lenz, A. G., Schmid, O., Parak, W. J., Gehr, P., Rothen-Rutishauser, B. (2010). Quantitative evaluation of cellular uptake and trafficking of plain and polyethylene glycol-coated gold nanoparticles. *Small*, *6*(15), 1669–1678. doi:10.1002/smll.201000528

102. Chithrani, D. B., Dunne, M., Stewart, J., Allen, C., & Jaffray, D. A. (2010). Cellular uptake and transport of gold nanoparticles incorporated in a liposomal carrier. *Nanomedicine: Nanotechnology, Biology and Medicine*, *6*(1), 161–169. doi:10.1016/j.nano.2009.04.009

103. Yao, M., He, L., McClements, D. J., & Xiao, H. (2015). Uptake of Gold Nanoparticles by Intestinal Epithelial Cells: Impact of Particle Size on Their

Absorption, Accumulation, and Toxicity. *Journal of Agricultural and Food Chemistry*, *63*(36), 8044–8049. doi:10.1021/acs.jafc.5b03242

104. Gunduz, N., Ceylan, H., Guler, M. O., Tekinay, A. B., (2017). Intracellular Accumulation of Gold Nanoparticles Leads to Inhibition of Macropinocytosis to Reduce the Endoplasmic Reticulum Stress. *Scientific Reports*, *7*(December 2016), 40493. doi:10.1038/srep40493

105. Dykman, L. A., & Khlebtsov, N. G. (2014). Uptake of engineered gold nanoparticles into mammalian cells. *Chemical Reviews*, *114*(2), 1258–1288. doi:10.1021/cr300441a

106. Bellas, E., Seiberg, M., Garlick, J., & Kaplan, D. L. (2012). In vitro 3D Full-Thickness Skin-Equivalent Tissue Model Using Silk and Collagen Biomaterials. *Macromolecular Bioscience*, *12*(12), 1627–1636. doi:10.1002/mabi.201200262

107. Bayat, A., McGrouther, D. A., & Ferguson, M. W. J. (2003). Skin scarring. *BMJ (Clinical ResearchEdition)*, *326*(7380), 88–92. doi:10.1136/bmj.326.7380.88

108. Gantwerker, E. A., & Hom, D. B. (2012). Skin: Histology and physiology of wound healing. *Clinics in Plastic Surgery*. doi:10.1016/j.cps.2011.09.005

109. Cella Zanacchi, F., Lavagnino, Z., Perrone Donnorso, M., Del Bue, A., Furia, L., Faretta, M., & Diaspro, A. (2011). Live-cell 3D super-resolution imaging in thick biological samples. *Nature Methods*, *8*(12), 1047–9. doi:10.1038/nmeth.1744

110. Galbraith, C. G., & Galbraith, J. a. (2011). Super-resolution microscopy at a glance. *Journal of Cell Science*, *124*(Pt 10), 1607–1611. doi:10.1242/jcs.080085

111. Weber, M., Mickoleit, M., & Huisken, J. (2014). Light sheet microscopy. *Methods in Cell Biology*, *123*, 193–215. doi:10.1016/B978-0-12-420138-5.00011-2

112. Jahr, W., Schmid, B., Schmied, C., Fahrbach, F. O., & Huisken, J. (2015). Hyperspectral light sheet microscopy. *Nature Communications*, *6*, 7990.

doi:10.1038/ncomms8990

113. Santi, P. A. (2011). Light Sheet Fluorescence Microscopy A Review. *Journal of Histochemistry & Cytochemistry*, *59*(2), 129–138. doi:10.1369/0022155410394857

114. Rossetti, F. C., Depieri, L. V., Bentely, M. V. L B., (2013). Confocal Laser Scanning Microscopy as a Tool for the Investigation of Skin Drug Delivery Systems and Diagnosis of Skin Disorders. *Intech*, 99–140. doi:10.5772/55995

115. Conde, J., Ambrosone, A., Sanz, V., Hernandez, Y., Marchesano, V., Tian, F., Child, H., Berry, C. C., Ibarra, M. R., Baptista, P. V., Tortiglione, C., De La Fuente, J. M. (2012). Design of multifunctional gold nanoparticles for in vitro and in vivo gene silencing. *ACS Nano*, *6*(9), 8316–8324. doi:10.1021/nn3030223

116. Freese, C., Uboldi, C., Gibson, M. I., Unger, R. E., Weksler, B. B., Romero, I. a., Couraud, P. O.,Kirkpatrick, C. J. (2012). Uptake and cytotoxicity of citrate-coated gold nanospheres : comparative studies on human endothelial and epithelial cells. *Particle and Fibre Toxicology*, *9*(1), 1. doi:10.1186/1743-8977-9-23

117. Prigodich, A. E., Randeria, P. S., Briley, W. E., Kim, N. J., Daniel, W. L., Giljohann, D. A., Mirkin, C. A. (2013). Multiplexed Nano-flares : mRNA Detection in Live Cells. *Analytical Chemistry*, *84*(4), 2062–2066. doi:10.1021/ac202648w.Multiplexed

118. Ilovitsh, T., Danan, Y., Meir, R., Meiri, A., & Zalevsky, Z. (2015). Cellular superresolved imaging of multiple markers using temporally flickering nanoparticles. *Scientific Reports*, *5*, 10965. doi:10.1038/srep10965

Chapter 5: Pilot study - Application of gold nanoparticles-oligonucleotide conjugates in SMAD3 knock-down for in vitro and in vivo models of scarring

Wound healing is a complex process that quickly unfolds to prevent the entry of bacteria, fungi or viruses into the affected area and to restore the tissues structure [1]. During this process, quick response genes are upregulated which induce the migration of immune cells to the wound and promote the production of stiff fibres (such as collagen) in an unilateral direction [2]. As a results, the wounded area accumulates fibrotic tissue with less elasticity, leading to the formation of scar tissue.

It has recently been shown that silencing genes that are directly involved in the scarring process, such as TGF-β [3–5] and CTGF [6–9], can reduce the level of scarring. Additionally, it has been suggested that the overexpression of TGF-β might be one of the major contributors of scar tissue formation [10]. However, TGF-β is still necessary to perform wound healing . As presented by Kulkarni *et al.* (1993) [11], Bottinger *et al.* (1997)[12] and Crowe *et al.* (2000) [13], mice completely depleted of any type of TGF-β exhibited a low level of wound healing in general, with higher levels of inflammation. Therefore, an alternative signalling pathway, either downstream or independent to TGF-β must be used in order to reduce scarring without compromising the wound healing process. One such pathway, the SMAD2/3 signalling pathway, has been previously reported to have a moderate effect on wound healing [14, 15], with knockout mice demonstrating either a slower re-epithelization[16] or an accelerated rate of wound healing [17, 18].

As mentioned in previous chapters, combinatorial nanomaterials based on oligonucleotide and gold nanoparticles conjugates have been applied on biological applications as therapeutic agents. [19, 20] In chapter 4 the successful application of AuNP-DNA conjugates as imaging tools for detecting Vimentin mRNA in different cellular and tissue models of the skin was demonstrated. Interestingly, recent studies have shown that this type of conjugates have the potential to be useful for a range of other applications. For example, Rosi *et al*. (2006) first described the use of gold cores coated with thiolated strands of double stranded RNA as a gene

silencing tool in cells [21]. In its primordial form, this new type of siRNA delivery agent relied on the activity of RNAses to deliver the target silencing sequences. Additional works by Ghosh *et al.* (2008) [22], Rhim *et al.* (2008) [23] and Elbakry *et al.* (2009) [24] further refined this method, improving the targeting by using other biomolecules such as lipids, peptides and polymers to coat the siRNA-AuNP conjugates. These methods overcame the degradation of the oligonucleotides by DNAses and took advantage of the naturally occurring and more sophisticated silencing pathways such as RNA-induced silencing complex (RISC) pathways (see section 2.6). Ever since, AuNP-siRNA conjugates have been used to silence many genes, such as β-galactosidase [25], galectin-1 [26] and ganglioside [27], in a range of different cell lines. [28–32]

Despite the potential of this approach, very few studies have been performed in *in vivo* models. For example, Wu *et al.* (2016) demonstrated that systemic administration of AuNP-siRNA complexes targeting TGF-β1 inhibited tumour growth and improved the survival rate of tumour-bearing mice when compared with control groups. [33] Additionally, Randeria *et al.* (2015) showed that this type of AuNP-siRNA conjugates are capable of penetrating the skin, altering the levels of GM3 in diabetic mice, by using a cream instead of a liquid solution as a delivery vehicle [34].

This chapter presents the preliminary results of a pilot study on the use of AuNP-siRNA conjugates for the silencing of the SMAD3/TGF-β pathway. This pilot study aimed to improve our understanding of the use of AuNP-siRNA conjugates in *in vivo* models and to understand the potential pitfalls to consider when planning a completel *in vivo* study. The conjugation of gold core with siRNA duplexes is demonstrated and characterised (section 5.1.), as well as the stability of the silencing probes in different conditions (section 5.2.). Additionally, the impact of conjugates in cell viability, protein expression and mRNA levels was studied in cultured cells (section 5.3.). Finally, the conjugates were applied to *in vivo* mouse models to investigate their potential ability to regulate the scarring level in a wounded area (section 5.4.).

5.1. Formation of siRNA-gold nanoparticle conjugates

As shown in Chapter 4, gold nanoparticles are excellent inorganic scaffolds for the attachment and delivery of oligonucleotides. These DNA covered gold nanoparticles are not cytotoxic and can be used as an imaging tool to detect and track specific mRNAs in different models of wound healing. Taking this into consideration, it was hypothesised that the same type of gold core could be used to attach siRNA duplexes in order to induce a silencing reaction in cells. To perform these experiments, the same type of gold cores described in Chapter 4 were used (Figure 4.1.). The sequences used for the siRNA were based on previously reported siRNA sequences for SMAD3 [35] and were matched using NCBI's BLAST tool. Some of these siRNA sequences were fluoro-tagged with Cy3 and Cy5 dyes for characterization purposes.

Since the RISC pathway requires double stranded siRNA, the siRNA duplex needed to be hybridized before attaching it onto the nanoparticles' surfaces. This process was monitored using gel electrophoresis (Figure 5.1.A) and fluorescence monitoring (Figure 5.1.B).

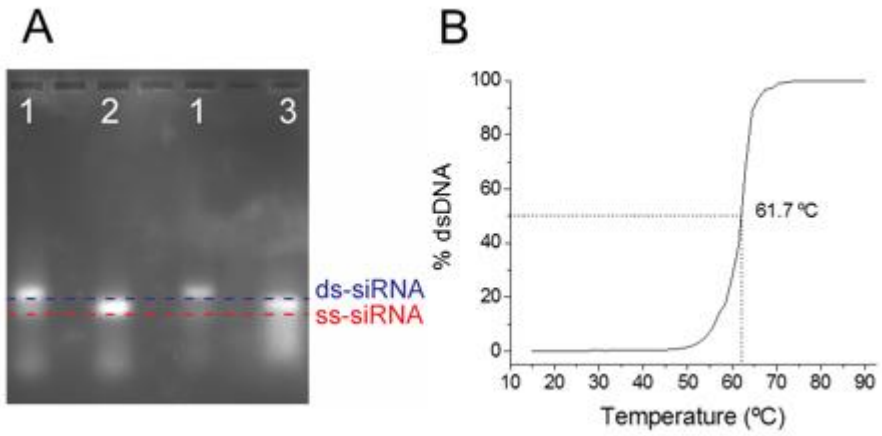

Figure 5.1. Characterization of the hybridization of sense and antisense SMAD3 siRNA strands. The successful formation of the siRNA duplex (SMAD3 Sense: Thiol Group - AAA AAA AAA AUU GGA GAA GUU GUA AUG GAG C; SMAD3 anti-sense: GCU CCA UUA CAA CUU CUC CAA) was observed *via* gel electrophoresis (A), where a clear retardation of the hybridized bands (1) could be seen when compared with the sense (2) and antisense (3) single strands. A fluorescence analysis was performed (B) in a fully

hybridized double stranded-siRNA solution and the melting temperature was determined to be 61.7 ºC.

As shown in figure 5.1.A, both sense (2) (Thiol Group - AAA AAA AAA AUU GGA GAA GUU GUA AUG GAG C) and antisense (3) (GCU CCA UUA CAA CUU CUC CAA) strands have similar size and therefore migrate approximately at the same distance in the agarose gel. The successful hybridization of the complementary strands doubles the resulting siRNA duplex in weight, leading to a slower movement through the gel (1). Furthermore, a DNA melting temperature experiment (Figure 5.1.B). reveals a sigmoidal curve, characteristic of a successful hybridization event. The melting temperature of the siRNA duplexes was determined (61.7 ºC). Both techniques (gel and melting temperature experiment) demonstrate that the siRNA sequences were successfully designed and hybridized.

The resulting ds-siRNA solution was incubated with gold nanoparticles to coat the nanoparticle surface. The final AuNP-siRNA conjugates were characterized using UV-Vis spectroscopy (Figure 5.2A-B), ζ-potential (Figure 5.2.C), gel electrophoresis (Figure 5.2.D.) and fluorescence spectroscopy (Figure 5.2.E).

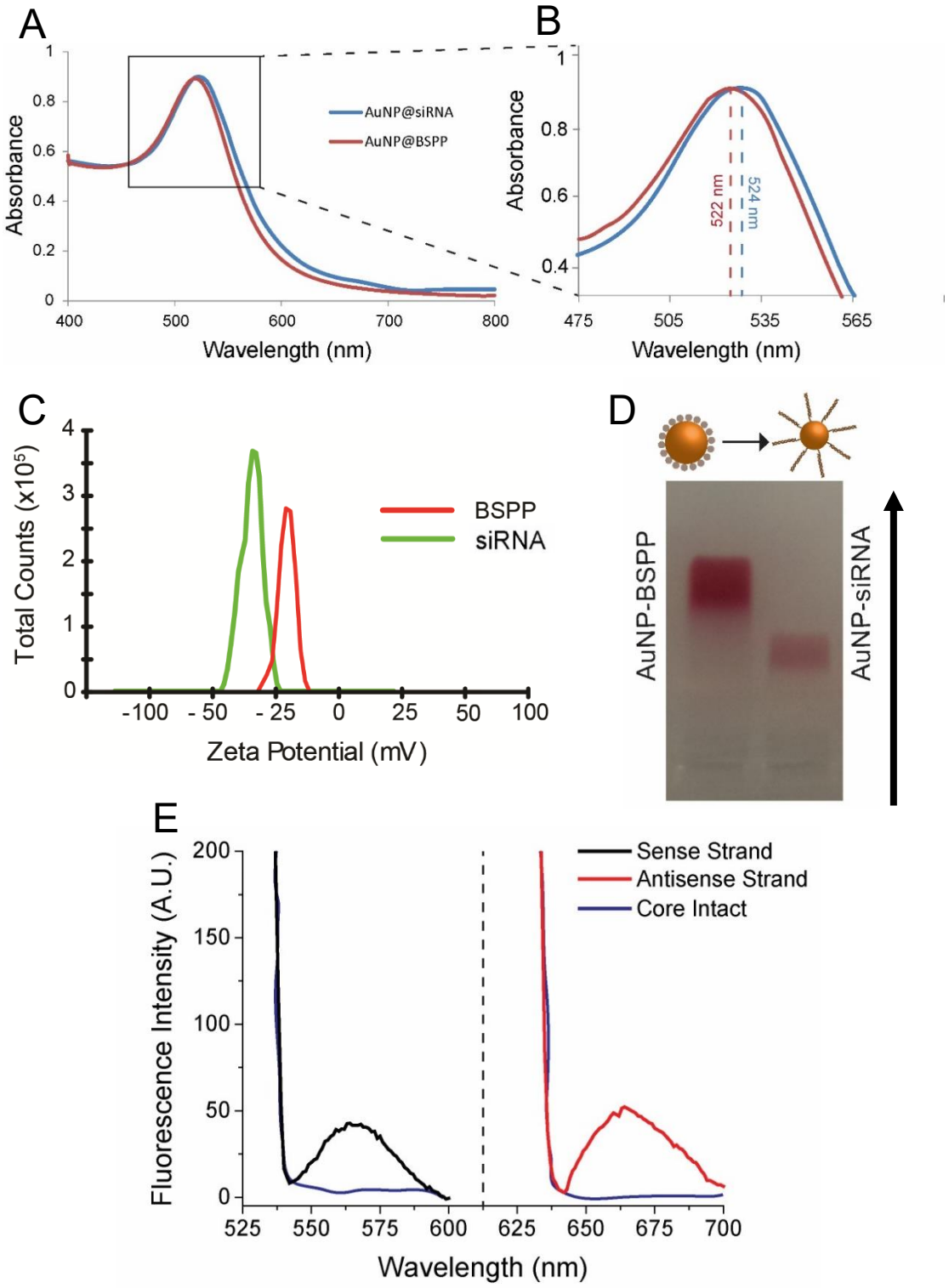

Figure 5.2. Characterization of siRNA duplex conjugation to AuNPs' surfaces. UV-Vis analysis (A-B) demonstrated a slight shift from 522 nm (red) to 524 nm (blue) when the siRNA duplexes (3 nmol) were attached to the AuNPs (10 nM, 1 mL). Additionally, ζ-potential analysis (C) of AuNP-siRNA conjugates showed that the presence of siRNA duplexes lowered the overall net charge from -17 mV (red) to −32 mV (green). Gel

electrophoresis (D) corroborated the results, where a retardation of the band containing AuNP-siRNA conjugates (right) was observed comparatively to the band correspondent to BSPP-coated gold nanoparticles (left). Fluorescence spectrum of Cy3 and Cy5 (E) tagged strands (SMAD3 Sense: Thiol Group - AAA AAA AAA AUU GGA GAA GUU GUA AUG GAG C - Cy3; SMAD3 Anti-sense: GCU CCA UUA CAA CUU CUC CAA - Cy5) after gold core dissolution shows the appearance of 570 nm and 662 nm peaks associated with the presence of the siRNA sense and antisense strands, respectively.

UV-Vis analysis (Figure 5.2.A-B) demonstrated the successful attachment of siRNA duplexes through a shift from the usual absorbance peak of BSPP-coated nanoparticles (red) from 522 nm to 524 nm (blue). This is a direct effect of the change of the refractive index surrounding the nanoparticle and indicates the binding of ligands. This correlates with the results previously shown in Chapter 4 (Figure 4.3.).

The successful attachment of siRNA duplexes was also confirmed *via* ζ-potential. In Figure 5.2.C the attachment of the siRNA sequences is observed by the net charge decreased from -17 mV (red) to −36 mV (green). This shift is induced by the negatively charged phosphate backbone of the RNA strands.

Furthermore, Figure 5.2.D shows the analysis of the conjugations of siRNA strands onto gold nanoparticles using gel electrophoresis. It is possible to observe two distinct bands: BSPP-covered gold nanoparticles (left) and siRNA-covered gold nanoparticles (right). The retardation of the right band is a clear indication that the gold nanoparticles have oligonucleotides attached. In fact, previous work from Pellegrino *et al*. (2007) [36] demonstrated that the presence of oligonucleotides on the surface of gold nanoparticles directly affects its hydrodynamic radius which, in turn, makes the conjugates run slower in gel electrophoresis when compared with particles covered with only small ligands (e.g. BSPP).

Finally, further characterization of the AuNP-siRNA conjugates was performed using fluorescently tagged sequences (Thiol Group - AAA AAA AAA AUU GGA GAA GUU GUA AUG GAG C - Cy3 for sense and GCU CCA UUA CAA CUU CUC CAA - Cy5 for antisense) conjugated with the gold cores in order to calculate how many

DNA strands attached per particle . The conjugates were dissolved *via* gold etching and the fluorescence of both strands was analysed. Figure 5.2.E shows that in the presence of the gold core, the dyes are quenched (blue), in line with the results observed with the imaging probes (section 4.1.). However, after dissolving the gold core, both Cy3 and Cy5 fluorescence peaks (570 nm and 662 nm, respectively) appear in the fluorescence analysis. This demonstrate that both the sense and antisense strands are conjugated to the surface of the gold nanoparticles.

Therefore, all the results presented in Figure 5.2. demonstrate that the conjugation between siRNA duplexes and gold cores was successful. However, silencing efficiency highly depends on the number of siRNA molecules inserted into cells [37, 38]. Taking advantage of the tagged sequences used in the fluorescence analysis in figure 5.2D, the number of siRNA duplexes per nanoparticle was determined. For this calibration curves for both the sense (Figure 5.3.A) and the anti-sense (Figure 5.3.B) strands were experimentally determined by analysing the fluorescence maxima of both Cy3 (570 nm) and Cy5 (662 nm) in a range of concentrations (50 nM to 2 µM

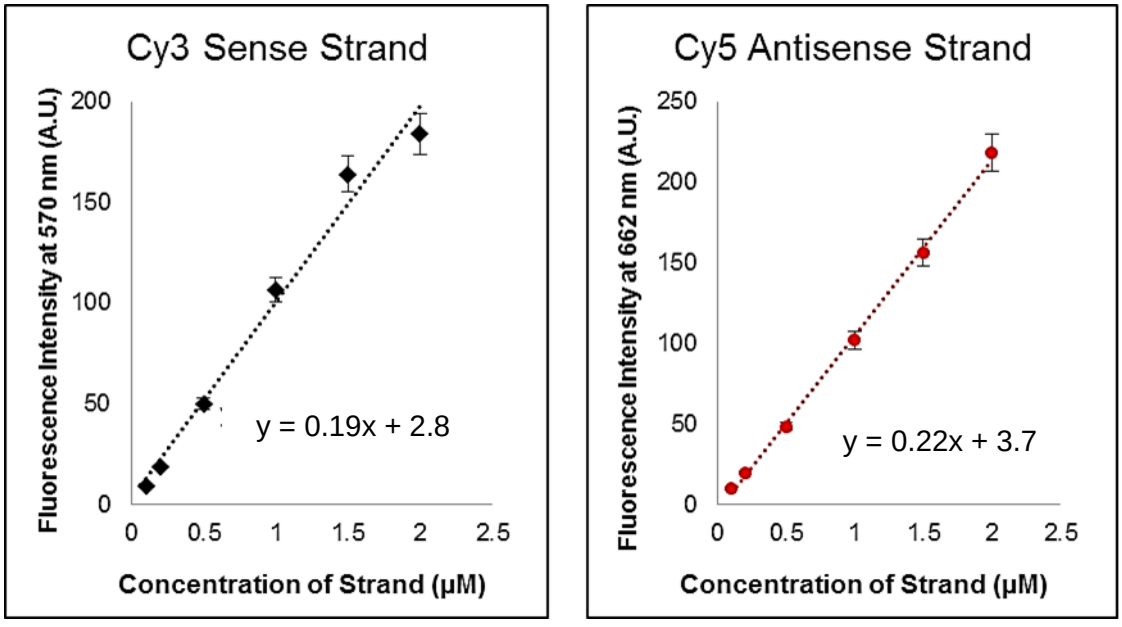

Figure 5.3.Quantification of the siRNA duplexes attached to AuNP cores *via*fluorescence analysis. The number of siRNA duplexes was determined by performing calibration curves in known concentrations (50 nM to 2 µM) of both the sense

(black) and the antisense (red) strands. Using the extracted equations, the average number of SMAD3 siRNA duplexes per particle was determined to be 48 ± 3.

Using the obtained equations, it was possible to determine that the average number of duplexes was about 48 ± 3 duplexes/particle (see Appendix B.3.). This ratio falls within the averages reported by Lee *et al.* (2009) [32] and Barnaby *et al.* (2016) [39], and falls in the optimal window of siRNA loading for successful silencing treatments [40].

5.2. Stability tests of RNA-gold nanoparticle conjugates

The overall stability of the AuNP-siRNA conjugates was tested by investigating three different parameters: melting temperature (section 5.2.1.), molecule displacement (section 5.2.2.) and stability in cell media (section 5.2.3.).

5.2.1 Thermal stability

As discussed in Chapter 4, the melting temperature of a duplex is extremely important to understand its thermal stability. In this case, the stability of the siRNA duplexes is essential for their recognition by the RISC complex, and subsequent gene silencing [41]. The melting curve was monitored using SYBR® Green. This dye is known to intercalate in double stranded oligonucleotides [42]. As a result, the increase of the fluorescence signal at its peak emission (520 nm) is directly related with the percentage of double strands present in solution. The siRNA strands were hybridized in the presence of 1 nM of SYBR® Green solution to ensure its intercalation in the double strands. The resulting solution was analysed at a range of temperatures between 15ºC and 90ºC(Figure 5.4.).

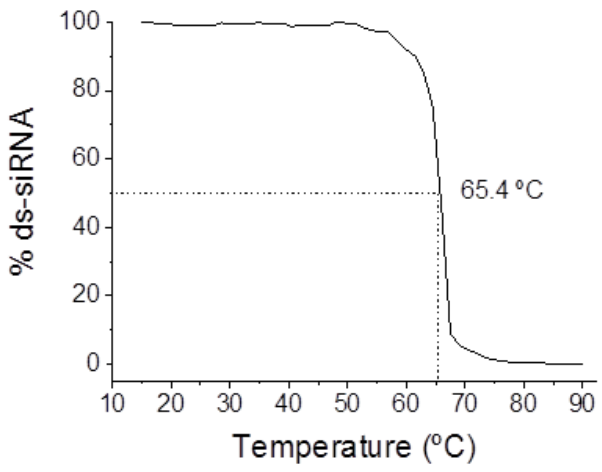

Figure 5.4. Thermal testing of AuNP-siRNA stability. By hybridizing the sense (Thiol Group - AAA AAA AAA AUU GGA GAA GUU GUA AUG GAG C) and antisense (GCU CCA UUA CAA CUU CUC CAA) strands in the presence of SYBR® Green, it was possible to determine that the duplexes are stable up until approximately 58 ºC, with the melting temperature of these strands being 65.4 ºC.

Figure 5.4. demonstrates an inversed sigmoidal curve, as the experiment started with double strands already formed. Consequently, the fluorescence signal of the intercalated SYBR® Green dye could be observed at lower temperature. However, at approximately 58 ºC the fluorescence intensity starts decreasing, reaching 50% of its signal at 65.4ºC. This is similar to the results obtained in the melting curve experiment (Figure 5.1.B), where the melting temperature was determined to be 61.7 ºC. These results show that these siRNA duplexes are stable at the physiological temperature (approximately 37 ºC).

5.2.2 Glutathione Assay

As explained in Chapter 4, the glutathione assay can demonstrate the resistance of the conjugates to the displacement of the siRNA duplexes from the nanoparticle core, since GSH has a free thiol group that can compete with the strands. In fact, Kim *et al.* (2012) reported that GSH can lead to the unspecific and premature release of the siRNA sequences in cells if not properly protected [25], Therefore, AuNP-siRNA probes were incubated with 5 mM of GSH similarly to the conditions used in section 4.3.2. For this assay the fluorescently tagged strands were used and monitored for 24h.

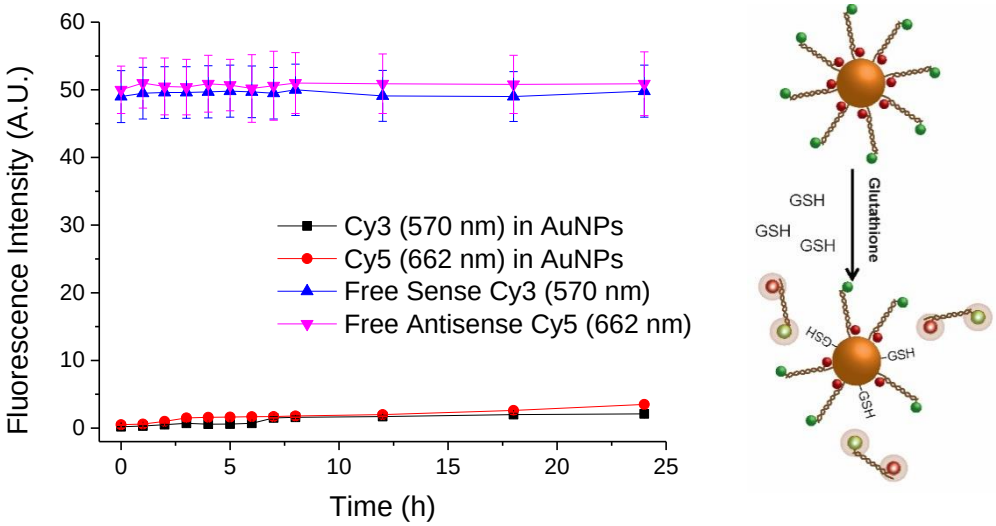

Figure 5.5.Stability of AuNP-siRNA conjugates in glutathione rich environment. Fully formed silencing probes were incubated with 5 mM of glutathione (GSH) and the fluorescence was monitored over 24h (left). In the event of displacement (right), the strands would come away from the nanoparticles and fluorescence would be restored. When compared with free strand solutions (blue and pink), the fluorescence signal of the strands attached to the nanoparticles (red and black) did not significantly change over time.

As shown in figure 5.5, at high concentrations of GSH, more than 95% siRNA duplexes were maintained in the surface of the nanoparticles. This is a strong indication of the high stability of these silencing agents and correlates with the results obtained in Chapter 4 (Figure 4.6.).

5.2.3 Stability in growth media for cell culture

As stated before in section 4.3.4., components of media used for cell culture, such as proteins and salts, can cover nanoparticles, altering their interaction with cells [43–45]. To test if the siRNA probes would still function in the in vitro experiments, probes were incubated with MEM culture media. The fluorescence of the siRNA duplexes was monitored for 18h using fluorescence spectroscopy (Figure

5.6.A). In addition, UV-Vis spectroscopy was used detect inter-particle aggregation after incubating with the cell culture medium (Figure 5.6.B).

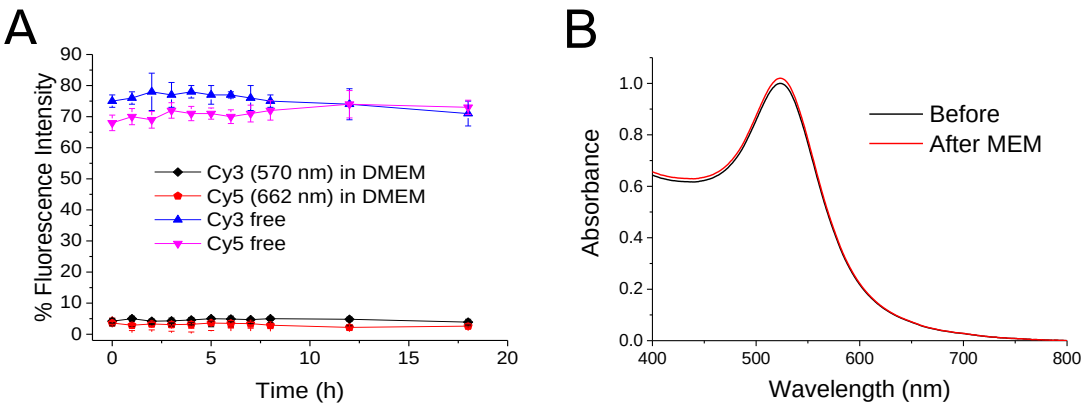

Figure 5.6.Stability of AuNP-DNA conjugates in cell culture media. Fully conjugated AuNP-siRNA probes were incubated with MEM media for 18h. Fluorescence analysis (A) showed that no significant displacement of the strands was observed. Additionally, UV-Vis analysis (B) demonstrated no significant aggregation of the AuNP-DNA conjugates.

The data shown in Figure 5.6. indicates that the AuNP-siRNA conjugates were not affected by incubation with cell media, as no significant fluorescence was observe for both the sense and the antisense strands (black and red, respectively) over time. This means that no unspecific release of both strands was observed due to interaction with cell medium's components. Furthermore, Figure 5.6.B shows that no aggregation between particles took place, as determined by the unchanged plasmon peak at 524 nm (red). Therefore, both results indicate that the conjugates were optimal to use in further experiments in *in vitro* (section 5.3.) and *in vivo* (section 5.4.)

5.3. Effect in *in vitro* models

With the AuNP-siRNA conjugates fully characterized, the conjugates were tested in mouse embryonic fibroblasts (MEFs) and their performance was analysed. The

conjugates used in these experiments were made using the non-tagged sequences (**SMAD3 Sense**: Thiol Group- AAA AAA AAA AUU GGA GAA GUU GUA AUG GAG C; **SMAD3 Antisense**: GCU CCA UUA CAA CUU CUC CAA; **Scramble Control Sense**: Thiol Group – AAA AAA AAA ACA CAG UAU CAA UCU CAA GCC C; **Scramble Control Antisense**: GGG CUU GAG UUG AUA CUG UG; see table 3.1. for more details). This was done to prevent alterations in the 3D configuration of the duplexes, since many studies have indicated that the activation of the RISC pathway is extremely sensitive to aspects such as 5' end chemical modifications, the sequence of the guiding strand and its length and configuration prior to the pre-RISC complex formation [46–49].

5.3.1 Toxicity

Although gene silencing is generally regarded as a directed tool that only affects one target gene, the use of some silencing sequences can lead to undesired side effects on the viability of the targeted cells. For example, a report from Jackson *et al*. (2006) demonstrated that base mismatches within the siRNA can lead to off-target silencing, which causes undesirable and potentially toxic side effects. [50] Also, Carralot *et al.* (2009) demonstrated that excessive siRNA concentrations can render an otherwise harmless siRNA into a toxic element. [51]

To test the cytotoxicity of AuNPs-siRNAs, MEFs were incubated with a range of AuNP-siRNA concentrations (0.1 – 50 nM). The impact of these conjugates in cell viability was studied using a MTT assay. Several controls were used to discard the effect of the incubation process, the particles and the presence of oligonucleotides.

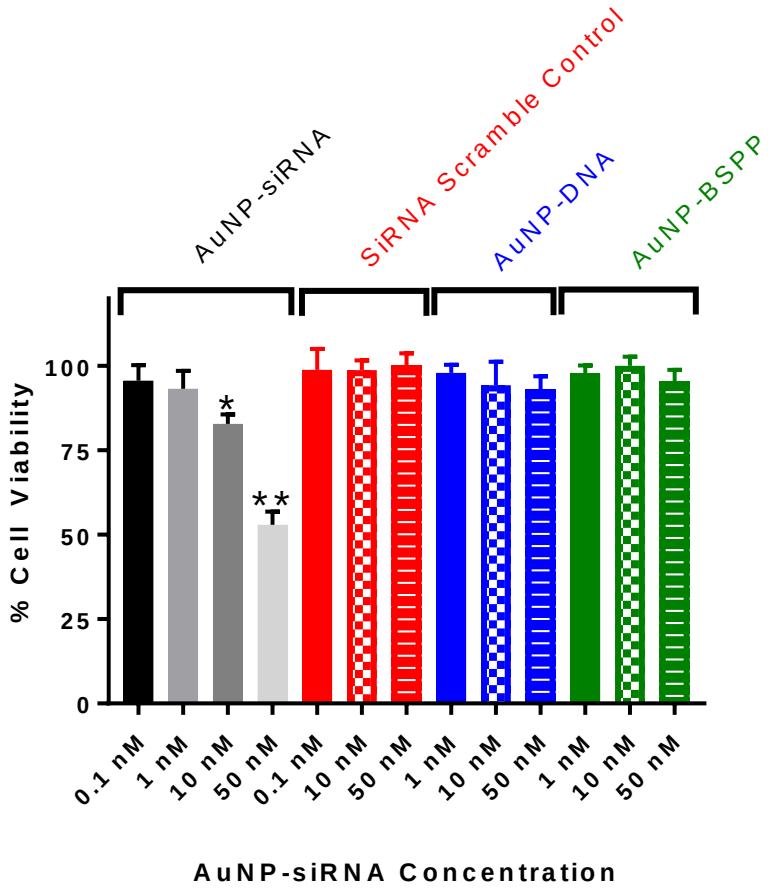

Figure 5.7. Impact of SMAD3 siRNA-covered AuNPs in the viability of MEFs. An MTT assay was conducted for cells treated with different solutions for 24h: SMAD3 AuNP-siRNA (0.1 – 50 nM, black), scramble AuNP-siRNA (0.1 – 50 nM, red), AuNP-DNA (1 – 50 nM, blue) and AuNP-BSPP (1 – 50 nM, green). Only SMAD3 siRNA-AuNP treated cells demonstrated a reduction on their viability. The viability of cells exposed to 10 nM of SMAD AuNP-siRNA decreased approximately 12%, while cells exposed to 50 nM of the same type of solution had approximately 43% of their viability decreased (*$p<0.05$, **$p<0.01$, student's t-test, n = 3, triplicates for each n)

As shown in Figure 5.7., SMAD3 siRNA coated AuNPs had an impact on cell viability (black). Even though at lower concentrations (0.1 nM and 1 nM) no significant changes were observed, at higher levels (50 nM), 43% of cells died due to the treatment. Interestingly, cells treated with medium concentrations (10 nM) demonstrated a small but significant decrease of about 12% in their viability. In contrast, BSPP-coated nanoparticles had no effect on cell viability, even at high

concentrations (50 nM). Additionally, particles coated with different oligonucleotides (i.e. DNA) did not significantly change cell viability (blue). Finally, particles coated with scramble RNA sequences also had no significant impact in the cells at any given concentrations (red).

These results demonstrate that: a) gold nanoparticles and DNA/RNA conjugates with unspecific sequences have no significant effect in this cell line; b) the presence of SMAD3 siRNA might have a specific impact in cells, which points to a successful design of the sequences; and c) this cellular impact is observable at medium concentrations (10 nM) and clear at high concentrations (50 nM). However, despite the significant decrease in cell viability at medium concentrations, the impact of AuNP-siRNA conjugates on the SMAD3 protein levels was still not clear. Due to the high cell mortality with 50 nM, the highest concentration of AuNP-siRNA conjugates used in the following experiments was 10 nM.

5.3.2 Impact on protein levels

With the indication that SMAD3 siRNA covered AuNPs had a slightly significant effect in cells, the impact of these silencing probes on SMAD3 protein levels was studied. For that, MEFs were incubated with a range of SMAD3 AuNP-siRNA concentrations (0.1 – 10 pmol/10^4 cells) in order to study if there was an effect on the expression of SMAD3 after 18h of exposure. SMAD3 levels were monitored using epifluorescence microscopy (Figure 5.7.) using a rabbit polyclonal ∝ -Mouse SMAD3 primary and Cy3 (570 nm) tagged secondary antibodies

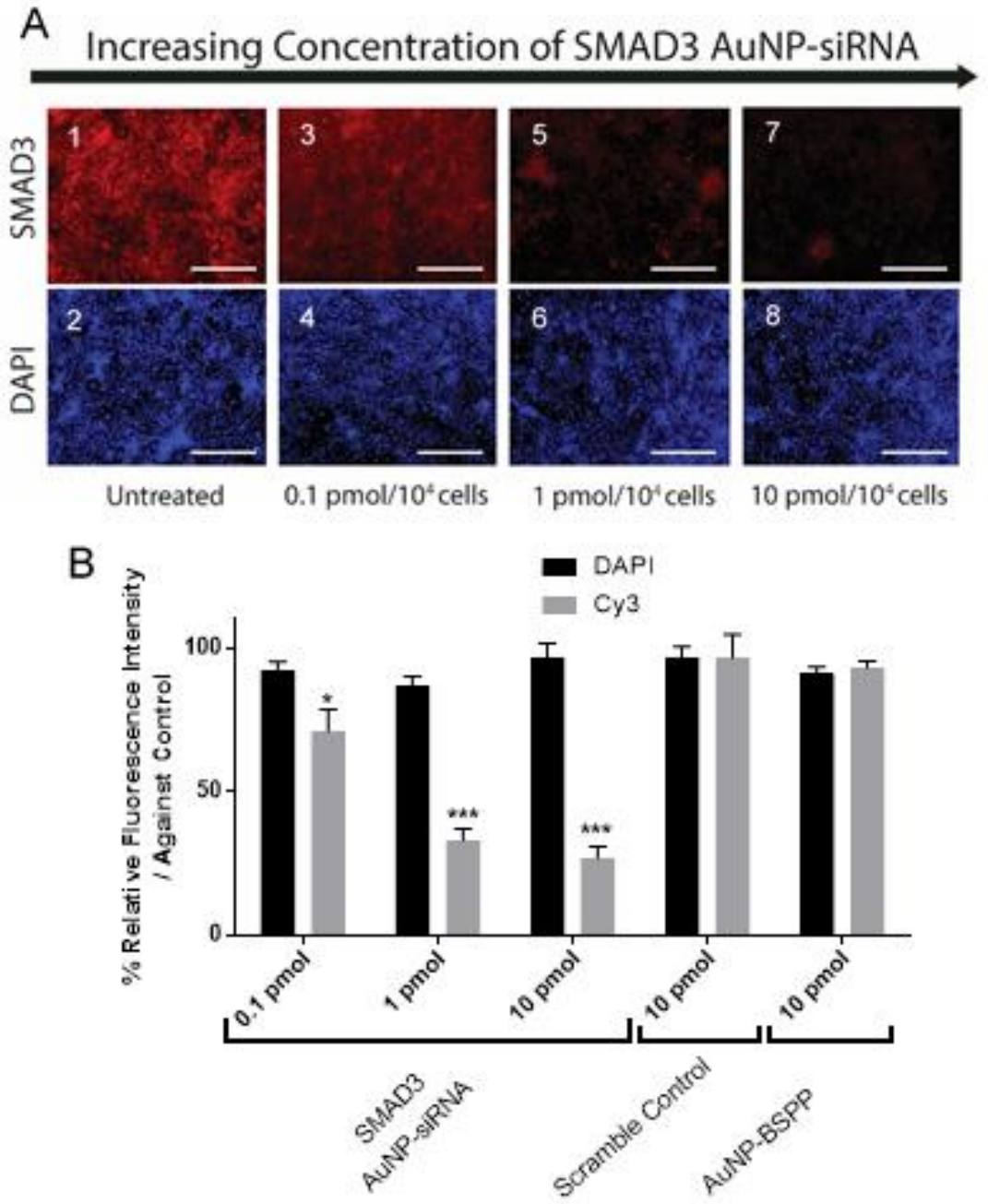

Figure 5.8. Immunofluorescence analysis of SMAD3 in MEF cells. MEF cells were treated with different concentrations of SMAD3 AuNPs-siRNA (0.1-10 pmol/10^4 cells), as well as a scramble control and BSPP-coated particles. SMAD3 levels were monitored using a rabbit polyclonal ∝ -Mouse SMAD3 primary and Cy3 tagged secondary antibodies after 18h of incubation (A). No difference was observed in untreated cells (1). However, the fluorescence intensity correspondent to SMAD3 (red) decreased gradually in the presence of increasing concentrations of SMAD3 probes (3, 5 and 7). The nuclear stain DAPI was used as a counterstain for cell counting (2, 4, 6 and 8). (Scale bar = 100 µm). The relative

fluorescence intensity was calculated using the untreated cells as standard (B). As shown, in the presence of increasing concentrations of SMAD3 AuNP-siRNA conjugates (0.1, 1 and 10 pmol / 10^4 cells), SMAD3 fluorescent signal decreased to approximately 73%, 38% and 32%, respectively, when compared to control cells. (*p<0.05, ***p<0.001, One-Way Anova test)

Figure 5.8A implies that at low concentrations of AuNP-siRNA conjugates (0.1 pmol/10^4 cells), there is already a reduction in the levels of SMAD3, as seen by the decrease in fluorescence. In fact, by increasing the concentration by 100-fold it is possible to see potentially significant decrease in the levels of SMAD3. To account for changes in cell viability, the quantification of SMAD3 levels was normalized using the levels of nuclear DAPI fluorescence (Figure 5.8A). Cells incubated with particles covered with either BSPP or a scramble sequence did not show any significant change in fluorescence intensity related with the levels of SMAD3. However, in the presence of 0.1 pmol/10^4 cells concentration, the fluorescence intensity associated with the levels of SMAD3 was reduced to 73%. By increasing the concentration of AuNP-siRNA by 10x, the fluorescence intensity was further reduced to 38%. Finally, cells incubated with 10 pmol /10^4 cells had their fluorescence intensity reduced to 32% when compared to control cells. DAPI intensity remained virtually unaltered across the samples. Furthermore, no changes in the levels of SMAD3 were observed in control conditions – (10 pmol/10^4 cells of AuNP-BSPP and AuNP-scramble sequence) (Figures B.6. in Appendix B).

To compliment this analysis, the levels of SMAD3 were analysed by western blot (Figure 5.9.A) and LICOR® In-cell western (Figure 5.9.B-C).

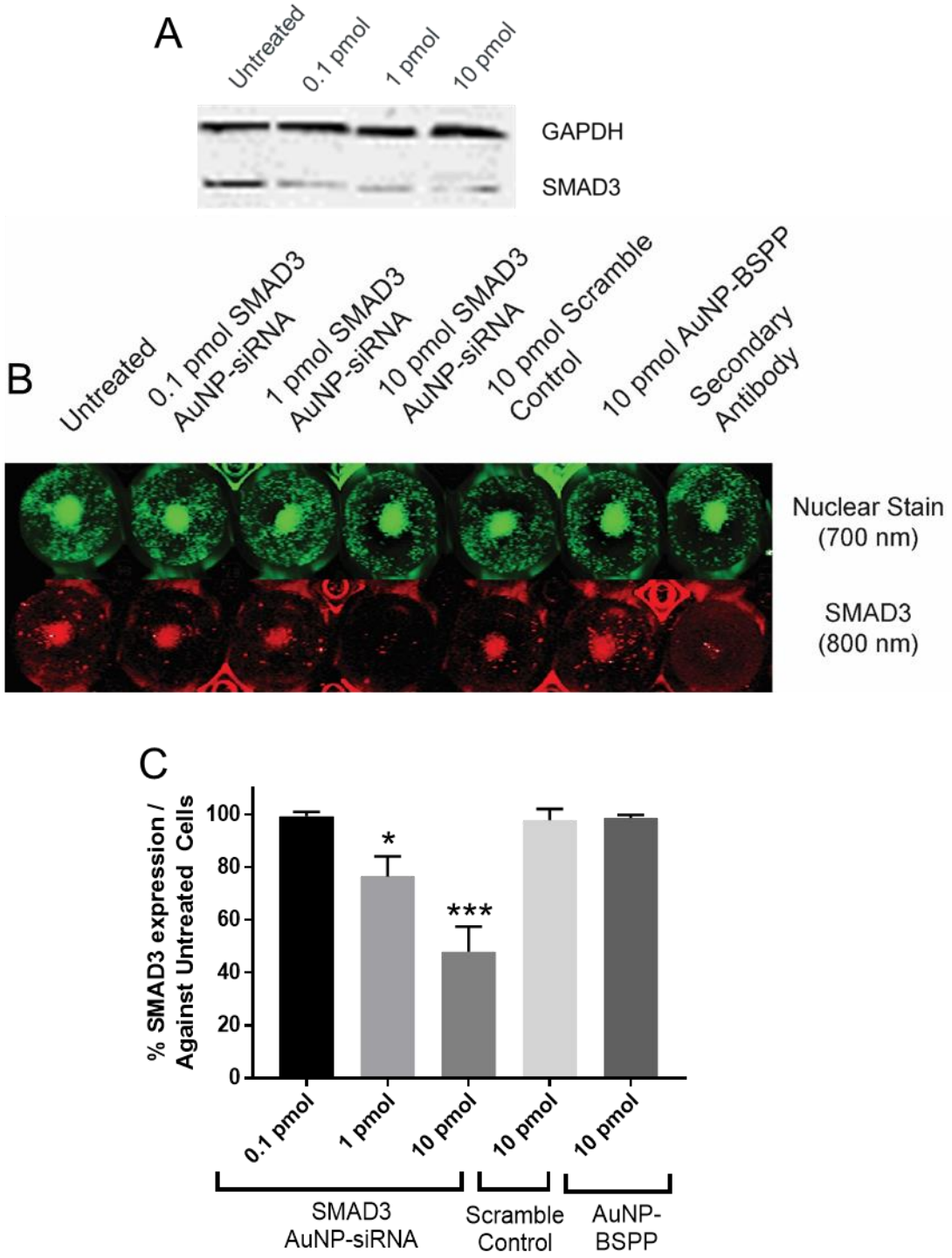

Figure 5.9. Analysis of the impact of SMAD3 AuNP-siRNA conjugates in protein levels using Western Blot and In-Cell Western. MEF cells were treated with different concentrations of SMAD3 AuNPs-siRNA (0.1-10 pmol/10^4 cells), as well as a scramble siRNA control and BSPP-coated particles for 18h. For the western blot (A), lysis was performed after the incubation and the resulting lysate solutions were run on a 10%

PAGE gel and blotted. GAPDH was used as a housekeeping gene (top). SMAD3 protein (bottom) was present in lower concentrations when treated with SMAD3 AuNP-siRNA conjugates compared with untreated cells (left). In addition, In-Cell western was performed (B) by seeding cells in conical bottom 12-well plates and treating them with the same type of solutions as with the Western Blot experiments for 24h. After fixation, cells were treated with a combination of SMAD3 primary and IRDye800 secondary antibodies (red). At the same time, CellTag 700 nuclear staining (green) was used for posterior normalization of quantified fluorescence and two different control wells (untreated and cells not incubated with SMAD3 primary antibody) were included. Although SMAD3 levels seem to decrease only in the presence of 10pmol of silencing probes, quantification of these results using a normalizing factor (nuclear staining) shows that in the presence of 1 and 10 pmol of SMAD3 AuNP-siRNA conjugates the relative SMAD3 levels were reduced to 77% and 48% respectively when compared with untreated cells. No significant difference was observed for any other sample. (*$p<0.05$, ***$p<0.001$, Student's t-test, n=3, triplicates for each n)

For western blot, MEFs cells were incubated with a range of different concentrations of SMAD3 siRNA conjugates (0.1-10 pmol/10^4 cells). After 24h the cells were lysed. The resulting samples were separated using a 10% PAGE gel and analysed using a LICOR Odyssey scanner. GAPDH was used as a loading control. Figure 5.9.A shows that the level of SMAD3 protein had an indicative decrease in samples treated with siRNA-covered gold nanoparticles.

For the In-cell western assay, MEFs were seeded in a conical 12-well plate and incubated with different concentrations of SMAD3 AuNP-siRNA (0.1-10 pmol), as well as 10 pmol of BSPP and scramble sequence covered gold nanoparticles. In this assay, cells were fixed and incubated with a SMAD3 primary antibody (except for the well used as a control for the secondary antibody) and a secondary antibody emitting at 800 nm. A nuclear stain provided with the kit (emission at 700 nm) was added to all wells to normalize the results. Cell were analysed in an Odyssey® Infrared imaging system. Figure 5.8.B shows that SMAD3 protein levels seem to decrease with higher concentrations of SMAD3 siRNA conjugates. Untreated cells and cells treated with BSPP and scramble sequence covered nanoparticles show no difference in fluorescence. These results were quantified using the counterstain channel as a normalization factor and the secondary antibody samples as a

background signal (Figure 5.8.C). Interestingly, no significant difference between cells treated with 0.1 pmol of SMAD3 siRNA probes and the controls was found (opposite to the results obtained in the western blot and the epifluorescence experiments). This observation could be linked to the reduced sensitivity of this technique in detecting lower variations of protein in cells. Despite this, the cells treated with 1 pmol of SMAD3 siRNA probes did show a small but significant decrease of SMAD3 protein levels by approximately 23%. However, it was at 10 pmol concentrations that a significant effect was seen, with the values of SMAD3 being approximately 52% lower than the untreated cells.

Therefore, combining all the results from epifluorescence, western blot and in cell western, there was a strong suggestion that the lowest concentrations of AuNP-siRNA at which a significantly different apparent effect was observed was at 1 pmol / 10^4 cells. This concentration also pointed for a non-significant toxicity effect in cells (as seen in the MTT experiment), and therefore was deemed the optimal concentration to use in further experiments

5.3.3 Impact in mRNA levels

After observing the indicative impact that SMAD3 silencing probes had on the levels of the SMAD3 protein, there was an interest on studying the impact of these probes in the mRNA levels of the cells. For that, MEFs were incubated with different solutions containing either SMAD3 siRNA-coated particles (0.1 – 10 pmol/10^4 cells) or control particles (BSPP coated or scramble sequence coated, 10 pmol/10^4 cells for each) and a quantitative polymerase chain reaction (qPCR) was conducted. For this experiment both TGF-β and SMAD3 levels were analysed, and GAPDH and SMAD1 were used as controls (loading and specificity of the siRNA). SMAD1 was interesting to study as well in order to investigate if the sequence designed was specific to only SMAD3 or if it affected other proteins of the same family. SMAD1 was therefore chosen due to its role in the Bone morphogenetic proteins (BMPs) pathway, related to but independent of the SMAD2/3 - TGF-β pathway [52–54].

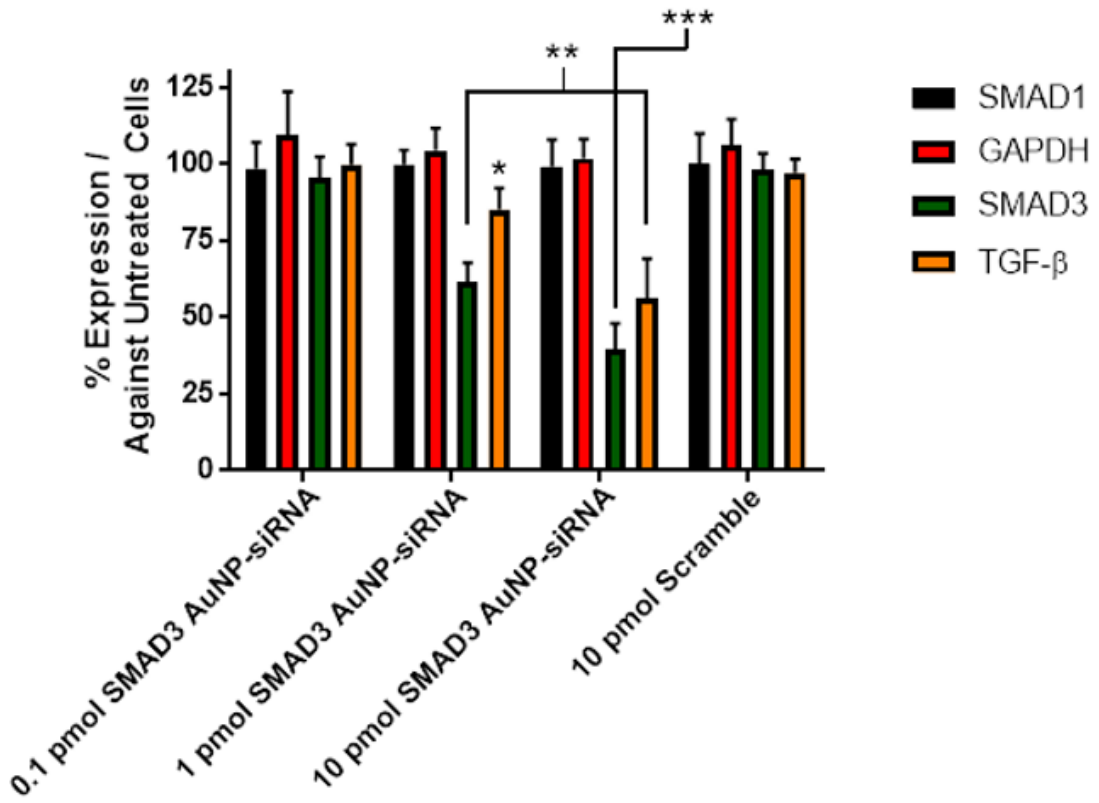

Figure 5.10. Analysis of the impact of SMAD3 AuNP-siRNA conjugates in mRNA levels using qPCR. MEF cells were treated with different concentrations of SMAD3 AuNPs-siRNA (0.1-10 pmol/10^4 cells), as well as a scramble control-coated particles for 18h. qPCR was then performed to monitor four different types of genes: SMAD1 (black), GAPDH (red), SMAD3 (green) and TGF-β (orange). No significant change on the levels of SMAD1 and GAPDH were observed across the samples. However, at concentrations of 1 and 10 pmol/10^4 cells of SMAD3 AuNP-siRNA conjugates, there was a decrease of mRNA levels of SMAD3 and TGF- β levels. SMAD3 mRNA levels decreased by 39% (1 pmol/10^4 cells) and by 62% (10 pmol/10^4 cells), while TGF-β mRNA levels decreased by 15% (1 pmol/10^4 cells) and 40% (10 pmol/10^4 cells). (*$p<0.05$, **$p<0.01$, ***$p<0.001$, Student's t-test, n=3, triplicates for each n)

Figures 5.10. hints to the possibility of the mRNA levels of both GAPDH (red) and SMAD1 (black) not being affected by the treatment with SMAD3 siRNA probes. This points to the specific targeting of the probes to SMAD3. When compared with untreated cells, the levels of SMAD3 RNA (green) were significantly lower in cells treated with 1 and 10 pmols of SMAD3 siRNA AuNP-siRNA probes (39% and 62%

respectively). Furthermore, low concentrations of AuNP-siRNA probes (0.1 pmol/10^4 cells) seemed not to affect the levels of SMAD3. Scramble siRNA coated particles similarly demonstrated no clear effect in the overall mRNA levels of SMAD3.

These results also pointed to a decrease of TGF-β mRNA levels, potentially as a consequence of SMAD3 silencing. Low concentrations of AuNP-siRNA, as well as scramble control particles, seemed not to have any significant impact on the mRNA levels of TGF-β. However, interestingly enough, the same concentrations that were observed to have an apparent impact on SMAD3 mRNA levels also translated onto indicative changes in the mRNA levels of TGF-β. 1 pmol SMAD3 AuNP-siRNA was related to an apparent decrease of TGF-β by approximately 15%, while 10 pmol had an apparent decrease of approximately 40%.

These results indicate that the design of the probes was successfully done and that these conjugates not only had an apparent impact on the levels of SMAD3 mRNA but also on the levels of the levels of TGF-β mRNA. Therefore, further studies were conducted *in vitro* to understand the impact that the presence of SMAD3 AuNP-siRNA probes might have in the migratory behaviour of MEFs (see section 5.3.4.), before proceeding to the application of these probes in *in vivo* models.

5.3.4 Migration assay

As previously stated, the SMAD3/ TGF-β pathway is involved in the regulation of cell movement and migration in wounded sites[55–57]. Au *et al*. (2015) [58] and Zhang *et al.* (2013) [59] demonstrated that cells in which TGF-β was either blocked or partially decreased led to a slower migration rate. To test if SMAD3 silencing had a similar effect on cell migration, cell dishes with 90% confluent MEFs were incubated with different concentrations of AuNP-siRNA probes (0.1-10 pmol/10^4 cells), as well as 10 pmol/10^4 cells of scramble coated nanoparticles for 12h. Afterwards, the cells were wounded (i.e. a scratch assay was performed) and the migration of the cells was photographed after 6h, 24h and 36h in order to assess if the presence of AuNP-siRNA probes would make any difference in the rate at which cells would close the wound.

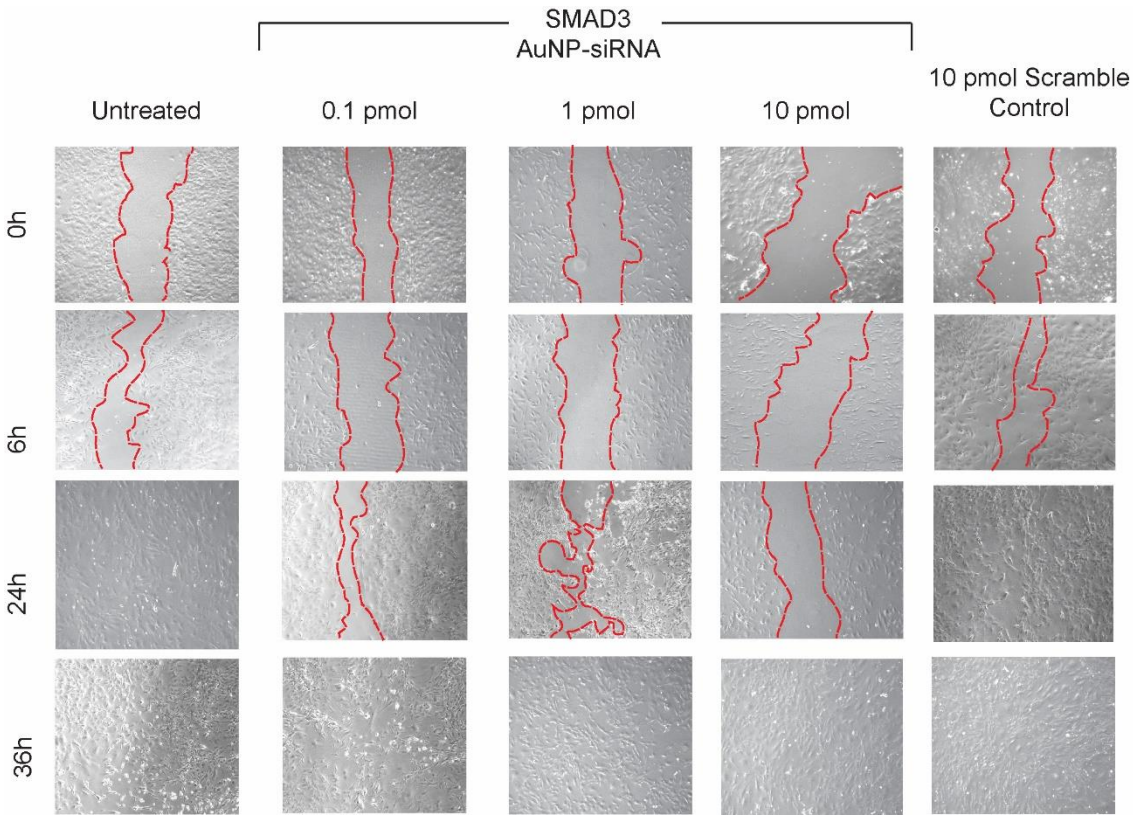

Figure 5.11. Migration assay on MEF cells in the presence of SMAD3 AuNP-siRNA conjugates. MEF cells were incubated with three different concentrations of AuNP-siRNA conjugates (0.1, 1 and 10 pmol/10^4 cells) for 12h. Control cells were incubated with 10 pmol/10^4 cells of scramble siRNA coated particles or untreated. After the incubation period, a scratch assay was performed and monitored over 6h, 24h and 36h. All cells demonstrate the scratch assay at the 0h time-point (top). After 6h, no significant difference between the samples was detected. However, after 24h, untreated cells had migrated to completely close the wounded area while cells treated with SMAD3 AuNP-siRNA conjugates showed a retardation on the migration rate. After 36h, all cells had recovered completely.

As seen in Figure 5.11., the wounded area (i.e. scratch area) was approximately of the same size in all cell dishes (0h). However, over time the migration rates of the MEFs varied with each treatment. After 6h, it was already possible to see small differences in the wound size. However, after 24h untreated cells and cells treated with scramble siRNA control solution had fully migrated from the edges of the wound towards the centre, closing the scratched area in the process. In the presence of

increasing concentrations of AuNP-siRNA probes, the wounded area was closed at a slower rate. After 36h all the wounded areas were completely closed. By measuring the relative size of the wounded area comparatively to the total area of the images across all the different samples, the rate of wound closure was calculated (Figure 5.12.A-B), as well as the recovery rate (Figure 5.12.C).

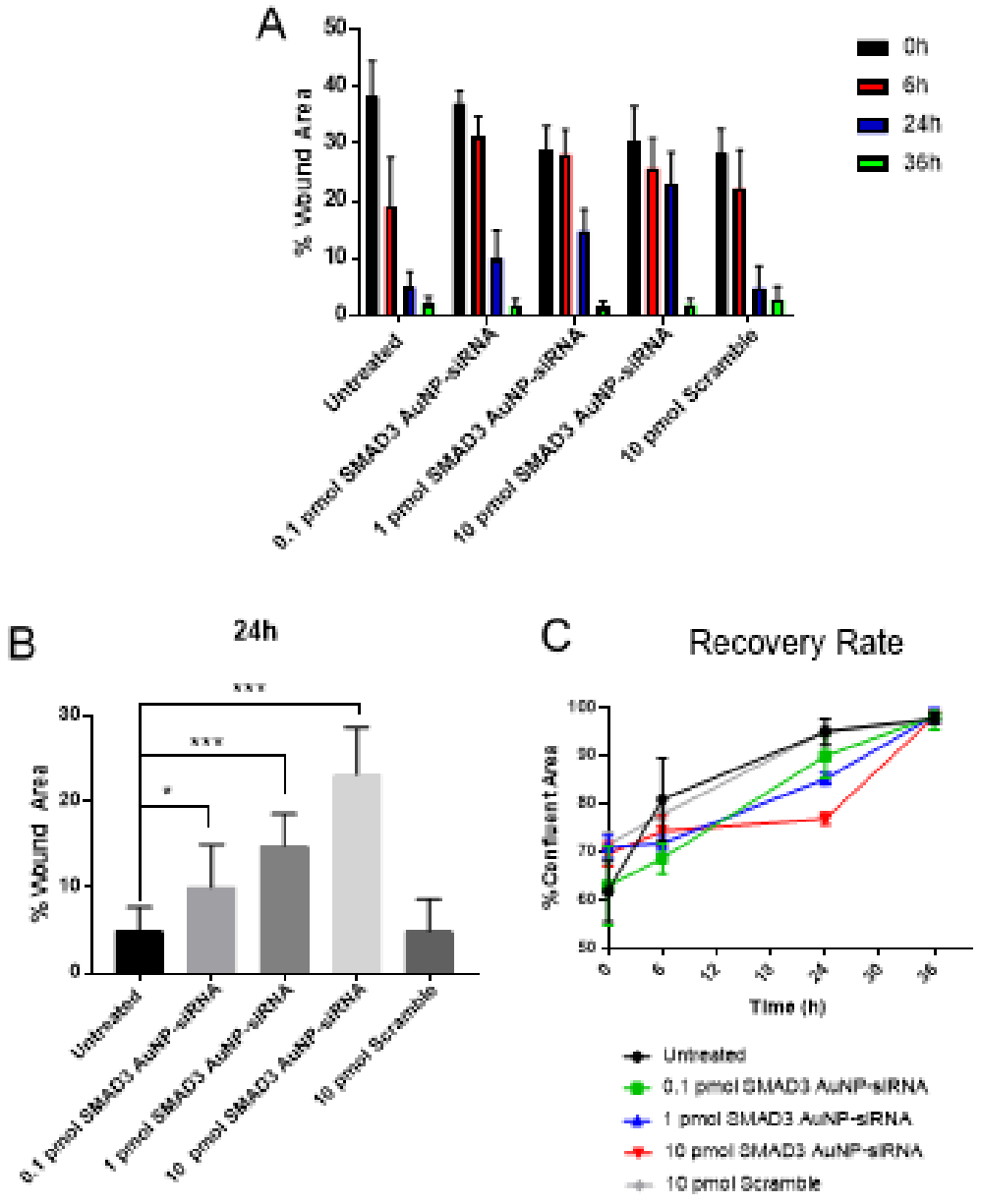

Figure 5.12. Analysis of the migration assay on MEF cells in the presence of SMAD3 AuNP-siRNA conjugates. Analysing the % wound area (A) over time, it was observed that the distribution of the % area that each wound took from the respective sample was random at both 0h (black) and 6h (red). However, at 24h (blue), cells treated

with AuNP-siRNA had a higher % of wounded area. In fact, zooming in at 24h (B), cells treated with 0.1, 1 and 10 pmol/10^4 cells of SMAD3 AuNP-siRNA conjugates had wounded areas that were 1.5x, 4x and 4.8x bigger than the control cells respectively. After 36h, all the cells had recovered. When looking at the recovery rate (C), cells treated with increasing concentrations of SMAD3 AuNP-siRNA conjugates recovered slower from the scratch performed. (n=8, *p<0.05, ***p<0.001, student's t-test)

During the three time points (6h, 24h and 36h), MEFs treated with different concentrations of AuNP-siRNA demonstrated a slower rate of wound healing/closure than untreated cells or cells treated with the scramble siRNA control (Figure 5.12.A). In fact, the percentage of wounded area in dishes that were treated with the silencing probes was at least 1.5x higher than the other cells, with the maximum concentration used (10 pmol) having a wounded area 4.8x higher than untreated cells for example. Additionally, Figure 5.12.C shows that cells treated with different concentrations of AuNP-siRNA had a significant slower rate of wound closure when compared to untreated cells or cells treated with the scramble siRNA. Control cells (untreated and scramble treated) had an initial burst in the recovery rate, plateauing after 24h. Oppositely, cells treated with 0.1 and 1 pmol/10^4 cells demonstrated a constant rate over time. Interestingly, concentrations of 10 pmol/10^4 cells showed an inverted recovery curve to untreated cells, with an initial slow recovery in the first 24h and a quicker rate in the last stages. This might have happened

These results strongly indicate that silencing of SMAD3 has a clear effect in the migratory rate of cells. However, recently reports by Gilleron *et al.* (2013) [60] and Wu *et al.* (2014) [61] discussed the possibility of nanoparticle siRNA delivery agents having great difficulty in escaping endosomes after cellular uptake. The endosomal escape mechanism has been studied over the years [62], with explanatory theories ranging from "proton sponge" effect [63] to pore formation in the vesicle membrane [64] with no definitive single answer. Furthermore, studies suggesting that the nanoparticle systems rarely or never leave endosomes have been reported [65]. Therefore, even though a clear effect was observed for SMAD3 siRNA-covered nanoparticles in protein and mRNA levels from our experiments, cells treated with

SMAD3 AuNP-siRNA conjugates were observed under transmission electron microscopy (Figure 5.13.) in order to evaluate the relative intracellular location of the probes.

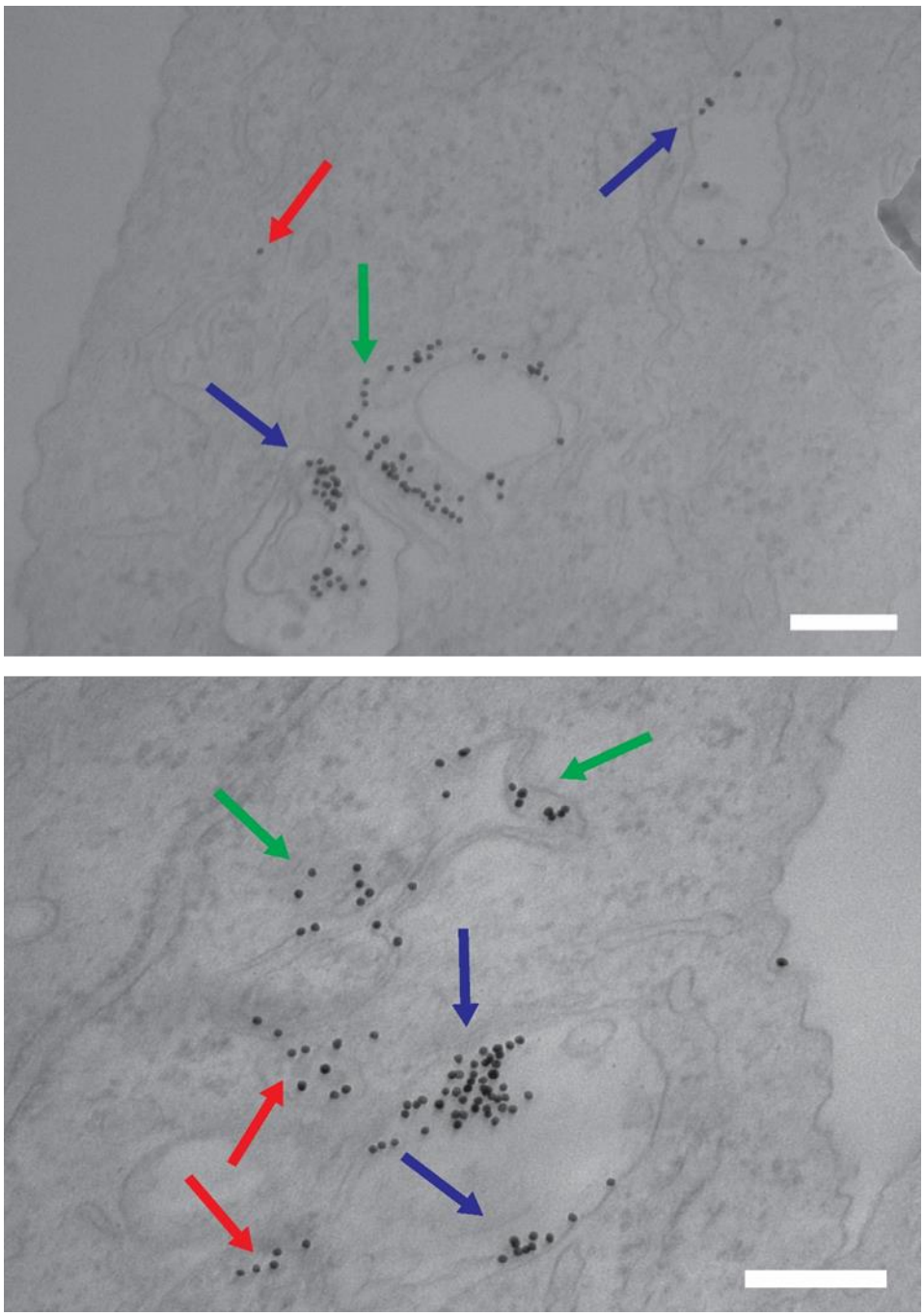

Figure 5.13. TEM cross sectioning of MEF cells incubated with SMAD3 AuNP-siRNA conjugates. Cells were incubated with 1 pmol/10^4 cells for 18h. After fixation, sectioning was performed and images were analysed under a TEM microscope. Gold cores (black dots) were found in three different locations: inside vesicles and endosomes (blue),

in the process of escaping the vesicles (green) and outside the vesicles (red). (Scale = 200 nm)

Based on these results, SMAD3 AuNP-siRNA conjugates were found in three different locations: inside either endosomes or multivesicular bodies (blue arrows), coming out of vesicles (green arrows) and in the cytosol (red arrows) (Figure 5.13). These results suggest that SMAD3 siRNA conjugates might undergo endosomal escape to some degree, based on both the silencing experiments performed and the representative TEM images taken of MEF cells after incubation with the silencing probes. The results relate with recent reports where only a small percentage (1-2%) of siRNA coated nanoparticles actually make it to the cytoplasmic intracellular environment and induce the silencing effect observed in the studied cell lines [60, 61]. However, in order to reach to more conclusive observations about endosomal escape, which is out of the scope of the pilot study shown in this chapter, more experiments should be performed in future studies.

5.4. Effect in vivo

As mentioned at the beginning of the chapter, the main purpose of developing the AuNP-siRNA probes used in this study was to investigate their potential as tools to prevent scarring by altering the signalling pathways that regulate the wound healing process. For this, the SMAD3 pathway was chosen as a target and probes aimed at silecing SMAD3 were developed. This pathway was chosen due to its involvement in the synthesis of extracellular matrix components (such as collagen fibres) which has been shown to be directly linked to the formation of scar tissue in organs such as the skin [66–68].

The overproduction of stiff fibres induced by wounding leads to the formation of scars [69, 70]. Scar tissue is heavily influenced by the stratification of collagen fibres in a more orderly fashion, reducing the tissue's natural elasticity [71]. In fact, reports

have demonstrated that the type of collagen produced during the scarring process and its organization are significantly different from that produced in healthy tissue.

Collagen-I is present in high levels when a tissue is scarred, comparatively to other types of collagen abundant in different types of healthy tissue. [72] This type of collagen is more densely packed than other types of collagen and, therefore, is normally found in stiffer tissue such as bone and muscular tissue [73]. It is usually the variance in the ratio between the various types of collagen that contributes to the overall difference in elasticity in tissues of varied nature [70, 74]. If that balance is broken, for example overproduction of collagen-I [75] or reduction of collagen-III levels [76], the final tissue might end up fibrotic. In addition, the organization of collagen molecules can also dictate the overall elasticity of the tissue, with highly organized and unilaterally oriented collagen formations being significantly less flexible than “basket wave” types of distribution.[72]

Therefore, since TGF-β levels are intertwined with the production of collagen fibres but are too important for cellular function to be directly manipulated, it was of interest to study the impact of silencing one of its downstream effectors, SMAD3, and its effects on scarring. In order to study this hypothesis, the AuNP-siRNA conjugates described in this chapter were applied in *in vivo* wound models as part of a preliminary study. For that, 9 male wild type C57BL/6 mice (12-16 weeks old) were wounded with a 6 mm biopsy punch blade to create a full-thickness subcutaneous wound on each side of the back of the mouse (see section 3.6.). On each animal, one wound was treated with a solution of AuNP-siRNA conjugates with a scramble sequence while the other was treated with a solution of SMAD3 AuNP-siRNA conjugates. The AuNP-siRNA conjugates with a scramble sequence were chosen as a control in order to investigate if either the particles or any unspecific siRNA sequence could have an impact in the wound healing process on their own. For monitoring purposes, the wound area was defined as the zone were scarred tissue was clearly visible, with scarred tissue being any portion of skin were fibrotic stiff tissue was present (red arrows in Fig. 5.14. provide an example). These wound areas were monitored and photographed for 15 days with the final aim of tracking the wound size, closure rate and general visual aspect of the wounded areas. Figure 5.14. represents the evolution of the wounded areas over time for one mouse.

The wound treated with the scramble control solution (left wound) closed at a slightly quicker rate than the wound treated with the SMAD3 siRNA conjugate solution (right wound). When comparing all the mice from this study (Figures B.7-14 in Appendix B), it is possible to see that most of the animals presented the same trend where the wound treated with the SMAD3 siRNA solution showed a slower rate of closure than the wounds treated with scramble control.

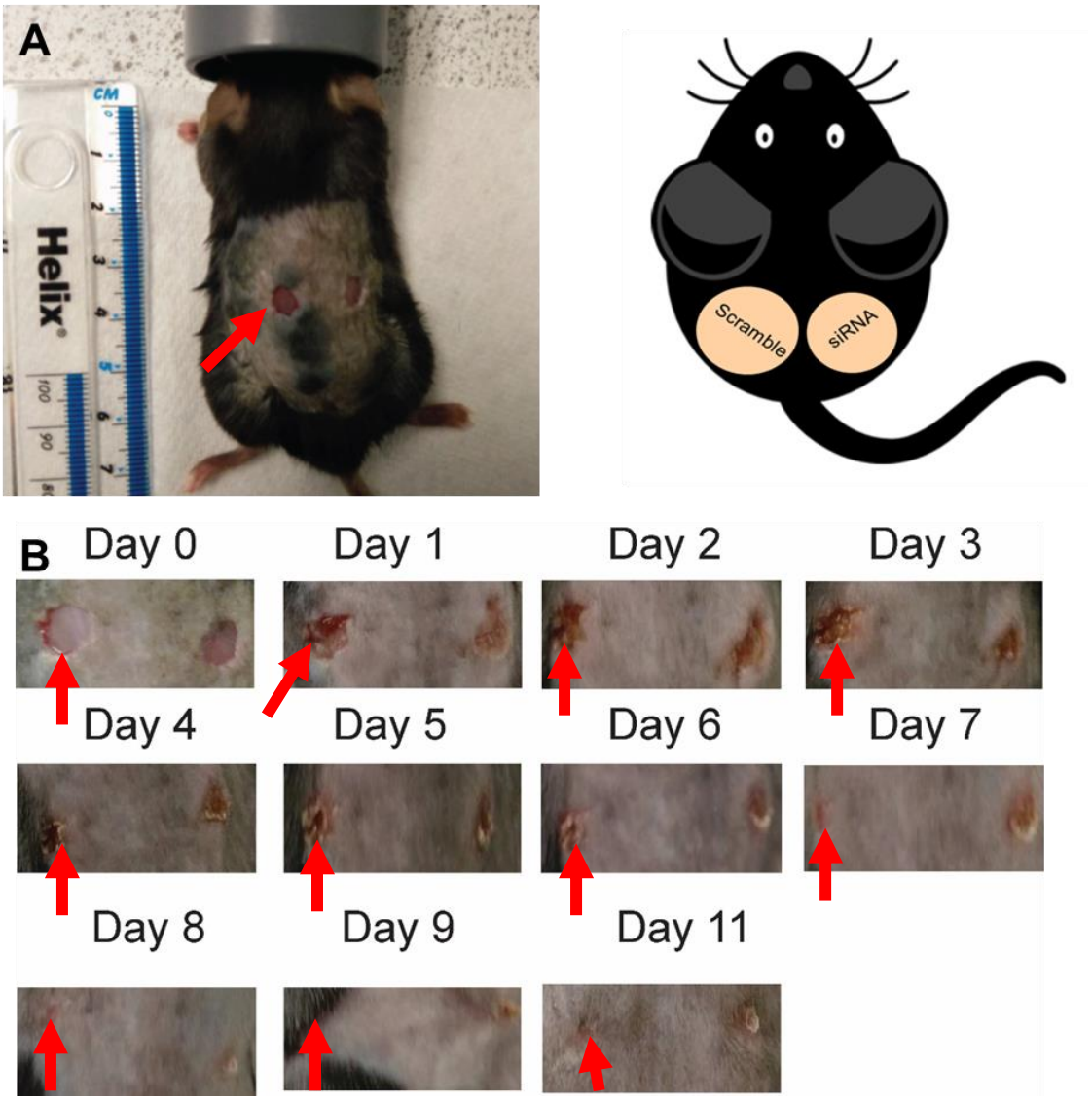

Figure 5.14.Monitoring of *in vivo* mouse model treated with scramble AuNP-siRNA and SMAD3 AuNP-siRNA solutions. Male C57BL/6 mice (12-16 weeks old) were wounded with a 6 mm biopsy punch blade in two different dorsal areas (A). The left wound was treated with a solution of scramble control AuNP-siRNA solution, whilst the right

wound was treated with a solution of SMAD3 AuNP-siRNA. The wounds were monitored over a period of 15 days. After day 11, wounds had completely healed. Red arrow points to one of the areas that was considered "wound area" and that was monitored over the course of the 15 days.

In order to observe the closure rate of the wounds, they were measured by placing a ruler next to the animal (Figure 5.14.A) as a reference scale. The total area of the wound was then plotted overtime for all nine mice (Figures B.15. in Appendix B). All but one mouse demonstrated a slower rate of wound closure when treated with SMAD3 AuNP-siRNA conjugates. In addition, this difference between control treated and SMAD3 siRNA treated wounds was significant across the mice for at least one day (mouse 7), with the majority being for 3 days or more (*p<0.05). Furthermore, in order to have a more general perspective of the overall effect of SMAD3 AuNP-siRNA in the wound closure rates, the average results across all mice were plotted (Figure 5.15.)

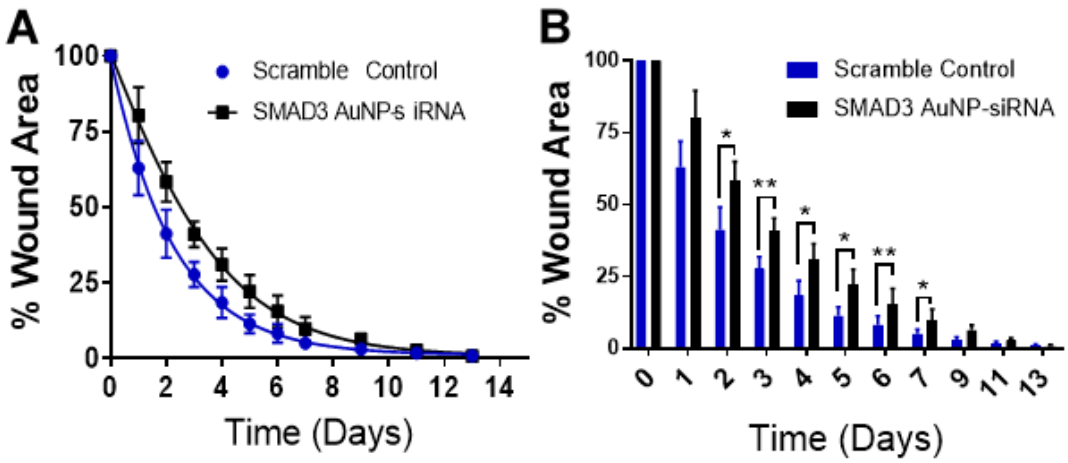

Figure 5.15. Wound area variation over time in the presence of SMAD3 AuNP-siRNA. Wound size was measured every day for 13 days and the mean sizes for all mice were analysed. The wound closure rate (A) demonstrated that there was a difference between the rate of wound closure of wounds treated with the scramble control and the wounds treated with SMAD3 AuNP-siRNA conjugates. In fact, when plotting the values individually of the two types of wounds (B), it is possible to see that between days 2 and 7,

there was a statistically significant difference on the wound area over time between the two treatments (*p<0.05,**p<0.01, student's t-test, n=3)

Figure 5.15.A shows wounds treated with SMAD3 AuNP-siRNA solutions seemed to have an overall slower rate of healing when compared to the control wounds. By analysing each time point (Figure 5.15.B), it is possible to observe hints of a significant difference between the two different types of wounds between days 2-7. The difference in healing rate only disappeared after day 8, where the wound is almost completely closed and therefore any changes to its size are minor.

These results imply that the presence of SMAD3 siRNA conjugates induce a retardation on the wound closure that is visible from external examination. However, these results should be considered with some caution as some of the experimental conditions were not ideal. First, the choice of device for the photographic monitoring was poor, leading to images of reduced quality, which in turn impaired the analysis of the wound area for more complete and precise measurements. Additionally, the angles in which the photographic images were taken were not constant, leading to variations in the final measurements of the wounded area. And finally, the comparison between wounds was done in an overly subjective manner, without using any type of reference scale or comparison charts. Therefore, even though the retardation of wound closure that was observed might indicate a potential effect of the conjugates, a better experimental design must be considered for the future experiments. For example, magnified images of the wounded area taken under a stereoscopic microscope could be taken in order to minimize the impact of variations in photographic images. Additionally, the use of a reference scale (e.g. Manchester Scale [77] or Vancouver Scar Scale [78]) should also be considered for future studies in order to normalize the comparison between scars of different animals and, therefore, to make the final results of the wound closure more robust.

Despite the gaps on the experimental design in the monitoring of the wound closure, histological analysis of the scarred tissue was conducted in order to further investigate the potential effect of SMAD3 siRNA conjugates on the restructuring of the skin. For that, 8mm biopsies were taken from the wounded areas and from a

non-wounded area as a control.. These biopsies were sectioned and treated with Movat's pentachrome staining protocol [79]. This type of staining protocol takes advantage of a multi-staged staining of different constituents of the skin tissue in a range of colours in order to distinguish between granular tissue, types of collagen and other markers that allow the assessment of scarring level [80]. Therefore, this staining was chosen to assess the presence of different types of collagen which indicate the levels of non-granular tissue re-structuring. Figure 5.16 shows the histological results of 2 mice. The different colours of the images correspond to different elements of the skin: light blue – granular tissue; yellow/faint pink – collagen; bright red/pink – fibrin and muscle tissue; dark blue/black – nuclei.

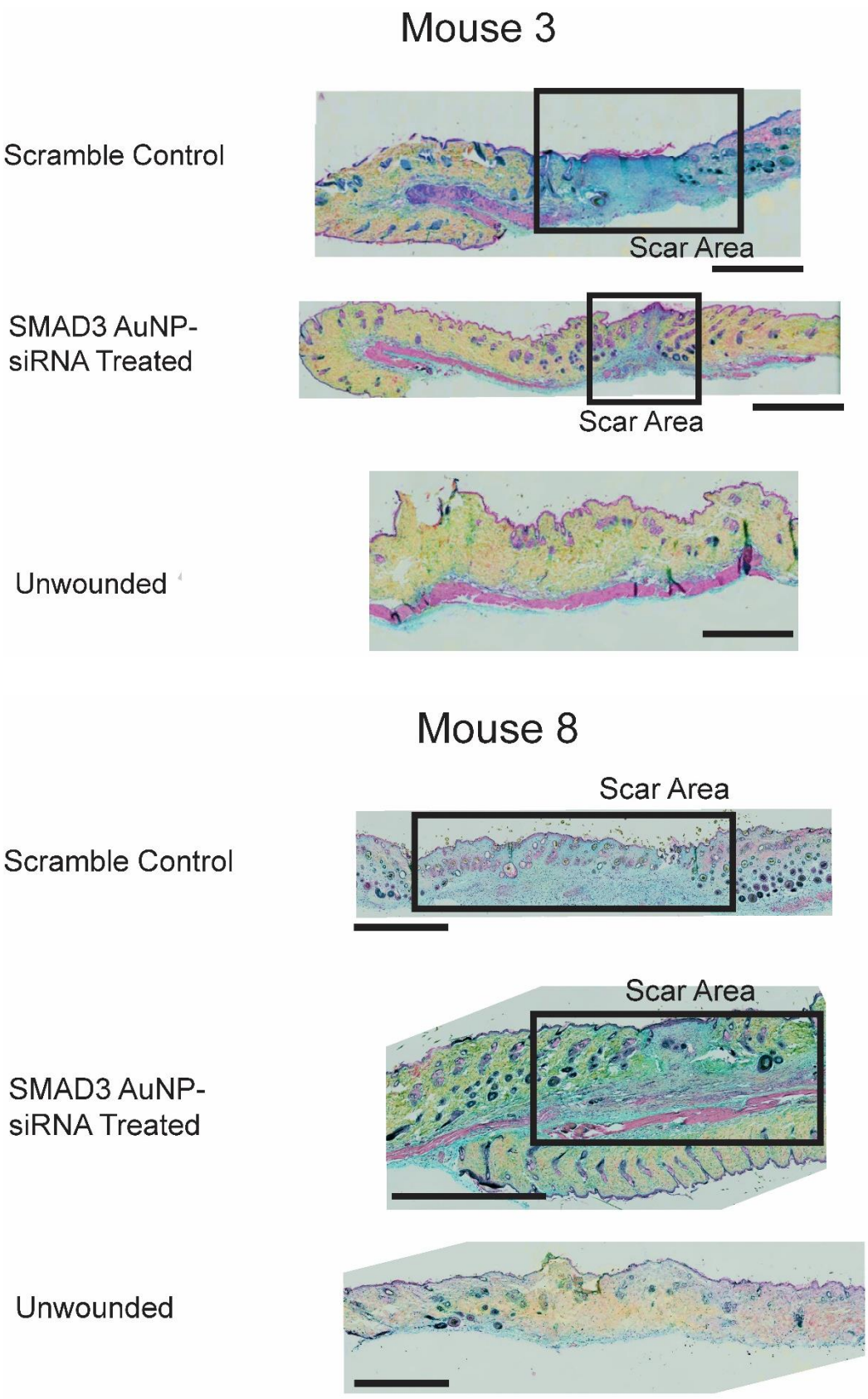

Figure 5.16. Movat's pentachrome staining of wounded and non-wound skin.

Three types of samples were gathered from the dorsal skin of each mouse: wounded area treated with a solution of gold nanoparticles coated with a scramble siRNA sequence, wounded area treated with a solution containing SMAD3 AuNP-siRNA conjugates and an unwounded area of the same specimen. All were sectioned and stained using Movat's pentachrome staining in order to identify different elements of the skin - light blue – granular tissue; yellow/faint pink – collagen; bright red/pink – fibrin and muscle tissue; dark blue/black – nuclei. Non-wounded skin demonstrated a dominance in yellow and pink colours as a result of minimal granular tissue content and normal levels of collagen fibres. However, wounded skin demonstrated an increase of blue colour, which indicated areas of increased granulation and, consequently, visible scarring. Black boxes point to scarred areas. (Scale bar = 1 mm)

As it can be observed in Figure 5.16, the samples from the unwounded skin have very low levels of the blue die, showing a there is almost no granular tissue in the top layers of the skin (epidermis and dermis) in healthy tissue. These findings are in accordance with reported literature of dermal histology [81]. However, when looking at samples of wounded skin, independently of what treatment was applied to them, there is a significant and visible increase on the extent of blue tinged areas. This points to an increase of granular tissue formation (Figure 5.16).

A more detailed analysis of the samples reveals other interesting similarities between samples treated with scramble control and with SMAD3 siRNA conjugates. Both demonstrate some characteristic features of wounded tissue, such as a clear depression on the scarred area leading to a difference of skin thickness across the tissue (Figure 5.16.A), an increase in granular components of the tissue (Figure 5.16.B) and linear stratification of fibres in the wounded area (Figure 5.16.C).

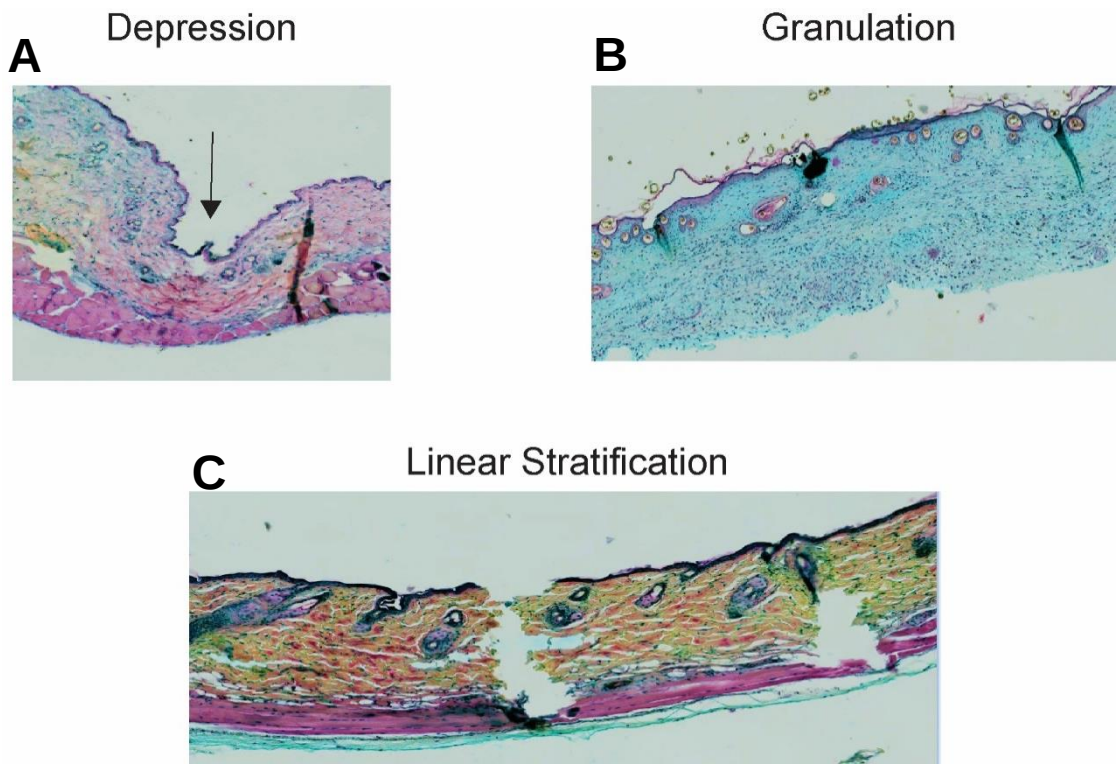

Figure 5.17. Histological characteristics of scarred skin in C57BL/6 mice. Both types of wounded skin showed three different types of characteristics: depression (A), granulation (B) and linear stratification (C). All were sectioned and stained using Movat's pentachrome staining in order to identify different elements of the skin - light blue – granular tissue; yellow/faint pink – collagen; bright red/pink – fibrin and muscle tissue; dark blue/black – nuclei.

Upon closer inspection of the wounded and non-wounded samples, it is possible to find two major differences. Samples treated with the scramble siRNA-AuNP solution seem to have a larger area of scarred tissue overall (Figure 5.18.A-B top) when compared with tissue treated with SMAD3 AuNP-siRNA solution. In fact, by analysing the relative area of tissue that demonstrates a clearly defined wound in the overall size of the sampled section, it was possible to observe that across all the data gathered the average size of scarred/wounded area in SMAD3 AuNP-siRNA treated wounds was 13 ± 2 % of total sample area, while samples from wounds treated with the scramble control solution demonstrated an average wounded/scarred area of 35 ± 3 %.

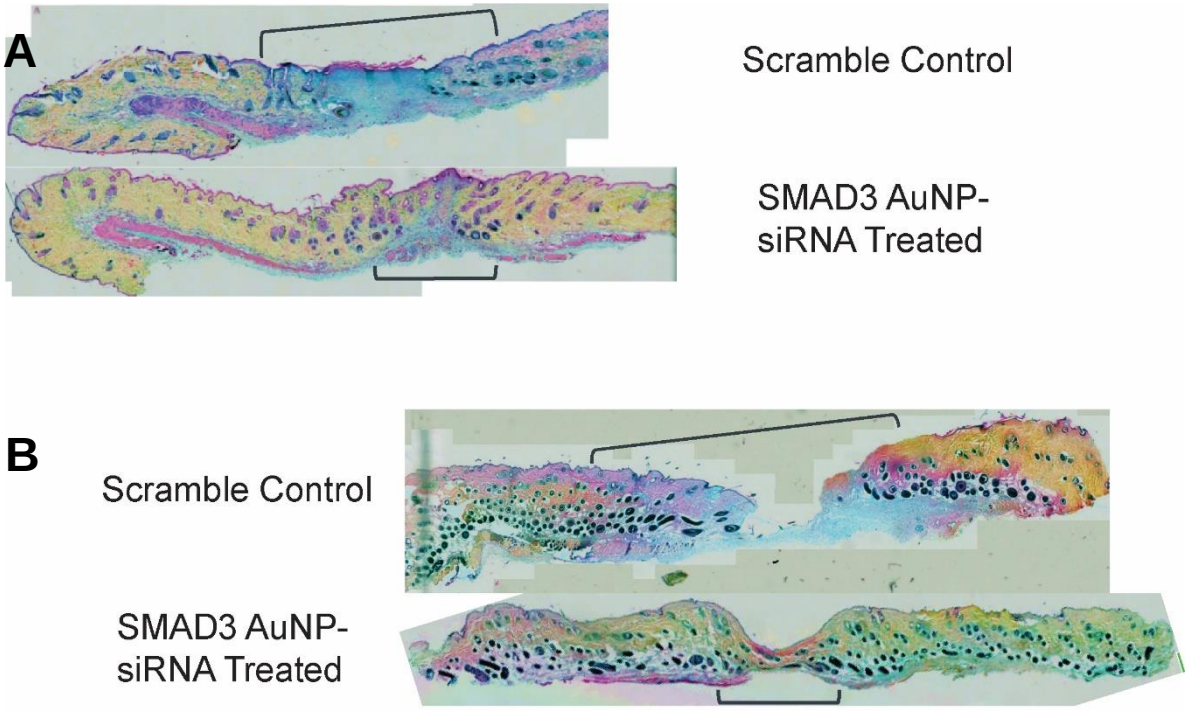

Figure 5.18. Histological analysis of the wound size. Samples were analysed using Movat's pentachrome staining protocol in order to identify different elements of the skin - light blue – granular tissue; yellow/faint pink – collagen; bright red/pink – fibrin and muscle tissue; dark blue/black – nuclei. Wounds treated with SMAD3 AuNP-siRNA solution were measured using ImageJ software and showed smaller areas of granulated tissue, when compared with wounds treated with scramble siRNA solution.

Additionally, taking advantage of the different colouring of the tissue components, it was possible to analyse the relative differences in the levels of collagen (yellow) and granular tissue (blue). While wounds treated with the SMAD3 probes had 60 ± 5 % (total area) of collagen fibres (yellow) and 12 ± 3 % of granulated tissue (blue), those exposed to scramble siRNA solutions had 46 ± 4 % of collagen fibres and 37 ± 6 % of granulated tissue. The distribution of collagen in tissue treated with SMAD3 silencing probes seemed to be more prevalent than in tissue treated with scramble siRNA solution. At the same time, the opposite was observed for the distribution of granulated tissue, with tissue treated with siRNA scramble control having a more prevailing presence of blue tainted granulated tissue when compared with tissue treated with SMAD3 probes.

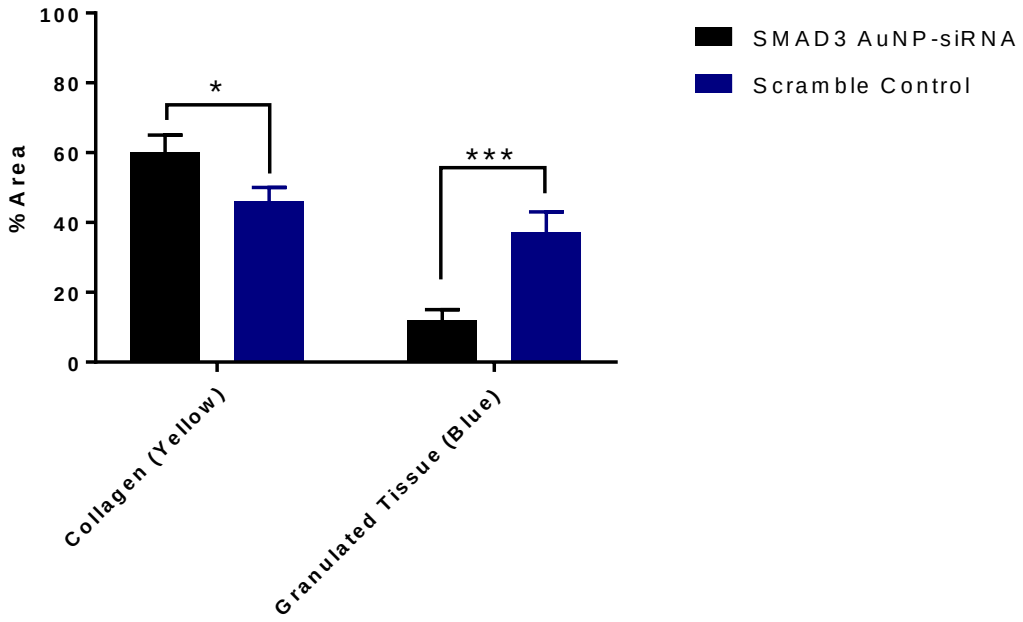

Figure 5.19. Distribution of collagen and granulated tissue across histological samples. The analysis of raw pixel values for yellow and blue colours allowed the calculation of the relative distribution of collagen and granulated tissue respectively in histological samples. Yellow coloured areas (collagen) constituted 60 ± 5 % of total area for wounds treated with SMAD3 silencing probes and 46 ± 4 % for wounds treated with scramble control. Blue coloured areas (granular tissue) constituted 12 ± 3 % of the total area for wounds treated with SMAD3 probes and 37 ± 6 % for wounds treated with scramble control. (*$p<0.05$, ***$p<0.001$, student's t-test, n = 5)

However, the histological analysis of the tissue samples has some limitations. On the one hand, the designation of the scarred area based on Movat's pentachrome stain was sometimes difficult. While in some samples the difference between the granular tissue (blue tinged tissue) and the non-granular tissue (yellow/pink) was clearly distinguishable, in other samples the difference was not as clear. This limited the reliability of the measurements, specifically of the overall size and granulation of the tissue across the different treatments. This limitation could be overcome in future studies by complementing the use of Movat's pentachrome with immunohistochemical stain specifically targeted to the different components of

interest (e.g. different types of collagen [82, 83]) in order to fully assess the extension of the fibrotic reconstruction of the skin.

Additionally, the use of an AuNP-siRNA scramble sequence control was deemed the most efficient when designing the experiment, since it would cover the potential effects of both the presence of the particles and the presence of a scramble siRNA. However, in hindsight, the controls should have been more carefully designed. Tackling two variables (the effect of the nanoparticles and the effect of siRNA) at the same time can mislead the conclusions driven from the controls. For example, a recent study from Syke *et al.* (2014) demonstrated that gold nanoparticles injected into mice can be accumulated in the skin, to the point of being visualized through UV imaging. [84] This study demonstrates that assuming a certain direction of uptake can sometimes misguide the conclusions derived from certain experiments. Consequently, even though differences were observed in the histological analysis between tissue treated with scramble control and tissue treated with SMAD3 silencing probes, the final results provide only evidence for the potential usefulness of AuNP-siRNA conjugates as silencing probes for scarring treatment. Therefore, for future *in vivo* studies using this type of AuNP-siRNA conjugates, three other control groups must be added to this type of experiment in order to improve its reliability: a control group without treatment to analyse the wound closure process, a control group only exposed to nanoparticles in order to assess the impact of particles alone, and another control exposed only to the siRNA sequence in order to analyse if the conjugations of the siRNA with gold nanoparticles would have any impact on the final results. These extra controls allow a better analysis of the effects of treating open skin wounds.

Furthermore, additional techniques should have been used to quantify the silencing capacity of the probes *in vivo*. These could range from histologically staining the samples with an antibody against SMAD3 to access changes in protein concentration, to the extraction of tissue mRNA and protein for qPCR and western blot analysis. Such techniques would help to verify the ability the AuNP-siRNA conjugates to silence SMAD3 expression in wounds.

In summary, in this chapter the successful synthesis of SMAD3 siRNA-coated nanoparticles was demonstrated and preliminary results on their application in both *in vitro* and *in vivo* models was performed. At the cellular level, the presence of SMAD3 silencing probes in concentrations of 1 – 10 pmol/10^4 cells indicated a potential significant reduction of the levels of SMAD3 expression in MEF cells, as demonstrated by different techniques. qPCR analysis of cells treated with SMAD3 silencing probes also pointed to the same trend, with a decrease in the mRNA expression levels of SMAD3 being observed. A consequent decrease of TGF-β was also observed due to the fact that both SMAD3 and TGF-β expressions are connected *via* the SMAD2/3 pathway. These apparent effects on protein and mRNA levels of SMAD3 expression translated onto a visible slower cell migration rate, despite indications of no clear toxicity from the presence of the probes at the concentrations used for the cell migration studies. When applied to *in vivo* murine wound models, the presence of SMAD3 silencing probes seemed to slow the recovery rate of wounds between day 2 and day 7. Histological analysis of the tissue hinted that this deceleration in wound healing rate might lead to the formation of more collagen-rich tissue and less granulated tissue. However, due to an inadequate experimental design, both the wound and the histological analyses provide interesting preliminary but incomplete results. Overall, the results of the pilot study presented in this chapter suggest that hybrid materials can be successfully directed to silencing applications for skin regeneration and wound healing, though further experiments need to be conducted in order to provide a more complete picture of these observations.

5.5. References

1. Markeson, D., Pleat, J. M., Sharpe, J. R., Harris, A. L., Seifalian, A. M., & Watt, S. M. (2015). Scarring, stem cells, scaffolds and skin repair. *Journal of Tissue Engineering and Regenerative Medicine*, *9*(6), 649–668. doi:10.1002/term.1841

2. Guo, S., & Dipietro, L. A. (2010). Factors affecting wound healing. *Journal of Dental Research*, *89*(3), 219–229. doi:10.1177/0022034509359125

3. Faler, B. J., Macsata, R. A., Plummer, D., Mishra, L., & Sidawy, A. N. (2006). Transforming growth factor-beta and wound healing. *Perspectives in Vascular Surgery and Endovascular Therapy*, *18*(1), 55–62. doi: unavailable

4. Gilbert, R., Vickaryous, M., & Viloria-Petit, A. (2016). Signalling by Transforming Growth Factor Beta Isoforms in Wound Healing and Tissue Regeneration. *Journal of Developmental Biology*, *4*(2), 21. doi:10.3390/jdb4020021

5. Ramirez, H., Patel, S. B., & Pastar, I. (2014). The Role of TGFβ Signaling in Wound Epithelialization. *Advances in Wound Care*, *3*(7), 482–491. doi:10.1089/wound.2013.0466

6. Gibson, D. J., Pi, L., Sriram, S., Mao, C., Petersen, B. E., Scott, E. W., Leask, A., Schultz, G. S. (2014). Conditional knockout of CTGF affects corneal wound healing. *Investigative Ophthalmology and Visual Science*, *55*(4), 2062–2070. doi:10.1167/iovs.13-12735

7. Sisco, M., Kryger, Z. B., O'Shaughnessy, K. D., Kim, P. S., Schultz, G. S., Ding, X. Z., Roy, N. K., Dean, N. M., Mustoe, T. A. (2008). Antisense inhibition of connective tissue growth factor (CTGF/CCN2) mRNA limits hypertrophic scarring without affecting wound healing in vivo. *Wound Repair and Regeneration*, *16*(5), 661–673. doi:10.1111/j.1524-475X.2008.00416.x

8. Castleberry, S. A., Golberg, A., Sharkh, M. A., Khan, S., Almquist, B. D., Austen, W. G., Yarmush, M. L.,Hammond, P. T. (2016). Nanolayered siRNA delivery platforms for local silencing of CTGF reduce cutaneous scar contraction in third-degree burns. *Biomaterials*, *95*, 22–34. doi:10.1016/j.biomaterials.2016.04.007

9. Layliev, J., Wilson, S., Warren, S. M., & Saadeh, P. B. (2012). Improving Wound Healing with Topical Gene Therapy. *Advances in Wound Care*, *1*(5), 218–223. doi:10.1089/wound.2011.0322

10. Penn, J. W., Grobbelaar, A. O., & Rolfe, K. J. (2012). The role of the TGF-β family in wound healing, burns and scarring: a review. *International Journal of Burns and Trauma*, *2*(1), 18–28. doi: unavailable

11. Kulkarni, A. B., & Karlsson, S. (1993). Transforming growth factor-beta 1 knockout mice. A mutation in one cytokine gene causes a dramatic inflammatory disease. *The American Journal of Pathology*, *143*(1), 3–9. doi:

unavailable

12. Böttinger, E. P., Letterio, J. J., & Roberts, A. B. (1997). Biology of TGF-beta in knockout and transgenic mouse models. *Kidney International*, *51*(5), 1355–60. doi: unavailable

13. Crowe, M. J., Doetschman, T., & Greenhalgh, D. G. (2000). Delayed Wound Healing in Immunodeficient TGF-β1 Knockout Mice. *Journal of Investigative Dermatology*, *115*(1), 3–11. doi:10.1046/j.1523-1747.2000.00010.x

14. Meng, X. M., Huang, X. R., Chung, A. C. K., Qin, W., Shao, X., Igarashi, P., … Lan, H. Y. (2010). Smad2 protects against TGF-beta/Smad3-mediated renal fibrosis. *Journal of the American Society of Nephrology : JASN*, *21*(9), 1477–1487. doi:10.1681/ASN.2009121244

15. Brown, K. A., Pietenpol, J. A., & Moses, H. L. (2007). A tale of two proteins: Differential roles and regulation of Smad2 and Smad3 in TGF-Beta signaling. *Journal of Cellular Biochemistry*. doi:10.1002/jcb.21255

16. Tomikawa, K., Yamamoto, T., Shiomi, N., Shimoe, M., Hongo, S., Yamashiro, K., Yamaguchi, T., Maeda, H., Takashiba, S. (2012). Smad2 Decelerates Re-epithelialization during Gingival Wound Healing. *Journal of Dental Research*, *91*(8), 764–770. doi:10.1177/0022034512451449

17. Ashcroft, G. S., Yang, X., Glick, A. B., Weinstein, M., Letterio, J. L., Mizel, D. E., Anzano, M., Greenwell-Wild, T., Wahl, S. M., Deng, C., Roberts, A. B. (1999). Mice lacking Smad3 show accelerated wound healing and an impaired local inflammatory response. *Nature Cell Biology*, *1*(5), 260–6. doi:10.1038/12971

18. Ashcroft, G. S., & Roberts, A. B. (2000). Loss of Smad3 modulates wound healing. *Cytokine and Growth Factor Reviews*. doi:10.1016/S1359-6101(99)00036-2

19. Ghosh, P., Han, G., De, M., Kim, C. K., & Rotello, V. M. (2008). Gold nanoparticles in delivery applications. *Advanced Drug Delivery Reviews*. doi:10.1016/j.addr.2008.03.016

20. Rosi, N. L. (2006). Oligonucleotide-Modified Gold Nanoparticles for Intracellular Gene Regulation. *Science*, *312*(5776), 1027–1030. doi:10.1126/science.1125559

21. Rosi, N. L., Giljohann, D. A., Thaxton, C. S., Lytton-Jean, A. K. R., Han, M. S., & Mirkin, C. A. (2006). Oligonucleotide-Modified Gold Nanoparticles for Intracellular Gene Regulation. *Science*, *312*(5776), 1027–1030. doi:10.1126/science.1125559

22. Ghosh, P. S., Kim, C. K., Han, G., Forbes, N. S., & Rotello, V. M. (2008). Efficient gene delivery vectors by tuning the surface charge density of amino acid-functionalized gold nanoparticles. *ACS Nano*, *2*(11), 2213–2218. doi:10.1021/nn800507t

23. Rhim, W. K., Kim, J. S., & Nam, J. M. (2008). Lipid-gold-nanoparticle hybrid-based gene delivery. *Small*, *4*(10), 1651–1655. doi:10.1002/smll.200800628

24. Elbakry, A., Zaky, A., Liebl, R., Rachel, R., Goepferich, A., & Breunig, M. (2009). Layer-by-layer assembled gold nanoparticles for sirna delivery. *Nano Letters*, *9*(5), 2059–2064. doi:10.1021/nl9003865

25. Kim, S. T., Chompoosor, A., Yeh, Y. C., Agasti, S. S., Solfiell, D. J., & Rotello, V. M. (2012). Dendronized gold nanoparticles for siRNA delivery. *Small*, *8*(21), 3253–3256. doi:10.1002/smll.201201141

26. Reynolds, J. L., Law, W. C., Mahajan, S. D., Aalinkeel, R., Nair, B., Sykes, D. E., Yong, K.-T., Hui, R., Prasad, P. N.,Schwartz, S. A. (2012). Nanoparticle based galectin-1 gene silencing, implications in methamphetamine regulation of HIV-1 infection in monocyte derived macrophages. *Journal of Neuroimmune Pharmacology* , *7*(3), 673–85. doi:10.1007/s11481-012-9379-7

27. Wang, X.-Q., Lee, S., Wilson, H., Seeger, M., Iordanov, H., Gatla, N., Whittington, A., Bach, D., Lu, J.-Y., Paller, A. S. (2013). Ganglioside GM3 Depletion Reverses Impaired Wound Healing in Diabetic Mice by Activating IGF-1 and Insulin Receptors. *The Journal of Investigative Dermatology*, *134*(5), 1–10. doi:10.1038/jid.2013.532

28. Kirkland-York, S., Zhang, Y., Smith, A. E., York, A. W., Huang, F., & McCormick, C. L. (2010). Tailored design of Au nanoparticle-siRNA carriers utilizing reversible addition - Fragmentation chain transfer polymers. *Biomacromolecules*, *11*(4), 1052–1059. doi:10.1021/bm100020x

29. Conde, J., Rosa, J., de la Fuente, J. M., & Baptista, P. V. (2013). Gold-nanobeacons for simultaneous gene specific silencing and intracellular tracking of the silencing events. *Biomaterials*, *34*(10), 2516–2523. doi:10.1016/j.biomaterials.2012.12.015

30. Guo, S., Huang, Y., Jiang, Q., Sun, Y., Deng, L., Liang, Z., Du, Q., Zing, J., Zhao, Y., Wang, P. C., Dong, A., Liang, X. J. (2010). Enhanced gene delivery and siRNA silencing by gold nanoparticles coated with charge-reversal polyelectrolyte. *ACS Nano*, *4*(9), 5505–5511. doi:10.1021/nn101638u

31. Lee, M. Y., Park, S. J., Park, K., Kim, K. S., Lee, H., & Hahn, S. K. (2011). Target-specific gene silencing of layer-by-layer assembled gold-cysteamine/siRNA/PEI/HA nanocomplex. *ACS Nano*, *5*(8), 6138–6147. doi:10.1021/nn2017793

32. Lee, J. S., Green, J. J., Love, K. T., Sunshine, J., Langer, R., & Anderson, D. G. (2009). Gold, poly(beta-amino ester) nanoparticles for small interfering RNA delivery. *Nano Letters*, *9*(6), 2402–2406. doi:10.1021/nl9009793

33. Wu, J., Liu, B., Wu, H., Wu, Y., Zhang, W., Zhao, S., Zhang, L., Pan, X., Gaow, W., Wang, X., Yuan, Y., Zhang, Y. (2016). A gold nanoparticle platform for the delivery of functional TGF-β1 siRNA into cancer cells. *Journal of Biomedical*

Nanotechnology, *12*(4), 800–810. doi:10.1166/jbn.2016.2217

34. Randeria, P. S., Seeger, M. A., Wang, X.-Q., Wilson, H., Shipp, D., Mirkin, C. A., & Paller, A. S. (2015). siRNA-based spherical nucleic acids reverse impaired wound healing in diabetic mice by ganglioside GM3 synthase knockdown. *Proceedings of the National Academy of Sciences of the United States of America*, *112*(18), 5573–8. doi:10.1073/pnas.1505951112

35. Yeom, S. Y., Jeoung, D., Ha, K. S., & Kim, P. H. (2004). Small interfering RNA (siRNA) targetted to Smad3 inhibits transforming growth factor-β signaling. *Biotechnology Letters*, *26*(9), 699–703. doi:10.1023/B:BILE.0000024091.90305.be

36. Pellegrino, T., Sperling, R. A., Alivisatos, A. P., & Parak, W. J. (2007). Gel electrophoresis of gold-DNA nanoconjugates. *Journal of Biomedicine & Biotechnology*, *2007*, 26796. doi:10.1155/2007/26796

37. Jackson, A. L., & Linsley, P. S. (2010). Recognizing and avoiding siRNA off-target effects for target identification and therapeutic application. *Nature Reviews Drug Discovery*, *9*(1), 57–67. doi:10.1038/nrd3010

38. Lee, S. D., Osei-Twum, J. A., & Wasan, K. M. (2013). Dose-dependent targeted suppression of P-glycoprotein expression and function in Caco-2 cells. *Molecular Pharmaceutics*, *10*(6), 2323–2330. doi:10.1021/mp300668e

39. Barnaby, S. N., Lee, A., & Mirkin, C. A. (2014). Probing the inherent stability of siRNA immobilized on nanoparticle constructs. *Proceedings of the National Academy of Sciences of the United States of America*, *111*(27), 9739–44. doi:10.1073/pnas.1409431111

40. Barnaby, S. N., Perelman, G. A., Kohlstedt, K. L., Chinen, A. B., Schatz, G. C., & Mirkin, C. A. (2016). Design Considerations for RNA Spherical Nucleic Acids (SNAs). *Bioconjugate Chemistry*, acs.bioconjchem.6b00350. doi:10.1021/acs.bioconjchem.6b00350

41. Leuschner, P. J. F., Ameres, S. L., Kueng, S., & Martinez, J., Cleavage of the siRNA passenger strand during RISC assembly in human cells. , *EMBO Reports,* 314–320 (2006). doi:10.1038/sj.embor.7400637

42. Zipper, H., Brunner, H., Bernhagen, J., & Vitzthum, F. (2004). Investigations on DNA intercalation and surface binding by SYBR Green I, its structure determination and methodological implications. *Nucleic Acids Research*, *32*(12). doi:10.1093/nar/gnh101

43. Smith, P. J., Giroud, M., Wiggins, H. L., Gower, F., Thorley, J. A., Stolpe, B., Mazzolin, J., Dyson, R. J., Rappoport, J. Z. (2012). Cellular entry of nanoparticles via serum sensitive clathrin-mediated endocytosis, and plasma membrane permeabilization. *International Journal of Nanomedicine*, *7*, 2045–2055. doi:10.2147/IJN.S29334

44. Wang, W., Huang, Y., Zhao, S., Shao, T., & Cheng, Y. (2013). Human serum

albumin (HSA) nanoparticles stabilized with intermolecular disulfide bonds. *Chemical Communications (Cambridge, England)*, *49*(22), 2234–6. doi:10.1039/c3cc38397k

45. Cifuentes-Rius, A., De Puig, H., Kah, J. C. Y., Borros, S., & Hamad-Schifferli, K. (2013). Optimizing the properties of the protein corona surrounding nanoparticles for tuning payload release. *ACS Nano*, *7*(11), 10066–10074. doi:10.1021/nn404166q

46. Tomari, Y., & Zamore, P. D. (2005). Perspective: Machines for RNAi. *Genes and Development*. doi:10.1101/gad.1284105

47. Rana, T. M. (2007). Illuminating the silence: understanding the structure and function of small RNAs. *Nature reviews. Molecular Cell Biology*, *8*(1), 23–36. doi:10.1038/nrm2085

48. Kim, D. H., & Rossi, J. J. (2008). RNAi mechanisms and applications. *BioTechniques*. doi:10.2144/000112792

49. Carthew, R. W., & Sontheimer, E. J. (2009). Origins and Mechanisms of miRNAs and siRNAs. *Cell*. doi:10.1016/j.cell.2009.01.035

50. Jackson, A. L., Burchard, J., Schelter, J., Chau, B. N., Cleary, M., Lim, L., & Linsley, P. S. (2006). Widespread siRNA “off-target” transcript silencing mediated by seed region sequence complementarity. *RNA*, *12*(7), 1179–1187. doi:10.1261/rna.25706

51. Carralot, J.-P., Kim, T.-K., Lenseigne, B., Boese, A. S., Sommer, P., Genovesio, A., & Brodin, P. (2009). Automated high-throughput siRNA transfection in raw 264.7 macrophages: a case study for optimization procedure. *Journal of Biomolecular Screening* , *14*(2), 151–160. doi:10.1177/1087057108328762

52. Liu, Z., Shi, W., Ji, X., Sun, C., Jee, W. S. S., Wu, Y., Mao, Z., Nagy, T. R., Li, Q., Cao, X. (2004). Molecules Mimicking Smad1 Interacting with Hox Stimulate Bone Formation. *Journal of Biological Chemistry*, *279*(12), 11313–11319. doi:10.1074/jbc.M312731200

53. Fuentealba, L. C., Eivers, E., Ikeda, A., Hurtado, C., Kuroda, H., Pera, E. M., & De Robertis, E. M. (2007). Integrating Patterning Signals: Wnt/GSK3 Regulates the Duration of the BMP/Smad1 Signal. *Cell*, *131*(5), 980–993. doi:10.1016/j.cell.2007.09.027

54. Eivers, E., Demagny, H., & De Robertis, E. M. (2009). Integration of BMP and Wnt signaling via vertebrate Smad1/5/8 and Drosophila Mad. *Cytokine and Growth Factor Reviews*. doi:10.1016/j.cytogfr.2009.10.017

55. Yu, H., Königshoff, M., Jayachandran, A., Handley, D., Seeger, W., Kaminski, N., & Eickelberg, O. (2008). Transgelin is a direct target of TGF-beta/Smad3-dependent epithelial cell migration in lung fibrosis. *FASEB Journal*, *22*(6), 1778–1789. doi:10.1096/fj.07-083857

56. Ungefroren, H., Groth, S., Sebens, S., Lehnert, H., Gieseler, F., & Fändrich, F. (2011). Differential roles of Smad2 and Smad3 in the regulation of TGF-β1-mediated growth inhibition and cell migration in pancreatic ductal adenocarcinoma cells: control by Rac1. *Molecular Cancer*, *10*(1), 67. doi:10.1186/1476-4598-10-67

57. Luwor, R. B., Hakmana, D., Iaria, J., Nheu, T. V, Simpson, R. J., & Zhu, H.-J. (2015). Single live cell TGF-β signalling imaging: breast cancer cell motility and migration is driven by sub-populations of cells with dynamic TGF-β-Smad3 activity. *Molecular Cancer*, *14*(1), 50. doi:10.1186/s12943-015-0309-1

58. Au, H. K., Chang, J. H., Wu, Y. C., Kuo, Y. C., Chen, Y. H., Lee, W. C., Chang, T.-S., Lan, P. C., Kuo, H. C., Lee, K. L., Lee, M. T., Tzeng, C. R., Huang, Y. H. (2015). TGF-BetaI regulates cell migration through pluripotent transcription factor OCT4 in endometriosis. *PLoS ONE*, *10*(12). doi:10.1371/journal.pone.0145256

59. Zhang, H., Zhang, H., Liu, L., Wang, Y., Zhao, G., Xie, R., Zhang, H., Fan, D. (2013). KLF8 involves in TGF-beta-induced EMT and promotes invasion and migration in gastric cancer cells. *Journal of Cancer Research and Clinical Oncology*, *139*(6), 1033–1042. doi:10.1007/s00432-012-1363-3

60. Gilleron, J., Querbes, W., Zeigerer, A., Borodovsky, A., Marsico, G., Schubert, U., Manygoats, K., Seifert, S., Andree, C., Stoter, M., Epstein-Barash, H., Zhang, L., Koteliansky, V., Fitzgerald, K., Fava, E., Bickle, M., Kalaidzidis, Y., Akinc, A., Maier, M., Zerial, M. (2013). Image-based analysis of lipid nanoparticle-mediated siRNA delivery, intracellular trafficking and endosomal escape. *Nature Biotechnology*, *31*(7), 638–46. doi:10.1038/nbt.2612

61. Wu, X. A., Choi, C. H. J., Zhang, C., Hao, L., & Mirkin, C. A. (2014). Intracellular fate of spherical nucleic acid nanoparticle conjugates. *Journal of the American Chemical Society*, *136*(21), 7726–7733. doi:10.1021/ja503010a

62. Ma, D. (2014). Enhancing endosomal escape for nanoparticle mediated siRNA delivery. *Nanoscale*, *6*(12), 6415–25. doi:10.1039/c4nr00018h

63. Yezhelyev, M. V., Qi, L., O'Regan, R. M., Nie, S., & Gao, X. (2008). Proton-sponge coated quantum dots for siRNA delivery and intracellular imaging. *Journal of the American Chemical Society*, *130*(28), 9006–9012. doi:10.1021/ja800086u

64. Peetla, C., Jin, S., Weimer, J., Elegbede, A., & Labhasetwar, V. (2014). Biomechanics and thermodynamics of nanoparticle interactions with plasma and endosomal membrane lipids in cellular uptake and endosomal escape. *Langmuir*, *30*(25), 7522–7532. doi:10.1021/la5015219

65. Sahay, G., Querbes, W., Alabi, C., Eltoukhy, A., Sarkar, S., Zurenko, C., Karagiannis, E., Love, K., Chen, D., Zoncu, R., Buganim, Y., Schroeder, A., Langer, R., Anderson, D. G. (2013). Efficiency of siRNA delivery by lipid nanoparticles is limited by endocytic recycling-supp. *Nature Biotechnology*,

31(7), 653–8. doi:10.1038/nbt.2614

66. Rifkin, D. B. (2005). Latent transforming growth factor-beta (TGF-beta) binding proteins: orchestrators of TGF-beta availability. *The Journal of Biological Chemistry*, *280*(9), 7409–12. doi:10.1074/jbc.R400029200

67. Massagué, J. (1998). TGF-beta signal transduction. *Annual Review of Biochemistry*, *67*, 753–91. doi:10.1146/annurev.biochem.67.1.753

68. Savage-Dunn, C. (2005). TGF-beta signaling. *WormBook*, 1–12. doi:10.1895/wormbook.1.22.1

69. Bayat, A., McGrouther, D. A., & Ferguson, M. W. J. (2003). Skin scarring. *BMJ (Clinical Research Edition)*, *326*(7380), 88–92. doi:10.1136/bmj.326.7380.88

70. Hardy, M. A. (1989). The biology of scar formation. *Phys Ther*, *69*(12), 1014–1024. doi: unavailable

71. Stuart, K., Paderi, J., Snyder, P. W., Freeman, L., & Panitch, A. (2011). Collagen-binding peptidoglycans inhibit MMP mediated collagen degradation and reduce dermal scarring. *PLoS ONE*, *6*(7). doi:10.1371/journal.pone.0022139

72. Verhaegen, P. D. H. M., Van Zuijlen, P. P. M., Pennings, N. M., Van Marle, J., Niessen, F. B., Van Der Horst, C. M. A. M., & Middelkoop, E. (2009). Differences in collagen architecture between keloid, hypertrophic scar, normotrophic scar, and normal skin: An objective histopathological analysis. *Wound Repair and Regeneration*, *17*(5), 649–656. doi:10.1111/j.1524-475X.2009.00533.x

73. Orgel, J. P. R. O., Irving, T. C., Miller, A., & Wess, T. J. (2006). Microfibrillar structure of type I collagen in situ. *Proceedings of the National Academy of Sciences of the United States of America*, *103*(24), 9001. doi:10.1073/pnas.0502718103

74. Burgeson, R. E., & Nimni, M. E. (1992). Collagen types. Molecular structure and tissue distribution. *Clinical Orthopaedics and Related Research*., 282, 250-272, doi:10.1007/s00216-009-3019-y

75. Syed, F., Ahmadi, E., Iqbal, S. A., Singh, S., McGrouther, D. A., & Bayat, A. (2011). Fibroblasts from the growing margin of keloid scars produce higher levels of collagen I and III compared with intralesional and extralesional sites: clinical implications for lesional site-directed therapy. *British Journal of Dermatology*, *164*(1), 83–96. doi:10.1111/j.1365-2133.2010.10048.x

76. Volk, S. W., Wang, Y., Mauldin, E. A., Liechty, K. W., & Adams, S. L. (2011). Diminished type III collagen promotes myofibroblast differentiation and increases scar deposition in cutaneous wound healing. *Cells Tissues Organs*, *194*(1), 25–37. doi:10.1159/000322399

77. Lowe, D. G. (2004). Distinctive image features from scale-invariant keypoints. *International Journal of Computer Vision*, *60*(2), 91–110.

doi:10.1023/B:VISI.0000029664.99615.94

78. Nedelec, B., Shankiowsky, H. A., & Tredget, E. E. (2000). Rating the resolving hypertrophic scar: comparison of the Vancouver Scar Scale and scar volume. *The Journal of burn care & rehabilitation*. doi:10.1067/mbc.2000.104750

79. Doello, K. (2014). A new pentachrome method for the simultaneous staining of collagen and sulfated mucopolysaccharides. *Yale Journal of Biology and Medicine*, *87*(3), 341–347.

80. Petrovic, a, Abramovic, M., Mihailovic, D., Gligorijevic, J., Zivkovic, V., Mojsilovic, M., & Ilic, I. (2011). Multicolor counterstaining for immunohistochemistry - a modified Movat's pentachrome. *Biotechnic & Histochemistry* , *86*(6), 429–35. doi:10.3109/10520295.2010.528026

81. Gantwerker, E. A., & Hom, D. B. (2012). Skin: Histology and physiology of wound healing. *Clinics in Plastic Surgery*. doi:10.1016/j.cps.2011.09.005

82. McGowan, S. E. (1992). Extracellular matrix and the regulation of lung development and repair. *FASEB journal : official publication of the Federation of American Societies for Experimental Biology*, *6*(11), 2895–904. Retrieved from http://www.ncbi.nlm.nih.gov/pubmed/1644255

83. Regeneration, T., & Healing, W. (2013). Tissue Regeneration and Wound Healing. *Journal of Investigative Dermatology*, *133*, S247–S259. doi:10.1038/jid.2013.107

84. Sykes, E. A., Dai, Q., Tsoi, K. M., Hwang, D. M., & Chan, W. C. W. (2014). Nanoparticle exposure in animals can be visualized in the skin and analysed via skin biopsy. *Nature Communications*, *5*. doi:10.1038/ncomms4796

Chapter 6: DNA-Upconversion-Graphene Oxide sensor for the detection of mRNA biomarkers

In chapters 4 and 5 the conjugation of gold nanoparticles with oligonucleotides and their applications for imaging of Vimentin mRNA and gene manipulation for wound healing improvement was discussed. However, despite their remarkable absorbance properties which were explored for cellular mRNA sensing system in Chapter 4, gold nanoparticles do not possess the sensitivity to detect biomolecules in the lowest range of concentrations [1]. The detection of mRNAs levels is specifically interesting due to its potential for the monitoring of disease progression [2–4], development of targeted drug treatments [5, 6] and early diagnosis of disorders [7–9]. Several techniques for the detection of specific mRNAs are available, such as Northern Blotting, *in situ* hybridization and DNA microarrays [10–13]. Furthermore, mRNA expression can be studied using real-time reverse-transcription quantitative polymerase chain reaction (RT-qPCR), which is considered the standard protocol for the quantification of intra-cellular RNA content [14]. While these techniques are useful tools for the study of mRNA expression and presence, either their low sensitivity or their high levels of sample processing are often presented as major disadvantages [15].

In order to overcome these disadvantages, a variety of sensors have been developed which are based on the Förster resonance energy transfer (FRET) effect. FRET is characterized by a transfer of energy between two light sensitive molecules: an electronic energy donor and an electronic energy receptor [16]. By studying the mechanism behind this energy transfer it is possible to develop sensors that react to the presence of a specific target (i.e. FRET sensors), creating a type of off/on detection system, where the presence of the target induces a response (voltaic, fluorescent, etc.) [17–19]. Basing themselves on this donor/acceptor pair system, FRET sensors have been shown to be highly sensitive for measurements of small quantities and volumes, versatile on their applicability to a variety of different targets and capable of providing spatial and kinetic information over a range of different time scales [1, 20–23]. Consequently, this type of sensors have been used to detect a range of different biomolecules, from proteins [24] and mRNAs [25], to ions [26] and enzymes [27]. Their ability of detecting low concentrations of the desired target

has been shown to be particularly effective in the detection of small variances in biomarkers related with diseases, such as the determination of MMP-2 levels oscillations for the early detection of metastatic cells [28], and the multiplex of five different biomarkers for the detection of lung cancer [29]. This permits the early detection of bio-alterations that can lead to a quicker and more precise diagnosis of diseases that otherwise would go undetected [30, 31]. As examples of biomarkers for early detection of diseases, Beta-Secretase 1 (BACE-1) [32] and Prostate Cancer Antigen-3 (PCA3) [33–35] were chosen due to their reported link to Alzheimer's and prostate cancer respectively (see section 2.3.2). However, the sensitivity of these sensors is highly dependent on the efficiency of the donor.

Commonly used dyes have drawbacks such as photo-bleaching, blinking effects and interference patterns consequent of overlapping absorption regions with different biomolecules [36]. To overcome these issues, lanthanide upconversion nanoparticles have emerged as alternative electronic energy donors due to their ability to absorb low energy light and convert it to higher energy wavelengths [37]. As a result, these upconversion nanoparticles commonly absorb on the near-infrared biological window (650-1350 nm) where most of interfering molecules are avoided and light propagates more rapidly [38, 39]. Additionally, UCNPs have great chemical and photochemical stability, low toxicity and an absence of photo-bleaching or blinking effects [40–42].

On the other hand, the electronic energy acceptor also plays a critical role on FRET sensors. An ideal acceptor must have a high electronic capacity, an absorption range overlapping the donor's emission and maintain some characteristics of the donor (such as biocompatibility, water-solubility, etc.) [43, 44]. In this line of thought, graphene oxide (GO) appears to be an ideal energy acceptor for FRET sensors. GO possesses several beneficial characteristics such as high solubility in water, high surface area, efficient quenching and its characteristic affinity to various biomolecules [45–48]. The latter provides an additional advantage, since single stranded oligonucleotides have been shown to preferentially adsorb to GO via π-π stacking interactions, whereas double stranded oligonucleotides do not bind [49]. This facilitates the development of a FRET sensor capable of distinguishing between hybridized and non-hybridized oligonucleotide strands.

In this chapter the use of upconversion nanoparticles (UCNPs) in combination with oligonucleotide strands and graphene oxide (GO) for the detection of biomarkers is discussed. Different aspects of the nanoparticle core were studied such as doping agents (section 6.1.) and strategies for dissolution in aqueous/hydrophilic solvents (section 6.2.). In addition, several oligonucleotide sequences were tested (section 6.3.) and their successful attachment was analysed and characterised (section 6.4.). Finally the UCNP-oligonucleotide conjugates were tested in the presence of the quenching agent (graphene oxide) and calibration tests were made to evaluate the UCNP-DNA/GO sensing system in different conditions (section 6.5.), including in complex biological environments, such as blood plasma and cell lysates, to assess its performance in medically relevant scenarios (section 6.6.).

6.1. Analysis of upconversion nanoparticle core

Upconversion nanoparticles are capable of a photon upconversion type of fluorescence, were two or more lower energy wavelengths can be absorbed by the core and through electronic energy transfer between constituent elements emit at higher energy wavelengths [50]. For this process to happen, the elements involved need to have partially overlapping energy levels, so that the electron in an excited state can transfer its energy from one element to the other (see section 2.1.2.). This is achieved through anti-Stokes shifts, were the element that can absorb the excitation wavelength (antenna) transmits a part of the energy derived from its excited electrons onto another element which has an emission of interest (emitter), thus transforming low energy light (e.g. IR) onto higher energy emissions (e.g. visible).

Therefore, the first aspect of the lanthanide upconversion core to be evaluated was the antenna and emitter elements. Several rare-earth elements have been used for both roles depending on the desired absorption and/or emission wavelength [51]. Thulium (Tm) and erbium (Er) on their own have been used to absorb at 800 nm and 980 nm, respectively, while emitting at 455/480/650/1400 nm (Tm) [52] and 550/670/800/970 nm (Er) [53]. By combining with other antennas such as ytterbium,

the absorption wavelength of thulium for example can be shifted to 980 nm while keeping the same emissions [51, 54]. Different ratios of Tm/Er allow a fine tuning of the emission wavelengths, varying from a bright blue colour (~450 nm) up to the green region (~525 nm) [55]. Finally, neodymium has been used as an emitter to achieve orange/red emissions (~600 nm) to obtain a smaller energy gap between the antenna and the emitter [56, 57]. Due to these flexible fluorescent properties, UCNPs are considered excellent fine-tuning fluorescence agents for the development of biosensors.

For this work ytterbium was chosen as an antenna due to its high yield of intersystem crossing (i.e. transitions between electronic states), long life of its triplet state and overlap of its energy bandgaps with bandgaps of a variety of other rare-earth compounds (including Tm and Er) [58, 59]. Both Tm and Er were investigated as emitters due to their efficient energy conversion and their emission wavelengths [60, 61]. Lanthanide upconversion nanoparticles were synthesised using a previously established thermal decomposition protocol. Both Tm and Er were added to independent synthesis reactions, and their properties were analysed (Fig. 6.1). As shown in Fig. 6.1 A-D, the crystals of both $NaYF_4$:Yb, Er (A-B) and $NaYF_4$:Yb,TM (C-D) were spherically shaped. Moreover, the analysis of TEM images (~1000 particles) showed that the average size of Er doped nanoparticles was 27 ± 2 nm while Tm doped nanoparticles averaged at 33 ± 2 nm in size (Figure 6.1.E-F).

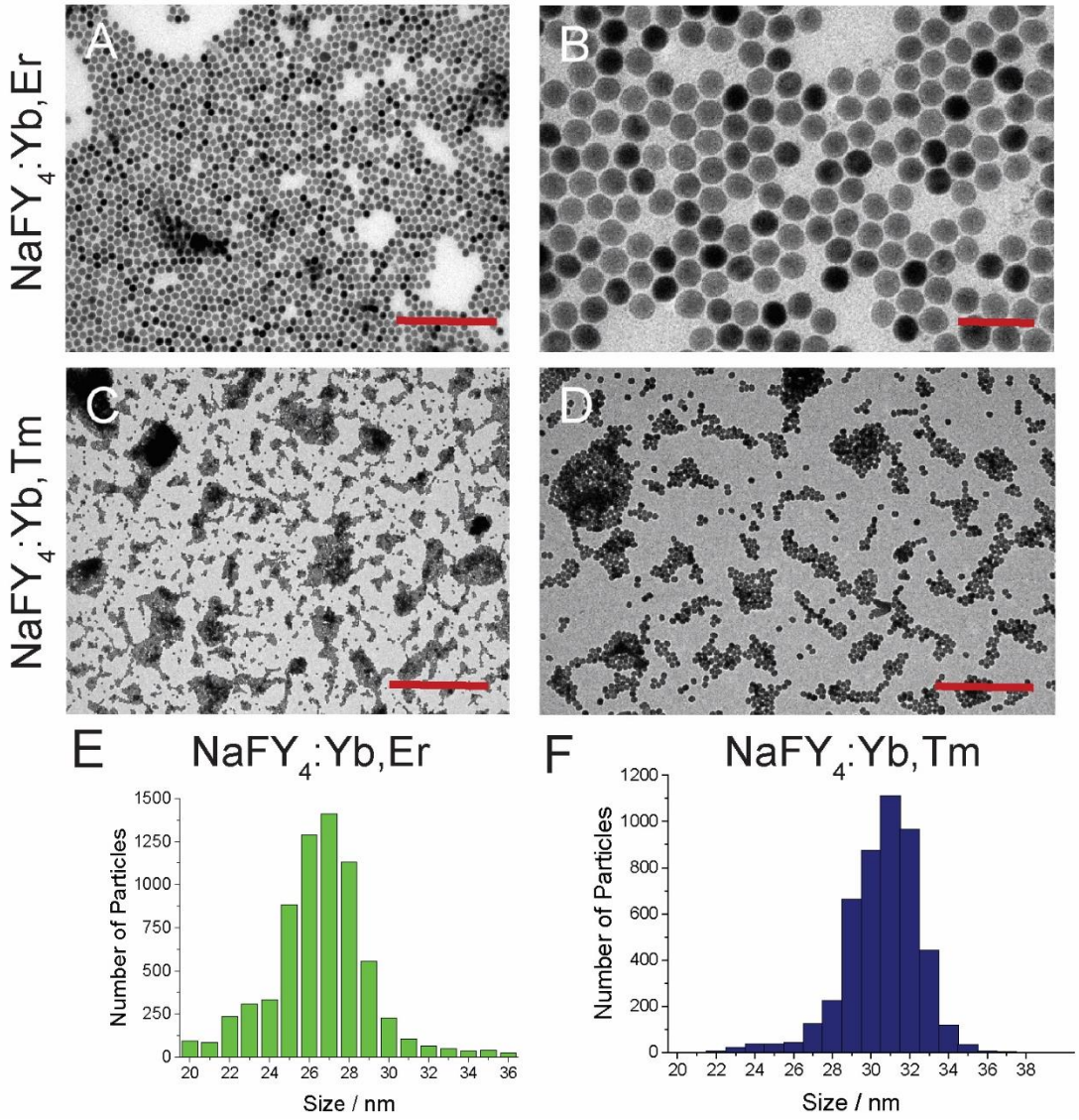

Figure 6.1.Shape and size of monodispersed upconversion nanoparticles.
$NaFY_4$:Yb,Er and $NaFY_4$:Yb,Er UCNPs were analysed using TEM. Both Erbium (A-B) and Thulium (C-D) doped lanthanide upconversion nanoparticles demonstrated a high degree of monodispersity. The average size of Er-doped particles was 27 ± 2 nm (E), while Tm-doped showed an average size of 33 ± 2 nm (F). (approx. 1000 particles counted for size distribution; Scale bars are – A/D: 500 nm; B: 100 nm; C: 2 µm)

To confirm that Tm and Er (doping agents) were present on the particles, these were analyse by energy dispersive X-Ray (EDX). Figures 6.2A and 6.2B

demonstrate the characteristic energy peaks of elements such as Y (1.9/14.968 keV), Na (1.04 keV), F (0.677 keV) and Yb (1.526/7.4 keV). All of these elements can be attributed to the crystalline matrix where the sensitizers were doped on. Other peaks such as O (0.525 keV), Cu (8.046 keV) and C (0.277 keV) can be attributed to unavoidable elements present in the analysis (i.e. oxygen from the air, carbon and copper from the grid). Nonetheless, when it comes to the specific doping of Tm and Er, the peaks seems to appear at 1.404/6.949 keV for erbium and 1.462/7.180 keV for thulium. In addition, the antenna (Yb) peaks appear at 1.5/7.4 keV. The close proximity of the peaks associated with the lanthanide elements can be explained by their similarity in key features that influence x-ray footprints, such as atom radii and energy levels However, the difference keV values are in accordance with characteristic values from the literature. [62].

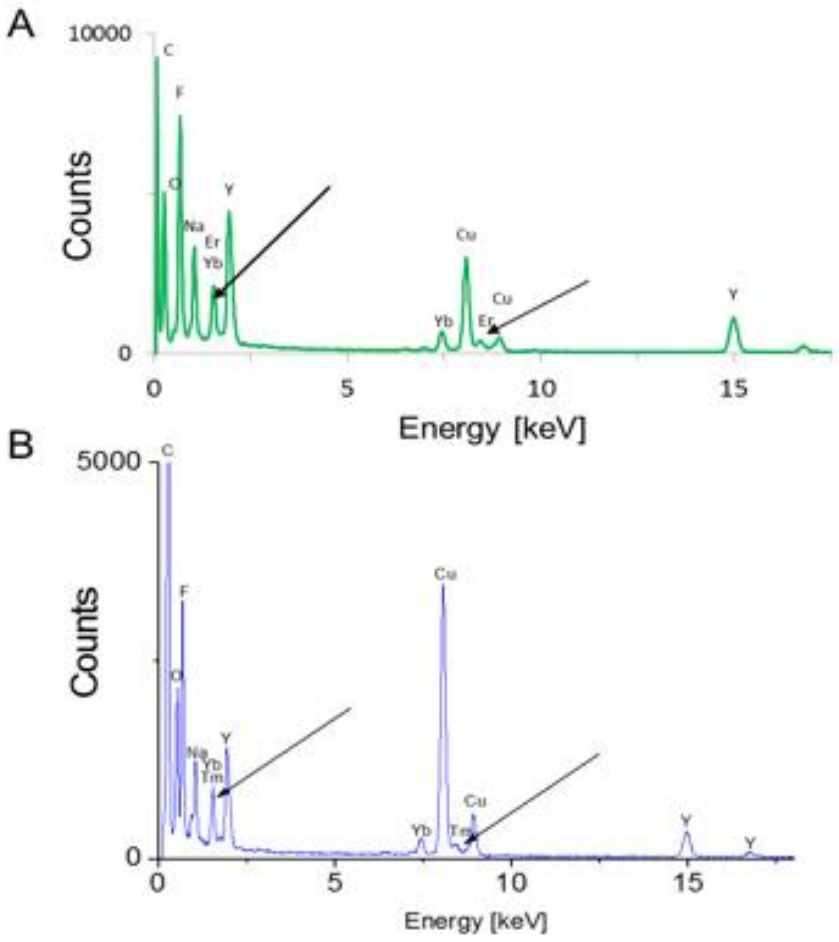

Figure 6.2. Elemental analysis of upconversion nanoparticles ($NaFY_4$:Yb,Er & $NaFY_4$;Yb,Tm). Both erbium (A) and thulium (B) lanthanide upconversion nanoparticles

show characteristic peaks at 1.404/6.949 keV and 1.462/7.180 keV, respectively (black arrows).

Finally, a spectroscopic analysis was performed of both types of particles to investigate their fluorescence profile (Fig. 6.3). Both types of UCNPs presented a high degree of upconversion fluorescence. $NaYF_4$:Yb,Er presented characteristic peaks at 530 nm, 545 nm and 660 nm (Figure 6.3A) with a visible green colour when under a 980 nm excitation laser (Figure 6.3B), whereas $NaYF_4$:Yb,Tm displayed characteristic peaks at 460 nm, 480 nm and 800 nm (Figure 6.3C) with a visible blue/purple colour when under the excitation laser (Figure 6.3D).

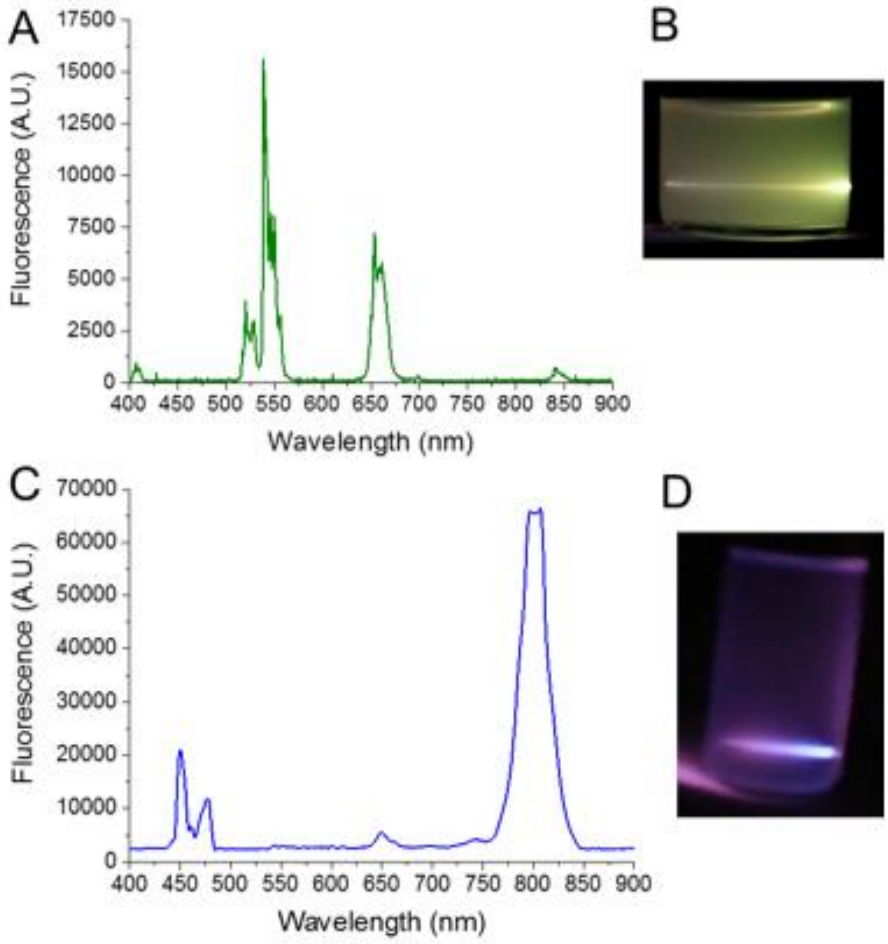

Figure 6.3. Spectroscopic profile of Er and Tm doped upconversion nanoparticles. $NaYF_4$:Yb,Er nanoparticles (10 mg/mL, dispersed in Hexane) exhibited a characteristic fluorescence spectrum (A) with the highest peak at 545 nm which reflected on a visible green colour when excited under a 980nm laser source (B). $NaYF_4$:Yb,Tm nanoparticles (10 mg/mL, dispersed in Hexane)demonstrated a fluorescence spectrum with

its highest peak in the NIR region – 800nm – (C), consequently demonstrating a blue colour when excited under the same type of laser source (D).

Furthermore, when analysing the ratio between the highest and the second highest peaks in both fluorescence spectra, erbium particles emit at an intensity ratio of 2:1 between 545 nm and 660 nm while thulium emits at an intensity ratio of approximately 4:1 between 800 nm and 460 nm. This is an indication that, even though both types of particles are efficient at upconverting light, erbium-dopped particles are better for an upconversion on the visible region. Therefore, in order to maximise the detection of the nanoparticles for sensing purposes, erbium-dopped nanoparticles were chosen to carry out future experiments.

6.2. Phase transfer of upconversion nanoparticles

With the emitter and antenna chosen, the next step was to transfer our UCNP from an organic solvent to water, so that these could be conjugated with oligonucleotide sequences. This step is necessary since oligonucleotides are easily degraded in non-physiological conditions such as low pH or organic solvents [63]. For this, two different strategies were chosen: silanization and ligand exchange.

Silanization of nanoparticles was first demonstrated by Loste *et* al (2004) to cover titanium dioxide [64] and Yamaura *et al.* (2004) to cover magnetic nanoparticles [65]. These groups coated their nanoparticles taking advantage of a well-known silano-hydrolyzation reaction used in electrochemistry to silanize surfaces [66, 67]. Silanization consists of covering of the nanoparticles' surface using an alkoxysilane compound (such as TEOS). The alkoxysilane molecules are anchored to the surface of the nanoparticles using a reverse microemulsion method and the respective silicate groups are hydrolysed to create an intercalated and translucent silica shell This way, the particles become soluble in more aqueous solvents without compromising their fluorescence properties.

In turn, ligand exchange is process of substitution of capping molecules that are located on a nanoparticle's surface after synthesis. This substitution can occur if the

target ligand has a higher affinity for the nanoparticle core [68]. For example, ligand exchange in metal cores such as gold and silver can be achieved by substituting ligands that are electrostatically linked to the core with ligands that form covalent-like thiol bonds with the metal core's surface [69].

Both coating methods were tested in $NaYF_4$:Yb,Er particles. Figure 6.4A shows the successful coating of UCNPs with silica, observed by the contrasting darker shade of the upconversion core against the lighter silica shell. However as previously shown in the literature, these shells are naturally thick, which can affect the emissions of different particles [70]. To counter this, the concentration of TEOS was altered while keeping the concentration of UCNPs constant (at 1 mg/ml). Different concentrations of TEOS were used to investigate the optimal window of silica coating (Figures 6.4B-D). As expected, higher concentrations of TEOS (10 µl, 25 µl and 50 µl) lead to thicker silica shells (from ~15 nm in B to ~30 nm in C and ~40 nm in D). Increasing too much the amount of TEOS generally increased the risk of an uneven coating of the UCNPs (as seen by Fig. 6.4E), due to the reactions between the silica molecules, leading to the formation of silica nanoparticles. [71, 72]

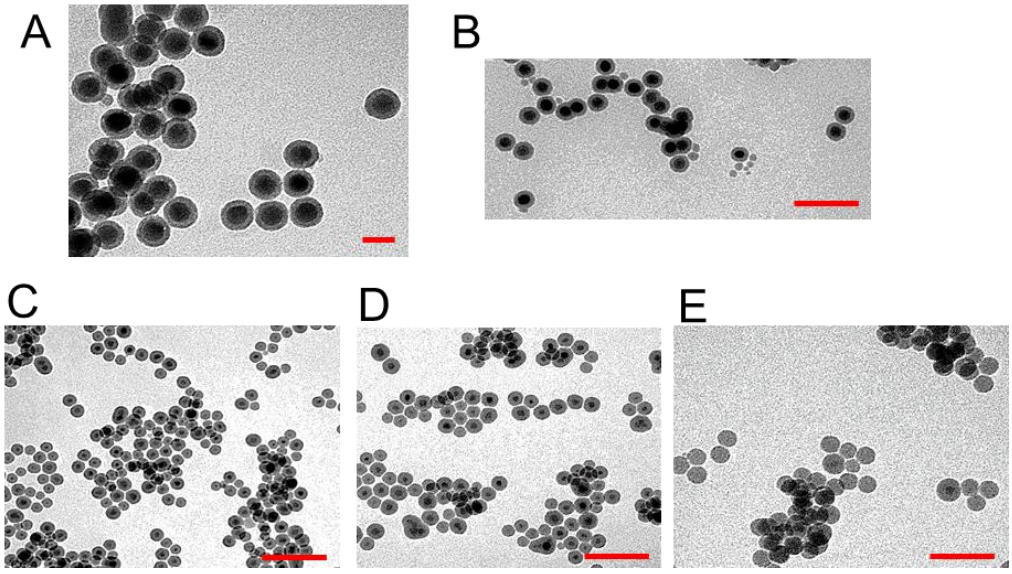

Figure 6.4. TEM of silanized $NaYF_4$:Yb,Er nanoparticles. (A) A constant concentration of 1 mg/mL of upconversion nanoparticles were successfully covered with a silica shell. By increasing the concentration of TEOS from 10 µl (B), 25 µl (C) and 50 µl (D), we observed the formation of an increasingly thicker silica shell. (E)

High concentrations of alkoxysilane (e.g. 75 µl) decreased nanoparticle silanization and increased the formation of silica particles (Scale bar are - A: 50 nm; B-E: 100 nm)

At this point, the Si-UCNPs were completely soluble in aqueous solvents, demonstrating a successful phase transfer using the silanization method. Next the impact of the shell thickness on the fluorescence of the nanoparticles was investigated. This was done by analysing the spectrum of particles with different thicknesses (15, 30 and 40 nm) to see at what concentration of TEOS all the UCNPs would be covered, while having a minimum impact on the fluorescence spectrum (Figure 6.5).

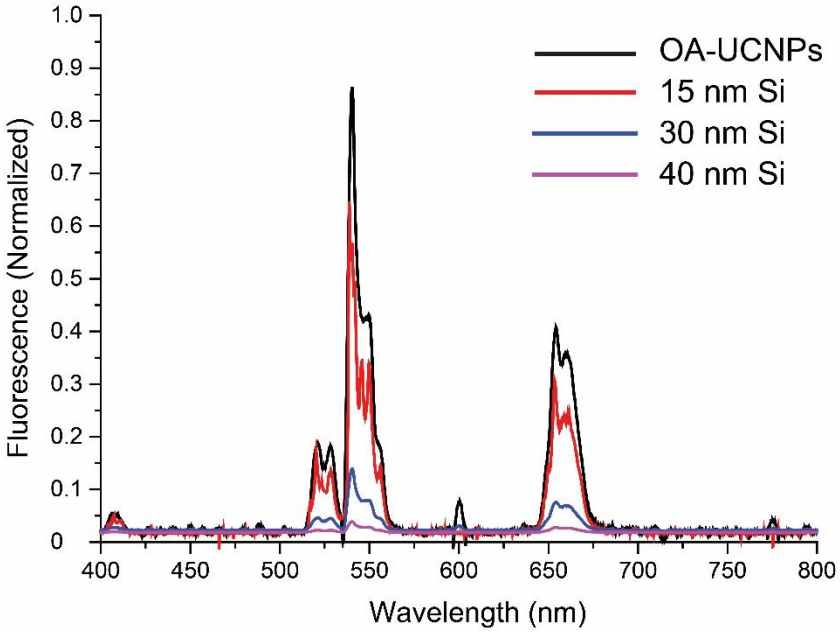

Figure 6.5. Effect of silanization on the upconversion fluorescence of $NaYF_4$:Yb,Er nanoparticles. When compared with oleic acid-coated upconversion nanoparticles (black, dispersed in hexane, 1 mg/mL), 15 nm of silica shell thickness (red, dispersed in ethanol, 1 mg/mL) decreases the overall signal by approximately 20%. If the thickness is increased to 30 nm (blue, dispersed in ethanol, 1 mg/mL) or even 40 nm (purple, dispersed in ethanol, 1 mg/mL), the signal decreases drastically by 90% and 98% respectively.

By analysing the maximum peaks, it was possible to observe that a shell thickness of 15 nm (which translates to a TEOS concentration of 10 µl) reduces the fluorescence intensity of the nanoparticles by approximately 20%. By comparison, thicker shells (30 nm and 40 nm) considerably reduce the overall fluorescence intensity of the nanoparticles, with decreases on the order of 90% and 98%, respectively. As a result, the amount of TEOS that had the least impact on the overall fluorescence intensity of the nanoparticles was 10 µl. In the end, the loss of fluorescence was compensated by successful transfer of the nanoparticles to an aqueous phase.

With the particles successfully transferred to an aqueous phase, the next step was to functionalize their surface in order to allow the attachment of oligonucleotides (see section 6.4.). Taking into account the amino functional groups present on the oligonucleotide strands used in this study (see Table 3.1. for full sequences), the EDC/sulfo-NHS coupling technique was tested. In order to prepare the silanized particles for the coupling reaction, carboxylic groups were added to their surface. This was achieved *via* a two-step process. The first step was to attach an amino-enriched silano compound through silica dioxide bonds. This method has been described in literature not only for the functionalization of silica surfaces [73] but also for the functionalization of silica coated nanoparticles [74]. 3-(Aminopropyl)trimethoxysilane (APTMS) was chosen due to the silano group (which facilitates the attachment onto silica surfaces) and due to the presence of the amino groups. Afterwards, the amino-enriched silanized particles were subjected to a ring opening reaction using succinic anhydride, converting the amino functional groups onto carboxylic and finishing the functionalization of the particles. The whole process was monitored using ζ-potential (Figure 6.6).

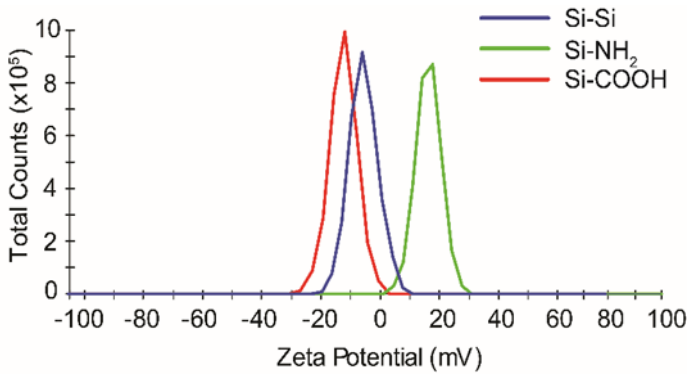

Figure 6.6. Functionalization of Silica-coated $NaYF_4$:Yb,Er UCNPs. The change in net charge from -3 mV (blue, dispersed in ethanol, 1 mg/mL), to +16 mV (green, dispersed in ethanol, 1 mg/mL) and finally to -12 mV (red, dispersed in ethanol, 1 mg/mL) indicates the different stages of functionalization of the particles: silica, amino-functionalized (NH_2) and carboxyl-functionalized (COOH), respectively.

Figure 6.6. shows the changes in the net charge of the particles as they go through the different stages of functionalization. Initially, with only a silica shell, particles have a slightly negative charge (-3 mV). With the attachment of the amino-enriched silano compound (APTMS) the charge increases to positive (+16 mV), reflecting the newly attached amino (NH_2). Finally, when the ring opening reaction occurs, the functional amino groups are transformed into carboxylic groups, bringing the charge down to a negative value (-12 mV).

Since this process of silanization and functionalization of silica-coated particles takes an average of 3 days, we decided to test a quicker method to transfer UCNPs to an aqueous solution. Taking advantage of the oleic acid coat that the nanoparticles present after synthesis, a ligand exchange was attempted. As described previously by groups such as Hutchinson and co-workers (2000) [75] and Rotello and co-workers (2002) [76], ligand exchange chemistry is a straightforward strategy to transfer inorganic nanoparticles to aqueous solutions. Ligand exchange is done *via* molecule-to-molecule substitution based on the fact that ligand molecules are interacting with the nanoparticles surface *via* electrostatic interactions. This makes it relatively easy to induce a swap between different ligands given the right conditions. Provided that the final ligand can interact with aqueous solvents *via* hydrogen bonding, the nanoparticles become soluble in aqueous solutions. One of the most used ligands for phase transfer of inorganic nanoparticles is polyacrylamide (PAA). PAA was chosen due to its hydrophilicity, its proneness to exchange with oleic acid molecules [77–79] and its high content of carboxylic groups which can be further functionalized with other molecules.

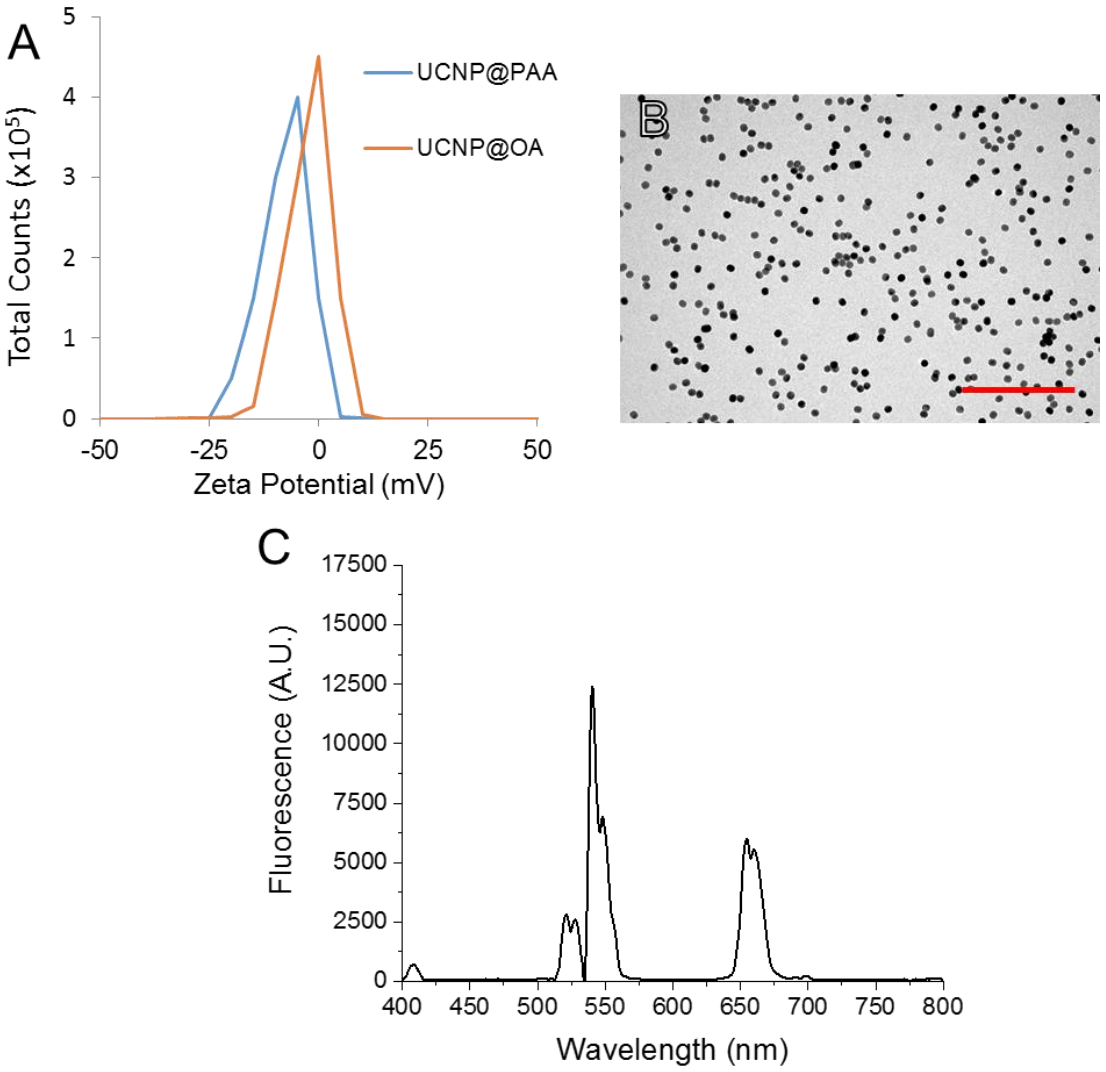

Figure 6.7. Characterization of PAA-coated $NaYF_4$:Yb,Er nanoparticles. The ligand exchange from oleic acid (OA) to polyacrylamide (PAA) can be observed by the shift of the overall net charge from 0 mV to -9 mV respectively (A). TEM micrograph of the PAA-coated particles (B – Scale bar = 500 nm) showed that the particles retained the same shape. At the same time, fluorescence profile (C) was extremely similar to as-synthesised nanoparticles. All particles analysed were dispersed in water in a concentration of 10 mg/mL.

As shown in Fig. 6.7A, the charge of UCNPs decreased from neutral (0 mV) when coated with oleic acid to slightly negative (-9 mV) when coated with polyacrylic acid. This decrease in the net charge can be attributed to the presence of carboxylic groups in the PAA polymer (which gives it a negative charge), as opposed to the

relatively non-polar oleic acid molecules. The clear change of the overall charge clearly indicates that the upconversion nanoparticles were successfully coated with PAA. At this point, the nanoparticles demonstrated a great solubility in water (not shown). At the same time, the nanoparticles maintained their overall shape (Figure 6.7B) and their fluorescence profile was not affected (Figure 6.7C). All of this was achieved after 24h, thus making PAA-exchange as an overall phase transfer method a good alternative to silanization.

Finally, with both types of phase transfer methods having their advantages and disadvantages, both silica coated and PAA coated upconversion nanoparticles were used in further experiments for both the successful attachment of the oligonucleotide sequences (see section 6.4) and the development of the biosensor (see section 6.5.).

6.3. Analysis of oligonucleotide sequences

For the development of the sensor, three of sequences were analysed: poly-T for the detection of characteristic poly-A tails present in every mature mRNA [80–82], BACE-1 as biomarker for the onset of Alzheimer's Disease [32, 83–85] and PCA3 as a biomarker for prostate cancer [33–35, 86]. The sequences for BACE-1 and PCA3 were chosen using the National Centre for Biotechnology Information's (NCBI) Basic Local Alignment Search Tool (BLAST) (see section 3.3.). The final sequences used were chemically altered to have an aminohexyl termination group to allow the use of sulfo-NHS/EDC coupling chemistry as a functionalization method. The sequences were kindly synthesised by ATDBio (Southampton, UK) as part of a collaboration.

The synthesised sequences (see Table 3.1. for full sequences) were tested for their melting temperature before being used as experimental targets of the UCNP-GO sensor. The melting temperature of the oligonucleotide sequences can affect their ability to hybridize with the target and maintain that state, affecting the sensor's reliability. The theoretical melting temperatures were calculated (Table 6.1.), and melting curves were measured in the presence of SYBR® Green II dye (Fig. 6.8). It

was observed that every experimental melting temperature differed only by approximately 1ºC from the respective theoretical temperature (Table 6.1.), demonstrating the stability of the sequences under the experimental conditions aimed for.

Target	Theoretical Melting Temperature (ºC)	Experimental Melting Temperature (ºC)
Poly-A	41.2	43.0
BACE-1	63.4	63.2
PCA3	62.1	62.7

Table 6.1. Theoretical vs Experimental melting temperatures of the difference sequences used

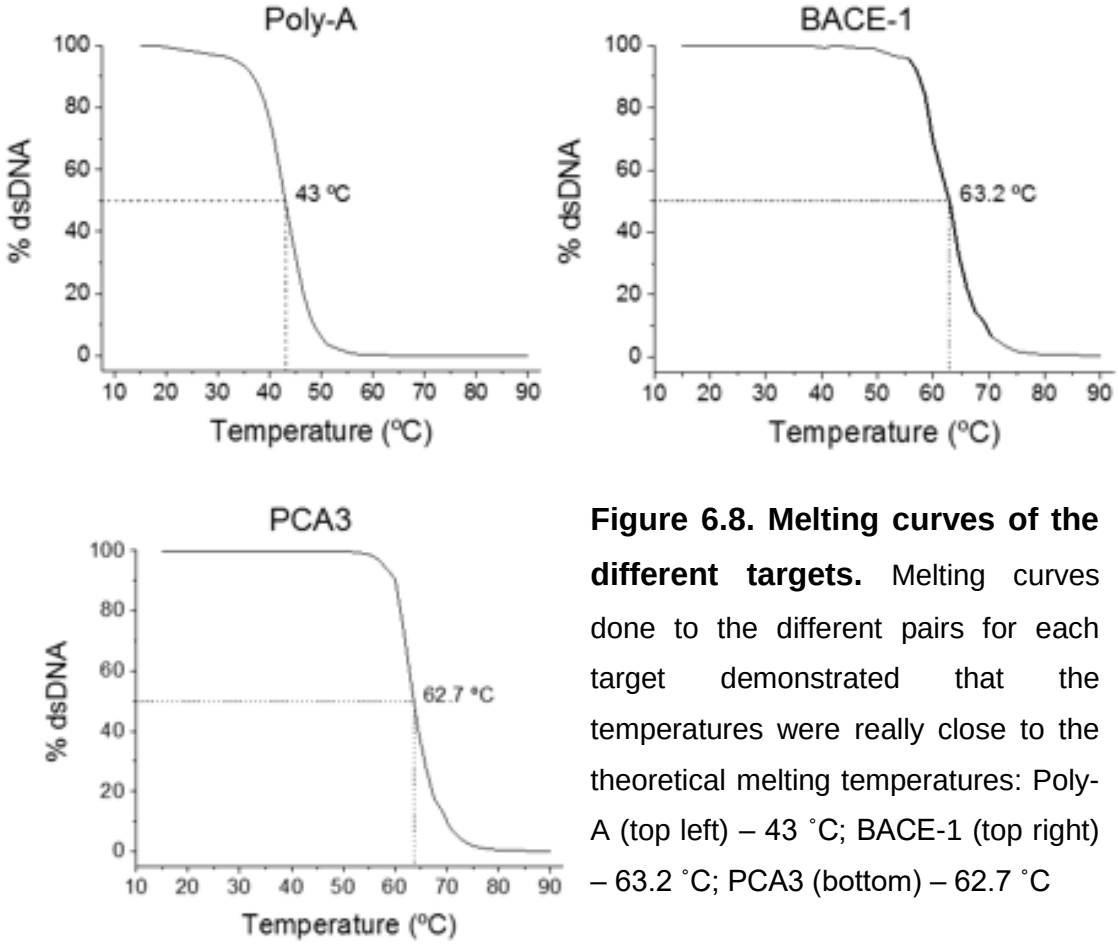

Figure 6.8. Melting curves of the different targets. Melting curves done to the different pairs for each target demonstrated that the temperatures were really close to the theoretical melting temperatures: Poly-A (top left) – 43 ˚C; BACE-1 (top right) – 63.2 ˚C; PCA3 (bottom) – 62.7 ˚C

Additionally, it was possible to conclude that the oligonucleotide pairs (target and sense strands) were successfully synthesised since SYBR® Green is known to only interact with double stranded oligonucleotides [87]. Since the initial signal of the curves presented high values of intensity, hybridization of the complementary strands was confirmed.

6.4. Attachment of oligonucleotides to upconversion nanoparticles

Due to the amino functional group present in the sense strands (and the carboxylic groups present in both the silanized and the PAA-coated upconversion

nanoparticles it was possible to use sulfo-NHS/EDC coupling chemistry to successfully attach the oligonucleotide strands to the nanoparticles. This reaction occurs when, in the presence of a ring opening agent (a carbomiide in this case), an amino and a carboxylic functional groups react with each other to create a covalent bond. Using this strategy, the attachment of the sense strands for all the targets (Poly-T, BACE-1 and PCA3) was performed and analysed using four different techniques: ζ-Potential (Fig. 6.9A), UV-Vis spectroscopy (Fig. 6.9B), fluorescence spectroscopy (Fig. 6.9C) and Fourier Transforming Infra Red (FTIR) spectroscopy (Fig. 6.9D).

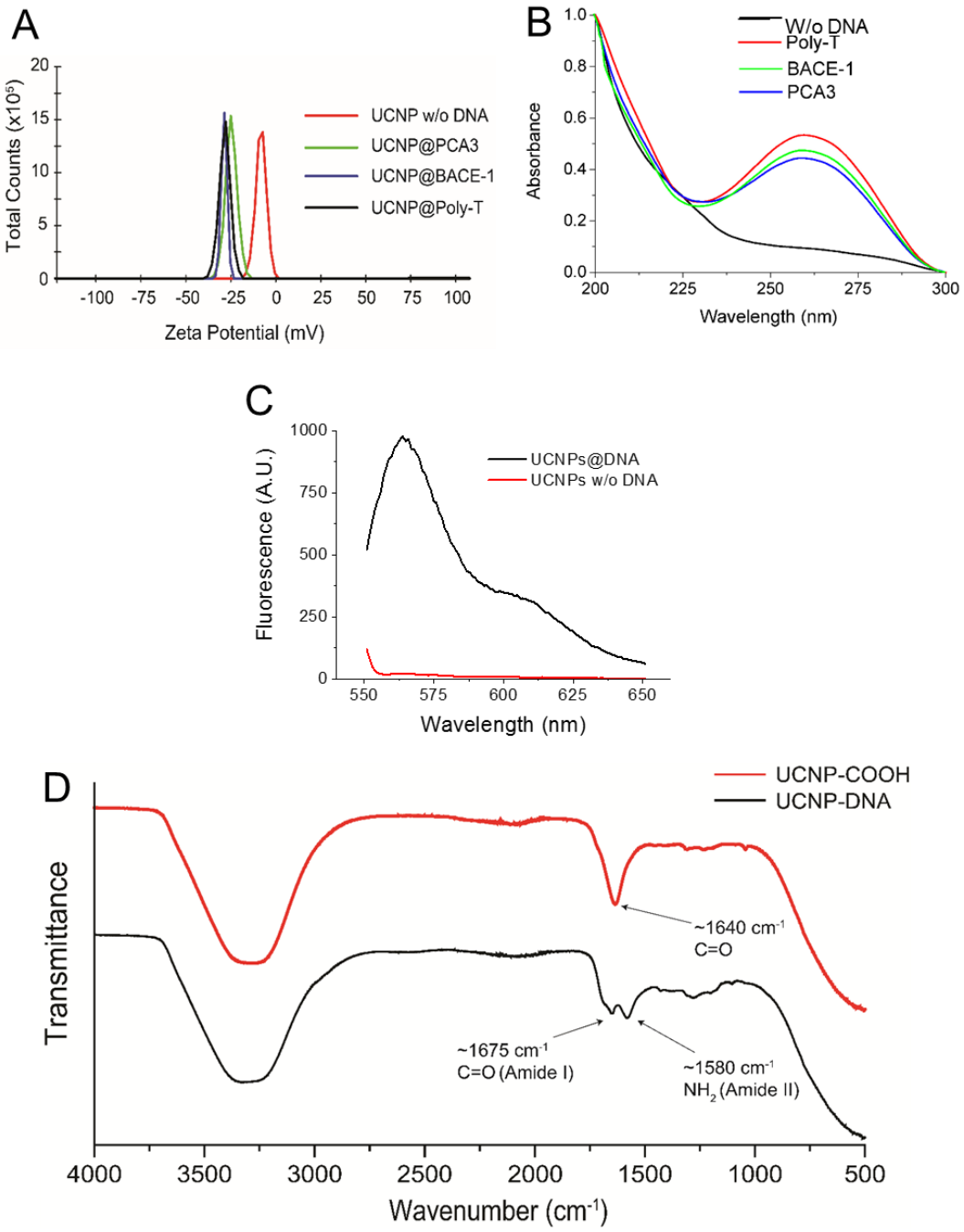

Figure 6.9. Characterization of the attachment of oligonucleotide sequences to upconversion $NaYF_4$:Yb,Er nanoparticles. The successful attachment of the oligonucleotide sense strands (Poly T: Thiol Group - TTT TTT TTT TTT TTT TTT TT; BACE-1: Thiol Group - AAA AAC AAC CTT CGT TTG CCC AAG A; PCA3: Thiol Group - AAA AAT GTT CAA AGA CCC TTC GTG T; See Table 3.1. for full details) was fully characterized with four different techniques. ζ-Potential (A) shows that the overall net charge decreases from -12 mV (COOH) to an average of -30 mV when any DNA sense strand was attached. UV-Vis spectroscopy (B) demonstrates that the particles covered with DNA gain a peak at

260nm characteristic of oligonucleotide strands. Fluoro-tagged strands (Poly T tagged: Thiol Group - TTT TTT TTT TTT TTT TTT TT - Cy3) can be seen *via* fluorescence spectroscopy (C) with the appearance of a peak at 556 nm from the Cy3 tag. Finally, FTIR spectroscopy (D) demonstrates the successful attachment of DNA strands via EDC/sulfo-NHS couplings by the shift from a single peak at ~1640 nm (C=O bond) to a double peak at ~1675 nm/~1580 nm (amide bonds).

Through the analysis of the change on the overall net charge (ζ-potential, Fig.6.9A), it was possible to observe that the UCNPs covered with carboxylic groups had an overall charge of -12 mV. However, upon the attachment of the oligonucleotide strands, the overall charge became more negative (average -30 mV). This decrease of the overall charge reflects the present of the ssDNA which is rich in highly negative phosphate groups on its backbone.

Similar results were obtained by observing the UV-Vis spectra of the particles before (black) and after (red, blue and green) the attachment of different oligonucleotide sequences, with the appearance of the characteristic 260nm peak associated with oligonucleotide strands.

The successful attachment of oligonucleotides to the surface of UCNPs was also investigated using fluorescence spectroscopy. For that, a model sequence (Poly-T, Thiol Group - TTT TTT TTT TTT TTT TTT TT - Cy3) was tagged on the 3' end with a cyanine 3 (Cy3) dye to monitor the coupling of the strand to the UCNPs. In Fig. 6.9C it is possible to observe that, upon an excitation at 545 nm, UCNPs without DNA are unreactive (i.e. no fluorescence profile). However, when the fluorophore-tagged strands were attached to the UCNPs, a peak at 556 nm was observed. This peak corresponds to the characteristic emission peak of Cy3 [88], indicating that the strands were attached to the nanoparticles.

Finally, FTIR spectroscopy was used to evaluate the changes in the functional groups present before and after coupling. For that, UCNPs coated with COOH functional groups were initially analysed. It was possible to observe the successful EDC/sulfo-NHS attachment via FT-IR (see Figure 6.9.D), where there is an evident shift of the peak at ~1640 cm^{-1} which corresponds to the C=O vibration of the

carboxylic acid groups on the PAA-coated nanoparticles (red) to a double peak at ~1580 cm-1 and ~1675 cm^{-1} on the oligonucleotide-coated nanoparticles, which corresponds to the C=O and the N-H bonds of the amide groups.

These techniques showed a successful attachment of DNA strands to the surface of UCNPs, indicating that the EDC/sulfo-NHS coupling was successful. Therefore, both silica-coated and PAA-coated UCNPs were covered with DNA and used for the sensor development.

6.5. Sensor calibration

As previously mentioned (see section 6.1), lanthanide upconversion nanoparticles worked as electronicenergy donors (i.e. fluorophore) and graphene oxide worked as an electronicenergy acceptor (i.e. quencher) in the development of the sensor. The mechanism behind these nanoparticles' fluorescence is based on an anti-Stokes shift (i.e. the absorbed photons are less energetic than the emitted ones), where the antenna element (yttrium) absorbs at lower wavelengths and transfers that energy to another element – emitter – which consequently emits at a higher wavelength (e.g. erbium). This transfer happens through upconversion emissions (see section 2.1.2) from near-infrared radiation to the visible region of the electromagnetic spectrum [50]. However, fluorescence detection instruments are usually equipped for normal Stoke fluorescence (lower to higher wavelengths), making it harder to characterise the GO-oligonucleotide-UCNP sensor. In addition, there was a great interest in this work to lower the limit of detection (LOD) to investigate the capability of the sensor in differentiating between noise and significant signal at lower target concentrations.

Therefore, a laser-setup was developed with the help of Prof. Otto Muskens that consisted of three major components: an excitation source, a 980 nm (500 mW) laser; spectrophotometer detector for fluorescence spectroscopy studies; and a photon detector as a more sensitive method of detection (see section 3.9.). By having both detectors incorporated on the same setup, a reliable comparison between a well-documented and robust technique (fluorescence spectroscopy) and

a more sensitive technique (single photon counting) was performed. Calibration studies were therefore conducted to determine the minimal concentration of graphene oxide that achieves maximum quenching (section 6.5.1), to observe the stability of the GO-oligonucleotide-UCNP sensor and the setup over time (section 6.5.2), to determine the optimal windows of concentration of target for a pinpoint detection (section 6.5.3) and finally to achieve a lower detection limit (section 6.5.4).

6.5.1 Graphene Oxide as a quenching agent

The sensor described in this chapter was developed based on two main characteristics of graphene oxide: the specific and selective interaction between the p-orbitals of the carbon rings and single stranded DNA sequences over double stranded sequences [47], and its electronic properties that allow it to receive the transfer of electronic energy from a great range of electronic energy donors (e.g. fluorophores), thus rendering it as a great quenching material [45, 89].

In order to determine the optimal concentration window of GO for the best performance of the sensor calibration experiments were conducted. For this, a fixed concentration of UCNPs was chosen (5 mg/ml) and all experiments were conducted in PBS solution to facilitate the interaction between particles and graphene oxide sheets. The size of the graphene oxide sheets was investigated prior to any experiments through transmission electron microscopy. Figure 6.10A-B shows the lower (A) and higher (B) size limits (0.5 μm and 5 μm respectively). In addition, the UV-Vis spectrum of graphene oxide (Fig. 6.10C) showed an expected broad curve with its peak at 260 nm and absorbance values between 0.2-0.4 in the region of interest for this study (450-600 nm). Both the sizes and the absorption were deemed optimal for the continuation of the experiments.

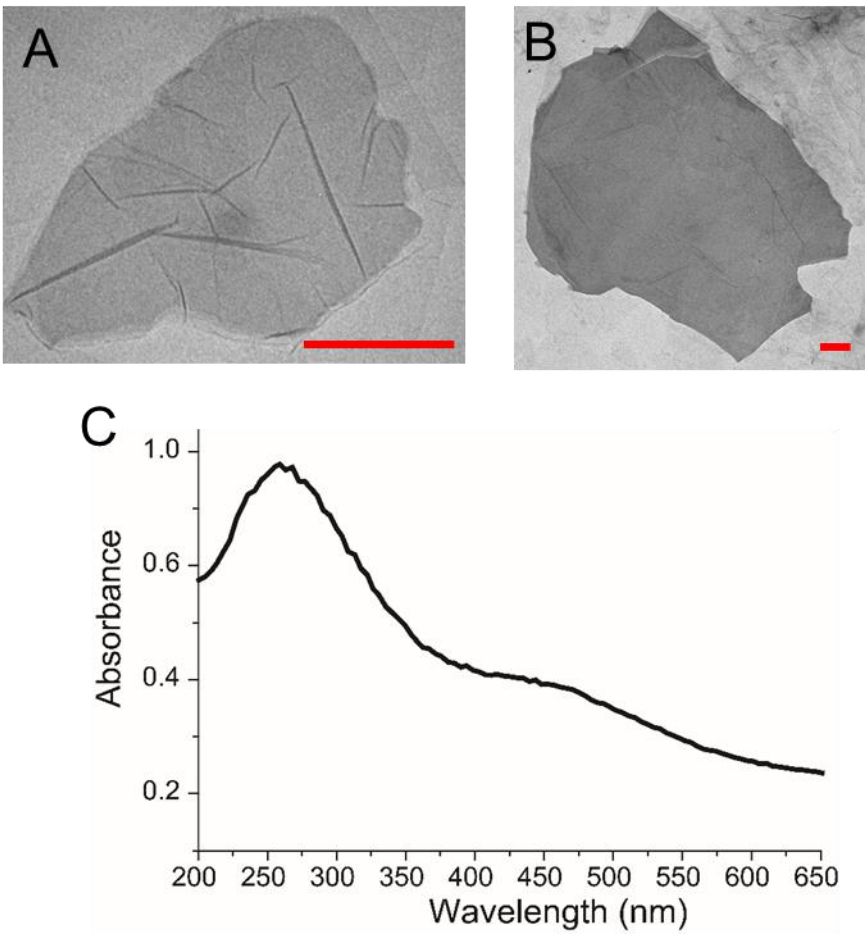

Figure 6.10.Characterization of graphene oxide. TEM micrographs of graphene oxide sheets demonstrated its size range to be from 0.5 µm (A) to 5 µm (B) (Scale = 500 nm). The absorption spectrum of a GO solution demonstrated a peak at 260 nm, with values of 0.2-0.4 in the region of interest for this study (450-650nm).

Afterwards, it was necessary to confirm that the quenching of the nanoparticles would only happen when these were covered with oligonucleotide strands. For this, PAA-coated, silica-coated and oligonucleotide-coated lanthanide UCNPs (all at 5 mg/ml, dispersed in water) were incubated with an excess of graphene oxide (1 mg/ml). Figure 6.11A shows that the presence of GO sheets is not sufficient to successfully quench the nanoparticles. Quenching of the fluorescence is only observed when the UCNPs are coated with ssDNA strands (red), ruling out non-specific interactions between UCNPs and GO.

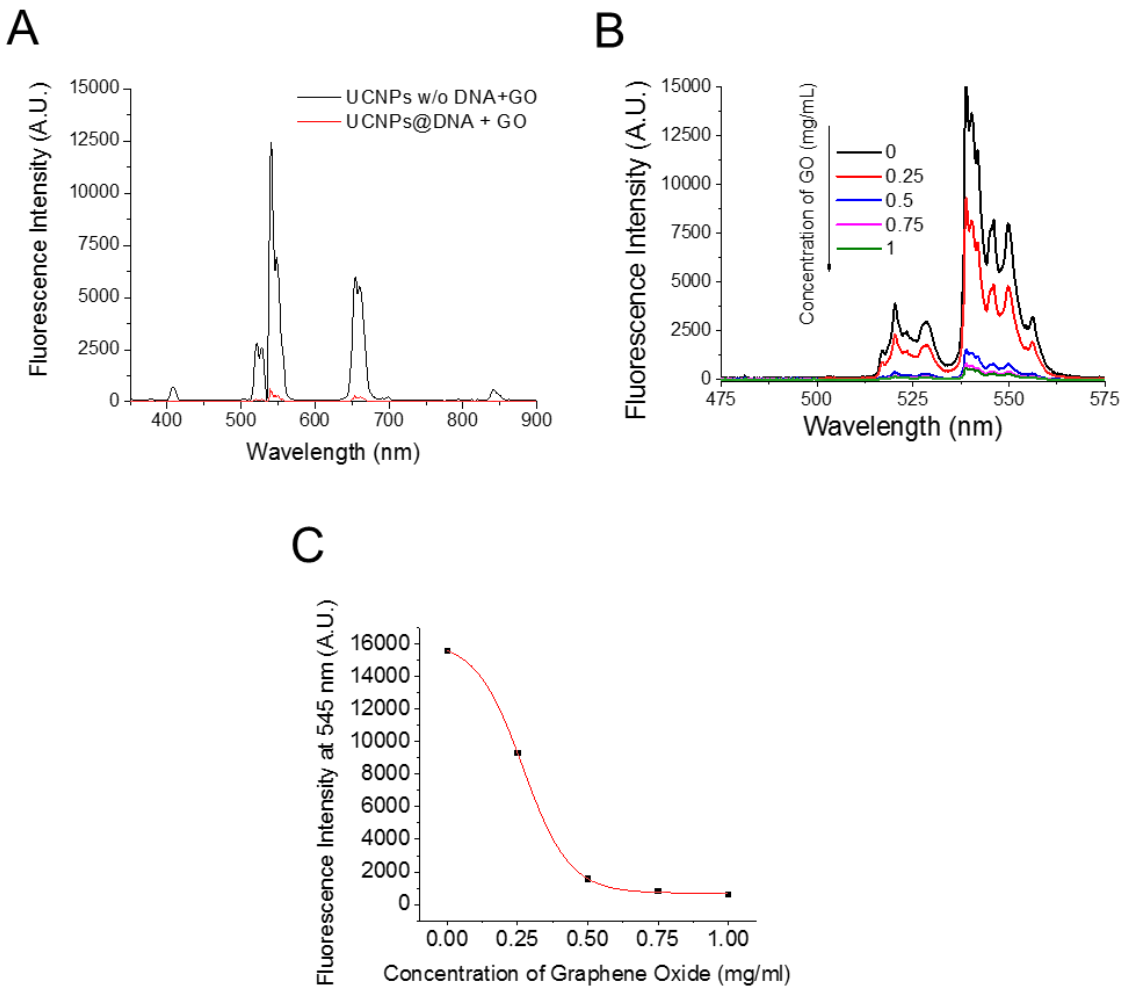

Figure 6.11. Calibration of graphene oxide quenching. In the presence of an excess of graphene oxide (1mg/ml), NaYF4:Yb,Er upconversion nanoparticles (5 mg/ml, dispersed in water) covered with DNA (Poly T: Thiol Group - TTT TTT TTT TTT TTT TTT TT) were quenched (red) while PAA/silica-coated NaYF4:Yb,Er upconversion nanoparticles were not (black) (A). When the DNA covered particles (5 mg/ml, dispersed in water) were incubated with different concentrations of graphene oxide (B), the quenching was efficient at 0.5 mg/ml GO. In fact, by plotting the maximum fluorescence intensity in the presence of different concentrations of GO (C), it is observed that an increase beyond 0.5 mg/ml has minimal impact

In order to identify the optimal window of quenching, the UCNP:GO ratio was investigated by changing the graphene oxide concentration between 0 and 1 mg/ml. Figure 6.11B demonstrates that with increasing concentrations of graphene oxide

the quenching of the UCNPs' fluorescence decreases. By plotting the intensity at the peak of higher intensity (545 nm), Figure 6.11C shows that this relationship adopts an exponential decay form. In other words, there is a quick decrease of fluorescence intensity with the initial concentrations (0, 0.25 and 0.5 mg/ml), which slows down with higher concentrations. Between 0.5 mg/ml and 1 mg/ml we achieve a saturation point, where increasing GO concentration has little impact on the quenching of the fluorescence. Therefore, to avoid any non-specific interaction of graphene oxide to other agents present in the mix (e.g. target strands), its concentration was kept as low as possible while still achieving maximum quenching. That concentration was determined to be 0.5 mg/ml and the value was fixed for any future experiments.

6.5.2 Stability of the sensor over time

With both the fluorophore and the quenching platform characterised, the stability of the sensor was investigated. To do that, NaYF4:Yb,Er nanoparticles either coated with ssDNA (Poly T: Thiol Group - TTT TTT TTT TTT TTT TTT TT; BACE-1: Thiol Group - AAA AAC AAC CTT CGT TTG CCC AAG A; PCA3: Thiol Group - AAA AAT GTT CAA AGA CCC TTC GTG T; See Table 3.1. for full details) or without ssDNA (with PAA or with silica) were observed every day over a period of 30 days in the presence of graphene oxide (0.5 mg/ml). This was done to understand if there was any major fluctuations on the data obtained that might compromise future experiments. Figure 6.12A shows that no significant changes were observed in the fluorescence spectra at maximum peak (545 nm) for all 30 days. The overall average of fluorescence intensity of ssDNA-covered nanoparticles was kept at a constant low level (494 ± 14 A.U.), while particles without DNA had a constant unquenched fluorescence of approximately 14800 ± 550 A.U. In addition, the photon detector was also tested at the same time. Figure 6.12B demonstrates that the number of photons obtained from unquenched particles (i.e. not covered with DNA) remained constant at around 145000 ± 2200 photons/measurement. On the other hand, particles covered with ssDNA demonstrated a constant low photon count

(approximately 78 ± 6 photons/measurement), close to the values obtained from the laser source alone (24 ± 3 photons/measurement).

These results show that the system was stable during an extended period of time. Consequently, the sensor was deemed ready to be used in the detection of targets for both fluorescence and photon detection.

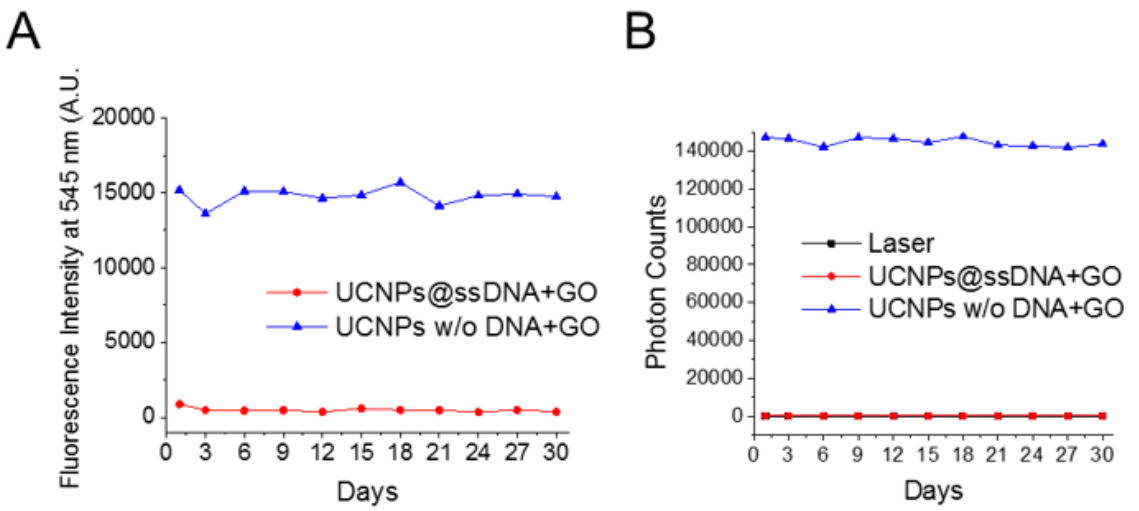

Figure 6.12.Stability of the UCNP + GO sensor. The sensor was tested over a period of 30 days for both fluorescence (A) and photon counting (B). There was no significant variation during the tested time period, and it was also confirmed that the nanoparticles were quenched by GO only when they were covered with ssDNA strands.

6.5.3 Detection of poly-A target

In order to proceed with initial tests to the sensor, a first analysis of poly-A target recognition was attempted. UCNPs were coated with untagged poly-T strands (see Table 3.1.) in a 1:1000 UCNP/ssDNA ratio. Once the nanoparticles were purified from excess strands, the poly-A target was added in different concentrations, ranging from 0 to 400 nM. Figure 6.13A shows that the fluorescence intensity detected was increasing proportionally with higher concentrations of the target. However, when presented with a different target (i.e. non-complementary sequence), the levels of fluorescence were negligible. Figure 6.13B shows that even

high concentrations of non-complementary target (400 nM) do not restore the fluorescence of the particles.

The experimental limit for poly-A detection using the spectrophotometer detector was determined at 0.1 nM. This limit is similar to most recently reported sensors [90].

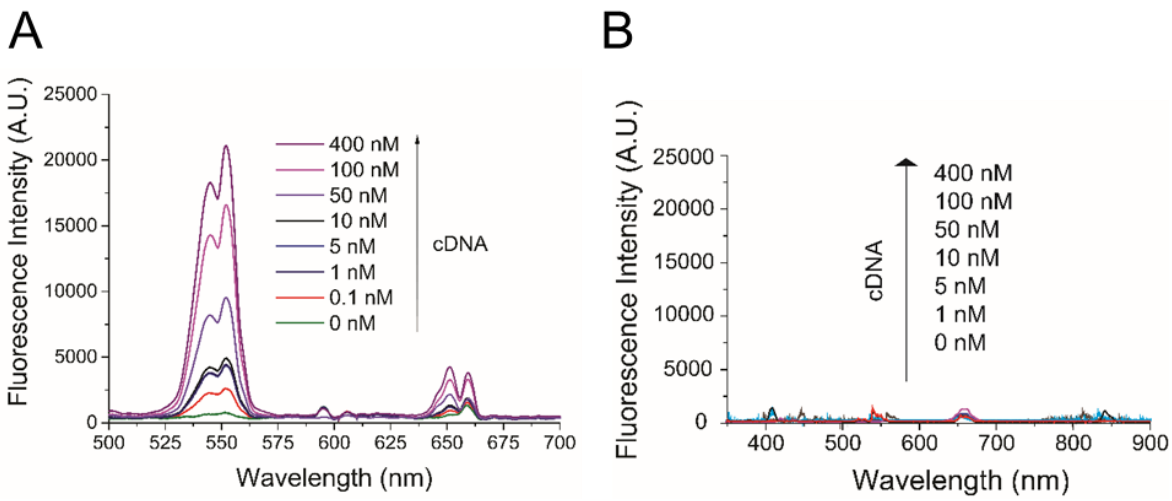

Figure 6.13. Response of the UCNP@ssDNA+GO sensor in the presence of different targets. When subjected to different concentrations of the complementary poly-A sequence (0-400 nM), the fluorescence intensity of poly-T coated UCNPs (1 mg/mL, dispersed in water) was directly proportional to the target concentration (A). In fact, at 0.1 nM it is already possible to significantly detect the presence of the target. However, when presented with a non-complimentary target (B), no significant detection was observed, independently of target's concentration.

6.5.4 Lower detection limit of sensor

One of the major obstacles of current sensor technology is the detection limit threshold. Currently reported sensors have different detection limits depending on the type of detection attempted [91–93]. Most sensors that aim to detect oligonucleotide strands in any form (e.g. DNA, RNA, etc.) are limited to detection limits on the pM-nM range [94, 95]. However, the ideal standard of a biosensor is to detect the smallest fluctuation possible in the target levels to provide a robust but

sensitive method of detection. In other words, the lowest the detection limit the better the sensitivity of the system.

Since our sensor demonstrated a great sensitivity on a broad spectroscopy analysis, it was hypothesised that by focusing on the region of most fluorescence output from the particles, it would be possible to lower the detection limit. This output was found to be around 545 nm from the fluorescence spectrum obtained from the particles (see sections 6.2 and 6.5.1). As a result, the laser setup was altered to have a specifically designed photon detector able to pick up emitted photons at the desired wavelength and, at the same time, block out any other photons directed at it.

Firstly, prerequisite GO experiments demonstrated that the previously determined optimal window of quenching was still applicable in the photon counting detection. Therefore, initial detection experiments were conducted with the same type of target as before. Poly-T coated UCNPs were subjected to different concentrations of the poly-A target (200 fM to 5 nM). Figure 6.14A shows that the photon counts obtained clearly distinguished between the different concentrations of the poly-A target. In fact, when focusing on the lowest concentrations (200 – 1000 fM), the target is still detected above the lowest sensing limit (shown on Figure 6.12.B to be 78 ± 6 photons/measurement). Thus, the experimental detection limit using photon counting detection was lowered by 500x to 200 fM. This demonstrated that not only the photon detection was comparable with the fluorescence detection, but also that the photon detection was more sensitive when it came to the lower concentrations of the target.

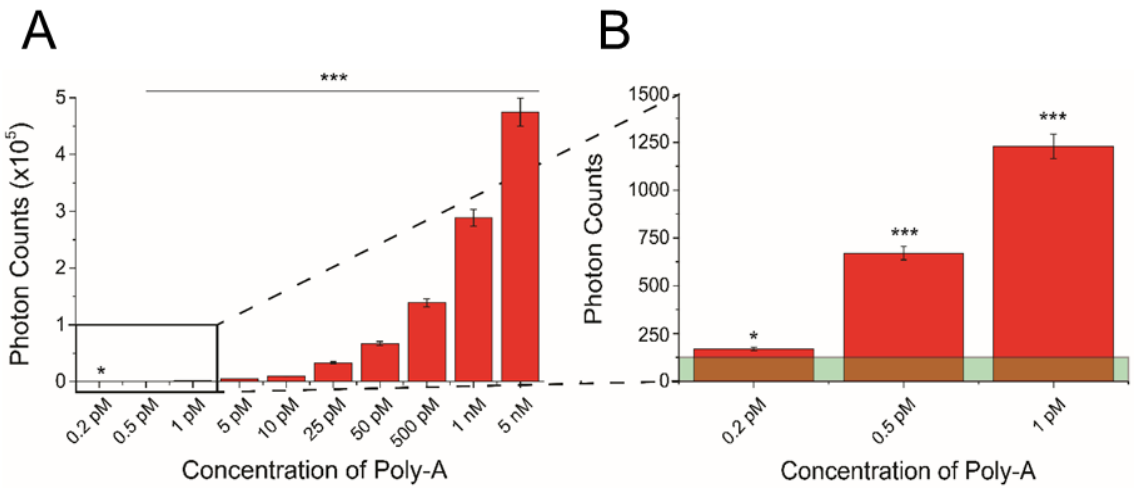

Figure 6.14. Photon counting for poly-A detection. The detection of poly-A (AAA AAA AAA AAA AAA AAA AA) was conducted in different concentrations of the target (200 fM – 5 nM) but at constant concentration (1mg/mL dispersed in water) of NaYF4:Yb,Er UCNPs coated with PolyT sense strand (Thiol Group - TTT TTT TTT TTT TTT TTT TT) (A). Target sequences were significantly detected in higher concentrations (>10 pM). However, at the lowest concentrations (200 fM – 1pM) (B), the number of photons was still significantly higher than the limit of the sensor when completely quenched (green area). (*p<0.01,***p<0.001)

6.5.5 Detection of BACE-1 and PCA3

Two different targets were chosen: BACE-1 as a biomarker for Alzheimer's disease and PCA3 as a biomarker for prostate cancer. Consequently, the respective sequences were synthesised and separately coupled to UCNPs (see section 6.4.). The UCNPs were then incubated with different concentrations of the respective target (200 fM to 5 nM). Figure 6.15 shows the photon counts for both BACE-1 and PCA3. As with poly-A, the targets are clearly detected until 10 pM. However, the lowest limit of these targets is slightly higher (500 fM) than that of poly-A. Therefore, the experimental detection limits were determined to be 500 fM for both PCA3 and BACE-1.

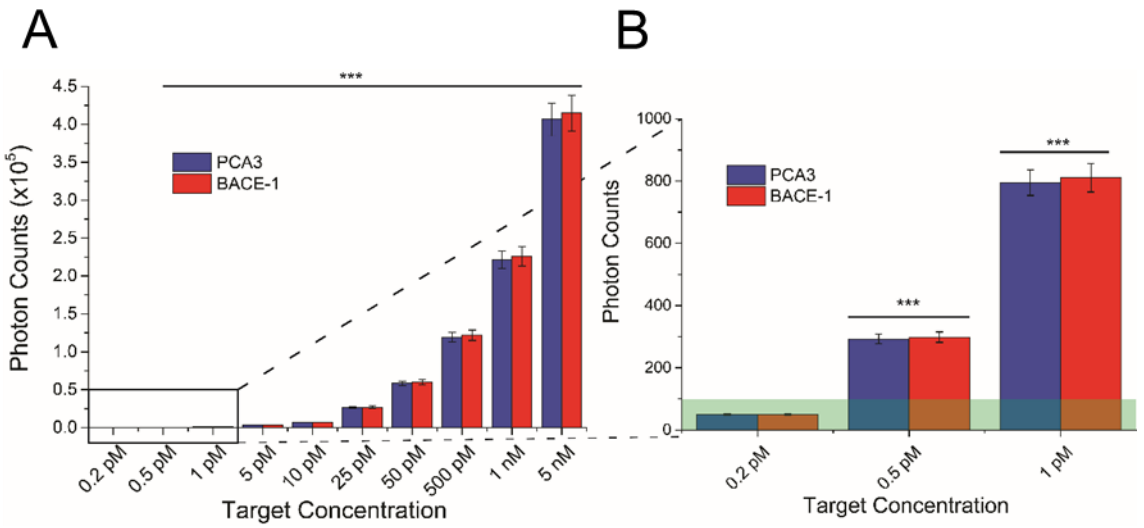

Figure 6.15. Photon detection of BACE-1 and PCA3. The detection of targets for BACE-1 (TCT TGG CGA AAC GAA GGT TG) and PCA3 (ACA CGA AGG GTG TTT GAA CA) was conducted in different concentrations of the respective targets (200 fM – 5 nM) but at constant concentration (1mg/mL dispersed in water) of NaYF4:Yb,Er UCNPs coated with sense strand (BACE-1: Thiol Group - AAA AAC AAC CTT CGT TTG CCC AAG A; PCA3: Thiol Group - AAA AAT GTT CAA AGA CCC TTC GTG T; See Table 3.1. for full details) (A). It was observed that the target was significantly detected in higher concentrations (>10 pM). However, when zooming in in the lowest concentrations (200 fM – 1pM) (B), it was possible to see that the number of photons was still significantly higher than the limit of the sensor when completely quenched (green area). (*p<0.01,***p<0.001)

Nonetheless, the determination of the LOD based on experiments alone is affected by equipment limitations. For example, the volume possible to use is limited to the pipette (minimum 0.1 µl) and the respective error. On the other hand, multiple dilutions of the solution containing the target introduces multiple errors from measurements done in different points of the process. Therefore, even though the experimental detection limit is more robust, it was hypothesised that, due to the number of data points obtained in the experiments, a theoretical curve could be extracted in order to calculate the theoretical detection limit as well. In this way, a clearer portrait of the sensor potential can be obtained and its full detection capabilities truly investigated. To do so, the data points for each of the three targets (poly-A, PCA3 and BACE-1) were plotted. As seen in Figure 6.16., the results from

the photon detection adopts a sigmoidal shape across the three targets. Subsequently, an equation was extracted from each curve (Table 6.2.).

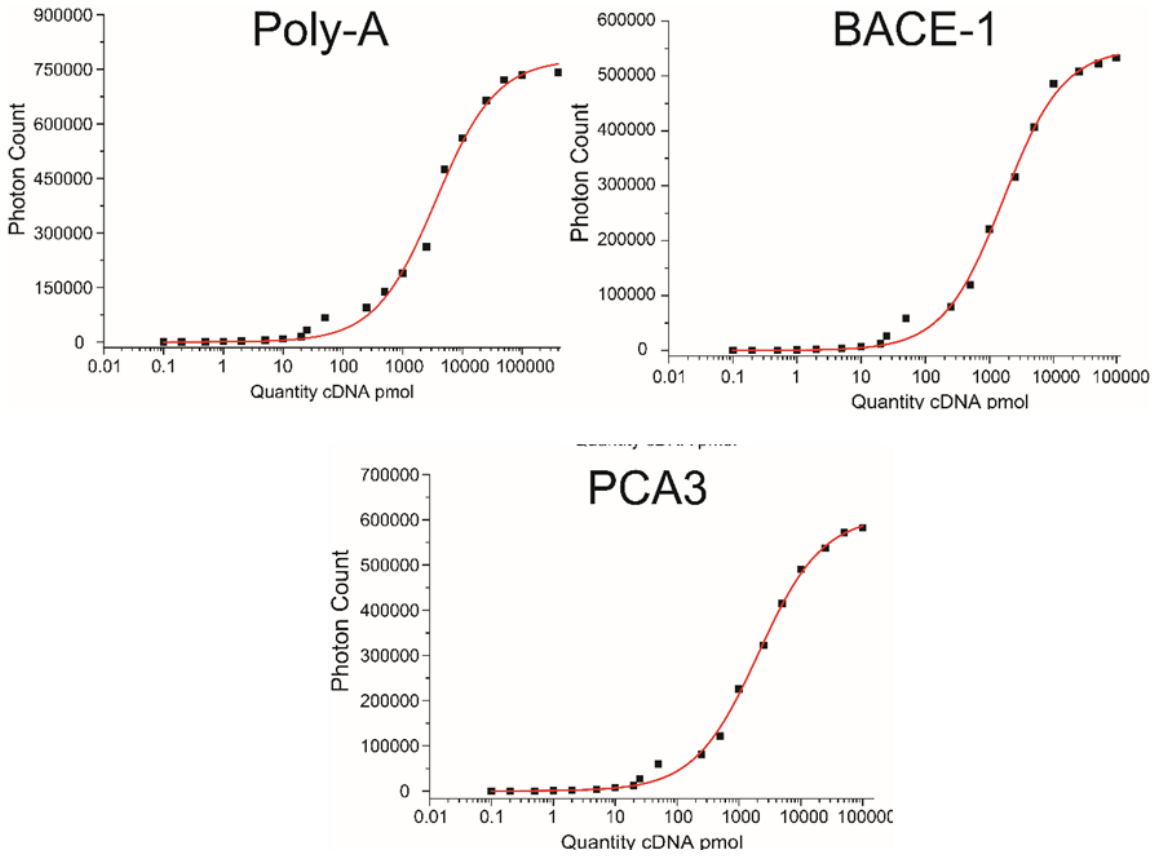

Figure 6.16. Fitted curves of experimental results of photon counting for the three targets. The results for all three targets – poly-A, BACE-1 and PCA3 – were plotted and the resulting curves adopted a sigmoidal shape. The resulting equations (Table 1) led to the determination of the theoretical limit of detection.

Target	Equation
Poly-A	$y = 778201 - \frac{778201}{1 + (\frac{x}{3590})^{0.86}}$
BACE-1	$y = 550560 - \frac{550560}{1 + (\frac{x}{1647})^{0.93}}$
PCA3	$y = 608658 - \frac{608658}{1 + (\frac{x}{2070})^{0.84}}$

Table 6.2. Fitted equations from photon detection of all three targets.

From the resulting equations it was possible to determine the theoretical limit of detection. To do so, it was assumed that the minimal number of photons for a significant detection was 100, which is slightly higher than the maximum error limit of the instrument in a scenario where UCNPs are completely quenched. It was also taken into consideration that the laser had an active region of approximately 20 x 20 x 250 μm^3 of volume (see Appendix B for example of an equation solution). Consequently, it was found that the theoretical limit for each of the target was the following: poly-A – 5.15 fM; PCA3 – 8.67 fM; BACE-1 – 7.56 fM. Therefore, the theoretical LOD was determined to be significantly lower (between 40-60x) than the experimental. Even though the theoretical results need to be analysed with frugality due to the different variables, the unproportionate difference between the two different LODs is suggestive of the common equipment limitations that these types of sensors can face.

Nevertheless, both experimental and theoretical detection limits are very low (e.g. a few molecules per litre), on par with some of the most sensitive systems reported in the literature [37].

6.6. Detection in complex biological environments

The development of a sensor and its application in real life scenarios, such as detection of biomolecules in blood, generally take several steps of optimization. The detection of biomarkers (e.g. RNA) in biological samples such as blood, urine or tissue entails present several problems. For example, the presence of different RNA forms can lead to non-specific interaction with the platform of the fluorophore agent if the design is not well-characterised. On the other hand, proteins present in solution can interfere with the binding of the fluorophore with the target, leading to a false-negative results. Therefore, it was important to test the sensor developed in this chapter in different adverse conditions.

Different solutions were chosen to represent situations where the detection of biomarkers can suffer from interferences: whole cell lysate (where cell contents such as organelles, proteins, lipids, etc., can coat the surface of the nanoparticles thus

blocking them from hybridizing with the respective target); and blood plasma, where protein complexes and cells such as platelets may hybridise with the graphene oxide platform rendering the FRET quenching useless. The system was tested in these two types of scenarios. On the one hand, a mix of blood cells (erythrocytes, leucocytes, thrombocytes and immune cells) was lysated in order to expose their intracellular contents. On the other hand, plasma was purified from blood samples in order to have a plasma solution.

Two different types of combinations for each scenario were tested: either the target correspondent to the UCNPs sensing strand was present alongside the other two targets (1 pM concentration for all strands involved), or only the non-specific target was present in solution. Overall, six combinations were obtained: poly-A present/absent alongside BACE-1 and PCA3; BACE-1 present/absent alongside Poly-A and PCA3; and PCA3 present/absent alongside Poly-A and BACE-1. Each of the combinations was additionally used to test the sensor in either cell lysis or blood plasma.

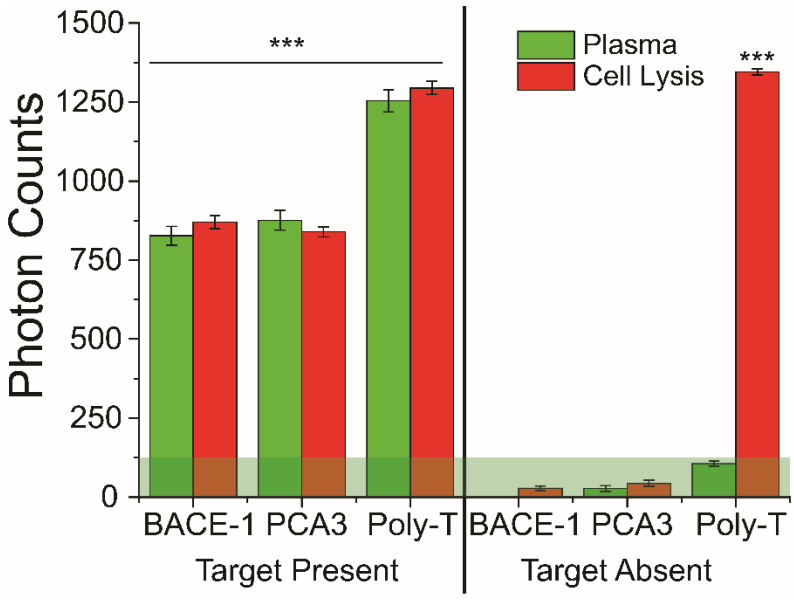

Figure 6.17. Detection of different targets in cell lysis and blood plasma. The performance of the sensor was tested in the presence (1 pM) and absence of the relevant

oligonucleotide targets in plasma (dark green) and cell lysis (red). In the absence of the target, the poly-T sensor is able to detect the poly-A tails of a range of different mRNAs in cell lysis (***p<0.001). The error associated with the equipment lower is represented by the light green area.

Figure 6.17 shows the signal correspondent to each one of the combinations. It is possible to see that a significant signal was detected in the presence of the respective target. For example, poly-T coated nanoparticles did not react in the absence of the poly-A target. Therefore, there was no signal detected by the sensor.

In comparison to the Alzheimer and prostate cancer sensors, which did not show a detection response in absence of the target sequence either in plasma or cell lysate, the poly-T oligonucleotide sequence sensor gave a strong fluorescent signal in the absence of the poly-A sequence in cell lysate. This observation is attributed to the presence of multiple mRNAs found in the cell lysate that carry a poly-A tail, which is detectable by the poly-T sensor, highlighting the excellent performance of the sensor for general mRNA targeting.

Therefore, it was observed that the sensor kept its selectivity in the presence of different targets in different biological conditions. Combining that with the high sensitivity of the system overall and its ability to be designed to any specific biomarker based on oligonucleotide sequences, it is possible to assume that the applications of this sensor are of a wide variety (see section 7.X for more discussion).

In summary, the conjugation, characterization and application of UCNPs and oligonucleotides was demonstrated in this chapter. By testing different types of phase transfer techniques, UCNPs of both blue ($NaYF_4$:Yb,Tm) and green ($NaYF_4$:Yb,Er) emission were successfully re-dispersed in aqueous solutions in order to conjugate with specifically designed oligonucleotide sequences. Furthermore, the resulting conjugates were used to design a GO-UCNP-DNA sensor that detects small oligonucleotides sequences relevant to general mRNA detection (Poly-A) and to the diagnosis of Alzheimer disease (BACE-1) and prostate cancer (PCA3). By comparing a new type of detection set-up (photon counter) with

a well-established technique (fluorescence spectroscopy), the sensor was demonstrated to be highly sensitive since it can detect sequences at the femtomolar range. All whilst avoiding drawbacks such as photo-blinking or biomolecule absorbance interferences by using UCNPs as the active fluorescent agent. Additionally, the sensor a very high selectivity for its target even in challenging environments such as the blood plasma and cell lysis, where the interference from biomolecule is high. The development of such a robust sensor can lead to a more "raw" detection, where less purification steps are needed to achieve a sensitive detection of biomolecules from samples gathered from patients suffering from certain diseases. These type of sensors can be applied in the detection of mRNA biomarkers, not only where these markers are present in low levels of detection (e.g. early stages of a disease) but also where time are a factor of utmost importance for the diagnosis of certain patients.

6.7. References

1. Shi, J., Tian, F., Lyu, J., & Yang, M. (2015). Nanoparticle based fluorescence resonance energy transfer (FRET) for biosensing applications. *J. Mater. Chem. B*, *3*(35), 6989–7005. doi:10.1039/C5TB00885A

2. Golub, T. R., Slonim, D. K., Tamayo, P., Huard, C., Gaasenbeek, M., Mesirov, J. P., Coller, H., Loh, M. L., Downing, J. R, Caligirui, M. A., BLoomfield, C. D., Lander, E. S. (1999). Molecular classification of cancer: class discovery and class prediction by gene expression monitoring. *Science*, *286*(5439), 531–537. doi:10.1126/science.286.5439.531

3. Beer, D. G., Kardia, S. L. R., Huang, C.-C., Giordano, T. J., Levin, A. M., Misek, D. E., Lin, L., Chen, G., Gharib, T. G., Thomas, D. G., Lizyness, M. L., Kuick, R., Hayasaka, S., Taylor, J. M. G., Iannettoni, M. D., Orringer, M. B., Hanash, S. (2002). Gene-expression profiles predict survival of patients with lung adenocarcinoma. *Nature medicine*, *8*(8), 816–24. doi:10.1038/nm733

4. Chang, H. Y., Sneddon, J. B., Alizadeh, A. A., Sood, R., West, R. B., Montgomery, K., Chin, J. T., van de Rijn, M., Botstein, D., Brown, P. O. (2004). Gene expression signature of fibroblast serum response predicts human cancer progression: Similarities between tumors and wounds. *PLoS Biology*, *2*(2). doi:10.1371/journal.pbio.0020007

5. Hughes, J. P., Rees, S. S., Kalindjian, S. B., & Philpott, K. L. (2011). Principles of early drug discovery. *British Journal of Pharmacology*. doi:10.1111/j.1476-5381.2010.01127.x

6. Sahin, U., Karikó, K., & Türeci, Ö. (2014). mRNA-based therapeutics--developing a new class of drugs. *Nature reviews. Drug discovery*, *13*(10), 759–80. doi:10.1038/nrd4278

7. Pipinikas, C. P., Carter, N. D., Corbishley, C. M., & Fenske, C. D. (2008). HIF-1alpha mRNA gene expression levels in improved diagnosis of early stages of prostate cancer. *Biomarkers : biochemical indicators of exposure, response, and susceptibility to chemicals*, *13*(7), 680–91. doi:10.1080/13547500802591992

8. Ng, C. F., Yeung, R., Chiu, P. K. F., Lam, N. Y., Chow, J., & Chan, B. (2012). The role of urine prostate cancer antigen 3 mRNA levels in the diagnosis of prostate cancer among Hong Kong Chinese patients. *Hong Kong medical journal = Xianggang yi xue za zhi / Hong Kong Academy of Medicine*, *18*(6), 459–65. Retrieved from http://www.ncbi.nlm.nih.gov/pubmed/23223645

9. Perdonà, S., Bruzzese, D., Ferro, M., Autorino, R., Marino, A., Mazzarella, C., Perruolo, G., Longo, M., Spinelli, R., Di Lorenzo, G., Oliva, A:, De Sio, M., Damiano, R., Altieri, V., Terracciano, D. (2013). Prostate health index (phi) and prostate cancer antigen 3 (PCA3) significantly improve diagnostic accuracy in patients undergoing prostate biopsy. *Prostate*, *73*(3), 227–235. doi:10.1002/pros.22561

10. Friess, H., Streit, S., Michalski, C. W., Erkan, M., & Kleeff, J. (2009). Northern blot analysis for detection and quantification of RNA in pancreatic cancer cells and tissues. *Nature protocols*, *4*(1), 37–43. doi:10.1038/nprot.2008.216

11. Katagiri, F., & Glazebrook, J. (2009). Overview of mRNA expression profiling using DNA microarrays. *Current protocols in molecular biology / edited by Frederick M. Ausubel*, *Chapter 22*(January), Unit 22.4. doi:10.1002/0471142727.mb2204s85

12. Brewer, P. B., Heisler, M. G., Hejátko, J., Friml, J., & Benková, E. (2006). In situ hybridization for mRNA detection in Arabidopsis tissue sections. *Nature protocols*, *1*(3), 1462–1467. doi:10.1038/nprot.2006.226

13. Stylianopoulou, E., Lykidis, D., Ypsilantis, P., Simopoulos, C., Skavdis, G., & Grigoriou, M. (2012). A rapid and highly sensitive method of non Radioactive colorimetric in Situ Hybridization for the detection of mRNA on tissue sections. *PLoS ONE*, *7*(3). doi:10.1371/journal.pone.0033898

14. Wong, M. L., & Medrano, J. F. (2005). Real-time PCR for mRNA quantitation. *BioTechniques*. doi:10.2144/05391RV01

15. Schwanhäusser, B., Busse, D., Li, N., Dittmar, G., Schuchhardt, J., Wolf, J., Chen, W., Selbach, M. (2011). Global quantification of mammalian gene expression control. *Nature*, *473*(7347), 337–342. doi:10.1038/nature10098

16. Li, N., Su, X., & Lu, Y. (2015). Nanomaterial-based biosensors using dual transducing elements for solution phase detection. *The Analyst*, *140*(9), 2916–43. doi:10.1039/c4an02376e

17. Zhang, C.-Y., Yeh, H.-C., Kuroki, M. T., & Wang, T.-H. (2005). Single-quantum-dot-based DNA nanosensor. *Nature materials*, *4*(11), 826–831. doi:10.1038/nmat1508

18. Cady, N. C., Strickland, A. D., & Batt, C. A. (2007). Optimized linkage and quenching strategies for quantum dot molecular beacons. *Molecular and Cellular Probes*, *21*(2), 116–124. doi:10.1016/j.mcp.2006.09.001

19. Suzuki, M., Husimi, Y., Komatsu, H., Suzuki, K., & Douglas, K. T. (2008). Quantum dot FRET biosensors that respond to pH, to proteolytic or nucleolytic cleavage, to DNA synthesis, or to a multiplexing combination. *Journal of the American Chemical Society*, *130*(17), 5720–5725. doi:10.1021/ja710870e

20. Clapp, A. R., Medintz, I. L., & Mattoussi, H. (2006). Förster Resonance Energy Transfer Investigations Using Quantum-Dot Fluorophores. *ChemPhysChem*, *7*(1), 47–57. doi:10.1002/cphc.200500217

21. Beljonne, D., Curutchet, C., Scholes, G. D., & Silbey, R. J. (2009). Beyond Förster Resonance Energy Transfer in Biological and Nanoscale Systems. *The Journal of Physical Chemistry B*, *113*(19), 6583–6599. doi:10.1021/jp900708f

22. Okumoto, S., Jones, A., & Frommer, W. B. (2012). Quantitative Imaging with Fluorescent Biosensors. *Annual Review of Plant Biology*, *63*(1), 663–706. doi:10.1146/annurev-arplant-042110-103745

23. Kumar, N., Bhalla, V., & Kumar, M. (2014). Resonance energy transfer-based fluorescent probes for Hg^{2+} , Cu^{2+} and Fe^{2+} /Fe^{3+} ions. *The Analyst*, *139*(3), 543–558. doi:10.1039/C3AN01896B

24. Yang, J., Zhang, Z., Lin, J., Lu, J., Liu, B., Zeng, S., & Luo, Q. (2007). Detection of MMP activity in living cells by a genetically encoded surface-displayed FRET sensor. *Biochimica et Biophysica Acta - Molecular Cell Research*, *1773*(3), 400–407. doi:10.1016/j.bbamcr.2006.11.002

25. Santangelo, P. J., Nix, B., Tsourkas, A., & Bao, G. (2004). Dual FRET molecular beacons for mRNA detection in living cells. *Nucleic acids research*, *32*(6), e57. doi:10.1093/nar/gnh062

26. Aper, S. J. A., Dierickx, P., & Merkx, M. (2016). Dual Readout BRET/FRET Sensors for Measuring Intracellular Zinc. *ACS Chemical Biology*, *11*(10), 2854–2864. doi:10.1021/acschembio.6b00453

27. Figueroa, R. A., Ramberg, V., Gatsinzi, T., Samuelsson, M., Zhang, M., Iverfeldt, K., & Hallberg, E. (2011). Anchored FRET sensors detect local caspase activation prior to neuronal degeneration. *Molecular neurodegeneration*, *6*(1), 35. doi:10.1186/1750-1326-6-35

28. Song, E., Cheng, D., Song, Y., Jiang, M., Yu, J., & Wang, Y. (2013). A graphene oxide-based FRET sensor for rapid and sensitive detection of matrix metalloproteinase 2 in human serum sample. *Biosensors and Bioelectronics*, *47*, 445–450. doi:10.1016/j.bios.2013.03.030

29. Geißler, D., Stufler, S., Löhmannsröben, H.-G., & Hildebrandt, N. (2013). Six-Color Time-Resolved Förster Resonance Energy Transfer for Ultrasensitive Multiplexed Biosensing. *Journal of the American Chemical Society*, *135*(3), 1102–1109. doi:10.1021/ja310317n

30. Mao, S., Benninger, R. K. P., Yan, Y., Petchprayoon, C., Jackson, D., Easley, C. J., Piston, D. W., Marriott, G. (2008). Optical lock-in detection of FRET using synthetic and genetically encoded optical switches. *Biophys J*, *94*(11), 4515–4524. doi:10.1529/biophysj.107.124859

31. Ai, H., Hazelwood, K. L., Davidson, M. W., & Campbell, R. E. (2008). Fluorescent protein FRET pairs for ratiometric imaging of dual biosensors. *Nature methods*, *5*(5), 401–403. doi:10.1038/nmeth.1207

32. Querfurth, H. W., & Laferla, F. M. (2010). Alzheimer's disease: mechanism of disease. *The New England Journal of Medicine*, *362*(4), 329–344. doi:10.1016/B978-0-12-803699-0.00045-1

33. De Kok, J. B., Verhaegh, G. W., Roelofs, R. W., Hessels, D., Kiemeney, L. A., Aalders, T. W., Swinkels, D. W., Schalken, J. A. (2002). DD3PCA3, a very

sensitive and specific marker to detect prostate tumors. *Cancer Research*, *62*(9), 2695–2698. doi:10.1016/s0022-5347(01)65160-7

34. Marks, L. S., & Bostwick, D. G. (2008). Prostate Cancer Specificity of PCA3 Gene Testing: Examples from Clinical Practice. *Reviews in urology*, *10*(3), 175–81. Retrieved from http://www.pubmedcentral.nih.gov/articlerender.fcgi?artid=2556484&tool=pmcentrez&rendertype=abstract

35. Crawford, E. D., Rove, K. O., Trabulsi, E. J., Qian, J., Drewnowska, K. P., Kaminetsky, J. C., Huisman, T. K., Bilowus, M. L., Freedman, S. J., Glover, W. L. Jr., Bostwick, D. G. (2012). Diagnostic performance of PCA3 to detect prostate cancer in men with increased prostate specific antigen: A prospective study of 1,962 cases. *Journal of Urology*, *188*(5), 1726–1731. doi:10.1016/j.juro.2012.07.023

36. Smith, A. M., & Nie, S. (2010). Semiconductor nanocrystals: Structure, properties, and band gap engineering. *Accounts of Chemical Research*, *43*(2), 190–200. doi:10.1021/ar9001069

37. Haase, M., & Schäfer, H. (2011). Upconverting nanoparticles. *Angewandte Chemie - International Edition*. doi:10.1002/anie.201005159

38. Discussion, A. (2011). Near-infrared window in biological tissue. *Cell*, 9–12.

39. Frangioni, J. V. (2003). In vivo near-infrared fluorescence imaging. *Current Opinion in Chemical Biology*. doi:10.1016/j.cbpa.2003.08.007

40. Xu, C. T., Svenmarker, P., Liu, H., Wu, X., Messing, M. E., Wallenberg, L. R., & Andersson-Engels, S. (2012). High-resolution fluorescence diffuse optical tomography developed with nonlinear upconverting nanoparticles. *ACS Nano*, *6*(6), 4788–4795. doi:10.1021/nn3015807

41. Wang, Y. F., Liu, G. Y., Sun, L. D., Xiao, J. W., Zhou, J. C., Yan, C. H., & Al, W. E. T. (2013). Nd 3 þ -Sensitized Upconversion Nanophosphors : E ffi cient In Vivo Bioimaging Probes with Minimized Heating E ff ect. *ACS Nano*, *7*(8), 7200–7206. doi:10.1021/nn402601d

42. Chen, F., Bu, W., Zhang, S., Liu, J., Fan, W., Zhou, L., Peng, W., Shi, J.

(2013). Gd3+-ion-doped upconversion nanoprobes: Relaxivity mechanism probing and sensitivity optimization. *Advanced Functional Materials*, *23*(3), 298–307. doi:10.1002/adfm.201201469

43. Jares-Erijman, E. A., & Jovin, T. M. (2003). FRET imaging. *Nature Biotechnology*, *21*(11), 1387–1395. doi:10.1038/nbt896

44. Hussain, S. A. (2009). An Introduction to Fluorescence Resonance Energy Transfer (FRET). *Energy*, *132*(6), 4. doi:10.7237/sjp/268

45. Lu, C. H., Yang, H. H., Zhu, C. L., Chen, X., & Chen, G. N. (2009). A graphene platform for sensing biomolecules. *Angewandte Chemie - International Edition*, *48*(26), 4785–4787. doi:10.1002/anie.200901479

46. Li, S., Aphale, A. N., MacWan, I. G., Patra, P. K., Gonzalez, W. G., Miksovska, J., & Leblanc, R. M. (2012). Graphene oxide as a quencher for fluorescent assay of amino acids, peptides, and proteins. *ACS Applied Materials and Interfaces*, *4*(12), 7069–7075. doi:10.1021/am302704a

47. Wu, M., Kempaiah, R., Huang, P. J. J., Maheshwari, V., & Liu, J. (2011). Adsorption and desorption of DNA on graphene oxide studied by fluorescently labeled oligonucleotides. *Langmuir*, *27*(6), 2731–2738. doi:10.1021/la1037926

48. Alonso-Cristobal, P., Vilela, P., El-Sagheer, A., Lopez-Cabarcos, E., Brown, T., Muskens, O. L., Rubio-Retama, J., Kanaras, A. G. (2015). Highly Sensitive DNA Sensor Based on Upconversion Nanoparticles and Graphene Oxide. *ACS Applied Materials & Interfaces*, *7*, 12422–12429. doi:10.1021/am507591u

49. Park, J. S., Goo, N.-I., & Kim, D.-E. (2014). Mechanism of DNA Adsorption and Desorption on Graphene Oxide. *Langmuir*, *30*(42), 12587–12595. doi:10.1021/la503401d

50. Ong, L. C., Gnanasammandhan, M. K., Nagarajan, S., & Zhang, Y. (2010). Upconversion: Road to El dorado of the fluorescence world. *Luminescence*, *25*(4), 290–293. doi:10.1002/bio.1229

51. Sun, L.-D., Dong, H., Zhang, P.-Z., & Yan, C.-H. (2015). Upconversion of rare Earth nanomaterials. *Annual review of physical chemistry*, *66*(January), 619–42. doi:10.1146/annurev-physchem-040214-121344

52. Zhang, H., Jia, T., Shang, X., Zhang, S., Sun, Z., & Qiu, J. (2016). Mechanisms of the blue emission of $NaYF_4:Tm^{3+}$ nanoparticles excited by an 800 nm continuous wave laser. *Phys. Chem. Chem. Phys.*, *18*(37), 25905–25914. doi:10.1039/C6CP04413A

53. Chen, G., Ohulchanskyy, T. Y., Kachynski, A., Ågren, H., & Prasad, P. N. (2011). Intense visible and near-infrared upconversion photoluminescence in colloidal LiYF4:Er3+ nanocrystals under excitation at 1490 nm. *ACS Nano*, *5*(6), 4981–4986. doi:10.1021/nn201083j

54. Boyer, J.-C., Cuccia, L. A., & Capobianco, J. A. (2007). Synthesis of Colloidal Upconverting NaYF4: Er3+ /Yb3+ and Tm3+ /Yb3+ Monodisperse Nanocrystals. *Nano letters*, *7*(3), 847–852. doi:10.1021/nl070235+

55. X., L. (2008). Upconversion Multicolor Fine-Tuning: Visible to Near-Infrared Emission from Lanthanide-Doped NaYF4 Nanoparticles. *J. Am. Chem. Soc.*, *130*, 5642.

56. Som, T., & Karmakar, B. (2009). Green and red fluorescence upconversion in neodymium-doped low phonon antimony glasses. *Journal of Alloys and Compounds*, *476*(1–2), 383–389. doi:10.1016/j.jallcom.2008.09.006

57. Skrzypczak, U., Seifert, G., & Schweizer, S. (2015). Highly efficient and broadband upconversion of NIR sunlight with neodymium-doped glass ceramics. *Advanced Optical Materials*, *3*(4), 541–545. doi:10.1002/adom.201400512

58. Börjesson, K., Rudquist, P., Gray, V., & Moth-Poulsen, K. (2016). Photon upconversion with directed emission. *Nature Communications*, *7*, 12689. doi:10.1038/ncomms12689

59. Zhao, J., Wu, W., Sun, J., & Guo, S. (2013). Triplet photosensitizers: from molecular design to applications. *Chem. Soc. Rev.*, *42*(12), 5323–5351. doi:10.1039/C3CS35531D

60. Jones, G. C., & Houde-Walter, S. N. (2005). Upconversion mechanisms in an erbium-doped transparent glass ceramic. *Journal of the Optical Society of America B: Optical Physics*, *22*(4), 825–830. doi:10.1364/JOSAB.22.000825

61. Sun, L. D., Wang, Y. F., & Yan, C. H. (2014). Paradigms and challenges for bioapplication of rare earth upconversion luminescent nanoparticles: Small size and tunable emission/excitation spectra. *Accounts of Chemical Research*, *47*(4), 1001–1009. doi:10.1021/ar400218t

62. Beye, M., Schreck, S., Sorgenfrei, F., Trabant, C., Pontius, N., Schüßler-Langeheine, C., Wurth, W., Föhlisch, A. (2013). Stimulated X-ray emission for materials science. *Nature*, *501*(7466), 191–194. doi:10.1038/nature12449

63. Meyers, R. A. (1995). Molecular Biology and Biotechnology: A Comprehensive Desk Reference. *Wiley-VCH*, 722.

64. Loste, E., Fanovich, M. A., Fraile, J., Woerlee, G. F., & Domingo, C. (2004). Anhydrous Supercritical Carbon Dioxide Method for the Controlled Silanization of Inorganic Nanoparticles. *Advanced Materials*, *16*(8), 739–744. doi:10.1002/adma.200306214

65. Yamaura, M., Camilo, R. L., Sampaio, L. C., Mac# Edo, M. A., Nakamura, M., & Toma, H. E. (2004). Preparation and characterization of (3-aminopropyl) triethoxysilane-coated magnetite nanoparticles. *Journal of Magnetism and Magnetic Materials*, *279*, 210–217. doi:10.1016/j.jmmm.2004.01.094

66. Angeletti, E., Canepa, C., Martinetti, G., & Venturello, P. (1988). Silica gel functionalized with amino groups as a new catalyst for Knoevenagel condensation under heterogeneous catalysis conditions. *Tetrahedron Letters*, *29*(18), 2261–2264. doi:10.1016/S0040-4039(00)86727-1

67. Kallury, K. M. R., Macdonald, P. M., & Thompson, M. (1994). Effect of Surface Water and Base Catalysis on the Silanization of Silica by (Aminopropyl)alkoxysilanes Studied by X-ray Photoelectron Spectroscopy and 13C Cross-Polarization/Magic Angle Spinning Nuclear Magnetic Resonance. *Langmuir*, *10*(2), 492–499. doi:10.1021/la00014a025

68. Dong, A., Ye, X., Chen, J., Kang, Y., Gordon, T., Kikkawa, J. M., & Murray, C.

B. (2011). A generalized ligand-exchange strategy enabling sequential surface functionalization of colloidal nanocrystals. *Journal of the American Chemical Society*, *133*(4), 998–1006. doi:10.1021/jal08948z

69. Woehrle, G. H., Brown, L. O., & Hutchison, J. E. (2005). Thiol-functionalized, 1.5-nm gold nanoparticles through ligand exchange reactions: Scope and mechanism of ligand exchange. *Journal of the American Chemical Society*, *127*(7), 2172–2183. doi:10.1021/ja0457718

70. Li, Z., Zhang, Y., & Jiang, S. (2008). Multicolor core/shell-structured upconversion fluorescent nanoparticles. *Advanced Materials*, *20*(24), 4765–4769. doi:10.1002/adma.200801056

71. Kim, K. D., & Kim, H. T. (2002). Formation of silica nanoparticles by hydrolysis of TEOS using a mixed semi-batch/batch method. *Journal of Sol-Gel Science and Technology*, *25*(3), 183–189. doi:10.1023/A:1020217105290

72. Rao, K. S., El-Hami, K., Kodaki, T., Matsushige, K., & Makino, K. (2005). A novel method for synthesis of silica nanoparticles. *Journal of Colloid and Interface Science*, *289*(1), 125–131. doi:10.1016/j.jcis.2005.02.019

73. Luechinger, M., Prins, R., & Pirngruber, G. D. (2005). Functionalization of silica surfaces with mixtures of 3-aminopropyl and methyl groups. *Microporous and Mesoporous Materials*, *85*(1–2), 111–118. doi:10.1016/j.micromeso.2005.05.031

74. An, Y., Chen, M., Xue, Q., & Liu, W. (2007). Preparation and self-assembly of carboxylic acid-functionalized silica. *Journal of Colloid and Interface Science*, *311*(2), 507–513. doi:10.1016/j.jcis.2007.02.084

75. Warner, M. G., Reed, S. M., & Hutchison, J. E. (2000). Small, water-soluble, ligand-stabilized gold nanoparticles synthesized by interfacial ligand exchange reactions. *Chemistry of Materials*, *12*(11), 3316–3320. doi:10.1021/cm0003875

76. Boal, A. K., Das, K., Gray, M., & Rotello, V. M. (2002). Monolayer Exchange Chemistry of γ-Fe 2 O 3 Nanoparticles. *Chemistry of Materials*, *14*(6), 2628–2636. doi:10.1021/cm011689p

77. Sperling, R. A., & Parak, W. J. (2010). Surface modification, functionalization and bioconjugation of colloidal inorganic nanoparticles. *Philosophical Transactions of the Royal Society of London A: Mathematical, Physical and Engineering Sciences*, *368*(1915).

78. Palui, G., Aldeek, F., Wang, W., & Mattoussi, H. (2014). Strategies for interfacing inorganic nanocrystals with biological systems based on polymer-coating. *Chemical Society reviews*, *44*, 193–227. doi:10.1039/c4cs00124a

79. Sedlmeier, A., & Gorris, H. H. (2015). Surface modification and characterization of photon-upconverting nanoparticles for bioanalytical applications. *Chemical Society Reviews*, *Advance*(2009), DOI: 10.1039/C4CS00186A. doi:10.1039/C4CS00186A

80. Gallie, D. R. (1991). The cap and poly(A) tail function synergistically to regulate mRNA translational efficiency. *Genes and Development*, *5*(11), 2108–2116. doi:10.1101/gad.5.11.2108

81. Chang, H., Lim, J., Ha, M., & Kim, V. N. (2014). TAIL-seq: Genome-wide determination of poly(A) tail length and 3' end modifications. *Molecular Cell*, *53*(6), 1044–1052. doi:10.1016/j.molcel.2014.02.007

82. Ito-Harashima, S., Kuroha, K., Tatematsu, T., & Inada, T. (2007). Translation of the poly(A) tail plays crucial roles in nonstop mRNA surveillance via translation repression and protein destabilization by proteasome in yeast. *Genes and Development*, *21*(5), 519–524. doi:10.1101/gad.1490207

83. Huang, W.-H., Sheng, R., & Hu, Y.-Z. (2009). Progress in the development of nonpeptidomimetic BACE 1 inhibitors for Alzheimer's disease. *Current medicinal chemistry*. doi:10.2174/092986709788186174

84. Zou, L., Wang, Z., Shen, L., Bao, G. B., Wang, T., Kang, J. H., & Pei, G. (2007). Receptor tyrosine kinases positively regulate BACE activity and Amyloid-beta production through enhancing BACE internalization. *Cell research*, *17*(5), 389–401. doi:10.1038/cr.2007.5

85. Vassar, R., Kovacs, D. M., Yan, R., & Wong, P. C. (2009). The -Secretase Enzyme BACE in Health and Alzheimer's Disease: Regulation, Cell Biology,

Function, and Therapeutic Potential. *Journal of Neuroscience*, *29*(41), 12787–12794. doi:10.1523/JNEUROSCI.3657-09.2009

86. Hessels, D., Klein Gunnewiek, J. M. T., Van Oort, I., Karthaus, H. F. M., Van Leenders, G. J. L., Van Balken, B., Kiemenev, L. A., Witjes, J. A., Schalken, J. A., (2003). DD3PCA3-based molecular urine analysis for the diagnosis of prostate cancer. *European Urology*, *44*(1), 8–16. doi:10.1016/S0302-2838(03)00201-X

87. Zipper, H., Brunner, H., Bernhagen, J., & Vitzthum, F. (2004). Investigations on DNA intercalation and surface binding by SYBR Green I, its structure determination and methodological implications. *Nucleic Acids Research*, *32*(12). doi:10.1093/nar/gnh101

88. Sanborn, M. E., Connolly, B. K., Gurunathan, K., & Levitus, M. (2007). Fluorescence properties and photophysics of the sulfoindocyanine Cy3 linked covalently to DNA. *Journal of Physical Chemistry B*, *111*(37), 11064–11074. doi:10.1021/jp072912u

89. Katsnelson, M. I. (2007). Graphene: carbon in two dimensions. *Materials Today*, *10*(1), 20–27. doi:10.1016/S1369-7021(06)71788-6

90. DaCosta, M. V., Doughan, S., Han, Y., & Krull, U. J. (2014). Lanthanide upconversion nanoparticles and applications in bioassays and bioimaging: A review. *Analytica Chimica Acta*, *832*, 1–33. doi:10.1016/j.aca.2014.04.030

91. Yuan, Y., & Liu, Z. (2012). An effective approach to enhanced energy-transfer efficiency from up-converting phosphors and increased assay sensitivity. *Chemical communications (Cambridge, England)*, *48*(60), 7510–2. doi:10.1039/c2cc33289b

92. Wang, Y., Bao, L., Liu, Z., & Pang, D.-W. (2011). Aptamer biosensor based on fluorescence resonance energy transfer from upconverting phosphors to carbon nanoparticles for thrombin detection in human plasma. *Analytical chemistry*, *83*(21), 8130–7. doi:10.1021/ac201631b

93. Lin, F., Yin, B., li, C., Deng, J., Fan, X., Yi, Y., Liu, C., Li, H., Zhang, Y., Yao, S. (2013). Fluorescence resonance energy transfer aptasensor for platelet-

derived growth factor detection based on upconversion nanoparticles in 30% blood serum. *Analytical Methods*, *5*(3), 699–704. doi:10.1039/C2AY25519G

94. Johnson, B. N., & Mutharasan, R. (2014). Biosensor-based microRNA detection: techniques, design, performance, and challenges. *The Analyst*, *139*(7), 1576. doi:10.1039/c3an01677c

95. Tiwari, J. N., Vij, V., Kemp, K. C., & Kim, K. S. (2016). Engineered Carbon-Nanomaterial-Based Electrochemical Sensors for Biomolecules. *ACS Nano*, *10*(1), 46–80. doi:10.1021/acsnano.5b05690

Chapter 7: Summary and Outlook

7.1. Summary

The work presented in this thesis focused on the use of nanotechnology and combinatory materials in biological applications.

In Chapter 4, the application of DNA-coated nanoparticles for the detection of Vimentin mRNA expression in both *in vitro* and *ex vivo* models was demonstrated. 13 nm were successfully synthesised using the Turkevich method. The resulting size of the gold nanoparticles presented in this work was in accordance with previous results presented by groups such as Mirkin *et al.* [1, 2], Tang *et al.* [3, 4] and Parak *et al.* [5, 6], were the average size of AuNPs used for bio-applications was between 12 and 14 nm. Consequently, the resulting absorption spectrum of the AuNPs presented in this thesis was similar to many other gold nanoparticles used in biomedical applications, with works such as Dulkeith *et al.* (2004) [7], Lee *et al.* (2005) [8] and Jain *et al.* (2006) [9] all pointing to a characteristic plasmon resonance absorption peak at approximately 520-523 nm for 13 nm sized gold nanoparticles.

The conjugation of labelled oligonucleotides was also successfully achieved taking advantage of the thiol termination groups present in the oligonucleotide sequences. This conjugation was confirmed by a multitude of characterization techniques, from a clear separation of the nanoparticles (TEM) to shifts in both the overall net charge (observed from ζ-potential results) and the absorption peak (observed from UV-Vis spectroscopy). The decrease of the overall net charge observed by ζ-potential is originated from the presence of oligonucleotides because, as discussed in detail in reviews by Giljohann *et al.* (2010) and Ding *et al.* (2014) [10, 11], the phosphate backbone of the DNA strands provides a negative shell around the gold core. This induces the overall net charge to be more negative than the non-conjugated gold nanoparticles.

At the same time, UV-Vis spectroscopy results seem to show that the presence of DNA attached to gold nanoparticles increase the hydrodynamic radii of the final conjugated nanoparticles. This is in accordance with recent literature, where works conducted by Xu *et al.* (2007) [12] and Zimbone *et al.* (2014) [13] have shown that

the presence of DNA strands conjugated to gold nanoparticles directly affects the resulting maximum absorption and their overall interaction with light. Therefore, AuNPs conjugated with DNA have an apparent increased sized when measured by techniques such as dynamic light scattering or UV-Vis spectroscopy, which consequently leads to a slight blue-shift on the absorption spectrum.

Finally, fluorescence spectroscopy confirmed the quenching ability of the gold core for the Cy3 and Cy5 tagged oligonucleotide sequences. Reviews done by Dulkeith *et al.* (2002) [14] and by Swierczweska *et al.* (2011) [15] discuss in detail that this type of quenching occurs due to the overlapping of the emission spectra of the fluorescence dyes and the absorption spectrum of the gold core. More specifically, work conducted by Reineck *et al.* (2013) demonstrated that the photons emitted by the fluorescent dyes interact with the LSPR band of AuNPs, leading to an electronic energy transfer from one to the other and a consequent total blockage of fluorescence (i.e. quenching). Therefore, the results presented in this thesis seem to fall in to this type of quenching mechanism. Additionally, by using a calibration curve for both Cy3 (570 nm) and Cy5 (662 nm) it was possible to calculate the average number of both sense and flare strands per particle (97 ± 2 and 47 ± 2 strands/particle, respectively).

The coverage obtained for the sense strand (i.e. the strands that are attached to the gold surface *via* gold-sulfur chemistry) is in accordance with multiple reports focused on the maximum density of oligonucleotide coverage of AuNPs. In fact, studies such as Hurst *et al.* (2006) [16] and Zhao *et al*. (2009) [17] demonstrated that it is possible to obtain a maximum of approximately 160 – 200 strands/particle coverage, which is almost double the one obtained in the work reported in Chapter 4. However, in the same study Hurst *et al.* (2006) discussed the possibility that at an average of approximately 120 strands/particle, the DNA shell around the gold core surface becomes so dense that the highly negative repulsive forces of the resulting shell might render the individual strands inaccessible. This hypothesis was later confirmed by Wong *et al.* (2010) were an electrostatic model for optimization of DNA coverage of gold surfaces was presented. [18] In this report, it was shown that at low DNA densities ($< 10^{13}$ DNA strands per cm^2), the negative electrostatic effect of the phosphate backbone are screened, resulting in faster and more complete hybridization events. However, at higher DNA densities, the hybridization

kinetics are slowed and the surface becomes over-crowded, leading to any attempt for strand hybridization extremely difficult. Furthermore, when it comes to the number of sense strands, multiple studies from Mirkin and co-workers demonstrated that there is an optimal range of flare hybridization at a ratio of 2:1 sense/flare strands in order to achieve a maximum detection of the target mRNA. [19–21] Similarly to the effect mentioned above for the hybridization of the two strands, if the DNA shell around the gold core is too densely packed, the target mRNA cannot interact with the sense strand due to highly negative repulsive forces present and, consequently, cannot displace the flare strand in order to induce a fluorescence signal. Therefore, the coverage of the gold core obtained in the work presented in this thesis was deemed optimal for imaging applications.

In terms of stability, AuNP-DNA conjugates shown in this thesis were demonstrated to be stable at body mimicking temperatures (37 ºC).. Previous work conducted by Li *et al.* (2013) [22] discussed the influence of temperature in thiol-conjugated DNA strands onto gold nanoparticles. In this study, it was shown that at body mimicking temperatures, DNA attached to nanoparticles *via* thiol conjugation were stable when compared to higher temperatures (85 ºC), supporting the observations done in the work here presented.

Furthermore, our AuNP-DNA conjugates were also stable in cell culture media, as seen by the fluorescence profile results. It was important to investigate the potential influence of a protein corona on AuNP-DNA conjugates' stability since previous reports have discussed its interference with different aspects of the probing process. For example, Singh *et al.* (2003) [23] showed that the presence of serum proteins decreased the release of DNA strands due to a partially blocking of the strands attached to the gold nanoparticle. However, Zagorovsky *et al.* (2016) [24] showed that this blocking can be counteracted with a higher DNA shell density. In this study it was shown that nanoparticles with an average density above 80 strands/particle withstand the formation of a blocking protein corona and remain accessible to enzymatic activity. In addition, this study showed that double stranded DNA shells around gold nanoparticles are more efficient at avoiding the formation of protein coronas that would render the probe inaccessible to its target. Finally, studies such as the ones conducted by Mahmoudi *et al.* (2014) [25] and Tenzer *et al.* (2013) [26] demonstrated that the formation of a thick protein corona can lead to

aggregation of gold nanoparticle based probes, as well as a consequent loss of function. However, other studies, such as Mirshafiee *et al.* (2013) [27] and Treuel *et al.* (2014) [28] showed that the presence and nature of the protein corona has a significant impact on the uptake of gold nanoparticles, independently of the ligands and/or conjugates that are below the protein corona layer.

This means that, even though avoiding the formation of a thick protein corona is important, its presence is still relevant since it can change the cellular uptake of the probes. Knowing this, it is possible to estimate that the coverage of our conjugates (approximately 100 strands per particle) falls into an optimal window of partial protection from a total targeting blocking while retaining some protein corona formation in order not to impact the uptake of the conjugates. However, more detailed studies need to be done in order to fully assess the total impact of the protein corona effect in our probes, as well as how different proteins can impact their probing power.

With regards to intracellular degradation, the AuNP-DNA conjugates showed to be stable in the presence of GSH, DNAseI and DNAseII. Gluthathione (GSH) has been presented as a model for any potential thiol-displacement events [29, 30] , with studies such as Li *et al.* (2002) [31] and Tsai *et al.* (2012) [32] demonstrating that the presence of a thiol displacement agent resulting in a loss of target specificity from nanoparticle-based probes. However, our probes were stable even at high concentration of GSH, being in accordance with works such as Kudelski *et al.* (2003) [33] , Marin *et al.* (2008) [34] and Hakkinen *et al.* (2012) [35], all of which point to thiol-stabilization as one of the best strategies for the design of AuNP-based probes.

Additionally, investigating the potential degradation by DNAseI and DNAse II enzymes was of interest, since both enzymes have been suggested by recent literature to be a potential barrier for the use of AuNP-DNA conjugates for cellular imaging. Li *et al.* (2012) demonstrated that DNAseI could not access the strands attached to gold nanoparticles, thus rendering its enzymatic activity null. [4] The results obtained for our probes demonstrated the same effect meaning that AuNP-DNA conjugates are relatively stable against DNAseI degradation. However, Wu *et al.* (2014) discussed the possibility that DNAseII could indeed induce degradation of double stranded DNA covered quantum dots. [36] However, work previously

conducted by our group demonstrated not only that AuNP-DNA conjugates were stable in the presence of both enzymes but also that the probes kept their specificity across different cells lines [37]. We hypothesise that the incorporation of a dye in the end of the sense strand (not seen in other studies) might reduce the access of DNAseII enzymes to the DNA shell around the gold core. However, further studies need to be conducted in order to fully understand the mechanisms behind this observed stability.

The AuNP-DNA conjugates described in Chapter 4 also demonstrated to have a fluorescent signal highly specific to the presence of the Vimentin mRNA target, even distinguishing between sequences with only 1 or 2 bases of mismatch. This high specificity has been shown previously not only by our group [37], but also for other targets, such as single cancer biomarkers (e.g. BRCA1 [38] or BCR-ABL [39]), or even a triple detection of c-myc, TK1 and GalNac-T mRNA targets [4].

Most of the stability and specificity properties of the probes presented in this thesis were in accordance with previous studies from different groups (including ours), and can lead to the design of imaging probes that avoid drawbacks such as low-detection limits or false-positive imaging.

Upon the applications of these AuNP-DNA conjugates in cells, it was shown that the conjugates could successfully distinguish between cells that naturally expressed Vimentin (confluent fibroblasts) and low-expressing Vimentin cells (confluent epithelial), in accordance with results shown previously by our group [37]. The fluorescence resultant of the release of the flare strand in the presence of Vimentin mRNA was localized in the same focal plane of the nucleus. Further testing of the probes in wound mimicking conditions (scratch assay) demonstrated that the variation of Vimentin mRNA expression could be detected when cells were forced to migrate. This correlates with results shown in previous reports [40–42], that point to Vimentin having a central role in the epithelial-to-mesenchymal transition (EMT) process by promoting cell migration and decreasing cell adhesion. In epithelial cells specifically, the difference of the fluorescence signal in the wound edges was significantly higher (approximately 1000x) than in areas away from the scratched region. These results were shown to be comparable with outcomes obtained through qPCR analysis of Vimentin mRNA expression.

Finally, Vimentin mRNA nano-probes demonstrated to be non-toxic to the cells used in this study. Reports such as Lewinski *et al.* (2008) [43] extensively reviewed the toxicity effects that were found for gold nanoparticles across different cell lines and point to AuNPs covered with anionic agents (such as DNA) being non-toxic across different studies. In fact, more recently Soenen *et al.* (2012) showed that even smaller gold nanoparticles (4 nm) have no significant toxic effect in cells when used in concentrations lower than 10 nM, agreeing with a study conducted by Massich *et al.* (2010) [44] were HeLa cells were incubated with AuNPs covered with different agents and only demonstrated significant toxic reactions to citrate covered particles, with DNA covered gold nanoparticles being one of the most mild types of probes with regards to toxicity. All these studies seem to indicate that, at the concentrations used for the work presented in this thesis, the observed non-toxic effect of our AuNP-DNA conjugates is to be expected.

Afterwards, the Vimentin mRNA nano-probes were applied to *ex vivo* skin samples in order to test their performance in the detection of mRNA in more complex models. The nano-probes successfully detected the presence of Vimentin mRNA in areas closer to the wounded regions of the skin samples. Utilizing the nano-probe ability to detect Vimentin mRNA in skin, three-dimensional maps of fluorescence were obtained using light sheet microscopy. It was possible to observe a time-lapse expression of Vimentin mRNA over 6h using this type of 3D mapping. Furthermore, the detection was distinguishably visible at the 2h mark, demonstrating that this type of nano-probe has the potential to also be used for early detection of mRNA in *ex vivo* samples.

These results, combined with the imaging of Vimentin mRNA in cells and two-dimensional wound models (scratch assay and *ex vivo* skin samples), demonstrated that these type of DNA-AuNP conjugates were successfully designed and are useful tools for multiplexed bio-imaging (Figure 7.1.).

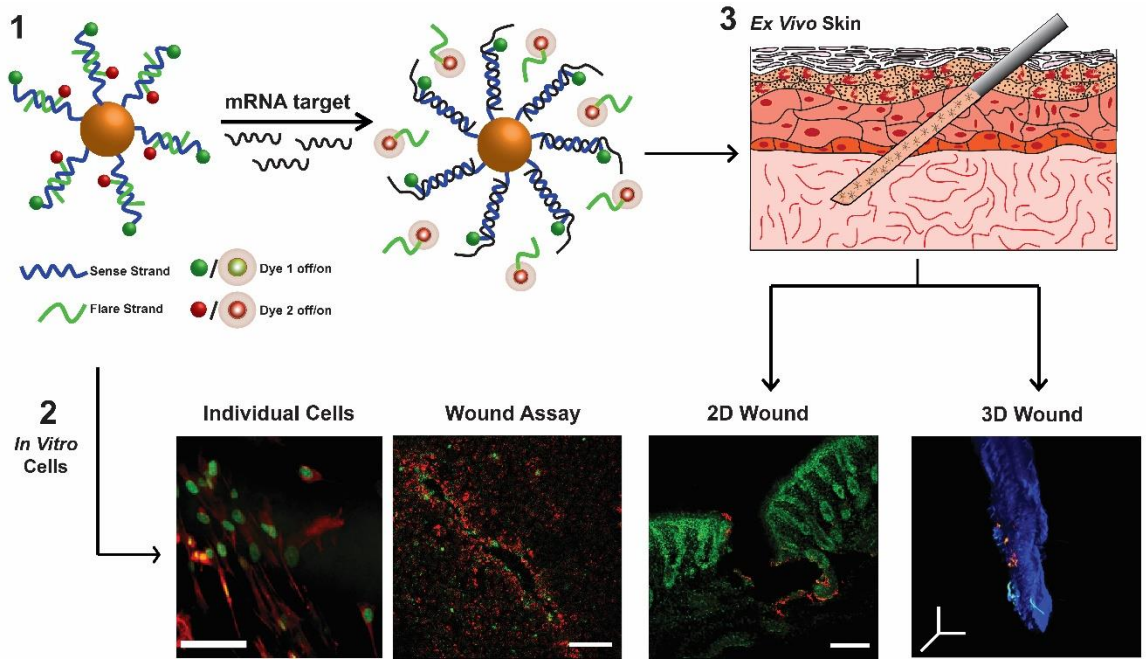

Figure 7.1. Summary of imaging results from Chapter 4

Taking advantage of the successful imaging results of Chapter 4, a siRNA-AuNP conjugate was also developed in order to test the capability of this type of hybrid material in gene knockdown applications (as shown in Chapter 5). The pathway of choice was SMAD3/TGF-β due to its importance in the wound healing process [45, 46].

Characterization of the SMAD3 silencing probes showed similar results as seen in the AuNP-DNA conjugates described in Chapter 4. This demonstrates that, not only AuNP-siRNA conjugates were successfully synthesised (as seen from spectroscopic, ζ-potential and gel electrophoresis results) but also that siRNA strands provide the same type of stability seen with AuNP-DNA conjugates in different conditions (temperature, enzyme degradation, etc.). The same stability was partially observed by Kim *et al.* (2014) [47] and Barnaby *et al.* (2014) [48], were siRNA-covered nanoparticles were found to be stable in different conditions. However, the latter study demonstrated that enzymatic degradation might still be a key factor when it comes to conjugating siRNA to gold nanoparticles, suggesting that the use of stabilizing agents (such as thiol-PEG) can contribute to the design of a more stable silencing probe. These results contradict the findings presented in this thesis. However, the enzymes used for the work here presented differ from the ones

presented by Barnaby *et al.* (2014), where the researchers focused more on RNAse-catalysed hydrolysis reactions. It is possible that PEGylated siRNA-AuNPs could present a higher degree of stability upon the presence of specific types of enzymes. Therefore, further research is necessary in order to evaluate the full extension of the stability of siRNA-AuNP probes in the presence of different enzymatic reactions.

The average number of siRNA complexes achieved in the coverage of AuNPs was significantly lower (48 ± 3 duplexes/particle) when compared with the coverage achieved with DNA sense strands (97 ± 2 strands/particle). As showed by Hurst *et al.* (2006) [16] and Wong *et al.* (2012) [18], the coverage density of a nanoparticle surface using oligonucleotides is strongly dependent on its spatial configuration. Hill *et al.* (2009) [49] demonstrated that the spatial footprint of individual strands highly affect the loading of oligonucleotides onto the surface of gold nanoparticles. In general, individual strands have a smaller spatial footprint than double strands and, consequently, more oligonucleotide strands can be fitted when theyare in a single strand form. Moreover, we hypothesise that double strands have negatively charged phosphate backbones pointed in multiple directions, meaning that due to electrostatic hindrance between duplexes, packing the same number of strands while using double stranded sequences is more difficult. However, specialised reports silencing, such as the ones conducted by Gregory *et al.* (2005) [50] and Leuschner *et al.* (2006) [51] suggested that, due to the nature of the RISC pathway, a double stranded siRNA is necessary in order to promote its spatial interaction with the Dicer protein and consequently trigger the silencing process. Therefore, single stranded siRNA coverage of AuNPs are possibly ineffective for silencing applications that rely on the RISC pathway. Thus, even though the coverage of the gold core using siRNA duplexes was smaller when compared with the DNA-AuNP imaging conjugates, the compromise of obtaining a smaller coverage by getting a more targeted silencing was deemed as an acceptable option for the fabrication of the final siRNA-AuNP conjugates.

In terms of toxicity, results show that SMAD3 targeted AuNP-siRNA conjugates at high concentrations (50 nM) induce a toxic effect in cells. Previously reported studies demonstrated that high concentrations of silencing probes can induce a negative cell response and lead to cell apoptosis. [52–54] Additionally, reports such as Tkachenko *et al.* (2004) and Shukla *et al.* (2005) demonstrated that gold

nanoparticles on their own at such high concentrations (>50 mM) demonstrate toxic effects in cells such as macrophages and dermal fibroblasts respectively. This suggests that the SMAD3 AuNP-siRNA conjugates at high concentrations of 50 nM might have triggered a similar type of reaction from the exposed cells. However, studies conducted by Reynolds *et al.* (2012) [55] and by Conde *et al.* (2013) [56] showed that AuNP-based silencing agents at lower concentrations (<20 nM) demonstrated no toxic effect in human macrophages and human colorectal carcinoma cells respectively. These results suggest that the concentration deemed optimal for experimental use in this work (10 nM), despite its small toxic effect, falls inside the optimal concentration window reported for gene knockdown applications.

Upon exposing cells to SMAD3 silencing probes, not only a reduction of SMAD3 protein levels was observed (as seen from immunofluorescence, in cell western and western blot results) but also a reduction of mRNA levels for SMAD3 and consequently TGF-β were observed. These results point to a knockdown effect of SMAD3 and might indicate a downstream silencing effect on the mRNA levels of TGF-β . These results are in agreement with literature study conducted by Yeom *et al.* (2005), were direct silencing of SMAD3 was observed to have a knockdown impact on the levels of TGF-β mRNA levels. [57] Furthermore, MEF cells treated with SMAD3 AuNP-siRNA demonstrated a retardation in migration when compared with other control cells. These results point to an effect of SMAD3 knockdown in cell mobility and agrees with the results presented by studies such as the one reported by Ungefroren *et al.* (2011) [58]. However, the full extension of the impact of our silencing probes in the SMAD3 pathway and, consequently, on cell mobility can only be revealed with further studies on different cells lines and using other types of migration assays.

When applied *in vivo*, AuNP-siRNA conjugates, initial results point to these conjugates having an impact on the velocity of wound closure. Wounds treated with the SMAD3 AuNP-siRNA conjugates demonstrated a statistically significant retardation of wound closure when compared with wounds treated with control conjugates. This effect was only seen between days 2 and 7. Interestingly, Broughton *et al.* (2009) showed that the critical point of the wound healing process falls into the first 2-3 days [59]. The retarded effect of our silencing AuNP-siRNA probes reflect the uncontrollable nature of dermal application of nanoparticles. As

shown by Sykes *et al.* (2014) [60], nanoparticle agents that are dermally injected can have different ways of interacting with the skin, either being uptaken by immune cells or by ending up in the blood stream and missing the intended target. The preliminary results reported in this thesis point to an effective but non-specific delivery of the silencing agent. Therefore, further investigation must be conducted using different methods of delivery in order to conclusively observe the full extension of the silencing potential of our AuNP-siRNA probes.

Histology results further marked the possibility of a reduction in scarring when wounds were treated with SMAD3 silencing probes, with scarred areas being apparently reduced in both size and percentage of granular tissue and with presence of collagen being higher. Previous studies have demonstrated that partly silencing TGF-β production in specific pathways (e.g. COL1A1 [61] or even TGF-β directly [62]) can lead to reduction of collagen-III production and an increase of collagen-I production and, consequently, to a reduction in scarring. Furthermore, Gilbert *et al.* (2016) demonstrated that silencing of SMAD2/3 dimerization can indeed have an impact in wound healing. [63] Therefore, it is hypothesized that, by having an apparent downstream reduction of the levels of TGF-β mRNA, the AuNP-siRNA probes used in this work might have a positive effect on the reduction of scarring in skin tissue. However, more comprehensive studies need to be conducted in order to fully understand the mechanism behind the observed results.

However, both the wound analysis and the histological results should be taken with some criticism. An incomplete experimental design let to a lack of information on the full extention of the effects of the SMAD3 silencing probes *in vivo*. Firstly, the imaging of the wounded animals was poorly executed due to both an improper choice of imaging device and a wrong execution of the imaging (e.g. lack of reference chart for wound categorisation and analysis). This lead to some variations in the measurement of the wounded area, which compromises the integrity of the wound analysis. Secondly, the histological analysis was incomplete. Due to the variation of the staining method (Movat's pentachrome staining), the resulting histology images were sometimes not completely clear on the location of the scar area. For future experiments, complementary immunohistology analysis should be conducted in order to provide a more complete picture on the ratio of elastic fibres and, consequently, fully assess the effect of these silencing probes on the wound

closure process. And finally, in hindsight, the controls chosen for the *in vivo* experiments were not adequate. The aim was to provide a complete picture on non-specific effects that both the particles and non-targeted siRNA sequences could have on the wounding process. However, tackling two variables at once proved to be misleading in the final analysis. Therefore, for future *in vivo* studies using this type of AuNP-siRNA conjugates, controls consisting of only siRNA duplexes (both scramble and specific for targeted silencing), only gold nanoparticles and untreated wounds should be included to provide more complete and thorough experimental results. Overall, the results showed in Chapter 5 showed a preliminary set of experiments to test the silencing potential of AuNP-siRNA probes targeted to SMAD3.Despite providing an incomplete set of conclusions, these preliminary results demonstrate the potential of AuNP-siRNA conjugates as silencing tools and their consequent potential impact on wound healing process both in cells and *in vivo* models through the TGF-β pathway (Figure 7.2.).

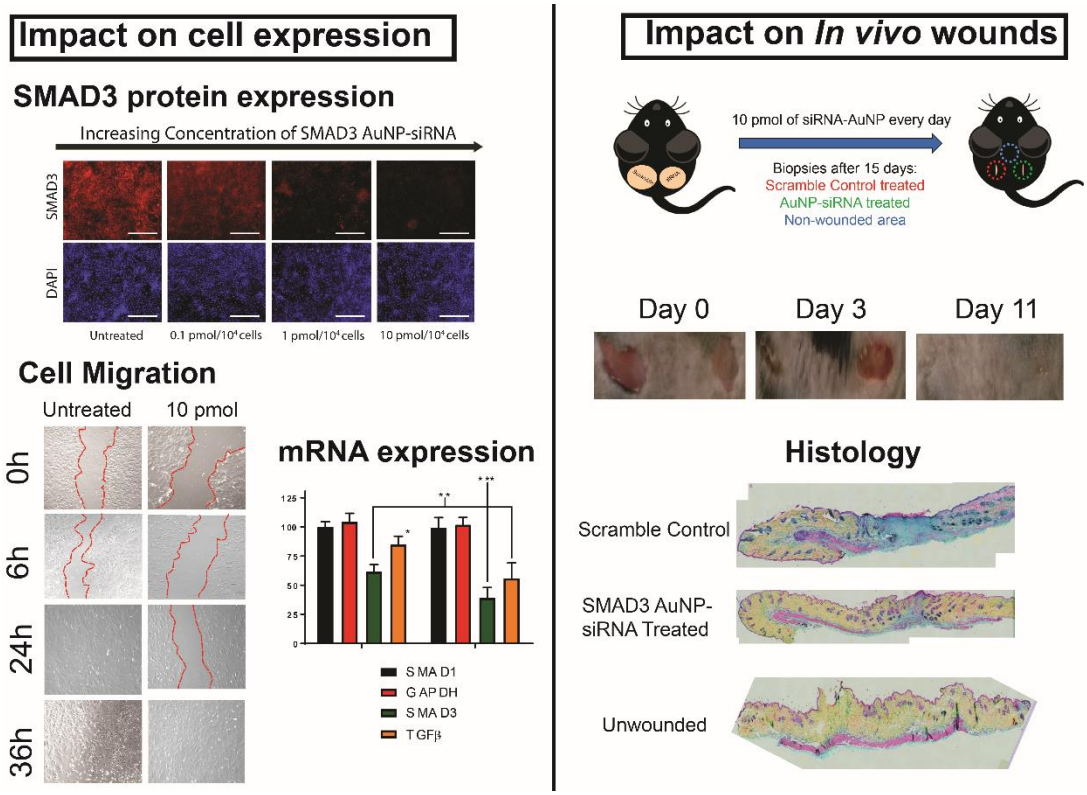

Figure 7.2. Summary of silencing results from Chapter 5

Finally, Chapter 6 demonstrated the successful development of a graphene oxide-UCNP FRET sensor for the detection of mRNA biomarkers. The upconversion electron donor was fully characterized and found to be in conformity with similarly

reported UCNPs based on the same combination of host matrix and antenna/emitter pair [64, 65]. For the development of the sensor described in this thesis, two different emitters were tested: erbium (Er) and thulium (Tm). The excitation wavelength of both is the same (980 nm) and the maxima emission wavelength is at 545 nm for Er and 800 nm for Tm. Further analysis of the emission spectra of both types of particles demonstrated that Er-dopped nanoparticles are more efficient in the upconversion process. These results are in accordance with reports such as Yi *et al.* (2006) [66] and Rivera *et al.* (2014) [67] were erbium was found to be more efficient emitter when compared with thulium. Therefore, Er-dopped UCNPs were chosen as the electron donors for the development of the sensor.

By testing two different phase transfer methods (PAA vs silanization), it was found that both had advantages and disadvantages. While a silica shell provides stability for a longer period of time when compared with other coating methods, as shown by Ge *et al.* (2008) [68] and by Lv *et al.* (2017) [69], and allows for the functionalization of the nanoparticles in more varied ways based on silano-based functionalization [70], this methods was found to be lengthy and its delicate optimization is dependent on different variants such as reagents concentration, time of reaction and solvent of choice [71, 72]. Oppositely, ligand exchange with PAA has been shown by studies such as Wisniewska *et al.* (2014) [73] to have lower stability than alternative methods. However, due to its high content of carboxylic groups, the presence of PAA unlocks the use a straightforward type of coupling chemistry (EDC/sulfo-NHS) which has been shown both by our group [74] and by other researchers [75, 76] to be an useful tool for conjugation of biological molecules onto the surface of nanoparticles. Additionally, for the main goals of the work described in this chapter, the speed of the whole phase transfer method (1 day for PAA ligand exchange vs 4 days for silanization) favoured the use of ligand exchange for the final stages of the sensor development.

After optimization of the GO and UCNPs concentrations to be used, the sensor was tested for a broader type of application: the detection of poly-A tails present in mature mRNAs[77]. Using a robust type of detection method (fluorescence spectroscopy), our results showed that the sensor could significantly detect its target sequence up to a concentration of 100 pM. This demonstrated a detection limit comparable to similar sensor reported in recent literature [78, 79]. However, another

main goal of this work was to lower the limit of detection (LOD) of this type of UCNP-DNA-GO sensor. For that, a home-made setup was used where a single photon detector was used as a detection platform. By focusing on the wavelength of highest output reported for Er UCNPs (545 nm), it was possible to lower the detection limit of the sensor from 100 pM (fluorescence spectroscopy) to 200 fM (photon counter) for the detection of poly-A sequences. Even though other group reported comparatively low detection limits for similar types of systems [81–83], this type of detection is one of the lowest overall reported for UCNP-based sensors.

Taking advantage of the high sensitivity capacity of the sensor, two targets of specific diseases were chosen to test its performance for the detection of biomarkers: BACE-1 for Alzheimer's disease and PCA3 for prostate cancer. Experimental sensing of both BACE-1 and PCA3 was significantly achieved at concentrations as low as 500 fM. Furthermore, after extrapolating equations for the fitted curves from the obtained data points, the theoretical LOD was calculated to be at 8.67 fM and 7.56 fM for PCA3 and BACE-1, respectively. This type of sensitive detection (both experimental and theoretical) was found to be one of the lowest for bio-sensing of mRNA biomarkers in recently reported literature [84].

Finally, the sensor was tested in two different biological environments: blood plasma (to mimic blood analysis conditions) and cell lysate (to mimic biopsy analysis conditions). The sensor successfully detected both biomarkers in the different environments that it was exposed to, demonstrating its potential for the sensing of biomarkers. Overall, the sensor could significantly detect the presence of specific biomarkers in low concentrations, even in the presence of complex biological environments (Figure 7.3.)

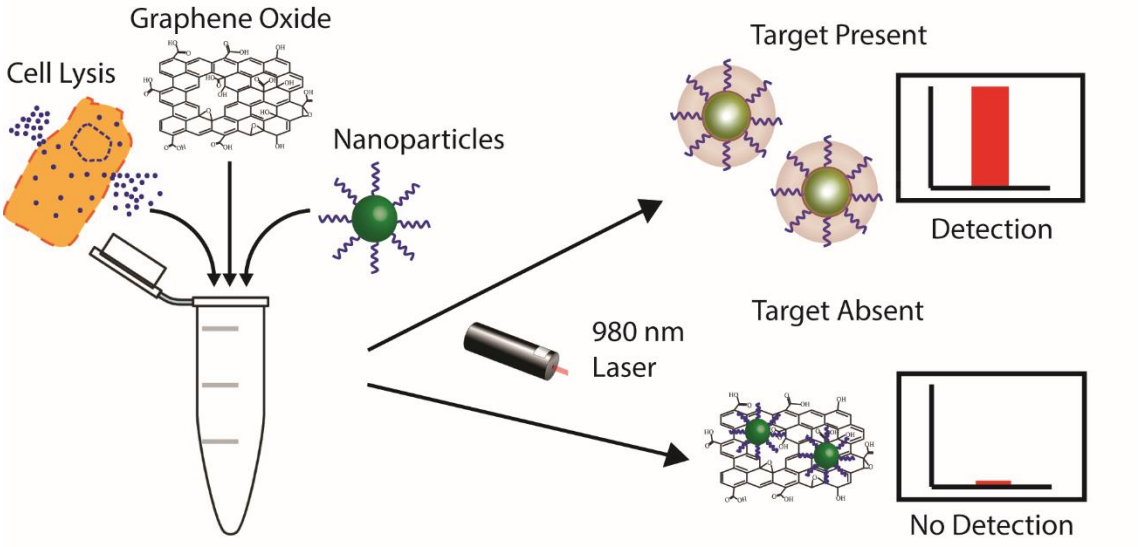

Figure 7.3. Summary of the working principle of the UCNP-DNA-GO sensor of Chapter 6

7.2. Outlook

All the work described in this thesis is a display of how interdisciplinary interplay between different areas such as nanotechnology, biology and imaging can achieve different solutions for problems that have been described previously.

For example, the use of DNA-AuNP conjugates for imaging demonstrated that was possible to map three-dimensionally the presence of Vimentin mRNA in wounded tissue. Similar studies have shown that 3D image rendering of tissue can provide useful information about protein interactions [85], cellular dynamics [86, 87] and biological processes as a whole. Therefore, the application of this type of imaging tool for the detection and visualization of different mRNA targets of wound healing can help in gathering deeper information on the whole process. Moreover, the use of DNA as a detection platform provides this type of imaging tool to a versatility unmatched by few other reported tools. Therefore, this type of conjugate can be target for the detection of other mRNA targets or even other biomolecules in order to help understanding underlying mechanisms of more complex biological events and processes.

Taking this type of oligonucleotide-AuNP conjugates a step further, using siRNA for the knockdown of SMAD3, preliminary tests pointed to this type of oligonucleotide-gold nanoparticle probes having a potentially successful application in *in vitro* and *in vivo* models. The results obtained are demonstrative of the silencing capability of this type of conjugates. However, more extensive and carefully planned research on the use of these probes for *in vivo* models (e.g. increasing the groups of animals and the number of control groups, expanding the imaging for live animals and modulating the toxicity of siRNA-AuNP probes in different organs), as well as more directed work in multiple target knockdown still needs to be conducted in order to achieve more conclusive experiments in order to unveil the full potential of siRNA-AuNP as silencing tools.

Results for both imaging and silencing experiments demonstrated that the versatility of DNA, combined with the chemical and optical properties of gold nanoparticles, can present itself as an alternative method for this type of applications. The conjugates here described have the potential to help reducing common drawbacks (e.g. control of dosage, unspecific drug release, probability of false positives, etc.) presented by other well studied silencing vectors or imaging probes. Additional work can be directed in combining both the imaging and the silencing capability of oligonucleotide-gold nanoparticle conjugates for the development of multipurpose theranostics probes (Figure 7.4.)

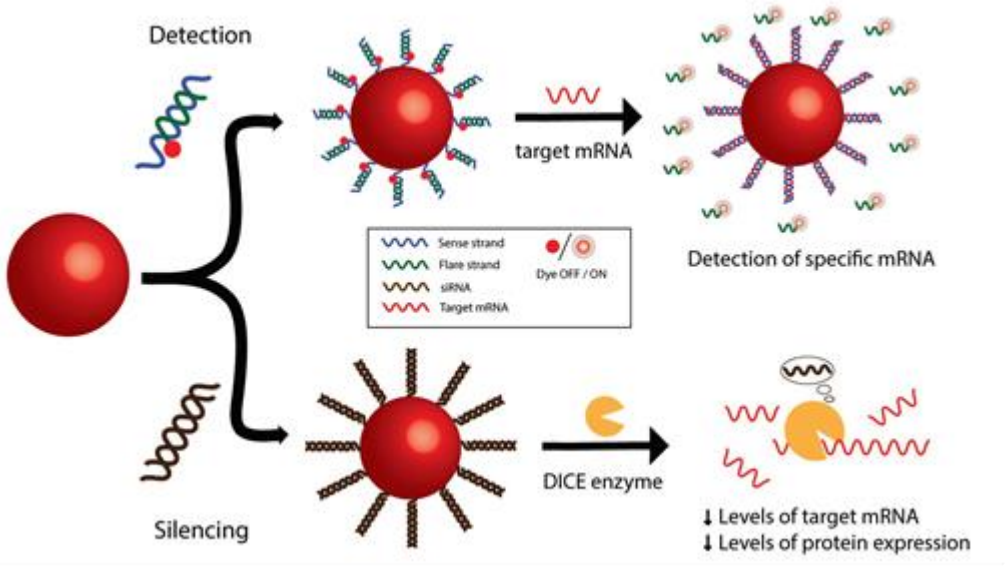

Figure 7.4. Combination of both imaging and silencing capabilities of AuNP-oligonucleotide conjugates

Finally, the development of a UCNP-GO sensor demonstrated that it is possible to use hybrid materials for the sensitive detection of low concentrations of mRNA biomarkers relevant for specific diseases (with the demonstrated limit of detection being on the femtomolar range). Additionally, the successful use of this type of sensor in complex biological media demonstrated that the system has the potential to be used in clinical studies. Future research should focus on the detection of mRNA biomarkers in patients suffering from one of the described diseases to study the full potential of this UCNP-DNA-GO sensor in early detection of conditions such as prostate cancer. Furthermore, due to the versatility of functionalization of the upconversion particles described in this thesis, future studies can also focus on the development of UCNP-GO sensors targeting other types of biomarkers (such as proteins or miRNAs).

In summary, the work presented in this thesis demonstrates the versatility and adaptability of hybrid materials in bio-sensing, imaging and therapeutic applications. The use of nanotechnology here described brings a new perspective on the understanding and treatment of wound healing and on the detection of biomarkers for early diagnostics of disease. Over time, hybrid materials will hopefully be fundamental tools for biological and medical areas, in a research world that is growing evermore interdisciplinary.

7.3. References

1. Chinen, A. B., Guan, C. M., & Mirkin, C. A. (2015). Spherical nucleic acid nanoparticle conjugates enhance G-quadruplex formation and increase serum protein interactions. *Angewandte Chemie - International Edition*, *54*(2), 527–531. doi:10.1002/anie.201409211

2. Cutler, J. I., Zhang, K., Zheng, D., Auyeung, E., Prigodich, A. E., & Mirkin, C. A. (2011). Polyvalent nucleic acid nanostructures. *Journal of the American Chemical Society*, *133*(24), 9254–9257. doi:10.1021/ja203375n

3. Pan, W., Li, Y., Wang, M., Yang, H., Li, N., Tang, B. (2016). FRET-based nanoprobes for simultaneous monitoring of multiple mRNAs in living cells using single wavelength excitation. *Chemistry Communications*, *52*(24), 4569–4572. doi:10.1039/C5CC10147F

4. Li, N., Chang, C., Pan, W., & Tang, B. (2012). A Multicolor Nanoprobe for Detection and Imaging of Tumor-Related mRNAs in Living Cells. *Angewandte Chemie International Edition*, *51*(30), 7426–7430. doi:10.1002/anie.201203767

5. Pellegrino, T., Sperling, R. A., Alivisatos, A. P., & Parak, W. J. (2007). Gel Electrophoresis of Gold-DNA Nanoconjugates, *Journal of Biomedicine and Biotechnology,* Vol. 2007. doi:10.1155/2007/

6. Yu, X., Lei, D. Y., Amin, F., Hartmann, R., Acuna, G. P., Guerrero-Martínez, A., Maier, S. A., Tinnefeld, P., Carregal-Romero, S., Parak, W. J. (2013). Distance control in-between plasmonic nanoparticles via biological and polymeric spacers. *Nano Today*, *8*(5), 480–493. doi:10.1016/j.nantod.2013.09.001

7. Dulkeith, E., Niedereichholz, T., Klar, T. A., Feldmann, J., Von Plessen, G., Gittins, D. I., Mayya, K. S., Caruso, F. (2004). Plasmon emission in photoexcited gold nanoparticles. *Physical Review B - Condensed Matter and Materials Physics*, *70*(20). doi:10.1103/PhysRevB.70.205424

8. Lee, K. S., & El-Sayed, M. A. (2005). Dependence of the enhanced optical scattering efficiency relative to that of absorption for gold metal nanorods on aspect ratio, size, end-cap shape, and medium refractive index. *Journal of Physical Chemistry B*, *109*(43), 20331–20338. doi:10.1021/jp054385p

9. Jain, P. K., Lee, K. S., El-Sayed, I. H., & El-Sayed, M. A. (2006). Calculated Absorption and Scattering Properties of Gold Nanoparticles of Different Size, Shape, and Composition: Applications in Biological Imaging and Biomedicine. *The Journal of Physical Chemistry B*, *110*(14), 7238–7248. doi:10.1021/jp057170o

10. Giljohann, D. A., Seferos, D. S., Daniel, W. L., Massich, M. D., Patel, P. C., & Mirkin, C. A. (2010). Gold nanoparticles for biology and medicine. *Angewandte Chemie - International Edition*. doi:10.1002/anie.200904359

11. Ding, Y., Jiang, Z., Saha, K., Kim, C. S., Kim, S. T., Landis, R. F., & Rotello, V. M. (2014). Gold nanoparticles for nucleic acid delivery. *Molecular therapy : the journal of the American Society of Gene Therapy*, *22*(6), 1075–83. doi:10.1038/mt.2014.30

12. Xu, J., & Craig, S. L. (2007). Influence of the extent of hybridization on the hydrodynamic radius of DNA-functionalized gold nanoparticles. *Langmuir*, *23*(4), 2015–2020. doi:10.1021/la0622830

13. Zimbone, M., Baeri, P., Calcagno, L., Musumeci, P., Contino, A., Barcellona, M. L., & Bonaventura, G. (2014). Dynamic light scattering on bioconjugated laser generated gold nanoparticles. *PLoS ONE*, *9*(3). doi:10.1371/journal.pone.0089048

14. Dulkeith, E., Morteani, a C., Niedereichholz, T., Klar, T. A., Feldmann, J., Levi, S. A., van Veggle, F. C., Reinhoudt, D. N., Gittins, D. I. (2002). Fluorescence quenching of dye molecules near gold nanoparticles: radiative and nonradiative effects. *Physical Review Letters*, *89*(20), 203002. doi:10.1103/PhysRevLett.89.203002

15. Swierczewska, M., Lee, S., & Chen, X. (2011). The design and application of fluorophore–gold nanoparticle activatable probes. *Physical Chemistry Chemical Physics*, *13*(21), 9929. doi:10.1039/c0cp02967j

16. Hurst, S. J., Lytton-Jean, A. K. R., & Mirkin, C. A. (2006). Maximizing DNA loading on a range of gold nanoparticle sizes. *Analytical Chemistry*, *78*(24), 8313–8318. doi:10.1021/ac0613582

17. Zhao, W., Lin, L., & Hsing, I. M. (2009). Rapid synthesis of DNA-functionalized gold nanoparticles in salt solution using mononucleotide-mediated conjugation. *Bioconjugate Chemistry*, *20*(6), 1218–1222. doi:10.1021/bc900080p

18. Wong, I. Y., & Melosh, N. A. (2010). An electrostatic model for DNA surface hybridization. *Biophysical Journal*, *98*(12), 2954–2963. doi:10.1016/j.bpj.2010.03.017

19. Cutler, J. I., Auyeung, E., & Mirkin, C. A. (2012). Spherical nucleic acids. *Journal of the American Chemical Society*, *134*(3), 1376–1391. doi:10.1021/ja209351u

20. Jensen, S. A., Day, E. S., Ko, C. H., Hurley, L. A., Luciano, J. P., Kouri, F. M., Merke, T. J., Luthi, A. J., Patel, P. C., Cutler, J. I., Daniel, W. L., Scott, A. W., Rotz, M. W., Meade, T. J., Giljohann, D. A., Mirkin, C. A., Stegh, A. H. (2013).

Spherical nucleic acid nanoparticle conjugates as an RNAi-based therapy for glioblastoma. *Science Translational Medicine*, *5*(209), 209ra152. doi:10.1126/scitranslmed.3006839

21. Stoeva, S. I., Lee, J. S., Thaxton, C. S., & Mirkin, C. A. (2006). Multiplexed DNA detection with biobarcoded nanoparticle probes. *Angewandte Chemie - International Edition*, *45*(20), 3303–3306. doi:10.1002/anie.200600124

22. Li, F., Zhang, H., Dever, B., Li, X.-F., & Le, X. C. (2013). Thermal Stability of DNA Functionalized Gold Nanoparticles. *Bioconjugate Chemistry*, *24*(11), 1790–7. doi:10.1021/bc300687z

23. Singh, B., Hussain, N., Sakthivel, T., & Florence, A. T. (2003). Effect of physiological media on the stability of surface-adsorbed DNA-dendron-gold nanoparticles. *The Journal of Pharmacy and Pharmacology*, *55*(12), 1635–1640. doi:10.1211/0022357022368

24. Zagorovsky, K., Chou, L. Y. T., & Chan, W. C. W. (2016). Controlling DNA–nanoparticle serum interactions. *Proceedings of the National Academy of Sciences*, *113*(48), 13600–13605. doi:10.1073/pnas.1610028113

25. Mahmoudi, M., Lohse, S. E., Murphy, C. J., Fathizadeh, A., Montazeri, A., & Suslick, K. S. (2014). Variation of protein corona composition of gold nanoparticles following plasmonic heating. *Nano Letters*, *14*(1), 6–12. doi:10.1021/nl403419e

26. Tenzer, S., Docter, D., Kuharev, J., Musyanovych, A., Fetz, V., Hecht, R., … Stauber, R. H. (2013). Rapid formation of plasma protein corona critically affects nanoparticle pathophysiology. *Nature Nanotechnology*, *8*(10), 772–781. doi:10.1038/nnano.2013.181

27. Mirshafiee, V., Mahmoudi, M., Lou, K., Cheng, J., & Kraft, M. L. (2013). Protein corona significantly reduces active targeting yield. *Chemical Communications*, *49*(25), 2557. doi:10.1039/c3cc37307j

28. Treuel, L., Brandholt, S., Maffre, P., Wiegele, S., Shang, L., & Nienhaus, G. U. (2014). Impact of protein modification on the protein corona on nanoparticles and nanoparticle-cell interactions. *ACS Nano*, *8*(1), 503–513. doi:10.1021/nn405019v

29. Hormozi-Nezhad, M. R., Seyedhosseini, E., & Robatjazi, H. (2012). Spectrophotometric determination of glutathione and cysteine based on aggregation of colloidal gold nanoparticles. *Scientia Iranica*, *19*(3), 958–963. doi:10.1016/j.scient.2012.04.018

30. Vanegas, J. P., Scaiano, J. C., & Lanterna, A. E. (2017). Thiol-Stabilized Gold Nanoparticles: New Ways to Displace Thiol Layers Using Yttrium or Lanthanide Chlorides. *Langmuir*, *33*(43), 12149–12154.

doi:10.1021/acs.langmuir.7b01898

31. Li, Z., Jin, R., Mirkin, C. A., & Letsinger, R. L. (2002). Multiple thiol-anchor capped DNA gold nanoparticle conjugates. *Nucleic Acids Research*, *30*(7), 1558–1562. Retrieved from http://nar.oxfordjournals.org/content/30/7/1558.abstract

32. Tsai, D. H., Shelton, M. P., DelRio, F. W., Elzey, S., Guha, S., Zachariah, M. R., & Hackley, V. A. (2012). Quantifying dithiothreitol displacement of functional ligands from gold nanoparticles. *Analytical and Bioanalytical Chemistry*, *404*(10), 3015–3023. doi:10.1007/s00216-012-6418-4

33. Kudelski, A. (2003). Chemisorption of 2-mercaptoethanol on silver, copper, and gold: Direct Raman evidence of acid-induced changes in adsorption/desorption equilibria. *Langmuir*, *19*(9), 3805–3813. doi:10.1021/la0209280

34. Marin, M. L., McGilvray, K. L., & Scaiano, J. C. (2008). Photochemical strategies for the synthesis of gold nanoparticles from Au(III) and Au(I) using photoinduced free radical generation. *Journal of the American Chemical Society*, *130*(49), 16572–16584. doi:10.1021/ja803490n

35. Häkkinen, H. (2012). The gold–sulfur interface at the nanoscale. *Nature Chemistry*, *4*(6), 443–455. doi:10.1038/nchem.1352

36. Wu, X. A., Choi, C. H. J., Zhang, C., Hao, L., & Mirkin, C. A. (2014). Intracellular fate of spherical nucleic acid nanoparticle conjugates. *Journal of the American Chemical Society*, *136*(21), 7726–7733. doi:10.1021/ja503010a

37. Heuer-Jungemann, A., El-Sagheer, A. H., Lackie, P. M., Brown, T., & Kanaras, A. G. (2016). Selective killing of cells triggered by their mRNA signature in the presence of smart nanoparticles. *Nanoscale*, *8*(38), 16857–16861. JOUR. doi:10.1039/C6NR06154K

38. Lee, K., Cui, Y., Lee, L. P., & Irudayaraj, J. (2014). Quantitative imaging of single mRNA splice variants in living cells. *Nature Nanotechnology*, *9*(6), 474–80. doi:10.1038/nnano.2014.73

39. Conde, J., de la Fuente, J. M., & Baptista, P. V. (2010). RNA quantification using gold nanoprobes - application to cancer diagnostics. *Journal of Nanobiotechnology*, *8*. doi:10.1186/1477-3155-8-5

40. Menko, A. S., Bleaken, B. M., Libowitz, A. A., Zhang, L., Stepp, M. A., & Walker, J. L. (2014). A central role for vimentin in regulating repair function during healing of the lens epithelium. *Molecular Biology of the Cell*, *25*(6), 776–790. doi:10.1091/mbc.E12-12-0900

41. Vuoriluoto, K., Haugen, H., Kiviluoto, S., Mpindi, J.-P., Nevo, J., Gjerdrum, C.,

Tiron, C., Lorens, J. B., Ivaska, J. (2011). Vimentin regulates EMT induction by Slug and oncogenic H-Ras and migration by governing Axl expression in breast cancer. *Oncogene*, *30*(12), 1436–48. doi:10.1038/onc.2010.509

42. Zhang, H., Zhang, H., Liu, L., Wang, Y., Zhao, G., Xie, R., Liu, C., Xiao, X., Wu, K., Niew, Y., Zhang, H., Fan, D. (2013). KLF8 involves in TGF-beta-induced EMT and promotes invasion and migration in gastric cancer cells. *Journal of Cancer Research and Clinical Oncology*, *139*(6), 1033–1042. doi:10.1007/s00432-012-1363-3

43. Lewinski, N., Colvin, V., & Drezek, R. (2008). Cytotoxicity of nanoparticles. *Small*, *4*(1), 26–49. doi:10.1002/smll.200700595

44. Massich, M. D., Giljohann, D. A., Schmucker, A. L., Patel, P. C., & Mirkin, C. a. (2010). Cellular response of polyvalent oligonucleotide-gold nanoparticle conjugates. *ACS Nano*, *4*(10), 5641–5646. doi:10.1021/nn102228s

45. Ashcroft, G. S., & Roberts, A. B. (2000). Loss of Smad3 modulates wound healing. *Cytokine and Growth Factor Reviews*. doi:10.1016/S1359-6101(99)00036-2

46. Ashcroft, G. S., Yang, X., Glick, A. B., Weinstein, M., Letterio, J. L., Mizel, D. E., Anzano, M., Greenwell-Wild, T., Wahl, S. M., Deng, C., Roberts, A. B. (1999). Mice lacking Smad3 show accelerated wound healing and an impaired local inflammatory response. *Nature Cell Biology*, *1*(5), 260–6. doi:10.1038/12971

47. Kim, H. J., Takemoto, H., Yi, Y., Zheng, M., Maeda, Y., Chaya, H., Hayashi, K., Mi, P., Pittella, F., Christie, R. J., Toh, K., Matsumoto, Y., Nishiyama, N., Miyata, K., Kataoka, K. (2014). Precise engineering of siRNA delivery vehicles to tumors using polyion complexes and gold nanoparticles. *ACS Nano*, *8*(9), 8979–8991. doi:10.1021/nn502125h

48. Barnaby, S. N., Lee, A., & Mirkin, C. A. (2014). Probing the inherent stability of siRNA immobilized on nanoparticle constructs. *Proceedings of the National Academy of Sciences of the United States of America*, *111*(27), 9739–44. doi:10.1073/pnas.1409431111

49. Hill, H. D., Millstone, J. E., Banholzer, M. J., & Mirkin, C. A. (2009). The role radius of curvature plays in thiolated oligonucleotide loading on gold nanoparticles. *ACS Nano*, *3*(2), 418–424. doi:10.1021/nn800726e

50. Gregory, R. I., Chendrimada, T. P., Cooch, N., & Shiekhattar, R. (2005). Human RISC couples microRNA biogenesis and posttranscriptional gene silencing. *Cell*, *123*(4), 631–640. doi:10.1016/j.cell.2005.10.022

51. Leuschner, P. J. F., Ameres, S. L., Kueng, S., & Martinez, J. (2006) Cleavage of the siRNA passenger strand during RISC assembly in human cells. , *Embo*

Reports, 314–320. doi:10.1038/sj.embor.7400637

52. Wittrup, A., & Lieberman, J. (2015). Knocking down disease: a progress report on siRNA therapeutics. *Nature Reviews Genetics*, *16*(9), 543–52. doi:10.1038/nrg3978

53. Wang, J., Lu, Z., Wientjes, M. G., & Au, J. L.-S. (2010). Delivery of siRNA therapeutics: barriers and carriers. *The AAPS Journal*, *12*(4), 492–503. doi:10.1208/s12248-010-9210-4

54. Burnett, J. C., Rossi, J. J., & Tiemann, K. (2011). Current progress of siRNA/shRNA therapeutics in clinical trials. *Biotechnology Journal*, *6*(9), 1130–1146. doi:10.1002/biot.201100054

55. Reynolds, J. L., Law, W. C., Mahajan, S. D., Aalinkeel, R., Nair, B., Sykes, D. E., Yong, K T., Hui, R>, Prasad, P N., Schwartz, S. A. (2012). Nanoparticle based galectin-1 gene silencing, implications in methamphetamine regulation of HIV-1 infection in monocyte derived macrophages. *Journal of Neuroimmune Pharmacology,7*(3), 673–85. doi:10.1007/s11481-012-9379-7

56. Conde, J., Rosa, J., de la Fuente, J. M., & Baptista, P. V. (2013). Gold-nanobeacons for simultaneous gene specific silencing and intracellular tracking of the silencing events. *Biomaterials*, *34*(10), 2516–2523. doi:10.1016/j.biomaterials.2012.12.015

57. Yeom, S. Y., Jeoung, D., Ha, K. S., & Kim, P. H. (2004). Small interfering RNA (siRNA) targetted to Smad3 inhibits transforming growth factor-beta signaling. *Biotechnology Letters*, *26*(9), 699–703. doi:10.1023/B:BILE.0000024091.90305.be

58. Ungefroren, H., Groth, S., Sebens, S., Lehnert, H., Gieseler, F., & Fändrich, F. (2011). Differential roles of Smad2 and Smad3 in the regulation of TGF-β1-mediated growth inhibition and cell migration in pancreatic ductal adenocarcinoma cells: control by Rac1. *Molecular Cancer*, *10*(1), 67. doi:10.1186/1476-4598-10-67

59. Broughton, G., Janis, J. E., & Attinger, C. E. (2006). Wound Healing: An Overview. *Plastic and Reconstructive Surgery*, *117*(7s), 1e-S–32e-S. doi:10.1097/01.prs.0000222562.60260.f9

60. Sykes, E. A., Dai, Q., Tsoi, K. M., Hwang, D. M., & Chan, W. C. W. (2014). Nanoparticle exposure in animals can be visualized in the skin and analysed via skin biopsy. *Nature Communications*, *5*. doi:10.1038/ncomms4796

61. Pan, X., Chen, Z., Huang, R., Yao, Y., & Ma, G. (2013). Transforming Growth Factor β1 Induces the Expression of Collagen Type I by DNA Methylation in Cardiac Fibroblasts. *PLoS ONE*, *8*(4). doi:10.1371/journal.pone.0060335

62. Cheng, K., Yang, N., & Mahato, R. I. (2009). TGF-beta1 gene silencing for treating liver fibrosis. *Molecular Pharmaceutics*, *6*(3), 772–9. doi:10.1021/mp9000469

63. Gilbert, R., Vickaryous, M., & Viloria-Petit, A. (2016). Signalling by Transforming Growth Factor Beta Isoforms in Wound Healing and Tissue Regeneration. *Journal of Developmental Biology*, *4*(2), 21. doi:10.3390/jdb4020021

64. Liu, C., Wang, H., Li, X., & Chen, D. (2009). Monodisperse, size-tunable and highly efficient β-NaYF4:Yb,Er(Tm) up-conversion luminescent nanospheres: controllable synthesis and their surface modifications. *Journal of Materials Chemistry*, *19*(21), 3546. doi:10.1039/b820254k

65. Boyer, J. C., Vetrone, F., Cuccia, L. A.,and, Capobianco, J. A., (2006). Synthesis of Colloidal Upconverting NaYF4 Nanocrystals Doped with Er3+, Yb3+ and Tm3+, Yb3+ via Thermal Decomposition of Lanthanide Trifluoroacetate Precursors. *Journal of the American Chemical Society, 128 (23),* pp. 7444-7445, doi:10.1021/JA061848B

66. Yi, G. S., & Chow, G. M. (2006). Synthesis of hexagonal-phase NaYF4:Yb,Er and NaYF 4:Yb,Tm nanocrystals with efficient up-conversion fluorescence. *Advanced Functional Materials*, *16*(18), 2324–2329. doi:10.1002/adfm.200600053

67. Rivera, V. A. G., Ledemi, Y., El-Amraoui, M., Messaddeq, Y., & Marega, E. (2014). Green-to-red light tuning by up-conversion emission via energy transfer in Er3 +-Tm3 +-codoped germanium-tellurite glasses. *Journal of Non-Crystalline Solids*, *392–393*, 45–50. doi:10.1016/j.jnoncrysol.2014.04.007

68. Ge, J., Zhang, Q., Zhang, T., & Yin, Y. (2008). Core-satellite nanocomposite catalysts protected by a porous silica shell: Controllable reactivity, high stability, and magnetic recyclability. *Angewandte Chemie - International Edition*, *47*(46), 8924–8928. doi:10.1002/anie.200803968

69. Lv, R., Wang, D., Xiao, L., Chen, G., Xia, J., & Prasad, P. N. (2017). Stable ICG-loaded upconversion nanoparticles: Silica core/shell theranostic nanoplatform for dual-modal upconversion and photoacoustic imaging together with photothermal therapy. *Scientific Reports*, *7*(1). doi:10.1038/s41598-017-16016-x

70. Liberman, A., Mendez, N., Trogler, W. C., & Kummel, A. C. (2014). Synthesis and surface functionalization of silica nanoparticles for nanomedicine. *Surface Science Reports*. doi:10.1016/j.surfrep.2014.07.001

71. Halliwell, C. M., & Cass, A. E. G. (2001). A factorial analysis of silanization conditions for the immobilization of oligonucleotides on glass surfaces.

Analytical Chemistry, *73*(11), 2476–2483. doi:10.1021/ac0010633

72. Schlecht, C. A., & Maurer, J. A. (2011). Functionalization of glass substrates: mechanistic insights into the surface reaction of trialkoxysilanes. *RSC Advances*, *1*(8), 1446–1448. doi:10.1039/C1RA00421B

73. Wiśniewska, M., Urban, T., Nosal-Wiercińska, A., Zarko, V., & Gun'ko, V. (2014). Comparison of stability properties of poly(acrylic acid) adsorbed on the surface of silica, alumina and mixed silica-alumina nanoparticles — application of turbidimetry method. *Central European Journal of Chemistry*, *12*(4), 476–479. doi:10.2478/s11532-013-0401-6

74. Bartczak, D., & Kanaras, A. G. (2011). Preparation of peptide-functionalized gold nanoparticles using one pot EDC/Sulfo-NHS coupling. *Langmuir*, *27*(16), 10119–10123. doi:10.1021/la2022177

75. Montenegro, J.-M., Grazu, V., Sukhanova, A., Agarwal, S., de la Fuente, J. M., Nabiev, I., Greiner, A., Parak, W. J. (2013). Controlled antibody/(bio-) conjugation of inorganic nanoparticles for targeted delivery. *Advanced Drug Delivery Reviews*, *65*(5), 677–688. doi:10.1016/j.addr.2012.12.003

76. Sperling, R. A., & Parak, W. J. (2010). Surface modification, functionalization and bioconjugation of colloidal inorganic nanoparticles. *Philosophical Transactions of the Royal Society of London A: Mathematical, Physical and Engineering Sciences*, *368*(1915).

77. Gallie, D. R. (1991). The cap and poly(A) tail function synergistically to regulate mRNA translational efficiency. *Genes and Development*, *5*(11), 2108–2116. doi:10.1101/gad.5.11.2108

78. Sheehan, P. E., & Whitman, L. J. (2005). Detection limits for nanoscale biosensors. *Nano Letters*, *5*(4), 803–807. doi:10.1021/nl050298x

79. Li, N., Su, X., & Lu, Y. (2015). Nanomaterial-based biosensors using dual transducing elements for solution phase detection. *The Analyst*, *140*(9), 2916–43. doi:10.1039/c4an02376e

80. Wang, M., Hou, W., Mi, C.-C., Wang, W.-X., Xu, Z.-R., Teng, H.-H., Mao, C. B., Xu, S.-K. (2009). Immunoassay of Goat Antihuman Immunoglobulin G Antibody Based on Luminescence Resonance Energy Transfer between Near-Infrared Responsive $NaYF_4$:Yb, Er Upconversion Fluorescent Nanoparticles and Gold Nanoparticles. *Analytical Chemistry*, *81*(21), 8783–8789. doi:10.1021/ac901808q

81. Wang, F., & Liu, X. (2009). Recent advances in the chemistry of lanthanide-doped upconversion nanocrystals. *Chemical Society Reviews*, *38*(4), 976. doi:10.1039/b809132n

82. Wolfbeis, O. S. (2015). An overview of nanoparticles commonly used in fluorescent bioimaging. *Chemical Society Reviews*, *44*(14), 4743–4768. doi:10.1039/C4CS00392F

83. Haase, M., & Schäfer, H. (2011). Upconverting nanoparticles. *Angewandte Chemie - International Edition*. doi:10.1002/anie.201005159

84. Chen, G., Qiu, H., Prasad, P. N., & Chen, X. (2014). Upconversion Nanoparticles : Design , Nanochemistry , and Applications in Theranostics. *Chemical Reviews, 114 (10),* pp. 5161-5214, doi:10.1021/cr400425h

85. Winter, C., Henschel, A., Tuukkanen, A., & Schroeder, M. (2012). Protein interactions in 3D: From interface evolution to drug discovery. *Journal of Structural Biology*. doi:10.1016/j.jsb.2012.04.009

86. Helmchen, F., Go, W., Göbel, W., & Kampa, B. M. (2007). Imaging cellular network dynamics in three dimensions using fast 3D laser scanning. *Nature Methods*, *4*(1), 73–79. doi:10.1038/nmeth989

87. Gao, L., Shao, L., Higgins, C. D., Poulton, J. S., Peifer, M., Davidson, M. W., Wu, X., Goldstein, B.,Betzig, E. (2012). Noninvasive imaging beyond the diffraction limit of 3D dynamics in thickly fluorescent specimens. *Cell*, *151*(6), 1370–1385. doi:10.1016/j.cell.2012.10.008

Appendix A

A.1 Materials

Sigma-Adrich: sodium tetrachloroaurate (III) (99% purity), sodium citrate (≥99% purity), bis(p-sulfonatophenyl)phenyl phosphine dihydrate dipotassium salt (BSPP, 97% purity), sodium chloride (99% purity), yttrium (III) chloride hexahydrate, ytterbium(III) chloride hexahydrate, erbium(III) chloride hexahydrate, thullium(III) chloride hexahydrate, oleic acid (90%), 1-octadecene (90%), sodium hydroxide (≥98% purity), absolute alcohol, phosphate buffered saline (PBS), sodium dodecyl sulfate (≥98% purity), monobasic phosphate (99%), dibasic phosphate (99%), Ethylenediaminetetraacetic acid (EDTA, 99%), Polyethylene glycol sorbitan monolaurate (Tween 20), 4-(2-Hydroxyethyl)piperazine-1-ethanesulfonic acid, N-(2-Hydroxyethyl)piperazine-N′-(2-ethanesulfonic acid) (HEPES, ≥99.5% purity), potassium acetate (≥99% purity), tetraethyl orthosilicate (TEOS, ≥99% purity), Polyoxyethylene (5) nonylphenylether (IGEPAL CO-520), polyacrylic acid (PAA, 1.8 kDa), tetrahydrofuran (THF, ≥99% purity), N-(3-Dimethylaminopropyl)-N′-ethylcarbodiimide hydrochloride (EDC, ≥99% purity), N-Hydroxysulfosuccinimide sodium salt (sulfo-NHS, >98% purity), (3-Aminopropyl)trimethoxysilane (APTMS, 97% purity), 2-(N-Morpholino)ethanesulfonic acid (MES, ≥99% purity), Corning® Transwell® (Polyester membrane, 12 mm, 0.4 µm pore), well plates (6, 12, 24 and 48 wells), Foetal Bovine Serum (FBS), calcium chloride (97% purity), magnesium chloride (97% purity), DNAse II (from porcine spleen), ethidium bromide (95% purity), rhodamine B (RhodB, 95% purity), 2-(4-Amidinophenyl)-6-indolecarbamidine dihydrochloride (DAPI), Mowiol (4-88, 31 kDa)

ThermoFisher: Dulbecco's Modified Eagle's Medium (DMEM), Minimum Essential Medium (MEM), Penicilin/Streptomycin, L-glutamine, Nystatin, Trypsin, Hank's Balanced Salt Solution (HBSS), phosphate buffered saline (PBS)

VWR: syringe (20G), syringe filter (0.2 µm), methanol (99% purity), hexane (90% purity), N,N-Dimethylformamide (DMF, 99% purity), falcon tube (50 mL)

Agar scientific: Spurr resin, formaldehyde, piperazine-N,N′-bis(2-ethanesulfonic acid) (PIPES), 200 mesh copper/nickel grid

Prochimia: thiolated polyethylene glycol (SH-PEG, 5 kDa)

APPENDIX A

SPI: Carbon film 400 mesh copper grid

Alfa Aesar: Succinic anhydride (99% purity)

Abcam: Rabbit polyclonal Anti-Mouse SMAD3 (AB28379), Goat Anti-Rabbity Cy3 (AB6939), Mouse monoclonal to GAPDH (AB8245)

Li-COR: IRDye® 800 CW Goat anti-Mouse or Donkey anti-Rabbit, Odyssey® Blocking buffer, Cell Tag® 700

Thorlabs: silver-coated mirrors (97% reflectance), plano-convex lens (AR 650-1050 nm), bi-convex lenses (AR 350-800nm), bandpass filter (540 ± 2 nm),

Top-Lasers: Laser pointer (980nm, 500mw)

A.2 Formulation of growth medium for cell and tissue culture

All formulations were taken from www.thermofisher.com

Ac. Material 1. Formulation of Cell Culture Dulbecco's Modified Essential Medium (DMEM)

Components	Molecular Weight	Concentration (mg/ml)	mM
Amino Acids			
Glycine	75	30	0.4
L-Arginine hydrochloride	211	84	0.398
L-Cystine 2HCl	313	63	0.201
L-Glutamine	146	584	4
L-Histidine hydrochloride-H2O	210	42	0.2
L-Isoleucine	131	105	0.801
L-Leucine	131	105	0.801
L-Lysine hydrochloride	183	146	0.798
L-Methionine	149	30	0.201
L-Phenylalanine	165	66	0.4
L-Serine	105	42	0.4
L-Threonine	119	95	0.798
L-Tryptophan	204	16	0.078
L-Tyrosine disodium salt dihydrate	261	104	0.398
L-Valine	117	94	0.803
Vitamins			
Choline chloride	140	4	0.029
D-Calcium pantothenate	477	4	0.008
Folic Acid	441	4	0.009
Niacinamide	122	4	0.033

Pyridoxine hydrochloride	206	4	0.019
Riboflavin	376	0.4	0.001
Thiamine hydrochloride	337	4	0.012
i-Inositol	180	7.2	0.04
Inorganic Salts			
Calcium Chloride (CaCl2) (anhyd.)	111	200	1.8
Ferric Nitrate (Fe(NO3)3"9H2O)	404	0.1	$2.47x10^{-4}$
Magnesium Sulfate (MgSO4) (anhyd.)	120	97.67	0.814
Potassium Chloride (KCl)	75	400	5.33
Sodium Bicarbonate (NaHCO3)	84	3700	44
Sodium Chloride (NaCl)	58	6400	110.3
Sodium Phosphate monobasic (NaH2PO4-H2O)	138	125	0.91
Other Components			
D-Glucose (Dextrose)	180	4500	25
Phenol Red	376.4	15	0.04

Ac. Material 2. Formulation of Minimum Essential Medium (MEM)

Components	Molecular Weight	Concentration (mg/ml)	mM
Amino Acids			
L-Arginine hydrochloride	211.0	126	297
L-Cystine 2HCl	240	24	0.1
L-Glutamine	146.0	292	2
L-Histidine hydrochloride-H2O	210.0	42	0.2

L-Isoleucine	131.0	52	0.397
L-Leucine	131.0	52	0.397
L-Lysine hydrochloride	183	73	0.399
L-Methionine	149	15	0.101
L-Phenylalanine	165	32	0.194
L-Threonine	119	48	0.403
L-Tryptophan	204	10	0.049
L-Tyrosine disodium salt dihydrate	181	36	0.199
L-Valine	117	46	0.393
Vitamins			
Choline chloride	140	1	$7.14x10^{-3}$
D-Calcium pantothenate	477	1	$2.1x10^{-3}$
Folic Acid	441	1	$2.27x10^{-3}$
Niacinamide	122	1	$8.2x10^{-3}$
Pyridoxine hydrochloride	204	1	$4.9x10^{-3}$
Riboflavin	376	0.1	$2.66x10^{-4}$
Thiamine hydrochloride	337	1	$2.97x10^{-2}$
i-Inositol	180	2	$1.11x10^{-3}$
Inorganic Salts			
Calcium Chloride (CaCl2) (anhyd.)	147	264	1.8
Magnesium Sulfate (MgSO4) (anhyd.)	246	200	0.813
Potassium Chloride (KCl)	75	400	5.33
Sodium Bicarbonate (NaHCO3)	84	2200	26.9
Sodium Chloride (NaCl)	58	6800	117.24
Sodium Phosphate monobasic (NaH2PO4-H2O)	156	158	1.01

APPENDIX A

Other Components			
D-Glucose (Dextrose)	180	1000	5.56
Phenol Red	376.4	10	0.0266

Ac. Material 3. Mice chow composition

Ingredient	Quantity	Ingredient	Quantity
Protein		Minerals	
Alanine %	1.44	Calcium %	0.95
Arginine %	1.57	Chloride %	0.64
Aspartic Acid %	2.81	Chromium ppm	0.01
Cystine %	0.39	Cobalt ppm	0.91
Glycine %	1.28	Copper ppm	15
Histidine %	0.62	Fluorine ppm	15
Isoleucine %	1.06	Iodine ppm	0.99
Leucine %	1.89	Iron ppm	240
Lysine %	1.48	Magnesium %	0.23
Methionine %	0.59	Manganese ppm	75
Phenylalanine %	1.11	Phosphorus %	1.12
Proline %	1.47	Potassium %	1.28
Taurine %	0.03	Selenium ppm	0.41
Tyrosine %	0.77	Sodium %	0.39
Threonine %	0.97	Sulfur %	0.36
Tryptophan %	0.28	Zinc ppm	85
Valine %	1.16	Vitamins	
Serine %	1.18	B12 mcg/kg	51
Fat		Biotin ppm	0.3
Arachidonic Acid %	0.02	Carotene ppm	2.3
Cholesterol ppm	209	Choline Chloride ppm	2250

Linoleic Acid %	1.05	Folic Acid ppm	7.1
Linolenic Acid %	0.09	Niacin ppm	120
Monounsaturated Fatty Acids %	1.62	Pantothenic Acid ppm	24
Omega-3 Fatty Acids %	0.3	Pyridoxine ppm	6
Saturated Fatty Acids %	1.48	Riboflavin ppm	4.7
Carbohydrates		Thiamin Hydrochloride ppm	16
Fiber (Crude) %	5.3	Vitamin A IU/gm	15
Fructose %	0.27	Vitamin D IU/gm	4.6
Glucose %	0.19	Vitamin E IU/gm	42
Lactose %	2.01	Vitamin K ppm	1.3
Starch %	21	Others	
Sucrose %	3.83	Fiber	5.3

Ac. Material 4. Recipes for different buffers and solutions

Method	Reagent	Recipe
Western Blot	Triton Lysis Buffer	- 25 mM Tris-HCl (pH 7.2)[1] - 50 mM Glycerol Phosphate[1] - 50 mM Potassium Chloride[2] - 1% Triton X-100[1] - 1 mM Dithiothreitol (DTT)[2] - 1 x Protease inhibitor Tablet[2]
	RIPA Lysis Buffer	- 25 mM Tris-HCl (pH 7.4)[1] - 150 mM NaCl[1] - 0.1% Sodium dodecyl sulfate (SDS)[2] - 0.5% Sodium Deoxycholate[2] - 1 mM Sodium Orthovanate[1]

	- 1% NP-40[1] - 1 x Protease Inhibitor Tablet[2]
Laemelli Buffer (2x)	- 4% SDS[2] - 20% Glycerol[1] - 120 mM Tris-HCl (pH 6.8)[1]
Running Buffer (10x)	- 25 mM Tris Base[1] - 190 mM Glycine[2] - 0.1% SDS[2] - Final adjusted pH 8.3 (using HCl)
Transfer Buffer	- 25 mM Tris Base[1] - 190 mM Glycine[2] - 10% Methanol - 0.1 % SDS[2] - Final adjusted pH 8.3 (using HCl)
Ponceau S Solution	- 0.2 % Ponceau S[2] - 5 % Glacial acetic acid[2]
Tris Buffered Saline-Tween 20 (TBST)	- 20 mM Tris-HCl (pH 7.5)[1] - 150 mM NaCl[1] - 0.1 % Tween-20[2]
SDS-Polyacrylamide Gel	<u>Resolving Gel</u> - 2.3 mL dH_2O - 1.5 mL 1.5 M Tris pH 8.8[1] - 160 µL 10% SDS[2] - 1.98 mL of 30% Acrylamide[1] - 60 µL of 10% Ammonium Persulfate (APS)[2] - 2.4 uL of Tetramethylethylenediamine (TEMED)[2] <u>Stacking Gel:</u>

		- 2.1 mL dH_2O - 380 µL 1.5 M Tris pH 6.8[1] - 30 µL 10% SDS[2] - 0.5 mL of 30% Acrylamide[1] - 30 µL of 10% APS[2] - 3 µL of TEMED[2]
Movat's Pentachrome Staining	Verhoff's haematoxylin	- 0.5% Haematoxylin[2] - 0.6 % ferric chloride[2] - 0.5 % concentrated HCl in 1:1 v/v ethanol:distilled water
	Crocein Scarlet-Acid fuchsin (8:2)	- 0.4 % crocein scarlet[2] - 1 % glacial acetic acid[2] - 0.1 % acid fuchsin[2]

N.B.: Every buffer and solution was made using deionised water; 1 – Product obtained from ThermoFisher; 2 – Product obtained from Sigma-Aldrich

Appendix B

B.1 Calculation of 13 nm AuNP concentration using extinction coefficient

Concentrations of colloidal gold solutions were determined from the corresponding absorption spectrum at the peak maximum (~520 nm for 13 nm gold nanospheres) using the Beer-Lambert Law (Equation 3.1.) and the appropriate molar extinction co-efficient. ε (13 nm AuNPs) = 2.27 × 108 L mol-1cm-1 [1].

As an example calculation, for an optical density of 0.5 and a dilution factor of 10, the concentration can be calculated as follows:

$$c = \frac{AD}{\varepsilon l}$$

$$c = \frac{0.5 \times 10}{1\ \text{cm} \times 2.27 \times 10^{8}\ \text{L mol}^{-1}\text{cm}^{-1}}$$

$$c = 22.02\ \text{nM}$$

B.2 Calculation of number of DNA strands per particle using extrapolated equations from calibration curves

The average number of strands per particle were determined using the extrapolated equations from the calibration curves obtained (Figure 4.4.). Knowing that the *x* axis was the concentrations of the specific strand and the *y* axis was the corresponding fluorescence intensity value of the maximum peak (570 nm for sense

strands and 662 nm for flare strands), the average number of strands was calculated as follows (sense strand used as example with *x* = 3.3936):

$$y = 2.1x\text{-}7.2$$

$$y = 2.1 \times 3.4\text{-}7.2$$

$$y = 0.99 \times 10^{-6}\ \mathrm{M}$$

Calculation of moles of DNA strands in a typical solution used for conjugation with AuNPs:

$$n = \frac{C}{V}$$

$$n = \frac{0.99\ \mu\mathrm{M}}{1\ \mathrm{ml}} = 0.99\ \mathrm{nmol}$$

Calculation of number of strands in 0.9827 nmol:

$N_A = 6.022 \times 10^{23}$

$$\mathrm{Nr\ strands} = N_A \times 0.99 \times 10^{-9}\ \mathrm{mol}$$

$$\mathrm{Nr\ particles} = 6.022 \times 10^{23} \times 9.9 \times 10^{-10} = 5.96 \times 10^{14}$$

Calculation of moles of AuNPs in a typical solution used for conjugation with DNA:

$$n = \frac{C}{V}$$

$$n = \frac{10\ \mathrm{nM}}{1\ \mathrm{ml}} = 10\ \mathrm{pmol}$$

APPENDIX B

Calculation of number of particles in 10 pmol:

$N_A = 6.022 \times 10^{23}$

$$\text{Nr particles} = N_A \times 10 \times 10^{-12}\ \text{mol}$$

$$\text{Nr particles} = 6.022 \times 10^{23} \times 10 \times 10^{-12} = 6.022 \times 10^{12}$$

Calculation of number of strands per particle:

$$\text{Nr strands per particle} = \frac{\text{Nr strands}}{\text{Nr Particles}}$$

$$\text{Nr strands per particle} = \frac{5.96 \times 10^{14}}{6.022 \times 10^{12}} = 99$$

This process was repeated 5 times in order to obtain the averages of 97 ± 2 sense strands per particle and 47 ± 2 flare strands per particle.

B.3 Calculation of number of siRNA duplexes per particle using extrapolated equations from calibration curves

The average number of strands per particle were determined using the extrapolated equations from the calibration curves obtained (Figure 5.3.). Knowing that the *x* axis was the concentrations of the specific strand and the *y* axis was the corresponding fluorescence intensity value of the maximum peak (570 nm for sense strands and 662 nm for antisese strands), the average number of strands was calculated as follows (sense strand used as example with *x* = 14.25):

$$y = 0.20x + 2.8$$

$$y = 0.20 \times 14.25 + 2.8$$

$$y = 0.47 \times 10^{-6}\ \text{M}$$

Calculation of moles of DNA strands in a typical solution used for conjugation with AuNPs:

$$n = \frac{C}{V}$$

$$n = \frac{0.47\ \mu M}{1\ ml} = 0.47\ nmol$$

Calculation of number of strands in 0.47 nmol:

$N_A = 6.022 \times 10^{23}$

$$\text{Nr strands} = N_A \times 0.47 \times 10^{-9}\ mol$$

$$\text{Nr particles} = 6.022 \times 10^{23} \times 4.7 \times 10^{-10} = 2.830 \times 10^{14}$$

Calculation of number of strands per particle:

Nr particles in 1 ml of 10 pM = 6.022×10^{12} (calculated previously in AII)

$$\text{Nr strands per particle} = \frac{\text{Nr strands}}{\text{Nr Particles}}$$

$$\text{Nr strands per particle} = \frac{2.83 \times 10^{14}}{6.022 \times 10^{12}} = 47$$

This process was repeated 5 times for both strands in order to determine that the average number of siRNA duplexes per particles was 48 ± 3.

B.4 Calculation of the theoretical detection limit of UCNP-DNA-GO sensor

The theoretical detection limit of each target (poly-A, BACE-1 and PCA3) was determined using the extrapolated equation from the curves obtained from experimental data. For this type of calculation, it was assumed that y ≥ 100 since it provides a significant margin for any error associated with the measurements (3σ = 96). Poly-A is shown as an example for calculation steps.

$$y = 778201 - \frac{778201}{1 + \left(\frac{x}{3590}\right)^{0.86}}$$

Therefore, if the photon count is minimal, y = 100

$$100 = 778201 - \frac{778201}{1 + \left(\frac{x}{3590}\right)^{0.86}}$$

$$\frac{778201}{778101} = 1 + \left(\frac{x}{3590}\right)^{0.86}$$

$$1 - 1 = \left(\frac{x}{3590}\right)^{0.86}$$

$$\sqrt[0.86]{1.285 \times 10^{-4}} = \frac{x}{3590}$$

$$x = 2.85 \times 10^{-5} \times 3590$$

$$x = 0.1023 \text{ pmol}$$

The concentration of 0.1023 pmol was given for 1 ml of volume. However, the laser pointer has a total volume of 20 x 20 x 250 μm^3, which is equivalent to 10 x 10^{-9} L. Therefore the final theoretical concentration was calculated as follows:

$$C = \frac{0.1023 \times 10^{-12}}{10 \times 10^{-9}} = 5.115 \text{ fM}$$

All the resulting theoretical detection limits (Table 6.2.), were obtained in a similar type of calculation.

B.5 Control experiment of Vimentin mRNA detection using a non-specific scramble sequence

Skin was injected with 100 nM of scramble sequence DNA-coated nanoparticles and incubated for 6 h. After wax embedding, sections of 2 µm were taken and observed under a confocal microscope. It was possible to notice that the fluorescence signal arising from the presence of Vimentin mRNA (Cy5) was not present. Specific detection (see Figure 4.18.) could only be observed with specifically designed Vimentin targeted DNA-AuNP conjugates.

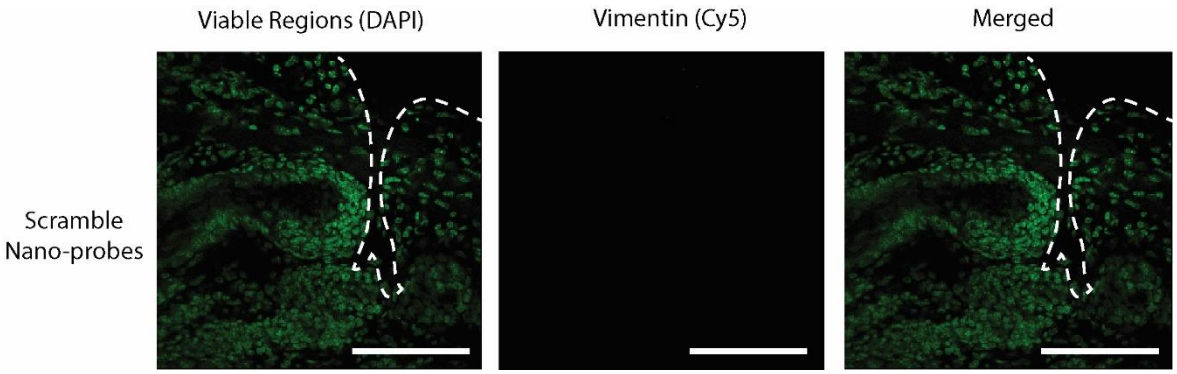

Ac. Material 5. Ex vivo detection of Vimentin expression using DNA-coated nanoparticles. (Scale bar = 500)

B.6 Temporal visualization of Vimentin mRNA expression in 3D *ex vivo* skin biopsies

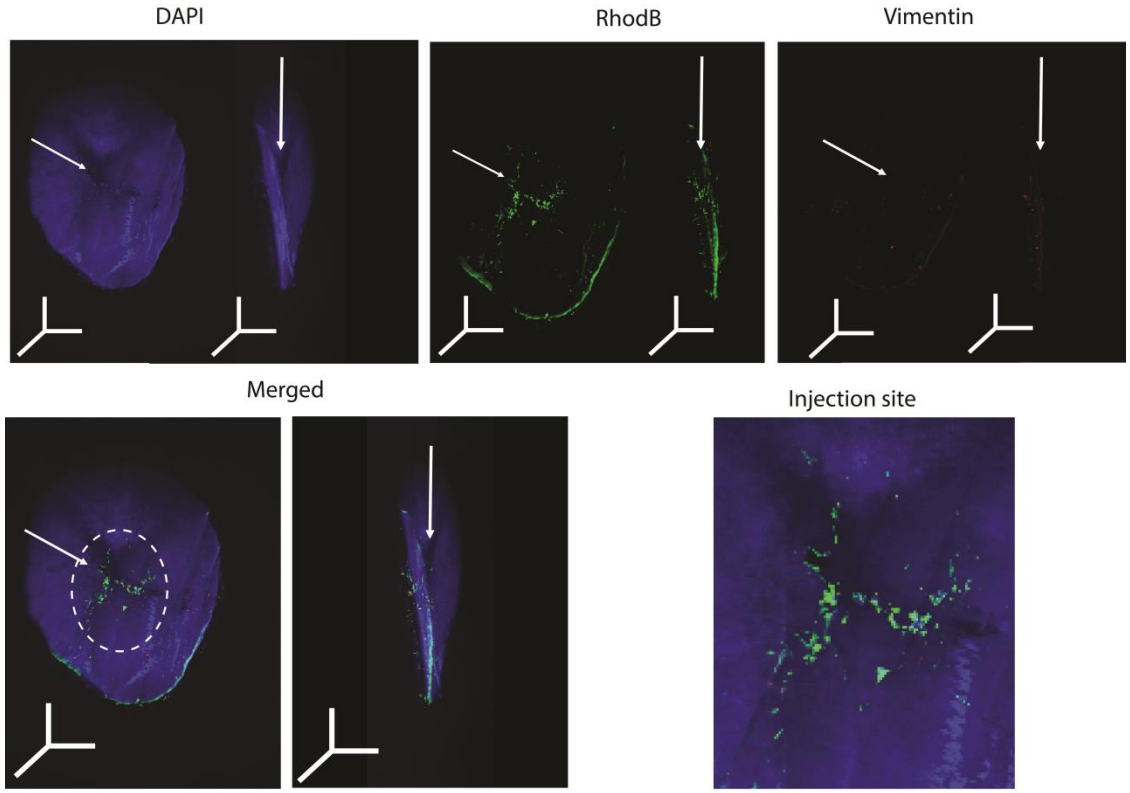

Ac. Material 6. 3D visualization of the expression of Vimentin mRNA at 1 h. Skin biopsies were incubated with a solution of 100 pmol of DNA-coated gold nanoparticles, which can detect vimentin mRNA, and the counter dye RhodB. After 1h, Vimentin mRNA expression (red channel) was not detectable, whilst RhodB counter dye (green channel) was visible. The green channel overlapped with the cellular regions of the skin (shown using DAPI counter stain and represented by the blue channel). (Arrows indicate the direction of injection; 3D scale bar = 1x1x1 mm in xzy axis)

APPENDIX B

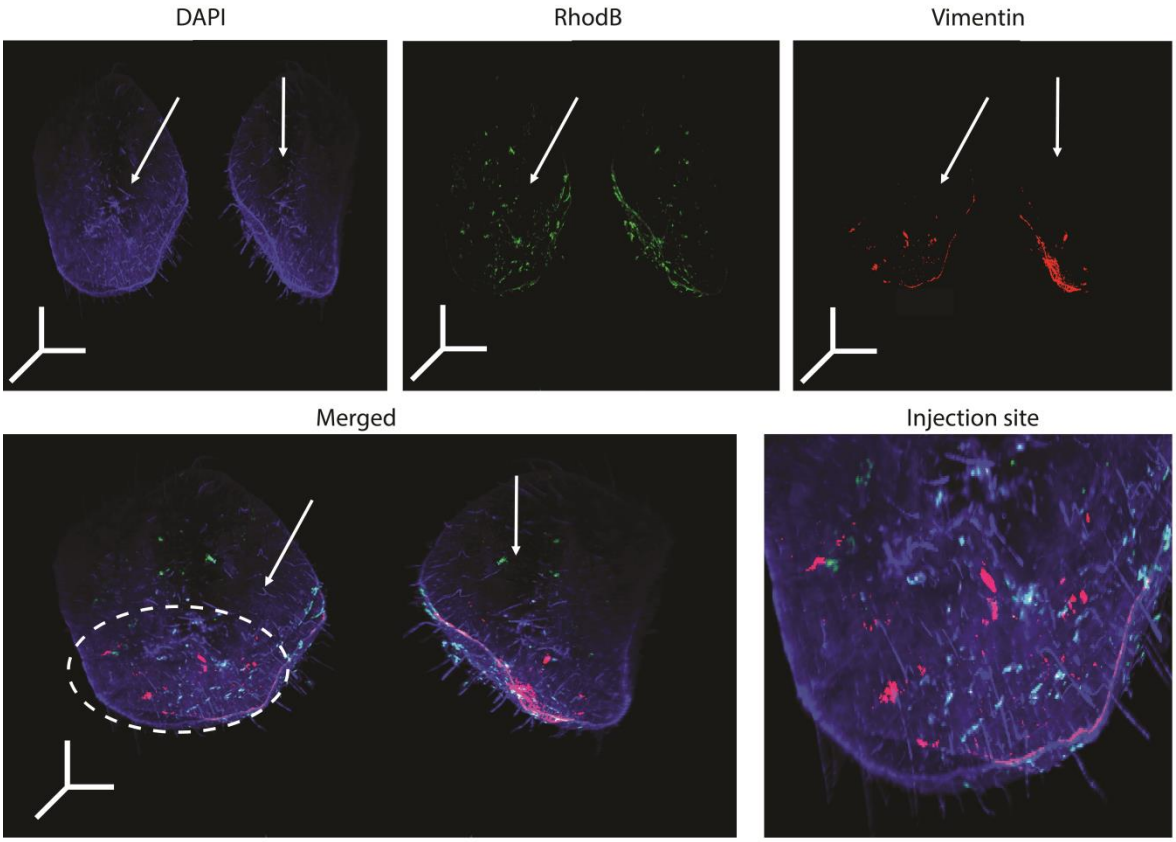

Ac. Material 7. 3D visualization of the expression of Vimentin mRNA at 3 h. Skin biopsies were incubated with a solution of 100 pmol of DNA-coated nanoparticles, which can detect Vimentin mRNA, and the counter dye RhodB. After 3h, a red fluorescent signal was significantly visible. All the channels overlapped approximately in the same region, showing that the expression was not only happening within the cellular regions of the skin (shown using DAPI counter stain and represented by the blue channel), but also in the injection site (shown using RhodB and represented as the green channel). (Arrows indicate the direction of injection; 3D scale bar = 1x1x1 mm in xzy axis)

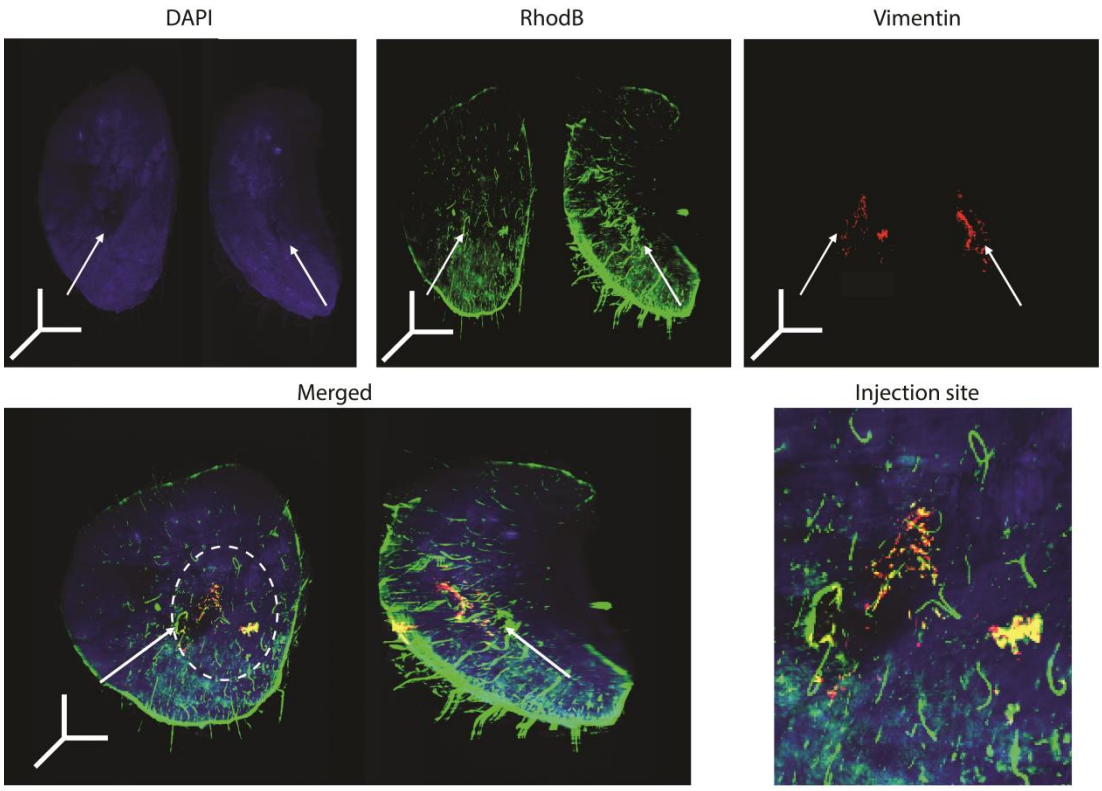

Ac. Material 8. 3D visualization of the expression of Vimentin mRNA at 4h. Skin biopsies were incubated with a solution countaining counter dyed RhodB and 100 pmol of DNA-coated nanoparticles capable of detecting Vimentin mRNA. After 4h of incubation a red fluorescent signal was significantly visible, associated with Vimentin mRNA. All the channels overlapped approximately in the same region, showing that the expression was not only happening within the cellular regions of the skin (shown using DAPI counter stain and represented by the blue channel), but also in the injection site (shown using RhodB and represented as the green channel). (Arrows indicate the direction of injection; 3D scale bar = 1x1x1 mm in xzy axis)

APPENDIX B

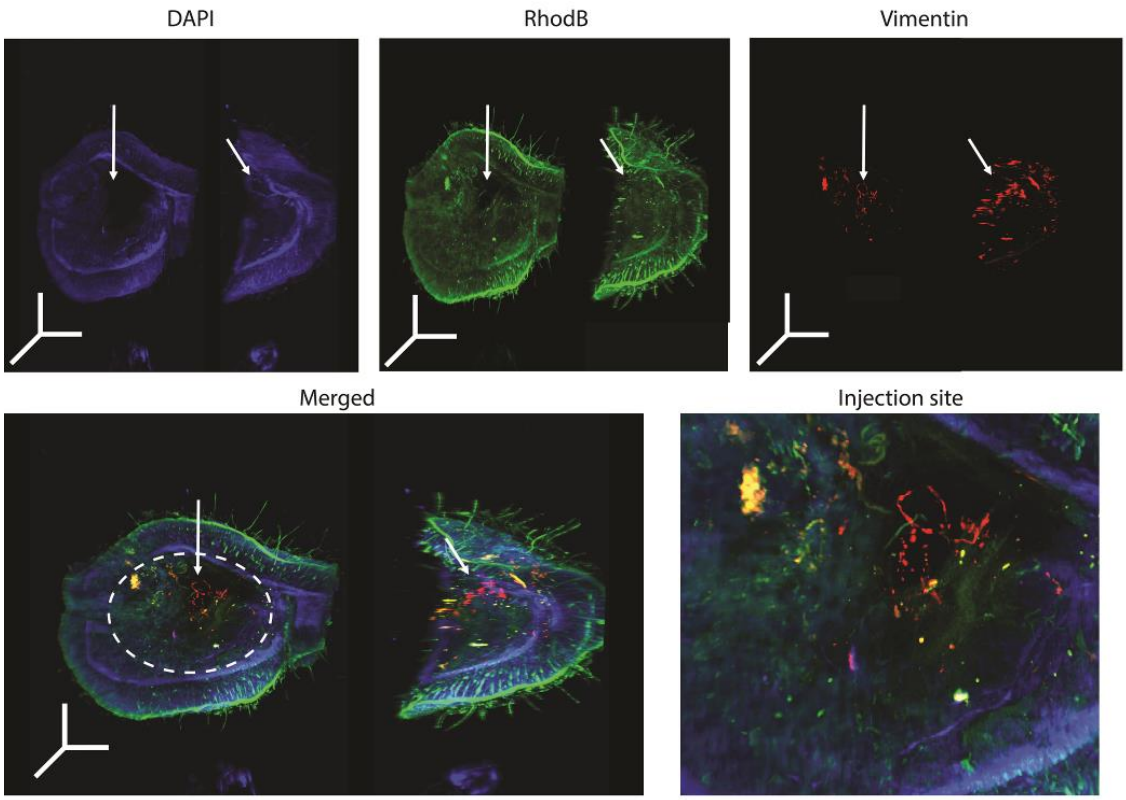

Ac. Material 9. 3D visualization of the expression of Vimentin mRNA at 5h. Skin biopsies were incubated with a solution of 100 pmol of DNA-coated nanoparticles for the detection of Vimentin mRNA and the counter dye RhodB for staining of the injection site. After 5h of incubation, the Vimentin mRNA expression (red channel) was significantly visible. All three channels overlapped approximately in the same region of the tissue, demonstrating that not only the Vimentin mRNA expression was happening in the cellular regions of the skin (blue channel) but also near the injection site (green channel). (Arrows indicate the direction of injection; 3D scale bar = 1x1x1 mm in xzy axis)

B.7 Control experiments of immunofluorescence detection of SMAD3 expresison

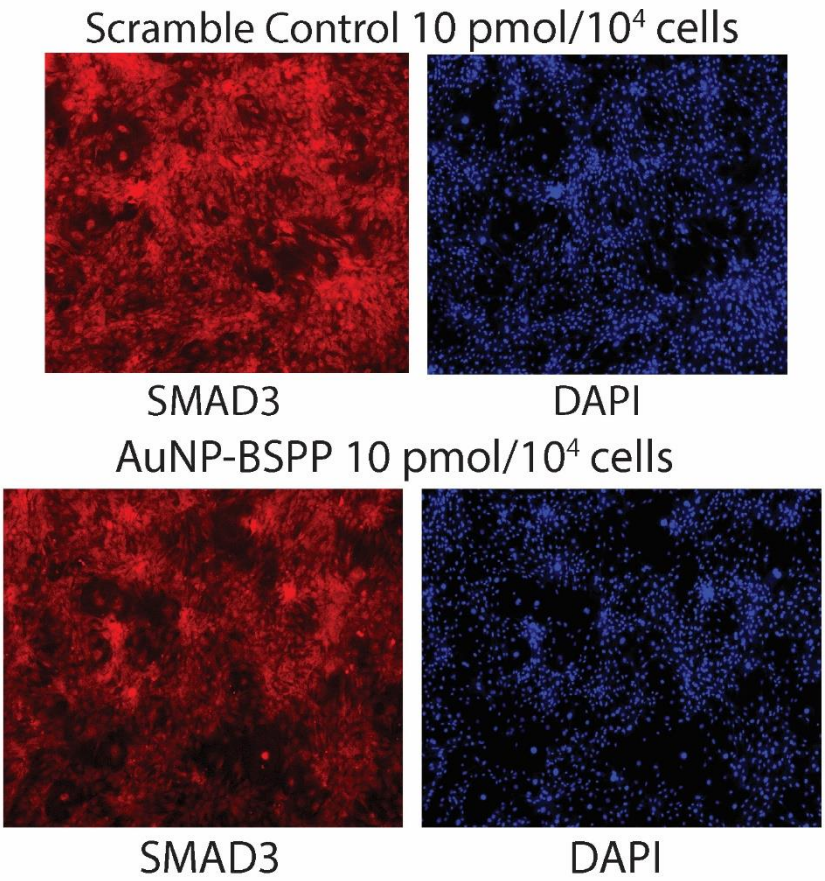

Ac. Material 10. Immunofluorescence controls of SMAD3 expression in MEF cells. MEF cells were treated with two types of controls: scramble sequence siRNA control (where particles were coated with a non-specific sequence); and particles coated with only BSPP. Both tests were performed in order to investigate if any effect on the SMAD3 protein expression was due to the presence of non-specific siRNA or even the core itself. No significant alterations were observed.

B.8 Effect of SMAD3 siRNA-AuNP conjugates on wound healing in *in vivo* models

B.8.1 Photographic monitoring

Male C57BL/6 mice (12-16 weeks old) were wounded with a 6 mm biopsy punch blade in two different dorsal areas (Figure 5.14). The left wound was treated with a solution of scramble control AuNP-siRNA solution, whilst the right wound was treated with a solution of SMAD3 AuNP-siRNA. The wounds were monitored over a period of 15 days. After day 11, wounds had completely healed.

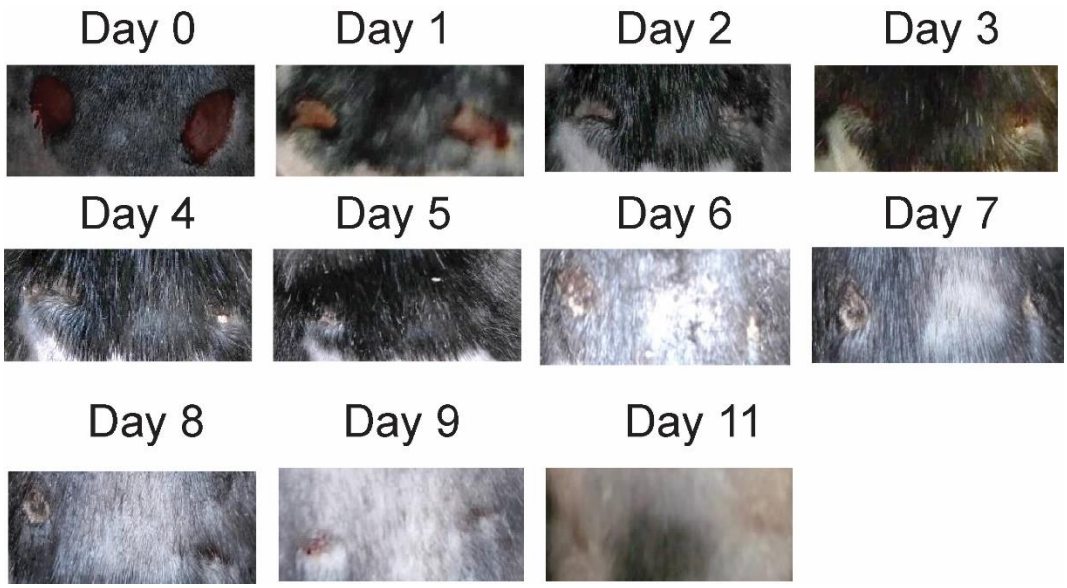

Ac. Material 11. Photographic monitoring of wound healing in mouse nr. 1

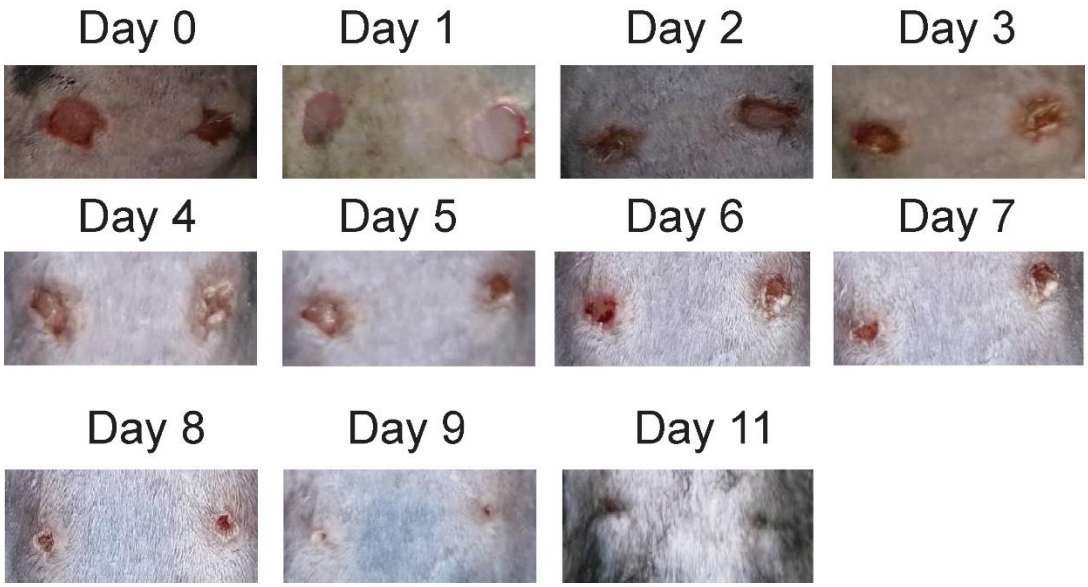

Ac. Material 12. Monitoring of wound healing in mouse nr. 2

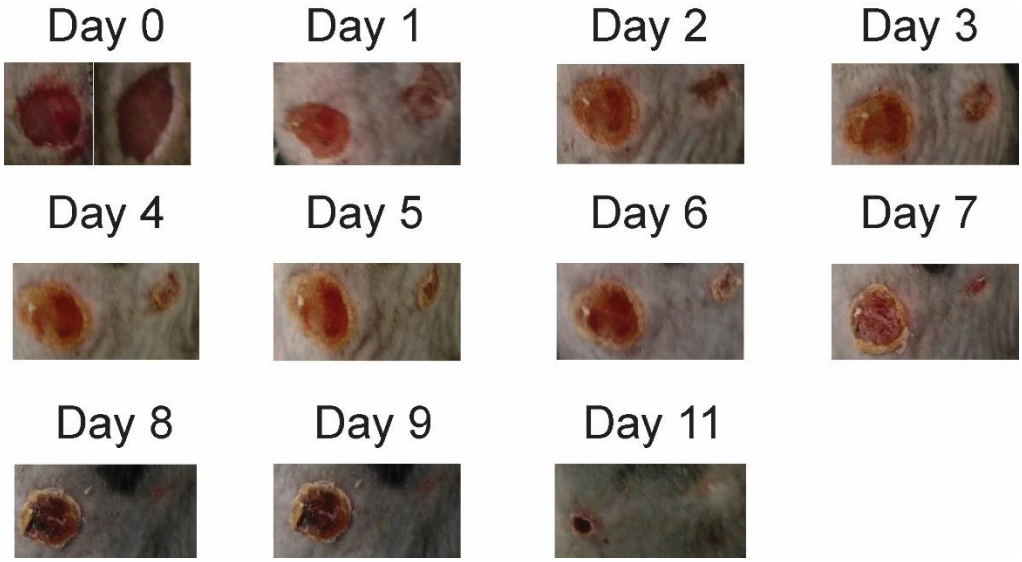

Ac. Material 13. Monitoring of wound healing in mouse nr. 4

APPENDIX B

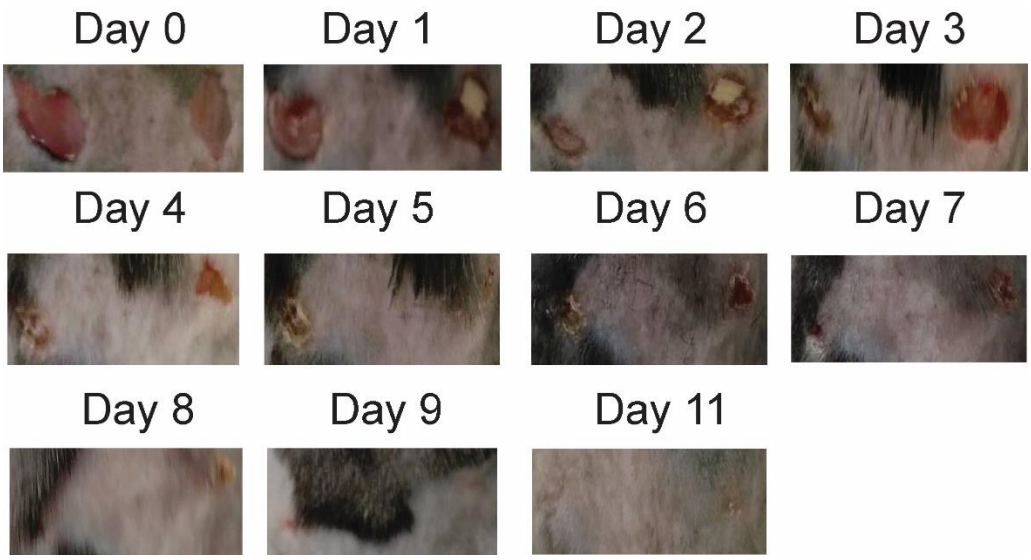

Ac. Material 14. Monitoring of wound healing in mouse nr. 5

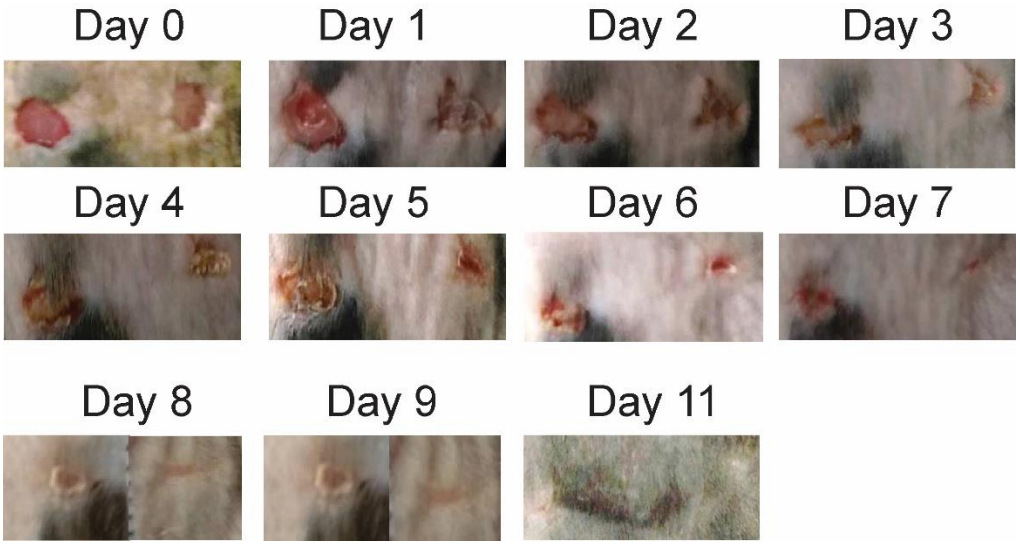

Ac. Material 15. Monitoring of wound healing in mouse nr. 6

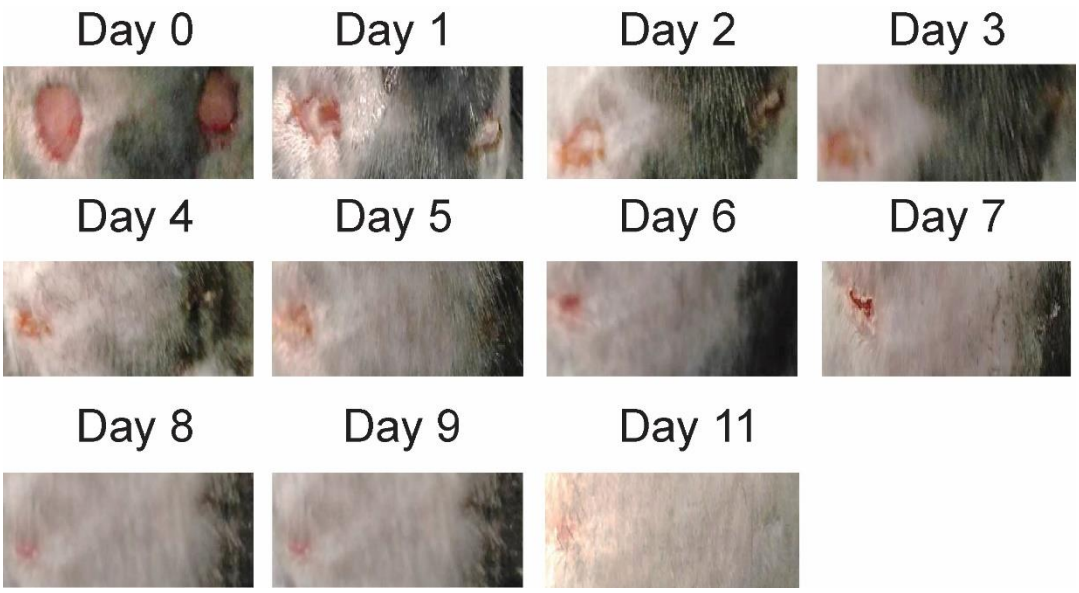

Ac. Material 16. Monitoring of wound healing in mouse nr. 7

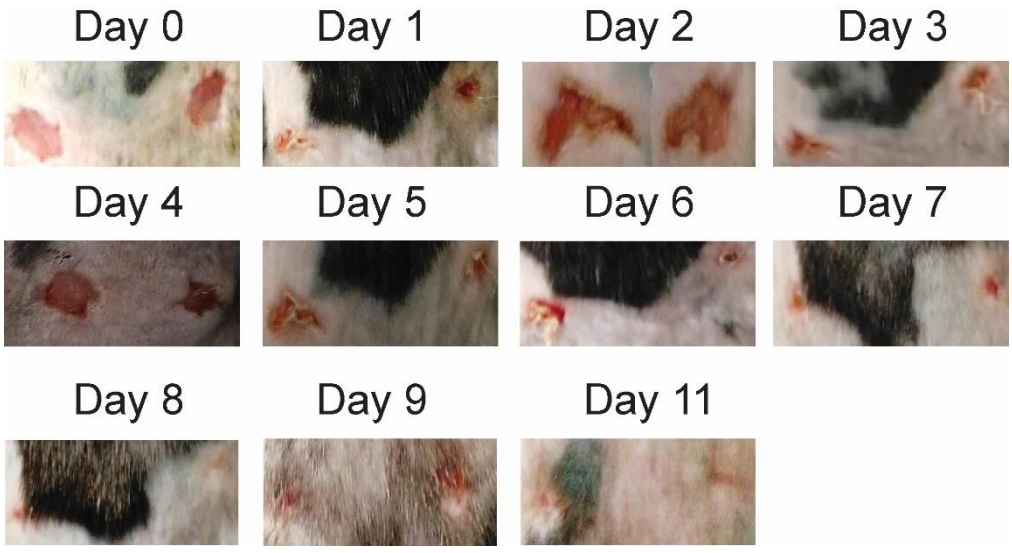

Ac. Material 17. Monitoring of wound healing in mouse nr. 8

APPENDIX B

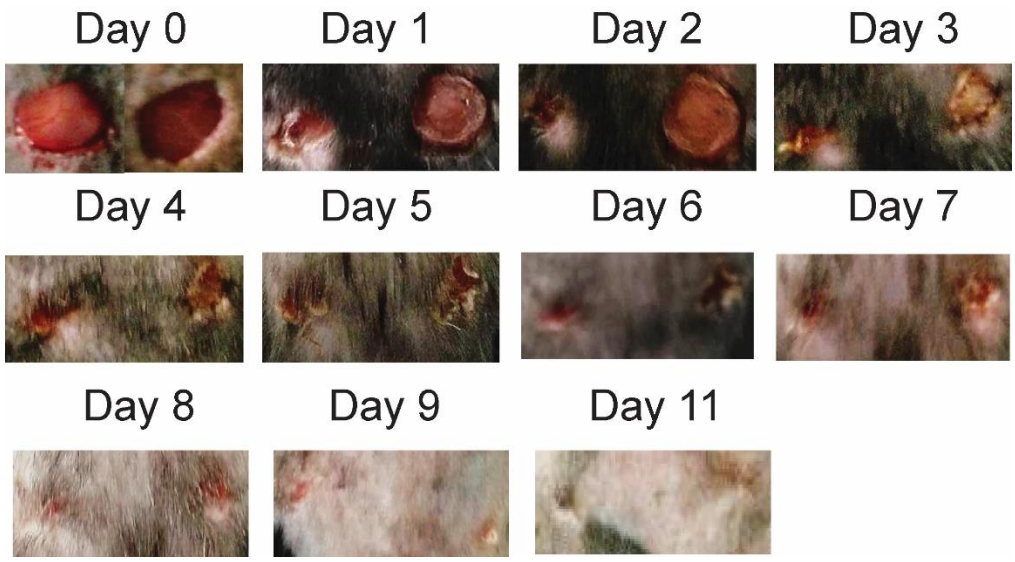

Ac. Material 18. Monitoring of wound healing in mouse nr. 9

B.8.2 Size measurement of wounds over time

Wound size was measured every day for 13 days and the mean sizes for all mice were analysed until day 11 (when the wounds were not visibly open anymore).The wound closure rate demonstrated that there was a difference between the rate of wound closure of wounds treated with the scramble control and the wounds treated with SMAD3 AuNP-siRNA conjugates across all the mice.

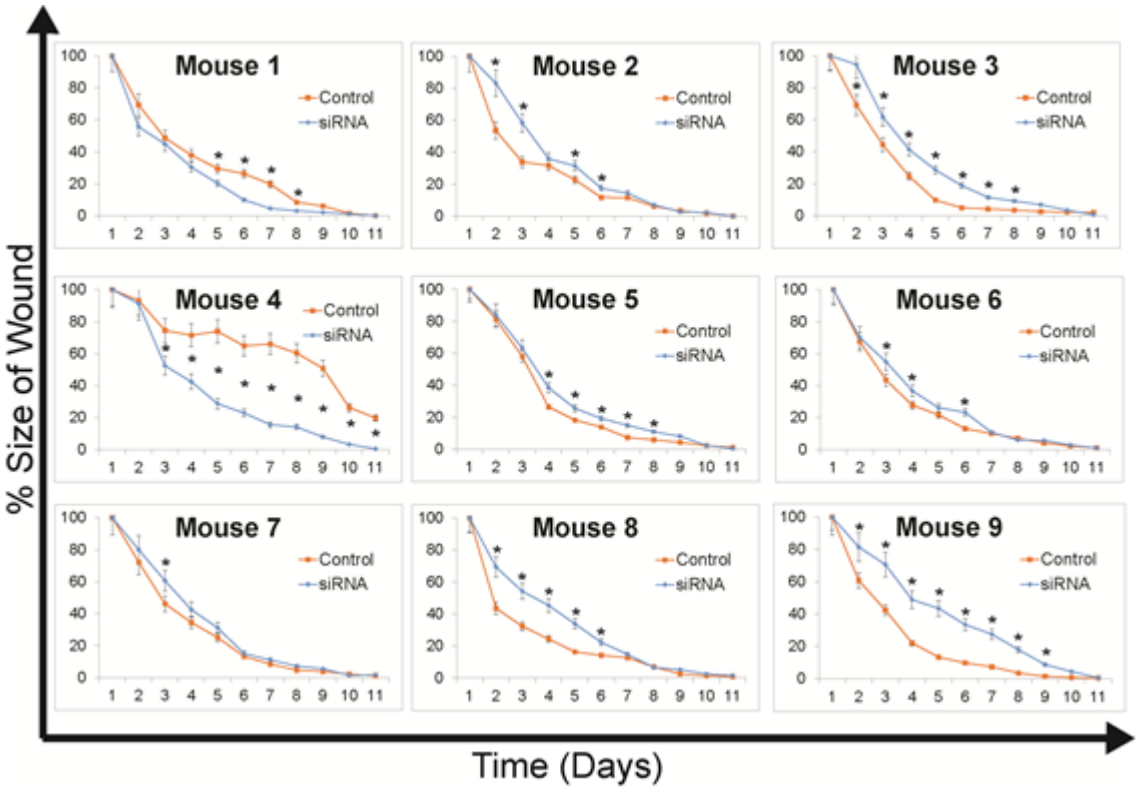

Ac. Material 19. Wound monitoring of all the mice across 11 days. (*p<0.05, student's t-test)

B.8.3 Histological analysis of wounds in *in vivo* models

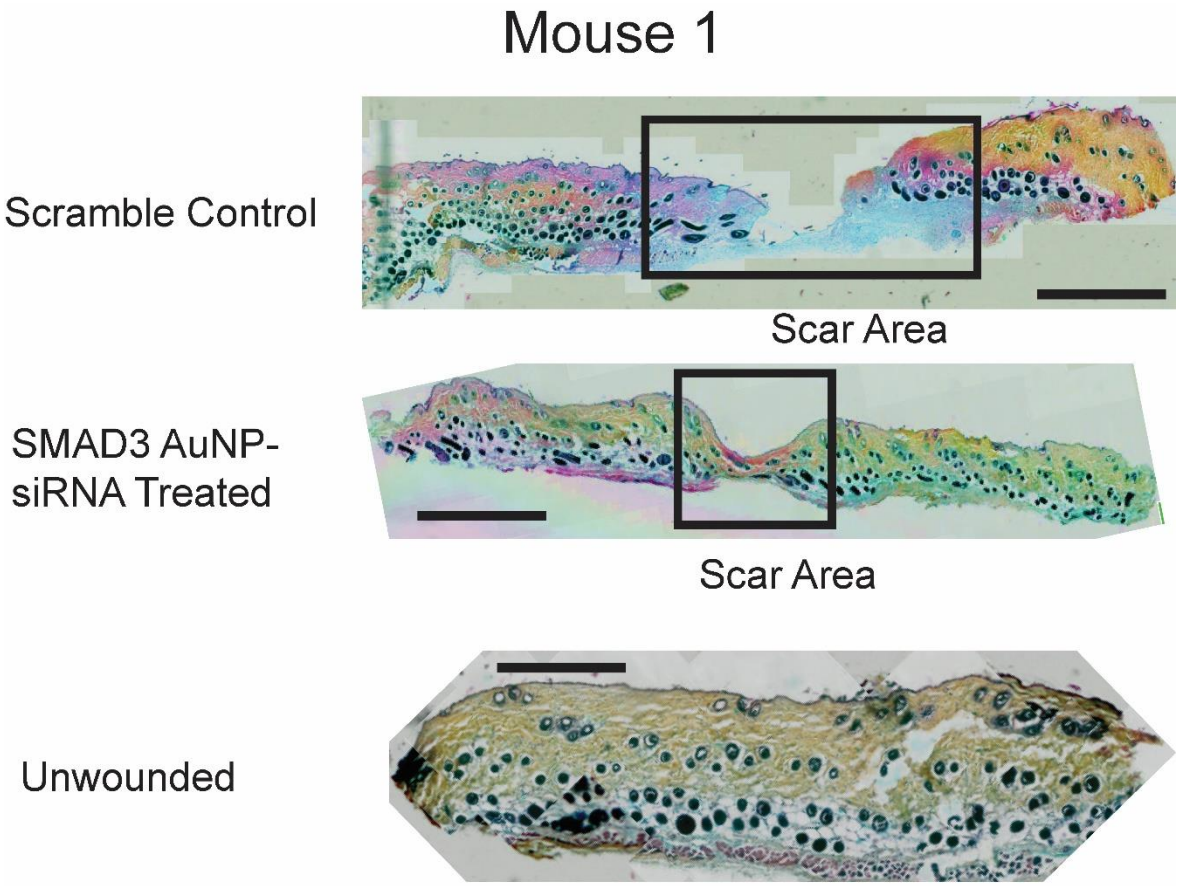

Ac. Material 20. Histological analysis of wounds in mouse nr. 1 (Scale bar = 1 mm)

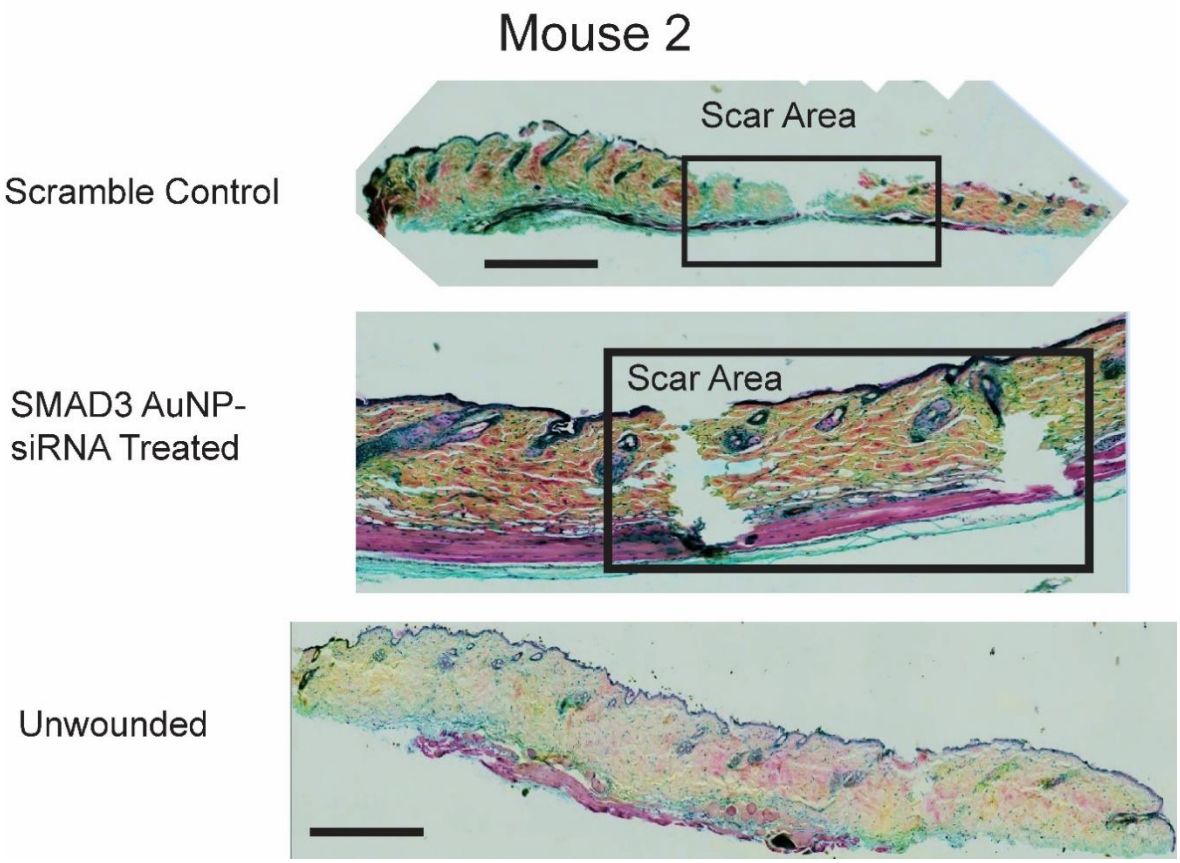

Ac. Material 21. Histological analysis of wounds in mouse nr. 2 (Scale bar = 1 mm)

APPENDIX B

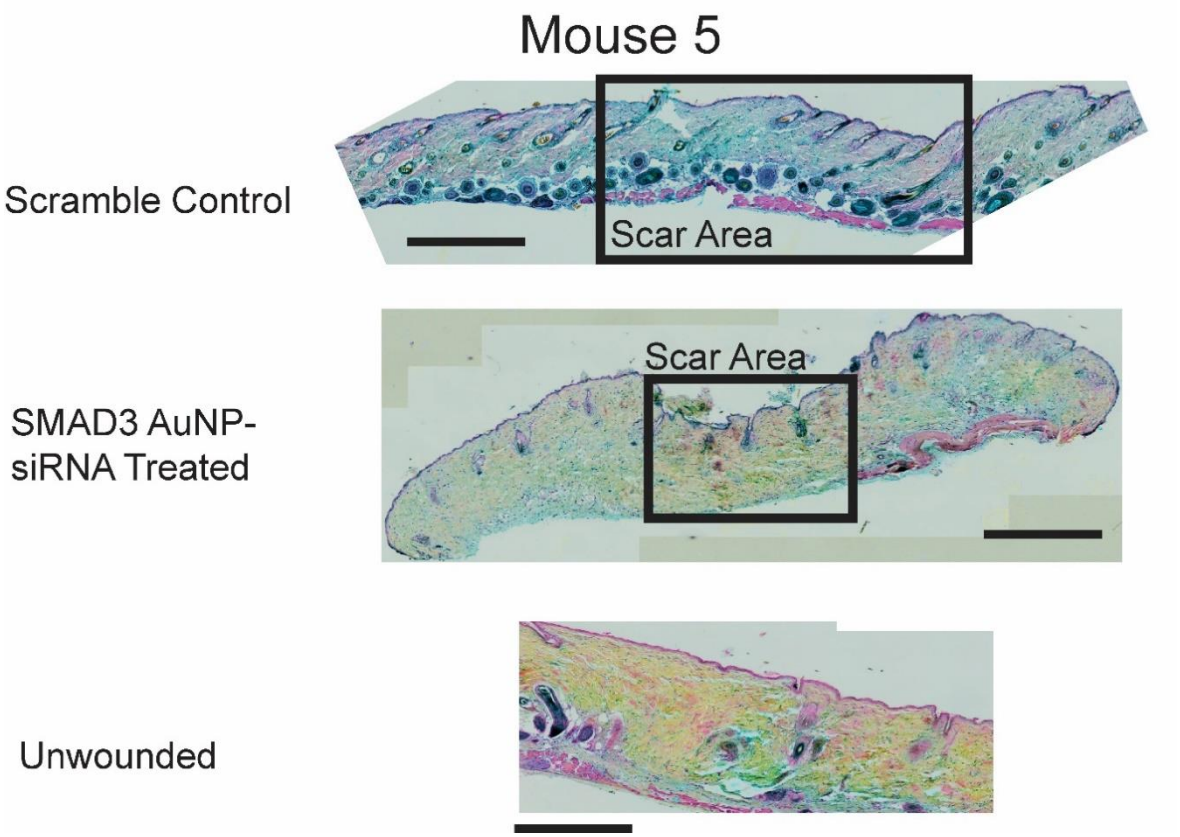

Ac. Material 22. Histological analysis of wounds in mouse nr. 5 (Scale bar = 1 mm)

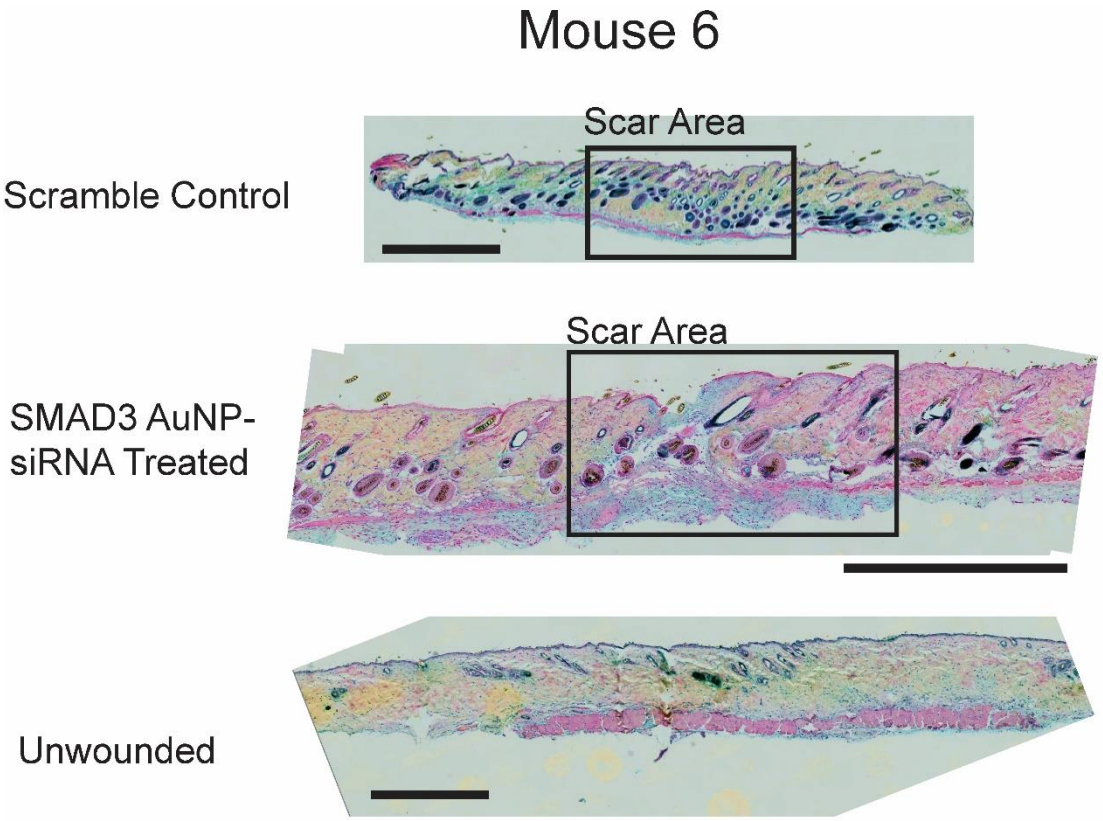

Ac. Material 23. Histological analysis of wounds in mouse nr. 6 (Scale bar = 1 mm)

APPENDIX B

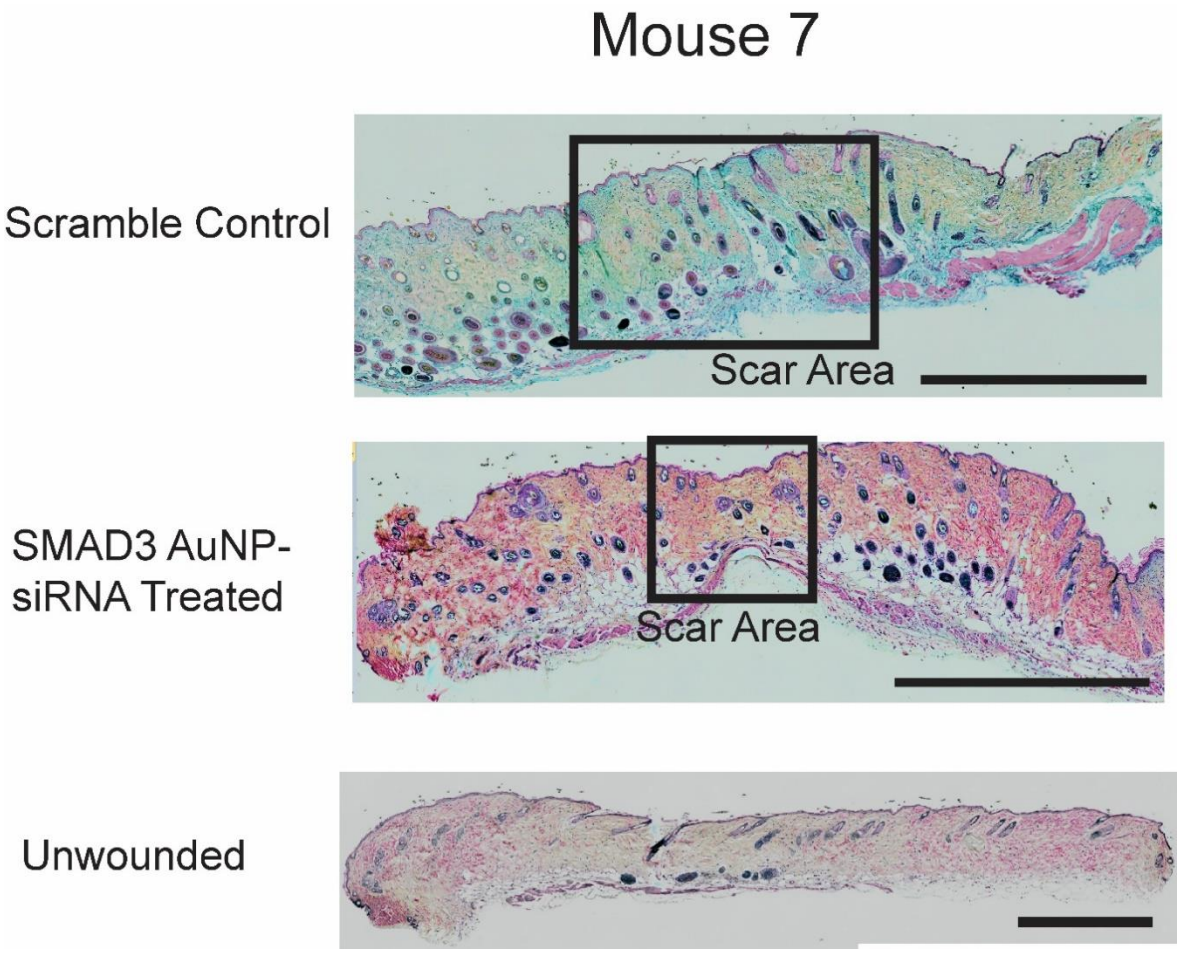

Ac. Material 24. Histological analysis of wounds in mouse nr. 7 (Scale bar = 1 mm)

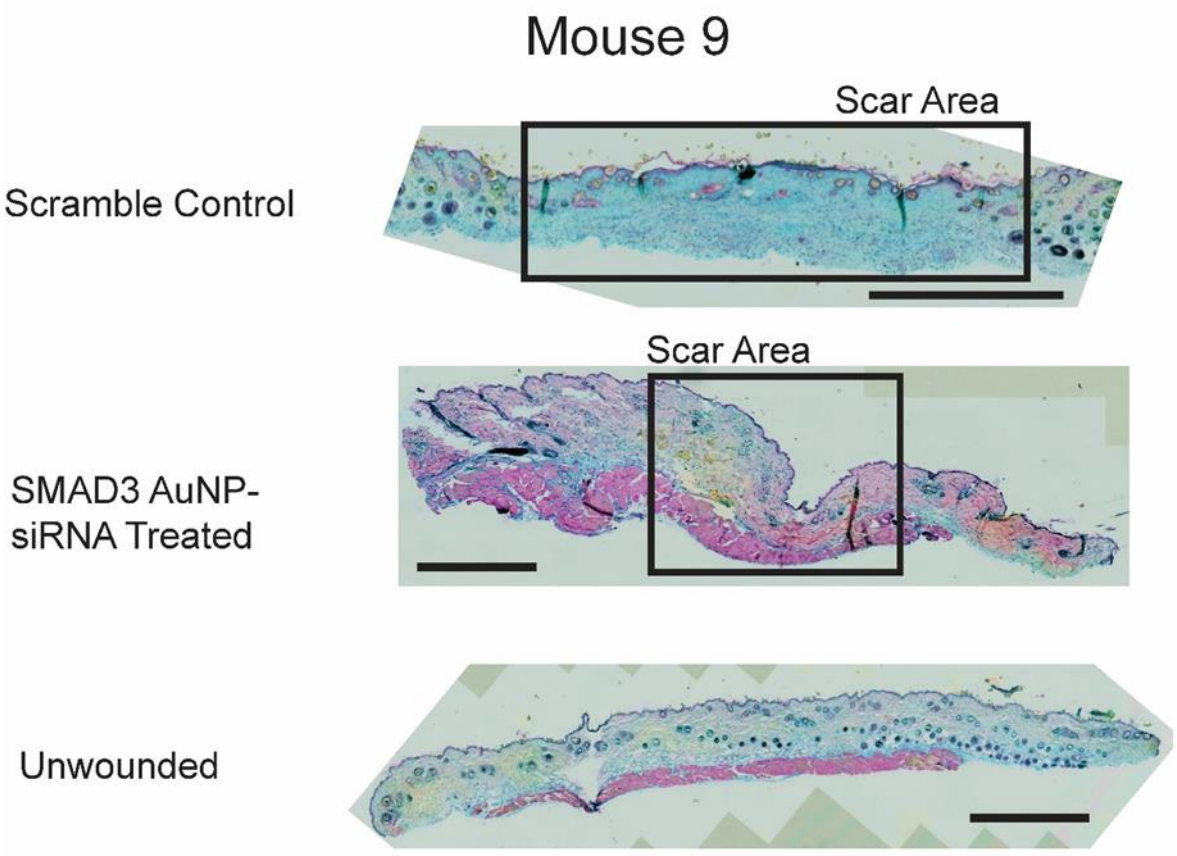

Ac. Material 25. Histological analysis of wounds in mouse nr. 9 (Scale bar = 1 mm)

B.9 References

1. Haiss, W., Thanh, N. T. K., Aveyard, J., & Fernig, D. G. (2007). Determination of size and concentration of gold nanoparticles from UV-Vis spectra. *Analytical Chemistry*, *79*(11), 4215–4221. doi:10.1021/ac0702084

APPENDIX B